To the Graduate Council:

I am submitting herewith a dissertation written by Anand Kumar Ojha entitled "Impact of Noise and Target Fluctuation on the Performance of Hybrid Coded Radar Signals." I have examined the final copy of this dissertation for form and content and recommend that it be accepted in partial fulfillment of the requirements for the degree of Doctor of Philosophy, with a major in Electrical Engineering.

Daniel B. Koch

Daniel B. Koch, Major Professor

We have read this dissertation
and recommend its acceptance:

Donald W. Bouldin

Edward R. Harris

Marshall Pace

Accepted for the Council:

Associate Vice Chancellor
and Dean of The Graduate School

IMPACT OF NOISE AND TARGET FLUCTUATION ON THE PERFORMANCE OF HYBRID CODED RADAR SIGNALS

A Dissertation

Presented for the

Doctor of Philosophy

Degree

The University of Tennessee, Knoxville

Anand Kumar Ojha

May, 1992

This dissertation is dedicated to my loving wife,

Neelam Ojha (Lily)

This dissertation would not have been possible without her support.

ACKNOWLEDGEMENT

I would like to extend my most sincere gratitude to Dr. Dan Koch for his guidance, patience, constructive criticism, advice, and assistance throughout the investigation and the preparation of this dissertation. In addition to the fact that this work is an extension of his doctoral dissertation, his excellent blend of knowledge from the industry and academia has tremendously influenced this dissertation. I distinctly remember two occasions when the investigation went off-track, but thanks to his timely suggestions which were of utmost importance in putting this work on the right course. He painstakingly edited the drafts, and persistently treated even a minor achievement as an important breakthrough to encourage and to instill confidence. Without his establishing the communications laboratory and acquiring the appropriate simulation facilities through funding from the BellSouth Foundation, conducting a thorough investigation of this magnitude would have been much more difficult. He, more than anyone, should be credited for establishing the Communications, Information, and Signal Processing (CISP) Group and the activities developed under its umbrella. He has a knack of creating an open and comfortable environment for discussing research, regardless of the setting. Througout, he has been strict, specific, and thorough in setting the goals of this research, but his accessibility, generosity, warmth, and fairness have been exemplary and have played no smaller role in creating the benevolent atmosphere under which this work was done.

Thanks also to my committee members Drs. Bouldin, Crilly, Harris, and Pace for their interest, comments, and suggestions from the beginning to the final stage of this dissertation. Their cogent comments, especially during the proposal stage, not only provoked me to reevaluate and ultimately better understand my work, but also provided insight into how one asks questions in science. Their helpful suggestions and friendly advice made my graduate experience rewarding, and also made this research stronger and more valuable.

One of the most enriching aspects of graduate school is the friendship offered by fellow students. To Troy Robinson, Masaki Kurosawa, Probir Das, Rick Mitchell, Curtis Jones, Steve Horner, Qin Wan, Luie Al-Baba, Mukul Sirvaikar, and Arun Dalmia: You are what made the good times good, and bad times bearable.

I admire the patience of my teenager son, Rohit, who understood his role during this tough period and was considerate enough not to make any conflicting demands that could distract me and jeopardize the common family goals. You may have missed me off and on, but I have carved a better path for you. You will not only realize the value of education, but will also understand that it is never too late in the search for truth and knowledge.

Finally, and most of all, I like to thank my loving wife Neelam (Lily) for her support and devotion. She provided unflinching financial assistance and continuous encouragement topped with love. Many times when the load seemed too heavy to bear, she gave me the much needed support and encouragement to continue. She deserves the most special thanks for always being there to help and for proudly encouraging me to pursue my dreams, wherever they should take me. I thank her for believing in me, respecting my dreams, and enabling me to achieve what I could never do alone. Her endless patience, quiet encouragement, and unconditional love have helped protect me from myself. This small triumph shine the brightest when reflected in her eyes.

ABSTRACT

Phase coding and linear frequency modulation, either in analog or in discrete form, have been used in the past for pulse compression in peak power limited radar systems to achieve high range resolution. In a recent work, a hybrid coded waveform, which uses phase coding together with frequency stepping, has been shown to improve range resolution. Pulse compression techniques have existed for quite some time, but the impact of operating conditions on their resolution performance has not been reported in the open literature. A major objective of this dissertation has been to fill this void by providing the resolution performance results in the presence of noise, target fluctuation, and channel fading for a few popular and efficient non-hybrid as well as hybrid coded radar pulse compression waveforms from the resolution standpoint.

This dissertation investigates non-hybrid PN sequences, Frank, and complementary coded waveforms, as well as frequency-stepped PN sequences and complementary coded hybrid waveforms. The resolution performance of these pulse compression methods have been evaluated for various combinations of statistical models which include noise, target fluctuation, and channel fading as may be encountered in a practical situation.

A few analytical results, and a large amount of simulation data relating the performance of the pulse compression methods to a wide class of practical situations have been provided in this dissertation. It is concluded that for all of the coding methods, non-hybrid and hybrid, a chip-to-chip amplitude variation is more detrimental at high noise

level than at low noise level. In contrast, a scan-to-scan amplitude variation causes more degradation at low noise level than at high noise level.

Among non-hybrid coding methods, complementary codes generally outperform the Frank and PN sequence codes, with the PN sequence codes having generally been found to demonstrate the worst resolution performance. The effect of codelength on the resolution performance of non-hybrid codes has also been investigated. In general, the statistical models qualitatively affect the hybrid coded waveforms in the same way as they affect non-hybrid coded waveforms. Finally, hybrid complementary coded waveforms always have better resolution performance than hybrid PN sequence coded waveforms.

TABLE OF CONTENTS

LIST OF TABLES

LIST OF FIGURES

CHAPTER 1

Introduction

1.1 Basic Radar Principles and the Need for Waveform Coding

A simple radar consists of a transmitter and a receiver. The transmitter radiates a particular electromagnetic waveform such as a pulse-modulated sinusoid, a portion of which is scattered in all directions by the intercepting object, called the target. The function of the receiver is to detect the energy reflected from the target and to extract information such as the distance and speed of the intercepting object. The time taken by the transmitted signal to travel to the target and back yields information about the distance or range. The Doppler frequency shift is used to extract information about the speed of the target.

An important parameter in the design of a radar system is range resolution, which is the accuracy with which it can distinguish two closely spaced targets as two separate objects. In a simple pulsed radar system, the range resolution can be increased by decreasing the pulse width. However, decreasing the pulse width also decreases the average energy in the echo signal, and adversely affects the reliability of detection in noise. The loss in average signal energy due to a decrease in pulse width can be compensated by increasing the pulse amplitude, but such a solution is often constrained by the peak radiated power limitations of the hardware, especially in airborne radars. Pulse compression waveform design techniques, which employ coded waveforms of longer duration, have been used for achieving most of the benefits of a narrow pulse without exceeding the practical constraints of peak power limitation [1, p. 421]. Using pulse compression, an RF pulse of duration T_p is divided into an integer number of subpulses, called chips, of duration T_c, where the phase or frequency of the RF signal within each chip is changed. Pulse compression has also been called coding in the literature, but is different from error-correction coding in which the objective is to correctly determine each individual bit. Here the purpose of coding for pulse compression is to reliably detect the presence of signal energy without determining the exact form of each transmitted chip. Efficient waveform coding techniques are discussed in detail in the next chapter.

1.2 Motivation

This comprehensive study was undertaken due to a renewed interest in complementary codes which constitute one of several pulse compression techniques for achieving improved range resolution. The properties of complementary codes have been known for about three decades [2], but except for initial limited use in altimetry, the full benefits of using them for efficient radar signal design was pursued only in the 1980's by Sivaswamy [3]. Still, there had been skepticism about the practical implementation of complementary codes in radar systems. Eaves and Reedy had concluded that although these codes might seem to represent the perfect solution to the sidelobe suppression problem, the difficulties involved in their implementation as well as their sensitivities to echo fluctuation would make them less than ideal [4, p. 487]. According to Nathanson, transmitting the subsequences of complementary codes at different times would degrade performance [5, p. 558]. However, these claims were never supported with any theoretical, experimental, or simulation results by any of the researchers.

Despite the above mentioned discouraging comments about the use of complementary codes in practical radar systems, two significant developments took place in the early 1990's. In the first development, a signal processing method, which applied phase compensation to the complementary code subsequences transmitted at different instants of time, was devised to achieve perfect sidelobe cancellation [6]. In a second related development, a hybrid waveform using complementary codes was shown to achieve ideal results after the proposed signal processing [7]. Although these encouraging developments gave a new impetus to complementary codes, the work done until then was limited to ideal situations and did not take into account the impact of noise, target scintillation, and propagation conditions which are well-known to significantly affect the performance of any radar system. It may be added that even for other pulse compression techniques presented in this dissertation no simulation results involving common degrading mechanisms were available in the open literature prior to this investigation. Researchers had put most of their effort in determining the ambiguity function of coded radar signals, defined later in (1.1), in an idealistic noise-free environment. Thus, with regard to the performance of coded radar waveforms in a realistic environment, there has been a lack of published results in the literature, and to this end this investigation is expected to fill that void. It should be mentioned that some of the mathematical analyses which assume realistic situations are too complicated to be solved by analytical methods, and due to the diversity of radar applications, no one model is perfect for all situations. However, with the availability of simulation tools, it has been possible to conduct a broader investigation to determine the behavior of a few efficient coded radar signals for a few widely used models under a worst case situation. This is the principal outcome of this dissertation.

While this research was under way, Hughes Aircraft in 1991 announced having successfully used a hybrid complementary coded waveform to achieve a range resolution of one foot from a distance of 700 feet [8]. This was another major concurrent development in this area, and precluded any doubts about the possibility of practical application of complementary codes. Furthermore, this also confirms that the results provided in this dissertation would be valuable to the radar industry in determining the tradeoffs and suitability of the various pulse compression techniques for the intended application.

The above developments motivated a thorough investigation into the behavior of complementary codes, and consequently necessitated that their suitability or otherwise be judged relative to other pulse compression techniques already in use.

1.3 The Receiver Model

Radar receivers, using either uncoded or coded waveforms, generally employ a matched filter, or correlator, followed by a threshold detector. A conceptual receiver is shown in Figure 1.1. If the matched filtered signal exceeds a given threshold voltage, V_T, the presence of a target is declared. The use of a matched filter is almost unavoidable, because in detection theory it is known to be optimal for recovering signals in a noisy environment. The ambiguity function, $|X(\tau,f_d)|^2$, of a complex signal $s(t)$ having a time shift, τ, and a Doppler frequency shift, f_d, naturally arises in matched filtering, and is defined with the help of the following equation [1, p. 412].

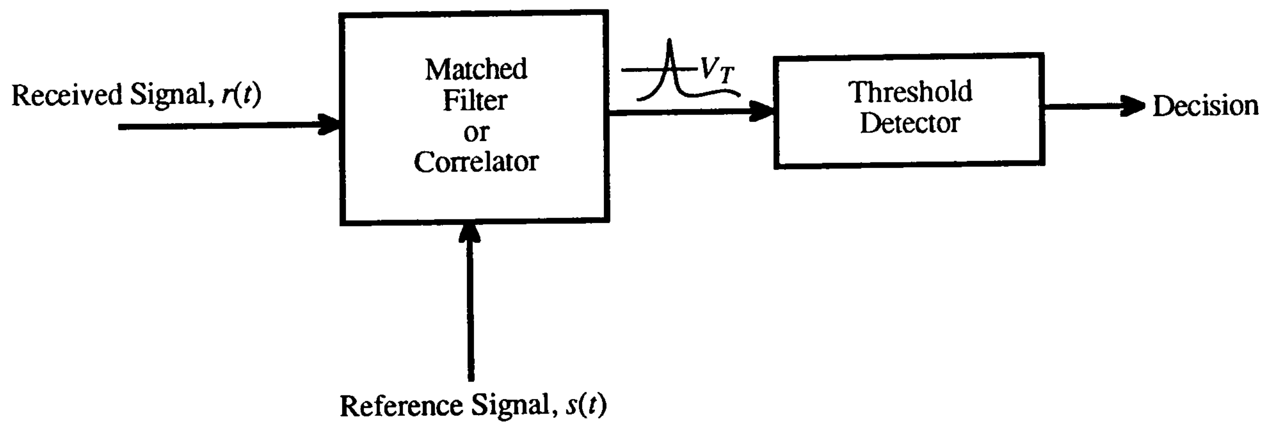

Figure 1.1. The Basic Radar Receiver.

$$X(\tau, f_d) = \int_{-\infty}^{\infty} s(t)s^*(t + \tau)\exp(j2\pi f_d t)dt \qquad (1.1)$$

In (1.1) a positive value of the delay, τ, indicates a target beyond a specific range, and a positive value of the Doppler frequency shift, f_d, indicates an approaching target. The three-dimensional plot of $|X(\tau, f_d)|$ versus τ and f_d is known as the ambiguity diagram and shows the response of the matched filter in the time domain in the presence of a Doppler shift, f_d. Note that for zero Doppler shift in (1.1), $X(\tau, f_d)$ is simply the autocorrelation of $s(t)$. The discrete form of the ambiguity function of a signal $s(t)$ sampled every T_c seconds is given by

$$x(mT_c, f_d) = \sum_{r=-\infty}^{\infty} s(rT_c)s^*[(r+m)T_c]exp[j2\pi f_d rT_c] \qquad (1.2)$$

Autocorrelation is the process of determining the similarity of the received signal with the reference transmitted signal and can be implemented in analog or in its corresponding discrete form. Since the latter lends itself to the power of digital signal processing, this is the approach used in this investigation. The autocorrelation sequence (ACS), R_m, of a real-time sequence, $s(m)$, of length M is given by [9, p. 115]

$$R_m = \sum_{i=0}^{m} s(M-1+i-m)s^*(i) \qquad (1.3)$$

In (1.3), $s(m)$ can be real or complex where the asterisk denotes complex conjugation. Also note that for R_m, $m = 0, 1, ..., 2M-2$, that is, m is non-negative, as would be expected in real-time processing; whereas in the traditional definition of an ACS, $m = -(M-1), ..., 0, ..., (M-1)$ and the ACS is symmetric about the origin. Thus the ACS in (1.3) is simply a shifted version of the traditional ACS. In the radar context, the received samples $r(m)$ are attenuated noisy versions of the transmitted samples, $s(m)$, and so (1.3) can be modified to yield

$$R_m = \sum_{i=0}^{m} r(M-1+i-m)s^*(i) \tag{1.4}$$

Equation (1.4) appears more like a cross-correlation of $r(m)$ and $s(m)$. In the case of simple attenuation of the transmitted signal, $r(t) = Vs(t)$, where V is the attenuation factor. Thus using (1.4) instead of (1.3) simply scales the result of (1.3) by the attenuation factor V. Generally, some normalization of the total energy or of the magnitude of $s(m)$ is often done. Such normalizations also simply scale the autocorrelation samples, but do not affect the final ACS shape. Even under such situations, the terminology *autocorrelation* will be used throughout this dissertation. Without loss of generality, the attenuation factor V and the signal amplitude of $s(t)$ will be assumed to be unity.

The process of performing an autocorrelation on a simple pulse is shown in Figure 1.2. Since radars always use radio frequency (RF) modulated pulses, the actual investigation of this dissertation is based on modulated signals. However, for the sake of simplicity in illustrating the concepts involved, the baseband (unmodulated) pulses have been used here, and a discussion using modulated pulses is temporarily deferred. A baseband pulse of length seven, shown in Figure 1.2(a), is first sampled once per time-unit to obtain the sampled version shown in Figure 1.2(b). The autocorrelation sequence, R_m, shown in Figure 1.2(c), is obtained using (1.4) with the amplitudes of $s(m)$ set to

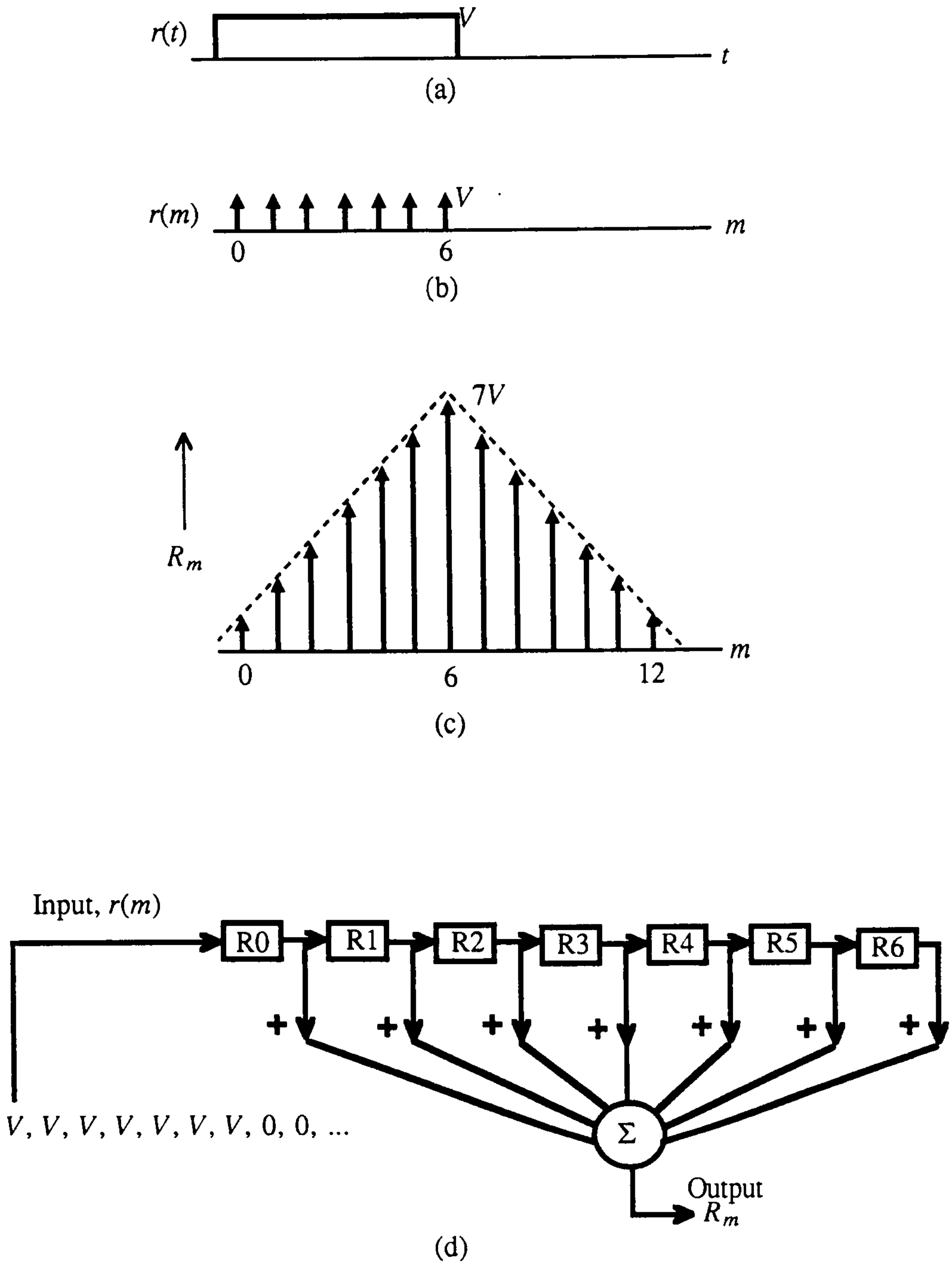

Figure 1.2 Illustration of Performing Sampled Autocorrelation on a Baseband Pulse. (a) The Baseband Pulse. (b) Samples of the Baseband Pulse. (c) Sampled Autocorrelation. (d) The Correlator.

unity. The triangular envelope of the ACS is shown by the dotted line, and is reminiscent of the autocorrelation of an analog pulse. Using (1.4) instead of (1.3) simply scales the amplitudes of the samples by V. Figure 1.2(d) shows a popular implementation of an autocorrelator [1, p. 428]. The system can be constructed using shift registers or delay lines. The next example will make it clear as to how this scheme performs discrete autocorrelation.

To clarify the autocorrelation process, a second example is shown in Figure 1.3. In this case, a data-stream is shown in Figure 1.3(a), which is sampled to obtain the discrete samples shown in Figure 1.3(b). The ACS shown in Figure 1.3(c) is obtained by using the autocorrelator in Figure 1.3(d). The plus and minus signs indicate multiplication of the outputs from the shift-registers by +1 and -1 respectively. It is important to note in this bipolar case that the plus and minus signs are in agreement with the signs of the input samples taken in reverse order. The autocorrelator of Figure 1.3(d) is also the matched filter for the given sequence, and hence is optimal from a detection point of view. The terminology, matched filter, or decoder, will be used interchangeably to describe the autocorrelator. Decoders for implementing autocorrelations of any sequence with arbitrary length can be easily structured in a similar manner.

The presence of the pulse of Figure 1.2 or the data-pattern of Figure 1.3 can be recognized by a threshold detector, which declares the presence of the pulse if the ACS exceeds a predetermined value, V_T, called the threshold. Having described the basic structure of a radar receiver, it is now possible to illustrate how coding improves range resolution. In the following, an example is given to illustrate this.

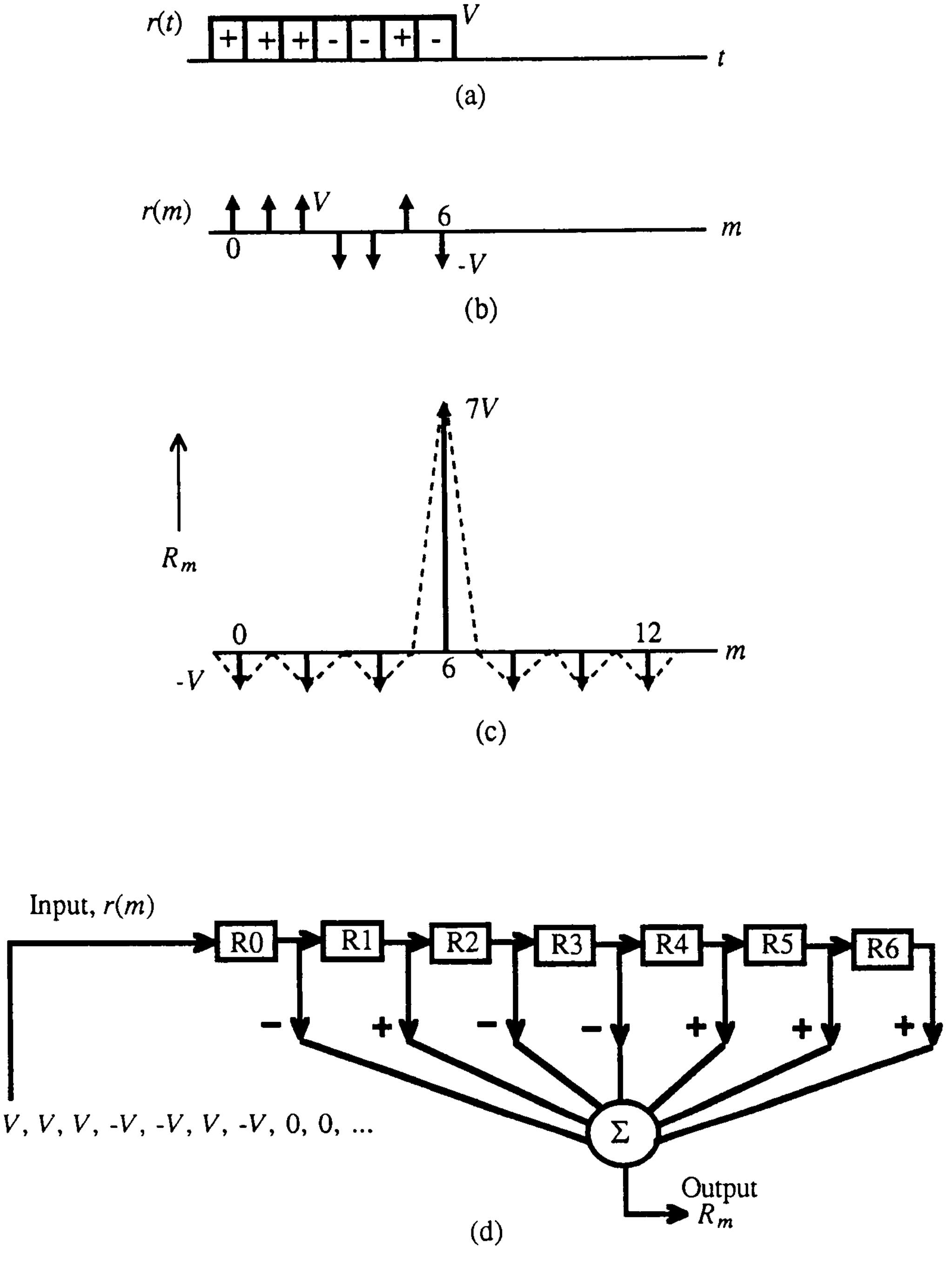

Figure 1.3. Illustration of Performing Sampled Autocorrelation on a Bipolar Baseband Data-stream. (a) A Bipolar Baseband Data-stream. (b) Samples of the Data-stream. (c) Sampled Autocorrelation. (d) The Correlator.

1.4 How Coding Improves Range Resolution

Again, for the sake of simplicity, samples of the baseband version of an echo signal in a noise-free environment are assumed for the present. Figure 1.4 shows the echo signals from two different targets, and their autocorrelations. Since the echoes have a wide separation between them, a threshold detector set to a threshold value, V_T, can clearly identify the two echoes to be from two separate entities. However, as shown in Figure 1.5, as the spacing $\Delta\tau$ shrinks, the autocorrelation triangles merge resulting in a longer single echo which can be incorrectly interpreted as the presence of a single target. In Figure 1.6, the echoes from two targets for a binary Barker coded signal are shown. It can be seen that for the coded radar signal in Figure 1.6, the autocorrelations have short duration peaks, and the echoes can be identified to be from two different targets. As shown in Figure 1.7, even as the spacing between the echoes decreases, unlike Figure 1.5 for the uncoded case, the echoes can still be clearly identified to be from two different targets due to the use of coding. The mainlobe peak will be referred to as the detection peak, and the values elsewhere as sidelobes. This large difference between the mainlobe peak and sidelobes is used to advantage in the reliable detection of radar signals.

1.5 The Quadrature Receiver

As mentioned before, sampled baseband pulses have been liberally used in the literature for the sake of simplicity in illustrating the concepts involved. However, actual radars always use RF modulated pulses. Since this investigation is based on realistic RF modulated pulses, the receiver used for detecting the modulated radar signals is described in this section. Such a receiver is also called a quadrature detector, I-Q detector, or

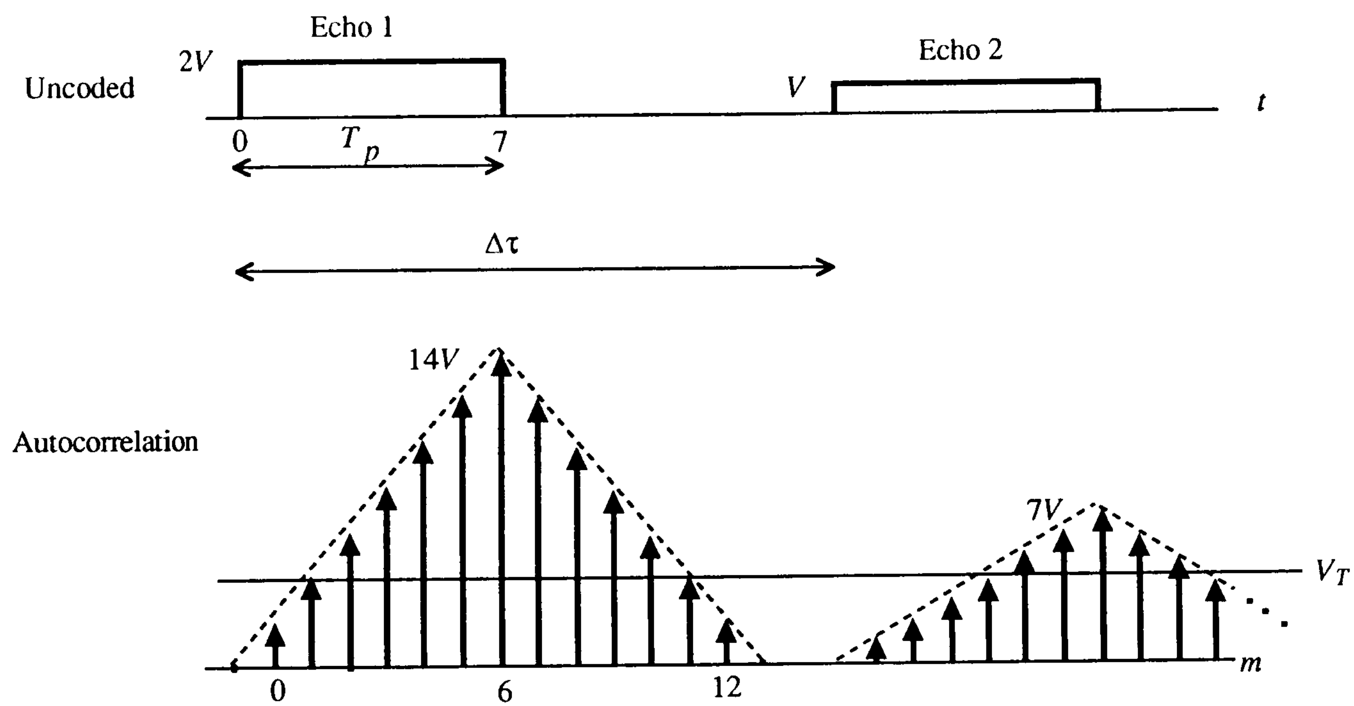

Figure 1.4. Detection of Radar Echoes by Sampled Autocorrelation.

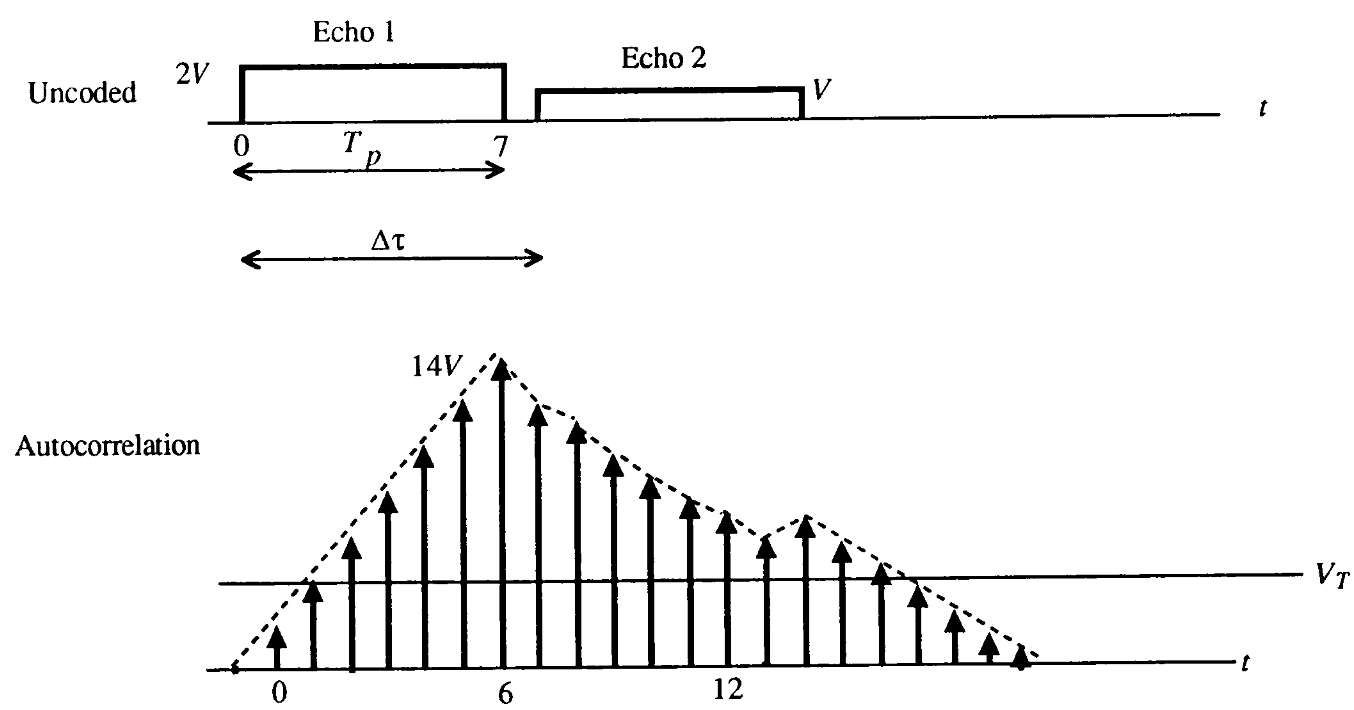

Figure 1.5. Detection of Closely Spaced Uncoded Radar Echoes by Sampled Autocorrelation.

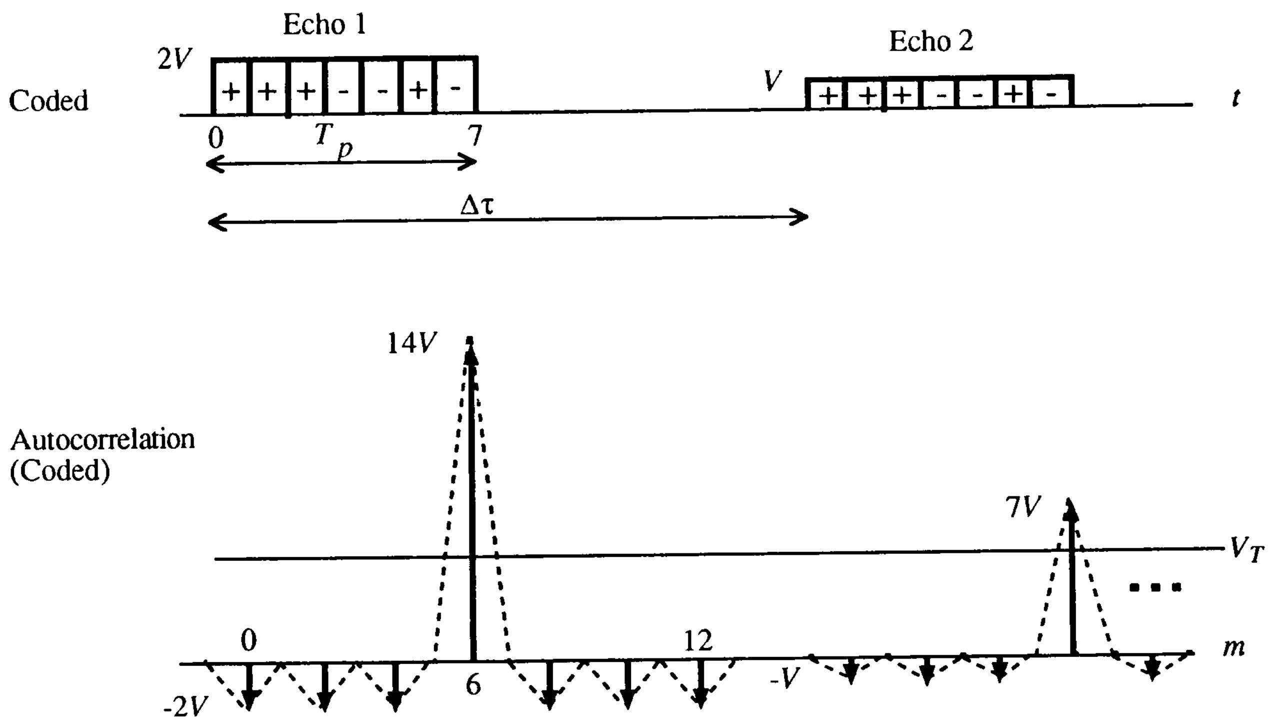

Figure 1.6. Detection of Coded Radar Echoes by Sampled Autocorrelation.

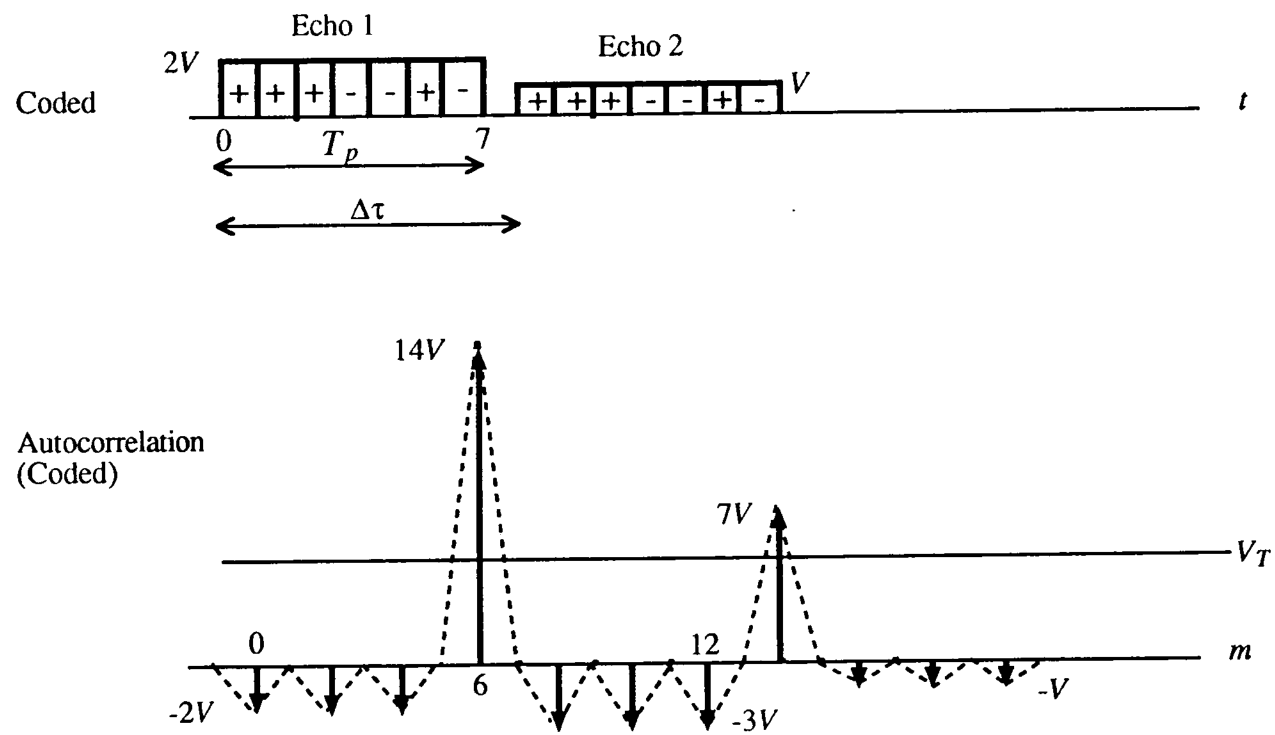

Figure 1.7. Detection of Closely Spaced Coded Radar Echoes by Sampled Autocorrelation.

bandpass processor in the literature. A possible implementation of such a bandpass processor is shown in Figure 1.8. First, the frequency of the received signal is down-converted by an RF local oscillator to some Intermediate Frequency (IF), and then bandpass filtered. The two IF oscillators together with the low pass filters produce the in-phase and quadrature analog signal components at a relatively low frequency, commonly referred to as the video frequency, f_o. The in-phase (I) and quadrature (Q) video signals are then sampled and separately match filtered to generate the final I and Q samples. A noise-free situation is discussed here, and it is shown in in the following discussion that the output of the quadrature receiver is the magnitude of the autocorrelation of the input sequence.

In Figure 1.8, A_m is the magnitude of the m-th sample out of the processor due to an arbitrary modulated input sequence, and is given by

$$A_m = |I(m) + jQ(m)| \tag{1.5}$$

An analysis of the quadrature receiver without a few restrictive assumptions about the relationship among some of the timing parameters loses touch with the physical process. Thus, in order to better clarify the physical process, the following assumptions are made:

1. The target is a point target, and there is no relative motion between the target and the radar. This implies that there is no Doppler shift. In the case of a known Doppler shift, such as in a ground mapping application, the video

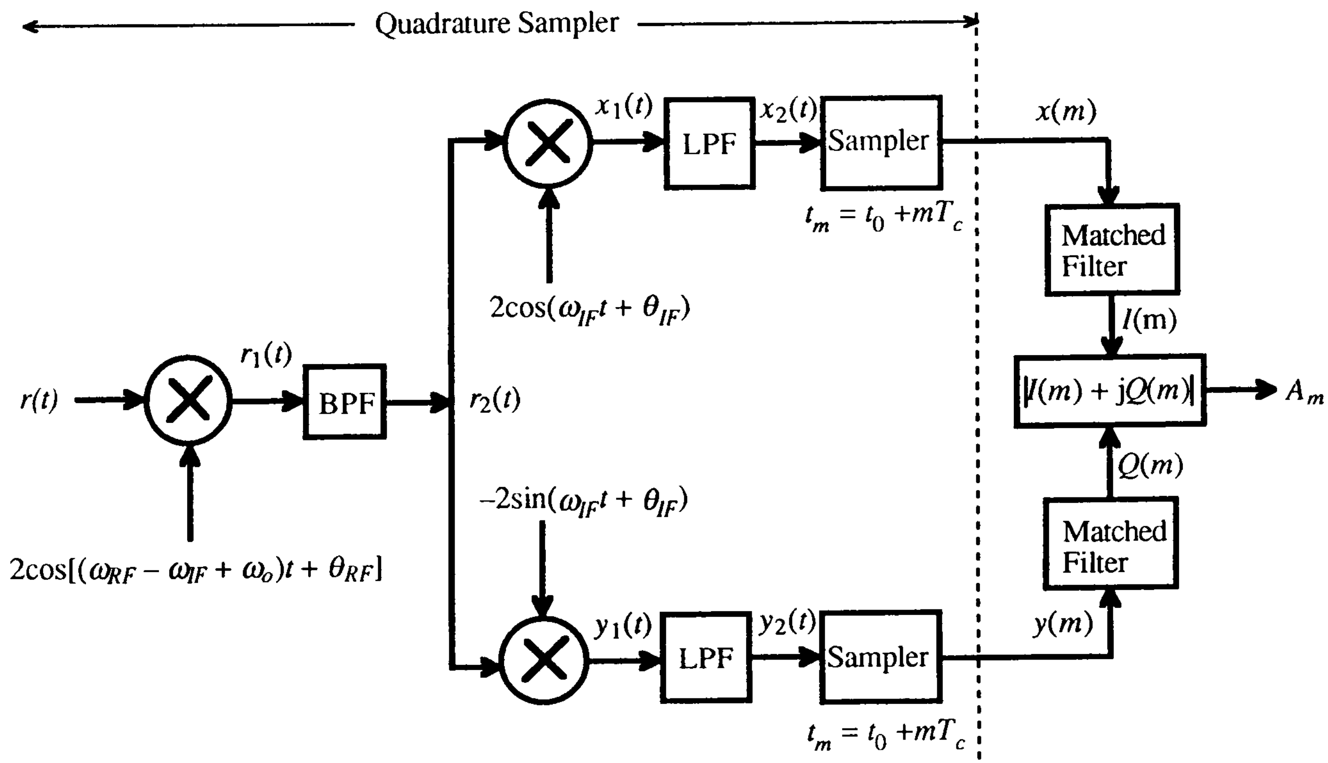

Figure 1.8 The Quadrature Bandpass Receiver.

frequency, f_o, can be properly adjusted to satisfy the next assumption. Otherwise, a phase compensation technique can be applied [6].

2. The chip time is an integer multiple of the time period of the video signal, i. e., $T_c = n/f_o$, where n is an integer.

In general, a unit amplitude, complex-valued, phase encoding sequence of length M can be described as

$$s(m) = \exp(j\phi_m); \quad m = 0, 1, ..., M-1. \tag{1.6}$$

As will be seen later, (1.6) can be used in a unified manner to conveniently represent any phase coded sequence – binary or polyphase. Note that $\phi_m = \{0, \pi\}$ corresponds to the binary phase coding. However, in a practical implementation, instead of a complex discrete signal as in (1.6), consider a real RF received signal, $r(t)$, in Figure 1.8 having the following representation during the m-th chip

$$r(t) = \begin{cases} \cos(\omega_{RF}t + \phi_m), & mT_c \leq t \leq (m+1)T_c; \\ 0, & \text{otherwise.} \end{cases} \tag{1.7}$$

where, T_c is the chip interval, $m = 0, 1, ..., M$-1, and ϕ_m is the phase of the m-th chip. It can be shown [see Appendix 1] that in Figure 1.8 the quadrature samples at $t_m = t_0 + mT_c$ are given by

$$x(m) = \cos(\gamma + \phi_m) \tag{1.8}$$

and

$$y(m) = \sin\left(\gamma + \phi_m\right) \tag{1.9}$$

where,

$$\gamma = -(\omega_o t_0 + \phi + \theta) \tag{1.10}$$

is some unknown but constant phase, and t_0 is the sampling instant of the first sample corresponding to $m = 0$. Figure 1.9 illustrates the relationship among various waveforms of only the I-channel for a real modulated signal derived from a 4-sample long encoding sequence, $s(m) = \{1, 1, 1, -1\}$, for the situation when the time period of the video frequency signal is equal to the chip time; this corresponds to $n = 1$ in Assumption 2 above. For this example encoding sequence $\phi_m = \{0, 0, 0, \pi\}$.

As required by (1.3), the quadrature samples in (1.8) and (1.9) must be matched filtered by separately correlating with the encoding sequence to obtain $I(m)$ and $Q(m)$ shown in Figure 1.8. Inserting (1.8) and (1.9) in (1.3) yields

$$I(m) = \sum_{i=0}^{m} \cos\left(\gamma + \phi_{M-1+i-m}\right) s^*(i) \tag{1.11}$$

and

$$I(m) = \sum_{i=0}^{m} \sin\left(\gamma + \phi_{M-1+i-m}\right) s^*(i) \tag{1.12}$$

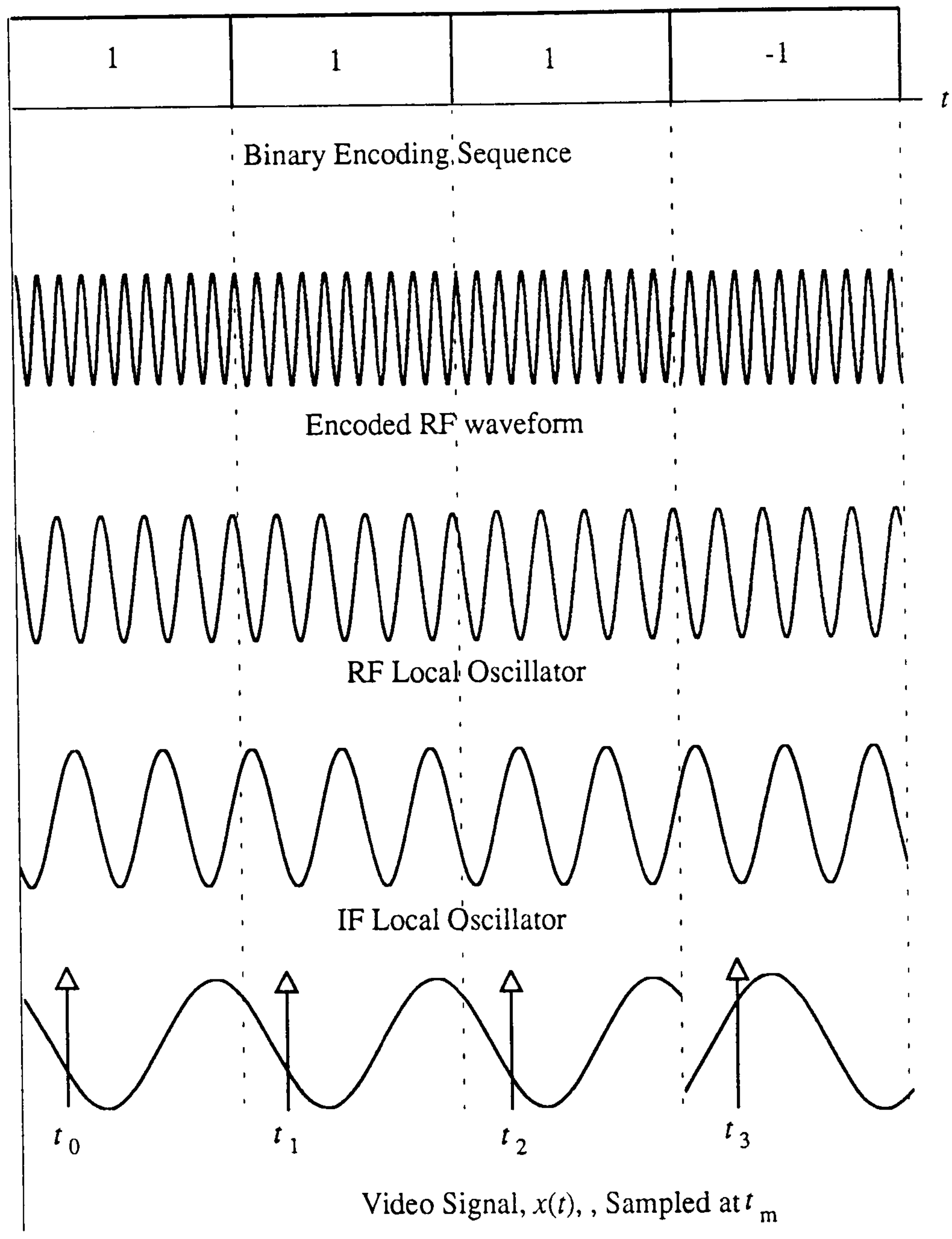

Figure 1.9. Waveform Relationship in the Quadrature Detector for the I-channel.

In the case of binary phase coding, $\phi_m = \{0, \pi\}$, and so the encoding sequence in (1.6) gets modified to $s(m) = \cos\phi_m$. Hence, it can be verified using (1.11) and (1.12) that in the special case of binary phase coding

$$I(m) = R_m \cos\gamma \quad \text{(Biphase case)} \tag{1.13}$$

and

$$Q(m) = R_m \sin\gamma \quad \text{(Biphase case).} \tag{1.14}$$

For the general case, A_m in Figure 1.8 can be found by substituting (1.11) and (1.12) in (1.5) resulting in

$$\begin{aligned} A_m &= \left| \sum_{i=0}^{m} \left[\cos\left(\gamma + \phi_{M-1+i-m}\right) + \mathrm{j}\sin\left(\gamma + \phi_{M-1+i-m}\right) \right] s^*(i) \right| \\ &= \left|\exp(j\gamma)\right| \left| \sum_{i=0}^{m} \exp\left[\mathrm{j}\phi_{M-1+i-m}\right] s^*(i) \right| \\ &= \left|\exp(j\gamma)\right| \left| \sum_{i=0}^{m} s(M-1+i-m) s^*(i) \right| \end{aligned} \tag{1.15}$$

Since $|\exp(\mathrm{j}\gamma)| = 1$, using (1.6) and (1.3) yields $A_m = |R_m|$, which confirms that the quadrature receiver shown is Figure 1.8 simply yields the magnitude of the autocorrelation of the encoding sequence, $s(t)$. In this sense, the quadrature receiver can be thought of as an envelope detector. The only difference between using a quadrature receiver for a realistic modulated radar signal and the simple matched filter for the corresponding convenient baseband sampled signal is that the former scheme yields only the magnitude of the ACS. The implication of this fact on the examples ACS's provided in Figures 1.3(c), 1.6, and 1.7 is that the negative values of the ACS's should actually be treated as positive values for a practical system.

1.6 Desirable Properties of Good Codes for Range Resolution

An ideal radar signal's autocorrelation should have a spike-like, non-zero value only at a single point in the time domain for maximum range resolution. This desirable shape for the autocorrelation function is commonly referred to in the literature as the "thumbtack" characteristic. Considering the power limitation and detectability in a noisy environment, the autocorrelation of a coded radar signal should have the following characteristics:

1. Small sidelobes.
2. Large peak-to-sidelobe ratio.
3. Low peak power (codelength of 100 or more) [10, p. 7]
4. Low average power (Pulsed radar.)
5. High probability of detecting the mainlobe, and low probability of false alarm at the sidelobes in a noisy environment.

1.7 Objective and Scope

This dissertation is concerned with the evaluation of the performance of coded radar signals from the resolution standpoint in a realistic environment. To achieve this objective, tasks of this research have been divided into the following four stages:

1. First, a few potential candidates from a host of well-known coding techniques have been identified. These are:
    a. Pseudonoise (PN) sequence codes.
    b. Frank codes.
    c. Complementary codes.
    d. Complementary codes with frequency stepping.
    e. PN sequence codes with frequency stepping.
2. Next, a few statistical models have been chosen to include the effect of realistic operating situations in the radar context. Three such statistical models have been used to simulate realistic situations. These are:
    a. The additive white Gaussian noise (AWGN) environment.
    b. The Swerling I and II models for fluctuating targets [11].
    c. The Rayleigh fading channel model.

    Various combinations of these models have been used in this investigation.

3. Then a methodology has been developed and a procedure has been outlined so that a fair comparison of the resolution performance could be made for the selected pulse compression techniques.

4. Finally, a combination of analytical methods and Monte Carlo simulations has been used to quantify the performance of the selected coding techniques under the chosen statistical models. Analytical methods have been applied to the maximum extent possible to make simulations efficient. However, due to the complexity of the problem, closed form solutions could not be obtained exclusively through analytical methods.

1.8 Length of Effort

This problem was undertaken in January 1990, and simulations alone required about 24 computer-months on the Macintosh IIx.

1.9 Preview of the Dissertation

The outline of the dissertation is as follows. The next chapter provides a literature review and related background material on the coding schemes of interest to this research. The statistical models considered in the investigation together with the metric and procedure of performance evaluation are discussed in Chapter 3. A few valuable analytical results are provided in Chapter 4, and the difficulties encountered in accomplishing the objective exclusively through mathematical methods are enumerated. Chapter 5 contains the results and a discussion on non-hybrid coded radar waveforms, and lastly, similar results and a discussion of hybrid coded radar waveforms are presented in Chapter 6.

CHAPTER 2

Literature Review

2.1 Historical Notes on Coding

Radar systems employing analog pulse compression were put into service in the early 1950's [12, p. 218]. Then in 1958, a coded waveform was used by Lincoln Laboratory (MIT) to accurately measure the distance to Venus [12, p.275]. Although the coding used in that system may appear to be primitive by modern standards, it demonstrated the ability of coding in extracting the desired information even in an extremely small signal-to-noise ratio situation. By 1960, coding had become an established technique to improve the resolution of radars operating under a limited power budget [13]. It should be noted that coding introduces additional complexity to a radar system. If a radar system is capable of delivering sufficient peak power, there is hardly enough justification to use coding [1]. However, for a peak power limited radar system, coding is an effective technique to achieve pulse compression which in turn results in better resolution. In pulse compression methods, a longer pulse duration is traded for better resolution.

The interdependence between range resolution and the autocorrelation function motivated researchers to find codes having the desirable thumbtack autocorrelation property, and coding techniques, both in the frequency and the time domain, have been used. In addition, in the hybrid form, encoding in time domain has also been combined with frequency stepping. A catalog of these methods is presented below.

2.2 Binary Phase Coding

In this section, a few efficient binary phase-coding schemes are discussed.

A. Barker: Binary sequences of length M, for which the ratio of the peak sidelobe to the detection peak value does not exceed $1/M$ are called Barker codes [1, pp. 428-429]. The coded sequence in Figure 1.2(a) is a Barker code of length seven. To a great extent, Barker codes possess the desirable thumbtack autocorrelation property; however the longest code found so far has a length of 13, which is considered too small to meet the resolution requirements of present-day radar systems which require code lengths of over one hundred. Due to this reason, Barker codes have been excluded from this investigation.

B. Pseudonoise (PN) Codes: Maximum Length (ML) binary sequences, generated by feedback shift registers, are called pseudonoise (PN) sequences, or m-sequences, because they possess many of the properties of a random binary sequence [5, pp. 543-554]. For longer sequences, the use of PN sequence coded waveforms has been suggested [5, pp. 543-554]. An important property of the PN sequence, that makes it suitable for radar signal design, is that the ACS of the antipodal version of the binary PN sequence has a large mainlobe peak and relatively small sidelobes.

Figure 2.1 shows the scheme used to generate a PN sequence of length seven. The 0's in the bipolar case are treated as -1's. It can be verified that the generated sequence $s(m)$ and its autocorrelation R_m are

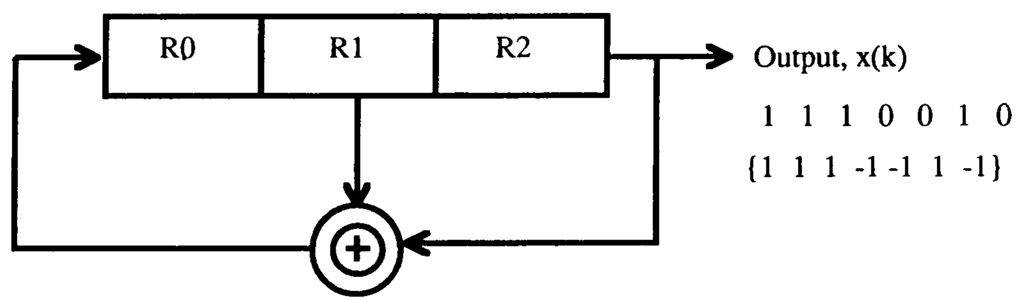

Figure 2.1. Three-stage Shift Register to Generate 7-Sample Long PN Sequence.

$$s(m) = \{1, 1, 1, -1, -1, 1, -1\} \tag{2.1}$$

$$R_m = \{-1, 0, -1, 0, -1, 0, 7, 0, -1, 0, -1, 0, -1\}. \tag{2.2}$$

The sequence in (2.1) was used in Figure 1.2 to illustrate the benefits of coding. As mentioned in Chapter 1, for a practical radar system using a binary phase coded PN sequence, the modulated phase coded signal can be described by (1.7), where $\phi_m = \{0, \pi\}$. For example, the sequence in (2.1) has $\phi_m = \{0, 0, 0, \pi, \pi, 0, \pi\}$. Using an N-stage shift register yields a PN sequence of length M, where N and M are related by

$$M = 2^N - 1. \tag{2.3}$$

It can be noted from (2.3) that PN sequences can have lengths 3, 7, 15, 31, 63, ... etc.

Each end-around shifted version of a PN sequence produces another PN sequence. It is therefore necessary to consider the ACS's of all end-around shifted versions of a particular PN sequence to find the one which has the smallest sidelobes. To illustrate this, consider the PN sequence of length 15 shown in Table 2A.1 of Appendix 2. Column 1 shows the sequence and column 2 the ACS of that sequence. The question is: Which of the 15 sequences has the best ACS for pulse compression? For a single sequence, such as in the present case, this question can be answered with the help of two simple quantities – the peak sidelobe level ratio (PSLR) and the integrated sidelobe level ratio (ISLR) [4, p. 467]. These two quantities are later defined in detail in Chapter 3. Simply stated, the PSLR is the ratio of the largest sidelobe peak to the detection peak value, whereas the ISLR is the ratio of the sum of the power in the sidelobes to the power in the detection peak. In Table 2A.1, there are two sequences with the same lowest value of PSLR and ISLR, and either of the two can be used. Perhaps the one marked with an asterisk (*) is a better choice, because it has zero sidelobe values adjacent to the mainlobe peak.

In the above discussion, a single PN sequence of length 15 was considered, but there are generally more than one unique PN sequences of a given length. Table 2.1 provided below, shows the number of unique PN sequences for a few given lengths [12, p. 296]. In addition to the PN sequence of length 15 shown in Table 2A.1, there is one more PN sequence of length 15 to be considered. However, it can be verified that the other sequence does not yield a better ACS than what is obtained from Table 2A.1. The foregoing explanation was given just to emphasize the need for a thorough evaluation of each of the PN sequences of a given length.

Table 2.1. Number of PN Sequences for a Given Length.

Length of the PN Sequence	Number of PN Sequences
7	2
15	2
31	6
63	6
127	18
255	16

In the above discussion on PN sequences of length 15, only 30 sequences were examined, 15 shifted versions for each of the two PN sequences. However, there are a total of 32768 unique binary sequences of length 15. A natural question arises at this point: Does the best PN sequence arrived at by examining only the PN sequences of a given length yield the optimum code for pulse compression? The answer is no. The following arbitrary sequence, obtained through a computer search of 32768 possible sequences, has a PSLR of 2/15, and an ISLR of 48/225.

$$s(m) = \{-1, -1, 1, 1, -1, -1, -1, -1, -1, 1, -1, 1, -1, 1, 1\} \tag{2.4}$$

$$R_m = \{-1, -2, 1, 2, -1, -2, -1, 0, 1, 0, 1, -2, 1, -1, 15, ...\} \tag{2.5}$$

Although, in a strict sense, the best PN sequence is suboptimal for pulse compression, it is still very close to the optimal sequence. The optimal arbitrary sequences have been called minimum peak sidelobe (MPS) sequences by Nathanson, and he has provided a compilation of such optimal codes up to length 48 [5, p. 540]. A formal theory to find such MPS sequences does not exit, and these optimal codes have been found only through a computer search; some researchers have used computers exclusively dedicated to this task [5, pp. 539-541]. The difficulty in applying a computer search for finding optimal codes of longer lengths can be gauged from the fact that if one attempts to find an MPS code of length 127, then the 127-point ACS for 2^{127} (= 1.7 X 10^{38}) sequences are required. Assuming that a super-fast vector computer takes only 1 pico-second to perform a 127-point ACS on each sequence, it will still take 5.4 X 10^{18} years! In contrast, there are only 18 PN sequences of length 127, and this requires examining only 2286 autocorrelation sequences, and the resulting best PN sequence has a "relatively good" PSLR and ISLR.

The approximate value of the PSLR of the ACS of a PN sequence of length M, is [1, p. 430]

$$\text{PSLR (dB)} \approx 10 \log\left(\frac{1}{M}\right) \tag{2.6}$$

Thus, the popularity of PN sequences in the radar context is due to the fact that they have "relatively good" pulse compression capability, and longer sequences can be easily generated using simple shift registers. These characteristics have motivated their inclusion in this research. It is not suggested here that other binary codes of longer lengths having better PSLR or ISLR than the PN sequence codes do not exist. Random computer searches have been used by various researchers to find codes of longer lengths possessing marginally better ACS's than the corresponding PN sequences, but it has not been ascertained if the codes found in this manner have optimal PSLR or ISLR values [5, p. 541].

C. Complementary Codes: Complementary codes, described below, have received greater interest over the years in the area of high-resolution radar signal design, because the algebraic addition of the autocorrelations of individual subsequences results in a single sharp mainlobe peak and zero time sidelobes [2, 3, 14–19]. Due to perfect sidelobe cancellation, complementary codes appear to be the ideal answer the researchers have been seeking.

A complementary code pair, as defined by Golay, consists of two equal length subsequences with the property that the algebraic sum of the ACS's of the subsequences is zero except for only one sample point [2]. One of the two subsequences will be referred to in this dissertation as the *direct subsequence* and the other one as the *complement subsequence.* No such names exist in the literature, but the purpose of coining these two terms is to add clarity. These two subsequences will be denoted by $s^D(m)$ and $s^C(m)$, respectively. In these notations, and all subsequent notations, the superscripts D and C will be used to identify the direct and the complement subsequences respectively. Since complementary codes use phase coding, $s^D(m)$ and $s^C(m)$ have the same form as (1.6). Specifically,

$$s^D(m) = \exp\left(j\phi_m^D\right) \tag{2.7}$$

and

$$s^C(m) = \exp\left(j\phi_m^C\right) \tag{2.8}$$

where, $\phi_m^D = \{0, \pi\}$ and $\phi_m^C = \{0, \pi\}$. In following the above notations, the received samples can be denoted by $r^D(m)$ and $r^C(m)$.

As an example of a complementary code pair, consider the following two subsequences.

$$s^D(m) = \{1, 1, 1, -1\} \tag{2.9}$$

$$s^C(m) = \{1, 1, -1, 1\} \tag{2.10}$$

The ACS of the subsequences in (2.9) and (2.10) are respectively

$$R_m^D = \{-1, 0, 1, 4, 1, 0, -1\} \tag{2.11}$$

$$R_m^C = \{1, 0, -1, 4, -1, 0, 1\} \tag{2.12}$$

Adding the two autocorrelation sequences together, element-by-element, yields the final decoded sequence R_m as

$$R_m = \{0, 0, 0, 8, 0, 0, 0\}. \tag{2.13}$$

Mathematically, the sidelobe cancellation property of a complementary code pair can be expressed as

$$R_m^D + R_m^C = \begin{cases} 2R_m^D = 2R_m^C, & m = \text{mainlobe;} \\ 0, & m = \text{sidelobe.} \end{cases} \tag{2.14}$$

The autocorrelations on the subsequences in (2.9) and (2.10) can be performed by separate decoders having structures similar to the one shown in Figure 1.2(d). Of course, the plus and minus signs at the output taps of the shift registers will be different for the two implementations.

Interesting algorithms for generating and decoding the complementary code pairs do exist [2, 19]. The general structure, known as the Golay Type I encoder, used to generate the complementary code pair above is shown in Figure 2.2. The rectangles shown therein are delay elements implemented by shift registers. The upper branch of the

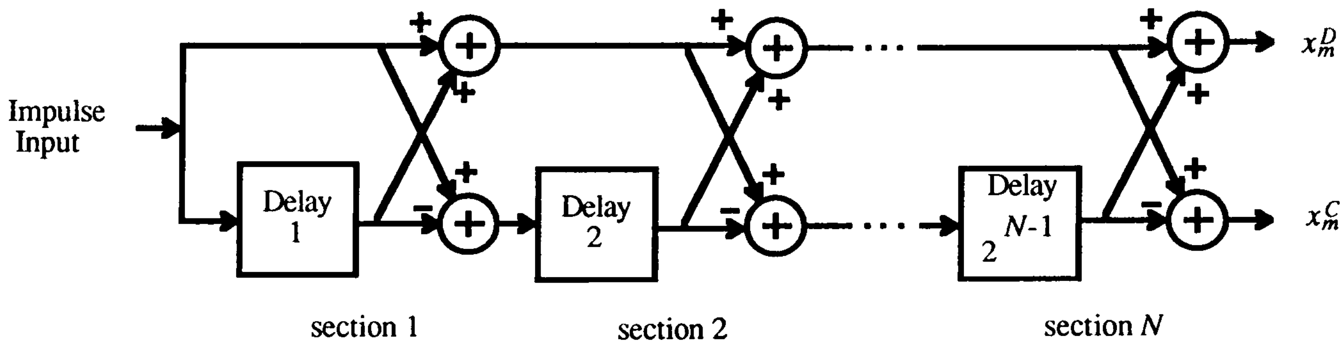

Figure 2.2. Golay Type I Encoder to Generate Complementary Code Pair.

encoder, consisting of N sections, generates the direct subsequence, and the lower branch generates the complement subsequence, each of length

$$M = 2^N, \tag{2.15}$$

when a unit impulse is applied to it. It can be verified that a two-section long encoder of the form shown in Figure 2.2 indeed generates the sequences in (2.9) and (2.10).

The structure of the decoder is also very simple to implement using shift registers and adders. The Golay Type I decoder, shown in Figure 2.3 can be used to perform an autocorrelation on either of the subsequences. If the input sequence is $s^D(m)$, followed by 2^N-1 zeros, the upper branch of Figure 2.3 produces R^D_m. Note that the required number of zeros needs to be appended to obtain the full length of the ACS. For example, if the subsequence length, M, is four, its ACS has to be of length seven. Therefore, the decoder must be clocked seven times with four data samples followed by three zeros. Similarly, if the input sequence is $s^C(m)$, followed by 2^N-1 zeros, the lower output branch produces R^C_m. Figure 2.4 provides a conceptual scheme to show how the same decoder can be used to sequentially perform autocorrelation on each of the received subsequences in the radar context, though it does not imply any specific implementation. Instead of using a sequential method, the two subsequences can be simultaneously transmitted or received on two separate frequencies [5, p. 558]. However, an additional purpose of introducing the schematic and the timing relationships is to define or clarify the following notations and terminologies for later use.

T_p = Pulse width: Time-duration of a pulse (sequence or subsequence.)

T_c = Chip time : Time-duration of a single coded entity of T_p.

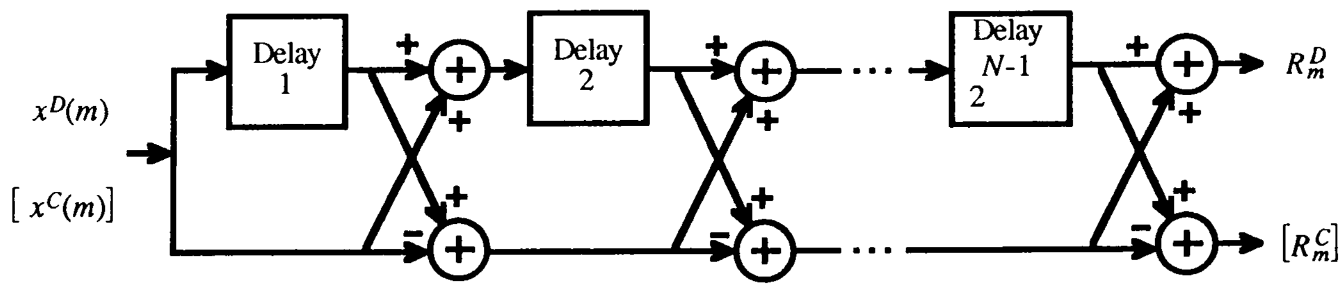

Figure 2.3. Golay Type I Decoder (Matched Filter)

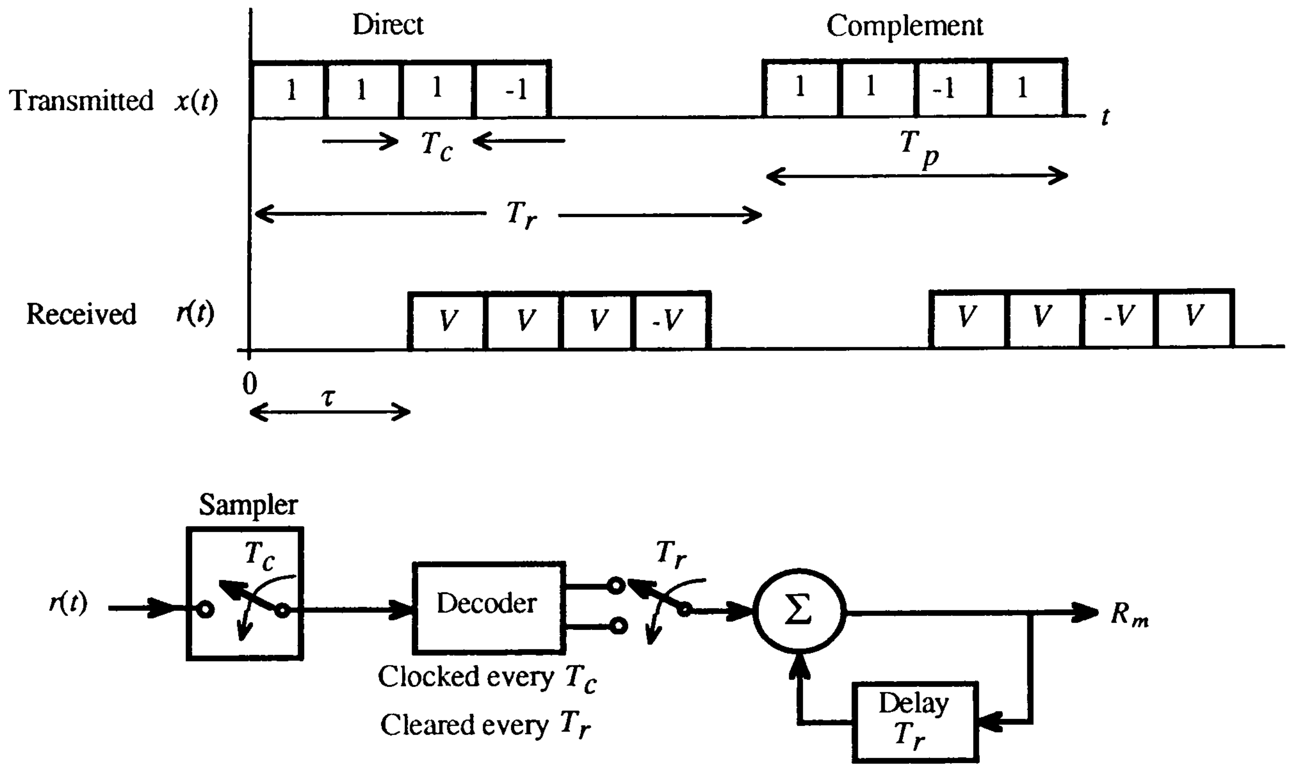

Figure 2.4. Timing Relationship and Decoding Scheme for Complementary Code Pair.

T_r = The interpulse (or inter subsequence) duration.

τ = The time delay between transmitting and receiving the pulse.

The decoder shown in Figure 2.4 is cleared when a new subsequence is transmitted. The sampler samples once every chip-duration, and the sampled outputs of the direct subsequence is delayed by T_r to perform addition with the complement subsequence. For proper operation, the timing relationship

$$T_r > \tau_{max} + T_p \tag{2.16}$$

must be satisfied. On the basis of PSLR and ISLR of the final decoded sequence, the complementary codes appear to be ideal, because they have zero sidelobe values, and so both of these quantities are zero in this case!

Complementary codes also use binary phase coding. Therefore, the modulated subsequences can be described by (1.7). The modulated RF signal of the direct coded subsequence can be expressed as

$$r^D(t) = \begin{cases} \cos\left(\omega_{RF}t + \phi_m^D\right), & mT_c \le t \le (m+1)T_c; \\ 0, & \text{otherwise}; \end{cases} \tag{2.17}$$

Similarly, the modulated form of the complement subsequence can be described as

$$r^C(t) = \begin{cases} \cos\left(\omega_{RF}t + \phi_m^C\right), & T_r+mT_c \le t \le T_r+(m+1)T_c; \\ 0, & \text{otherwise}; \end{cases} \tag{2.18}$$

and as mentioned before, T_r is the time-delay between transmitting the two subsequences. Following the analysis in Appendix 1, it can be shown that if T_r is an integer multiple of the chip-time, T_c, the direct and complement quadrature samples of a complementary coded waveform are given by

$$x^D(m) = \cos\left(\gamma + \phi_m^D\right) \tag{2.19}$$

$$y^D(m) = \sin\left(\gamma + \phi_m^D\right) \tag{2.20}$$

$$x^C(m) = \cos\left(\gamma + \phi_m^C\right) \tag{2.21}$$

$$y^C(m) = \sin\left(\gamma + \phi_m^C\right) \tag{2.22}$$

Note the similarity of the above equations with (1.8) and (1.9) in Chapter 1. In order to match filter, the quadrature samples of the direct subsequence in (2.19) and (2.20) are correlated with the reference direct subsequence, and the quadrature samples of the complement subsequence in (2.21) and (2.22) are correlated with the reference complement subsequence. The conceptual process of match filtering the quadrature subsequences and adding them to obtain sidelobe cancellation is shown in Figure 2.5 which is an extension of the concepts illustrated in Figure 2.4. The quadrature sample pairs in (2.19)–(2.22) are generated using the quadrature sampler shown in Figure 1.8, and the direct coded quadrature samples are delayed by T_r in order to perform a coherent addition with the complement code quadrature samples. It can be shown that in the absence of any noise, the output sample, A_m, in Figure 2.5 is simply the magnitude of the sum of the autocorrelations of the encoding subsequences [see Appendix A2.1].

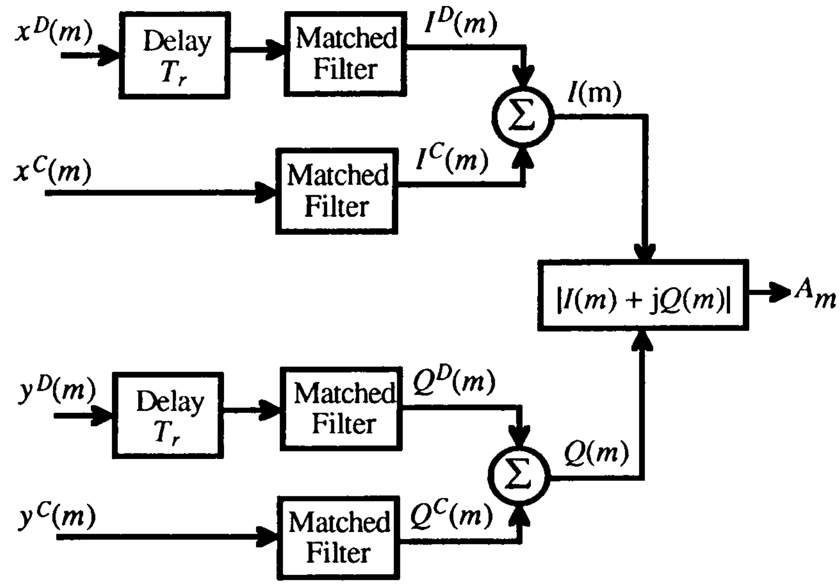

Figure 2.5. Detection of Complementary Coded Radar Signal.

Complementary codes and their properties were known for about three decades, but a major cause of concern in their practical utilization in a radar system was possibly the fact that they required the transmission of the subsequences at different times. Transmitting the subsequences at different times results in an additional phase term as a result of which sidelobe cancellation is not achieved. Furthermore, binary phase coded waveforms have been known to be more sensitive to Doppler shift. These factors might have contributed to a limited study of complementary codes in the radar context. However, signal processing methods have been devised to compensate for the additional phase terms arising out of transmitting the two subsequences at different times and also to cancel the sidelobes even in the presence of Doppler shift [7].

2.3 Frequency Modulation Coding

The codes considered below achieve pulse compression using frequency modulation.

A. Linear Frequency Modulation: Historically, linear frequency modulation (FM), or "chirp" was the first pulse compression technique put to practice [12, pp. 216-218]. In this case, the transmitted pulse of width T is modulated by a radio frequency (RF) carrier whose frequency linearly increases from f_1 to f_2. The received signal, $r(t)$, which is an attenuated version of the transmitted signal, is shown in the time-domain in Figure 2.6(a). The frequency-time characteristic of the received signal is shown in Figure 2.6(b). The received signal is then passed through a delay network which has a longer delay for lower frequencies than for the higher frequencies. The delay network, which

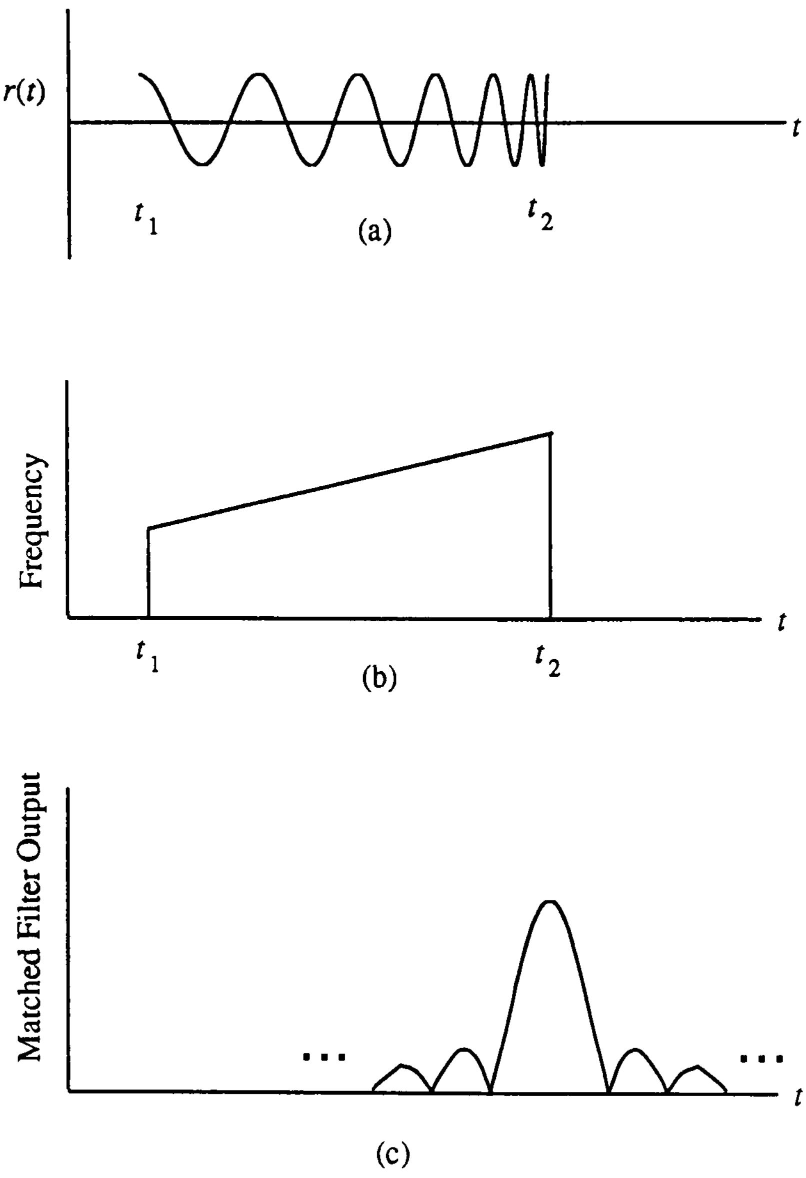

Figure 2.6. Illustration of Pulse Compression Using Linear Frequency Modulation. (a) The Received Signal in the Time-domain. (b) The Time-frequency Characteristic of the Received Signal. (c) The Compressed Matched Filter Output.

consists of dispersive delay lines, in effect, causes all the frequencies to show up at about the same time in the time-domain, and from the conservation of energy principle, the resulting decoded waveform appears to be similar to the one shown in Figure 2.6(c).

To compute the numerical values for the sidelobes, matched filter analysis can be performed as follows [4, pp. 469-475]. Consider the received chirp signal as

$$r(t) = \cos\left[\omega_o t - \frac{1}{2}\mu t^2\right], \quad -\frac{T}{2} < t < \frac{T}{2}. \tag{2.23}$$

In (2.23), the time-derivative of the term inside the bracket gives the instantaneous frequency, which linearly varies at a rate of μ radians/second per second during the pulse interval T. Also, μ can have positive or negative values, and is described by

$$\mu = \frac{2\pi(f_2 - f_1)}{T} \tag{2.24}$$

The filter matched to the signal in (2.23) should have the impulse response

$$h(t) = \sqrt{\frac{2\mu}{\pi}}\cos\left[\omega_o t + \frac{1}{2}\mu t^2\right], \quad -\frac{T}{2} < t < \frac{T}{2}. \tag{2.25}$$

The term in the radical simply ensures unity filter gain. Convolving (2.23) and (2.25) yields the final matched filtered signal as

$$R(t) = \sqrt{\frac{\mu T^2}{2\pi}}\,\frac{\sin\left(\frac{\mu T t}{2}\right)}{\left(\frac{\mu T t}{2}\right)}\,\mathrm{Re}\left\{\exp\left[j\left(\omega_o t + \frac{\mu t^2}{2} + \frac{\pi}{4}\right)\right]\right\}, \quad -T < t < T. \tag{2.26}$$

When plotted, the magnitude of $R(t)$ in (2.26) looks like Figure 2.6(c). The largest sidelobe occurs adjacent to the peak value, and the resulting PSLR is only 0.219, or -13.2 dB. Amplitude weighting or filter mismatching methods have been used to improve the PSLR to value of -30 to -40 dB [1, p. 426].

B. Linear Frequency Stepping: Linear frequency stepping is the discrete version of linear frequency modulation. In this method, a pulse is divided into N subpulses or chips, and each successive chip is transmitted at a constant incremented frequency. The compressed output of the receiver has almost the same PSLR as that for the analog linear FM discussed in the previous section [5, pp. 604-605]. Random sequencing of discrete frequency subpulses have been used to manipulate the delay-Doppler characteristic of the ambiguity diagram, but such random frequency sequencing does not affect the zero-Doppler compression characteristic, that is, the autocorrelation function remains the same, regardless of the sequence used [4, p. 475].

The frequency stepping method is preferred over linear FM, because of the following three advantages [5, pp. 605-606]. The most important advantage is that the components for each frequency channel require only $1/N$ times the total processing bandwidth. The second advantage is that by scrambling the order of the frequencies, the range-Doppler ambiguity can be controlled and almost eliminated. In contrast, the range-Doppler characteristic for linear FM has a "knife-edge" shape and cannot be changed. The third advantage is that the discretization of the frequency channels provides the system with the additional capability of selective limiting in automatic detection and constant false alarm rate (CFAR) receivers. Furthermore, this method is considered to be more versatile than its analog counterpart, because instead of using expensive and bulky dispersive delay lines, it uses conventional electronics, and can also use efficient digital signal processing techniques.

C. Frank Polyphase [20]: A two-dimensional Frank polyphase complex sample matrix $s(p,q)$ used to obtain a Frank polyphase sequence of length $M = N^2$ for any integer N is given by

$$s(p,q) = \exp\left(j\phi_{p,q}\right) \tag{2.27}$$

where; $p = 0, 1, \ldots, N\text{-}1$; $q = 0, 1, \ldots, N\text{-}1$; and

$$\phi_{p,q} = \frac{2\pi p\,q}{N} \tag{2.28}$$

In the above, p is the row index and q is the column index. The Frank sequence of length N^2 is then constructed by concatenating the N rows each consisting of N samples. The phase $\phi_{p,q}$ of the p-th row and q-th column is given by (2.28).

As an example, consider the construction of the Frank sequence with $N = 4$. The four rows, each consisting of four complex-valued samples, are shown in Table 2.2. The phases have been calculated from (2.28). Concatenating the four rows, gives the complex-valued representation of the Frank sequence, $s(m)$, as,

$$s(m) = \{1, 1, 1, 1, 1, j, -1, j, 1, -1, 1, -1, 1, -j, -1, j\}. \tag{2.29}$$

Table 2.2. The Frank Matrix $s(p,q)$ for $N = 4$.

p ↓ q→	0	1	2	3
0	exp(j0)	exp(j0)	exp(j0)	exp(j0)
1	exp(j0)	exp(jπ/2)	exp(jπ)	exp(j3π/2)
2	exp(j0)	exp(jπ)	exp(j2π)	exp(j3π)
3	exp(j0)	exp(j3π/2)	exp(j3π)	exp(j9π/2)

Equation (1.2) can be used to find the ACS of the complex sequence in (2.29), where,

$$s^*(m) = \{1, 1, 1, 1, 1, -j, -1, -j, 1, -1, 1, -1, 1, j, -1, -j\}. \tag{2.30}$$

It can be easily verified that the ACS of (2.29) is given by

$$R_m = \{-j, -1-j, -1, 0, -1, 1+j, j, 0, j, -1+j, 1, 0, 1, 1-j, -j, \underline{16}, j, 1+j, \ldots\}. \tag{2.31}$$

Note that the peak value, corresponding to the middle sample, is 16. Also, the sequence being a complex one, is complex-symmetric about the middle sample. The peak sidelobe values are $(\pm 1 \pm j)$, that is, the magnitude of the peak sidelobe is $\sqrt{2}$.

Instead of expressing a Frank coded sequence as a two-dimensional matrix as in (2.27), a one-dimensional complex-valued Frank polyphase sequence, $s(m)$, is represented in this dissertation in the unified form of (1.6), where

$$\phi_m = \frac{2\pi p\, q}{N}; \tag{2.32}$$

and the integers m, p, and q are related by

$$m = Np + q. \tag{2.33}$$

This one-dimensional representation of the Frank code with ϕ_m in (2.32) permits in a unified manner the use of the expression for the modulated RF signal, $r(t)$, as in (1.7) in the quadrature receiver of Figure 1.8.

The Frank polyphase code has been shown to be a discrete approximation of the Linear FM method. The PSLR of the Frank code of length M is approximately given by [4, p. 487]

$$\text{PSLR (dB)} \approx 10 \log\left(\frac{1}{\pi^2 M}\right) \tag{2.34}$$

For a code of length 16, (2.34) yields a PSLR of -21.98 dB, whereas the actual PSLR of the sequence in (2.31) is -21 dB. It is recalled that the PSLR of unweighted linear FM is only -13.2 dB, and in that sense, Frank codes have a better PSLR. Theoretically, by making M very large, the PSLR in (2.34) of Frank codes can be made close to zero, but in practice, it is difficult to maintain an exact phase relationship when the phase difference becomes small [9, p. 157]. However, due to its similarity with the linear FM, and its discrete nature, the Frank code is a better choice to be included in this quantitative investigation than linear FM.

2.4 Hybrid Waveforms

It was shown in the preceding sections that pulse compression can be achieved either by binary phase coding, or by employing frequency modulation methods. A hybrid waveform, which combines frequency stepping and complementary coding, has been recently shown to achieve not only high pulse compression, but also possess electronic counter-countermeasure (ECCM) capabilities [7]. An example of a hybrid waveform using a 2x8 complementary code with N repetitions and K frequency steps is shown in Figure 2.7. The carrier frequency of the hybrid waveform can be changed in a random order providing frequency agility, which in turn gives the system low probability of intercept (LPI) and low anti-jam (AJ) capabilities; this idea is similar to the discrete sequence frequency hopping (DSFH) used in spread spectrum communications. A possible scheme for generating a hybrid coded waveform is shown in Figure 2.8. Designing a hybrid waveform by combining frequency stepping and binary coding makes the system very flexible and somewhat complex as well, but the basic principle of ECCM is that the use of complex, flexible, and dissimilar systems place the maximum burden on the electronic countermeasure (ECM) [5, p. 605].

The hybrid waveform discussed in [7] used frequency stepping with complementary codes. Intuitively, it should be possible to design hybrid waveforms by

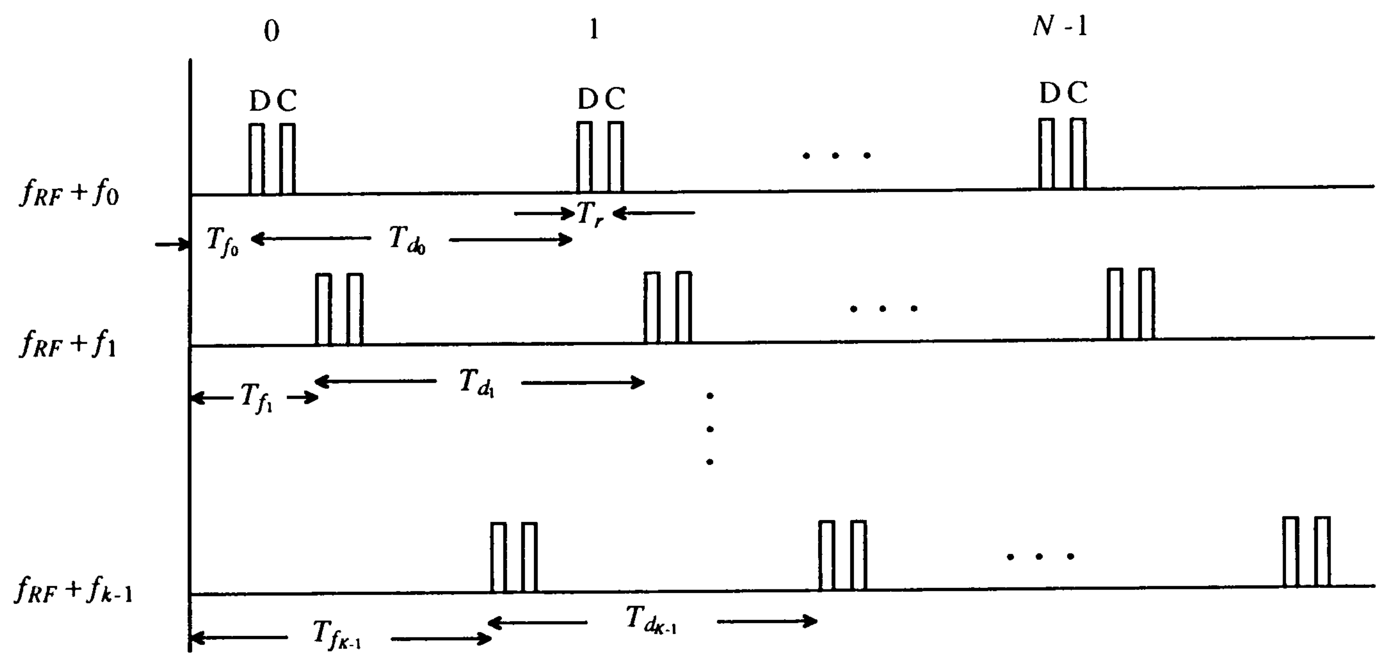

Figure 2.7. A Frequency Stepped Hybrid Waveform Using K Frequency Steps and N-group Repetitions of a Complementary Code Pair.

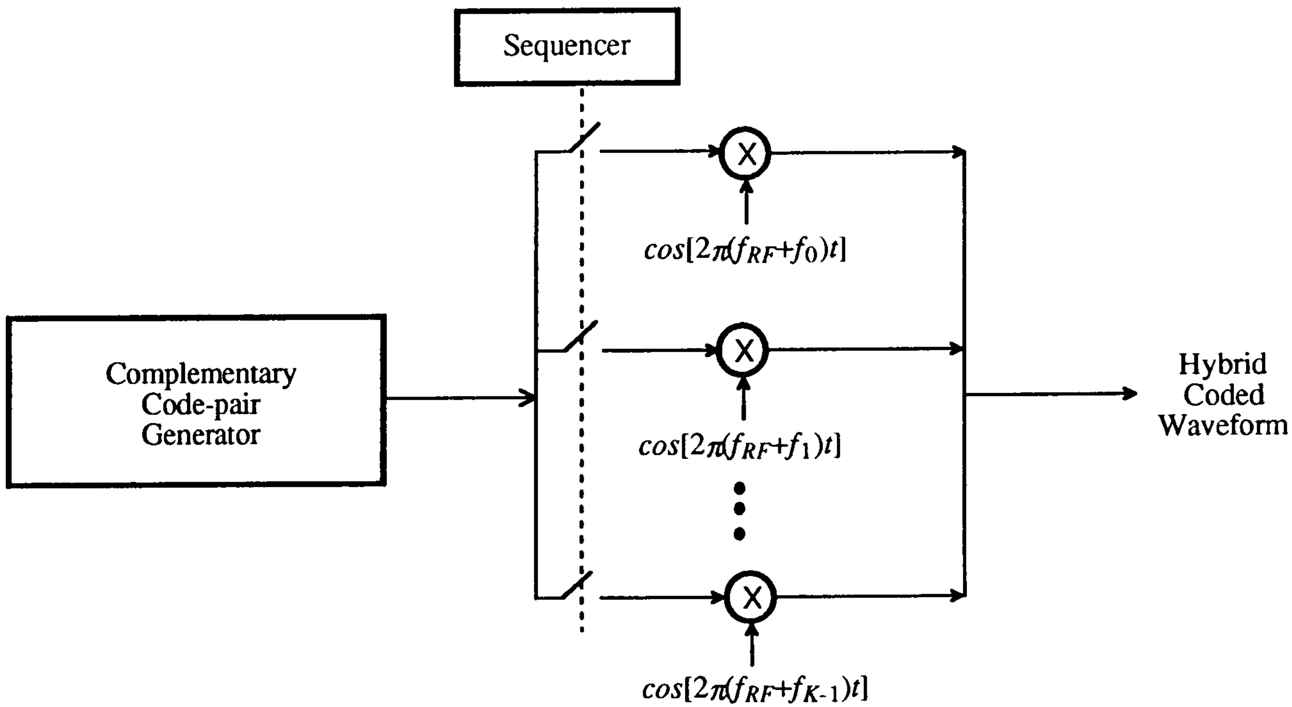

Figure 2.8. Generating a Complementary Coded Frequency Stepped Hybrid Waveform.

combining frequency stepping with PN sequences as well. This investigation evaluates the performance of these two hybrid coded waveforms in realistic environments. Mathematical details concerning hybrid coded waveforms and the performance results are later presented in Chapter 6.

To summarize, a few popular and efficient pulse compression techniques were discussed in this section. This is not to suggest that no other coding schemes exist in the literature. Coding schemes with minor variations of the techniques presented here do exist in the vast literature of radar technology. However, the basic techniques presented here form the backbone of pulse compression methodology, and the general procedures of this investigation can be applied to other variations as well. The details of the statistical models to incorporate the effects of the realistic environment in a radar situation are presented in the next chapter.

CHAPTER 3

Modeling and Performance Evaluation

In order to evaluate the performance of pulse compression techniques under realistic operating conditions, appropriate statistical models are required. The statistical models used in this investigation to incorporate the effect of realistic operating conditions are drawn primarily from classical communication theory, because a radar system can be considered to be similar to a communication link. Such models have also been used in the past to evaluate the performance of not only communication systems but also of uncoded radar systems. There are three major factors which significantly affect the performance of radar systems. The first well-known factor is noise, ambient or intentional. The second factor is due to the variation in echo signals with time; this is also called target fluctuation or scintillation. Lastly, channel fading, caused by propagation conditions, is also an important factor that invariably degrades the performance of radar systems. The effect due to each of these factors has been incorporated into the performance evaluation procedure by applying appropriate statistical models to the problem. Figure 3.1 shows the radar system model used in this dissertation. An ideal point target is shown in the figure at the left and an ideal noise-free receiver at the right. The blocks shown inside the dotted box are the statistical models which incorporate the effect of the above three factors. Each component of the figure is described in detail in the following sections of this chapter. In addition, this chapter also discusses the procedure used for performance evaluation of the coding methods.

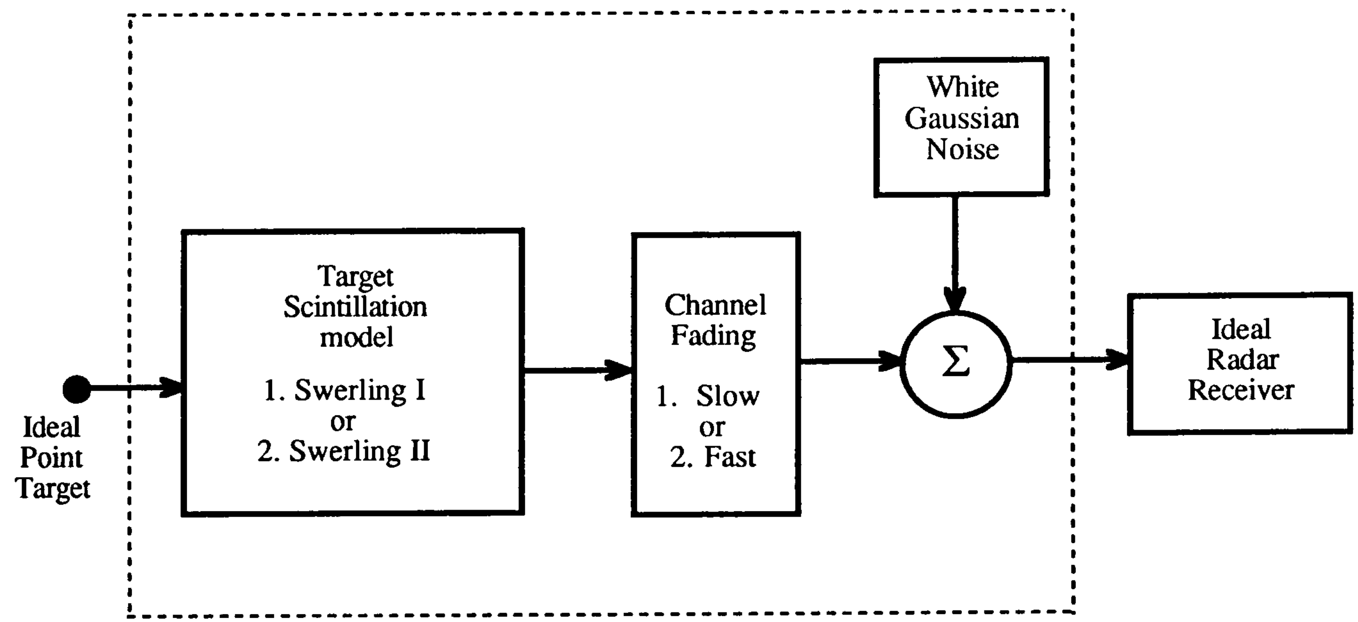

Figure 3.1. A Practical Radar System Model.

3.1 Target Scintillation

Real radar targets are not point targets; they are complex objects. Therefore, the resulting echo consists of a large number of reflected signals from various parts of the target. Thus the actual signal at the input to the radar receiver is a vector sum of the multiple signals of varying amplitude and phase. Furthermore, due to any change in the aspect of the target with respect to the radar receiving antenna, the amplitude of the received echo changes with time. Such fluctuations of the signal amplitude with respect to time is called target scintillation or target fluctuation.

A variety of statistical models for target scintillation, based on experimental data under different situations, exist, e. g., Swerling, chi-square, Rician, log-normal, Weibull, etc. [1, pp. 46 - 52]. Higher order chi-square distributions are for specific situations, and the Weibull model is good for sea clutter. No model fits all situations, but the Swerling I and II models which assume the echo amplitude to have a Rayleigh distribution are often used, first, because they cover more general situations, and second, because they are known to yield a more conservative performance estimate than other models cited before [1, p. 52]. For this reason, this investigation uses these two Swerling models to account for target scintillation. In the case of a Swerling I model the amplitudes of the chips within a single scan are assumed to be constant but having Rayleigh distributions from scan-to-scan, whereas for Swerling II the amplitudes even within the same scan are assumed to be independently distributed Rayleigh random variables [11]. Summarizing the preceding statement, the two Swerling models are:

Swerling I: No chip-to-chip fluctuation; only scan-to-scan fluctuation.

Swerling II: Chip-to-chip fluctuation.

The amplitude of a chip of the echo signal for either one of the models is assumed to have a Rayleigh distribution. In Chapter 2, the amplitude of the echo signal in the absence of any noise or target scintillation was assumed to be unity. However, to account for target scintillation the signal amplitude is now assumed to be a Rayleigh random variable A_T, whose pdf is given by

$$p_{A_T}(a_T) = \frac{a_T}{\sigma_T^2} exp\left[-\frac{a_T^2}{2\sigma_T^2}\right] \tag{3.1}$$

where σ_T^2 is the Rayleigh parameter. Physically, σ_T is the median value of the echo amplitude. The mean, variance, and the second moment of A_T in (3.1) are given by

$$\mathrm{E}\{A_T\} = \sigma_T \sqrt{\frac{\pi}{2}} \tag{3.2}$$

$$\mathrm{Var}\{A_T\} = \left(2 - \frac{\pi}{2}\right) \sigma_T^2 \tag{3.3}$$

$$\mathrm{E}\{A_T^2\} = 2\sigma_T^2 \tag{3.4}$$

Most computer systems have the facility to generate a random quantity, U, uniformly distributed between 0 and 1. A Rayleigh random variable, R, having parameter σ^2, can be obtained from such a uniformly distributed random variable, U, by the following transformation [see Appendix 3.2].

$$R = \sigma \sqrt{-2 \ln(1-U)} \tag{3.5}$$

Note that the term inside the radical in (3.5) is always positive because $0 \leq U \leq 1$.

It has been suggested that if a single parameter is to be used to describe a complex target, the Rayleigh statistics with the median value of the signal as the Rayleigh parameter should be used [1, p. 52]. Referring to Figure 3.1, the unit amplitude echo signal from an ideal point target is shown moving from left to right. During a particular chip interval, the echo signal from the ideal target has the form $\cos(\omega_{RF}t + \phi_m)$ as in (1.7). The target scintillation model box which incorporates the effect of target scintillation causes the output of the box to be $A_T\cos(\omega_{RF}t + \phi_m)$. The two Swerling models are mutually exclusive, because only one of them is needed at any time.

3.2 Channel Fading

As shown in Figure 3.1, the echo signals propagate back toward the receiving antenna through the atmospheric medium, called the channel. Atmospheric attenuation and multipath effects due to scattering cause a large number of attenuated and randomly phase-shifted versions of the original signal to be received by the radar antenna. Thus the received echo is the vector sum of a large number of such attenuated and phase shifted signals. This vector sum varies with time due to atmospheric effects, and causes variation in the signal amplitude, called fading. The end result due to atmospheric effects and propagation conditions is similar to the effect due to target scintillation, but the physical processes causing them are different. This dissertation considers fast fading which implies that the amplitude of each chip within a code is an independent Rayleigh random variable.

The effect of channel fading can thus be incorporated by multiplying the amplitude of the received signal by a Rayleigh random variable, A_F, having a Rayleigh parameter σ_F^2. The form of the pdf and the moments of A_F are similar to (3.1)–(3.4). The fading channel box of Figure 3.1 models the effect due to channel fading. The output from the fading channel box is $A_T A_F \cos(\omega_{RF} t + \phi_m)$.

3.3 Additive White Gaussian Noise

Noise is inherently present in all electrical systems and can result from sources internal as well as external to the system. In radar systems, the signal levels are very low, so even the presence of low-level noise can seriously degrade the overall performance. Neglecting the effect of noise can lead to highly misleading conclusions about system-performance. Sklar has documented an exhaustive list of the sources of signal loss and noise in communication systems, and most of the items are applicable to the radar situation as well [21, pp. 190-195]. In addition to ambient noise, there can be intentional noise, such as jamming in electronic counter measures (ECM). Such noise should also be accounted for in the design if the system is expected to be used under such conditions.

The zero-mean additive white Gaussian noise (AWGN) model has been used to analyze communications and radar systems in the past. As suggested by the terminology, the noise is considered to be additive and derived from a stationary Gaussian random process. A white noise source has a constant power spectral density over the entire spectrum. The implication of the noise being treated as white is that the samples taken from white noise are uncorrelated, and therefore for a Gaussian distribution, the samples are independent as well. The reason for using the zero-mean AWGN model is that this model results in the worst-case degradation in performance [22, p. 245, 252]. Noise-sources as diversified as thermal noise, local oscillator phase error, or cosmic noise can all be lumped together in such analyses. Furthermore, since the noise generated by a broadband jammer (barrage jammer) simply adds to the uniform power spectral density of the ambient noise, the effect of jamming noise can also be easily included in the AWGN model [5, pp. 60-64]. These are the reasons why AWGN has been used as one of the models for performance evaluation. The white Gaussian noise box of Figure 3.1 adds zero-mean Gaussian noise samples of variance σ^2 before the echo signal is detected by an ideal noiseless receiver.

If the overall two-sided noise power spectral density is $N_o/2$, then the total noise in the two-sided system bandwidth $2B$ is BN_o. Since the noise has zero mean, the variance, σ^2, of the noise equals the average noise power, that is,

$$\sigma^2 = BN_o. \tag{3.6}$$

In the rest of the dissertation, σ^2, will be used to denote the total noise power, or to denote the variance of the samples taken from the AWGN process at the input to the matched filter shown in Figure 1.8, and B is the single-sided bandwidth of the system before the sampler.

Since the quadrature receiver in Figure 1.8 is a linear system, the expressions for the quadrature samples $x(m)$ and $y(m)$ due to noise alone can be separately determined and then superimposition can be used to find the overall quadrature sample values. Using the narrowband representation of the noise, $n(t)$, as

$$n(t) = n_c(t)\cos(\omega_{RF}\, t) - n_s(t)\sin(\omega_{RF}\, t) \tag{3.7}$$

it can be shown that for the noise alone case [Appendix A3.1]

$$x(m) = N_c(m)\cos\gamma - N_s(m)\sin\gamma \tag{3.8}$$

and

$$y(m) = N_c(m)\sin\gamma + N_s(m)\cos\gamma \tag{3.9}$$

In (3.8) and (3.9), $N_c(m)$ and $N_s(m)$ are independent m-th Gaussian samples with zero mean and variance, σ^2, because they are samples from zero-mean stationary and orthogonal Gaussian processes having noise power of σ^2.

3.4. Target Scintillation, Fading, and AWGN

Applying the target scintillation, fading, and AWGN models of Sections 4.1–4.3, general equations for the quadrature samples for a single subsequence, such as for PN sequences or Frank sequences, become

$$x(m) = A_T A_F \cos(\gamma + \phi_m) + N_c(m)\cos\gamma - N_s(m)\sin\gamma \tag{3.10}$$

$$y(m) = A_T A_F \sin(\gamma + \phi_m) + N_c(m)\sin\gamma + N_s(m)\cos\gamma \tag{3.11}$$

Similar expressions using (2.19)–(2.22) can be written for complementary code pair as well. Equations (3.10) and (3.11) have been used in the simulation. An arbitrary value of γ can be used, but to make the simulation more efficient, γ can be set to zero. From the statistical models discussed above, the following six combinations have been used in this dissertation.

1. AWGN (AWGN).
2. AWGN, and Swerling I (S1).
3. AWGN, and Swerling II (S2).
4. AWGN, Swerling I, and fast channel fading (S1 & FF).
5. AWGN, Swerling II, and fast channel fading (S2 & FF).
6. AWGN, Swerling I, and slow channel fading (S1 & SF).

The abbreviations used in the performance curves presented in the later chapters are shown above in parentheses. It should be noted that S1 and SF use independent scan-to-scan Rayleigh distribution. Similarly, S2 and FF use independent chip-to-chip Rayleigh distribution. Therefore, the results for "S1 & FF" in listed as item 4 above would be identical to the results obtained by using a possible combination of AWGN, Swerling II target model, and slow fading (S2 & SF). Thus, as far as final results are concerned, the above six models cover all possible combinations for target fluctuation and channel fading.

3.5 Metric for Performance Evaluation

In this section, the metric used to evaluate and compare the performance of the coding methods in a noisy environment is discussed. First, in order to see how noise and target scintillation affect range resolution, consider the noiseless and non-fluctuating ideal output sequence shown in Figure 2.2(c). A threshold detector with the threshold set anywhere between zero and $7V$ will unambiguously determine the detection peak with complete certainty; the sidelobes, which always remain below the threshold, will not cause the false presence of a target at any of the sidelobe sample points. However, noise and target scintillation cause the output sample values to vary according to some statistical rule. No matter what the threshold setting is, there will be instances when the noise will cause the detection peak to be less than the threshold value, and the presence of the target will be missed. Similarly, for any given threshold setting, there will be instances when the noise will cause the sidelobe sample values to exceed the threshold value, and will incorrectly declare the presence of a target at those sidelobe points. Therefore, associated with any threshold is a probability of detecting the detection peak and a probability of having false alarms at the sidelobe sample points in a noisy situation. A false alarm at a sidelobe together with the detection of a detection peak would incorrectly declare the presence of two different targets at different ranges. Similarly, a false alarm together with a missed detection peak would incorrectly declare the presence of a target at an incorrect range. Each one of these example situations results in an erroneous conclusion.

It was briefly mentioned in Chapter 2 that the quality of a coding scheme for an ideal point target and noiseless channel is judged by the Peak Sidelobe Level Ratio

(PSLR) and the Integrated Sidelobe Level Ratio (ISLR) of the noise-free decoded output, A_m. The PSLR of a code in decibels is defined as [4, p. 467]

$$\text{PSLR (dB)} = 10 \log \frac{\text{peak sidelobe power}}{\text{mainlobe power}} \tag{3.12}$$

In terms of the sampled values, the PSLR is defined as

$$\text{PSLR} = \frac{|\text{largest sidelobe}|}{|\text{mainlobe peak}|} \tag{3.13}$$

The ISLR in decibels is defined as [4, p. 467]

$$\text{ISLR (dB)} = 10 \log \frac{\text{total sidelobe power}}{\text{mainlobe power}} \tag{3.14}$$

Similarly, in terms of the sampled values, the ISLR is defined as

$$\text{ISLR} = \frac{\sum (\text{sidelobe})^2}{(\text{mainlobe peak})^2} \tag{3.15}$$

It may be recalled that the PSLR and ISLR of the codes in Table 2A.1 were calculated using (3.13) and (3.15) respectively. The smaller the PSLR and ISLR, the better the code.

The PSLR and ISLR calculated for noiseless situation may be useful for comparing codes which undergo identical processing, but they may not be appropriate for comparing codes that undergo different kinds of processing. Note, for example, that the processing of complementary and PN sequence codes are not identical. In the case of complementary coding, the ACS of the two subsequences are finally added, which is not the case with PN sequence coding. When random variables are added, the result is Gaussian only for Gaussian random variables, but manipulations with non-Gaussian random variables generally result in much more complicated distributions. This investigation uses the models involving Gaussian as well as Rayleigh distributions, and that is why a difference in the processing of statistical quantities may lead to misleading conclusions.

It has been suggested that PSLR is closely associated with the probability that a false alarm in a particular range bin is due to the presence of a target in a neighboring range bin [4, p. 467]. A low PSLR is especially important in scenarios where a high density of targets of different cross sections are expected. The ISLR, a measure of the energy distributed in the sidelobes, is also important in dense target scenario, as well as when distributed clutter is present.

When statistical quantities are involved, a natural metric is the statistical average of the result. For example, in data communications, one of the performance criteria is the *average probability of error*. Along these same lines, this investigation uses the statistical average values of the PSLR and ISLR in (3.13) and (3.15) as the performance metrics. These two quantities have been used by Kretschmer in studying the impact of quadrature channel imbalance on Frank codes [10].

3.6 The Performance Evaluation Procedure

It may appear at this point that in evaluating the average PSLR and ISLR of any coding scheme there are three independent parameters: σ_T^2, σ_F^2, and σ^2. This requires a large number of combinations of these three quantities to obtain a meaningful conclusion. However, after performing a few simulations it can be verified that regardless of the values of the parameters σ_T^2, σ_F^2, and σ^2, exactly the same result can be obtained for a fixed value of the *average received energy to noise ratio* (ENR), defined next.

The ENR is the ratio of the average received energy in a signal to the average noise power when the chip-time, T_c, is normalized to unity. Consider a received waveform, non-hybrid or hybrid. The average signal energy of each chip of duration T_c of the received signal having the form $A_T A_F \cos(\omega_{RF} t + \phi_m)$ as in (1.7) with target scintillation and channel fading is

$$\mathrm{E}\left\{\frac{(A_T A_F)^2}{2} T_c\right\} \tag{3.16}$$

Therefore, the general expression of the total average energy contained in a coded waveform, after normalizing T_c to unity, is

$$MLKN\ \mathrm{E}\left\{\frac{(A_T A_F)^2}{2}\right\} \tag{3.17}$$

where,

M = Number of chips in a subsequence,

L = Number of subsequences,

K = Number of frequency steps,

N = Number of repetition groups.

As expressed before in (3.1), the average noise power of the zero-mean AWGN of variance σ^2 is simply the variance σ^2 itself. Therefore, dividing (3.17) by σ^2, and from the independence of A_T and A_F, the average received energy to noise ratio (ENR) can be written as

$$\mathrm{ENR} = MLKN \frac{\left(2\sigma_T^2\right)\left(2\sigma_F^2\right)}{2\sigma^2} \tag{3.18}$$

In view of the fact that the results depended only on the ENR, σ_T^2 and σ_F^2 were set to a constant value of 0.5 to make the terms inside the parentheses in (3.18) to unity, and the value of σ^2 was changed to obtain the desired value of the ENR.

The three sets of codes used in this dissertation are listed in Tables 3.1 – 3.3. It is important to note that a major purpose of coding is to achieve better range resolution when the radar system is constrained by a peak power limitation. Therefore, for a fair comparison of the codes the total number of the chips in the coding schemes should be approximately equal so that the transmission takes almost equal time and the peak energy constraint is almost identical for each of the codes. Ideally, it would be desirable to compare the codes having equal number of chips. However, there is no unique number of chips for which all of the coding sequences exist. For example, whereas a Frank code of

Table 3.1. Non-hybrid 15/16-chip Codes

Code	No. of Chips	Remarks
PN sequence	15	The sequence marked with an asterisk in Table 2A.1. $L = 1, M = 15, N = 1, K = 1$.
Frank	16	$L = 1, M = 16, N = 1, K = 1$.
Complementary code	16	$L = 2, M = 8, N = 1, K = 1$.

Table 3.2. Non-hybrid 255/256-chip Codes

Code	No. of Chips	Remarks
PN sequence	255	The best sequence in [5, p. 553]. $L = 1, M = 255, N = 1, K = 1$.
Frank	256	$L = 1, M = 256, N = 1, K = 1$.
Complementary code	256	$L = 2, M = 128, N = 1, K = 1$.

Table 3.3. Hybrid Codes

Code	No. of Chips	Remarks
PN sequence	960	The sequence marked with an asterisk in Table 2A.1. $L = 1, M = 15, N = 8, K = 8.$
Complementary code	1024	$L = 2, M = 8, N = 8, K = 8.$

16 chips exists, the closest length of a PN sequence code is 15. That is why the number of chips in the three tables are only approximately equal.

As an example of using (3.18) for calculating the ENR, consider the hybrid complementary code in Table 3.3. As mentioned before, $\sigma_T^2 = 0.5$, and $\sigma_F^2 = 0.5$. Also, from Table 3.3, $L = 2$, $M = 8$, $N = 8$, and $K = 8$. Therefore, $\sigma^2 = 10$ results in an ENR of 51.2 (or 17.093 dB). It can be verified that $\sigma^2 = 10 \bullet (960/1024)$ is required to obtain the same value of ENR for the hybrid PN sequence code in Table 3.3. Although it is not necessary to determine the PSLR and ISLR of the codes for the same value of ENR, in order to have a more accurate point-by-point comparison, the value of σ^2 has been adjusted as above to have the same value of the ENR for the codes to be compared. The PSLR and ISLR (y-axis) have been plotted versus ENR (x-axis) to compare different coding techniques. The procedure has been repeated for various values of σ^2 to get an overall picture. The code whose PSLR and ISLR are smaller for the same ENR is better. The next chapter presents a few analytical results related to this research.

CHAPTER 4

Analytical Results

In this chapter, a few related analytical results, which grew out of this research, are presented. As stated in Chapter 3, the PSLR and ISLR are related to the probabilities of detection and false alarm of the radar echo. The objective of the analytical approach in the following sections is to determine the statistics of the matched filtered output samples using various coding schemes in the presence of AWGN. These statistical results have then been applied to derive convenient expressions for the probability of detection of the mainlobe and the probability of false alarm at the sidelobe samples. Some of these results have also been used to verify the intermediate data obtained through simulations.

4.1 Output of the Discrete Matched Filter for a Binary Phase Coded Sequence in AWGN

The case of a quadrature receiver is deferred until Section 4.3. This section considers the simple case of determining the statistics of the output samples of a discrete matched filter due to an arbitrary binary phase coded sequence in the presence of AWGN. These results are later used in analyzing the output of the quadrature receiver. Consider the simple example of matched filtering a seven sample long binary phase coded sequence, $s(m)$, using the discrete filter in Figure 1.3(d) in the presence of sampled AWGN, $N(m)$, which is independent and is assumed to have zero mean and variance σ^2. The situation is reproduced in Figure 4.1 where the input sequence is shown above the dashed line and the

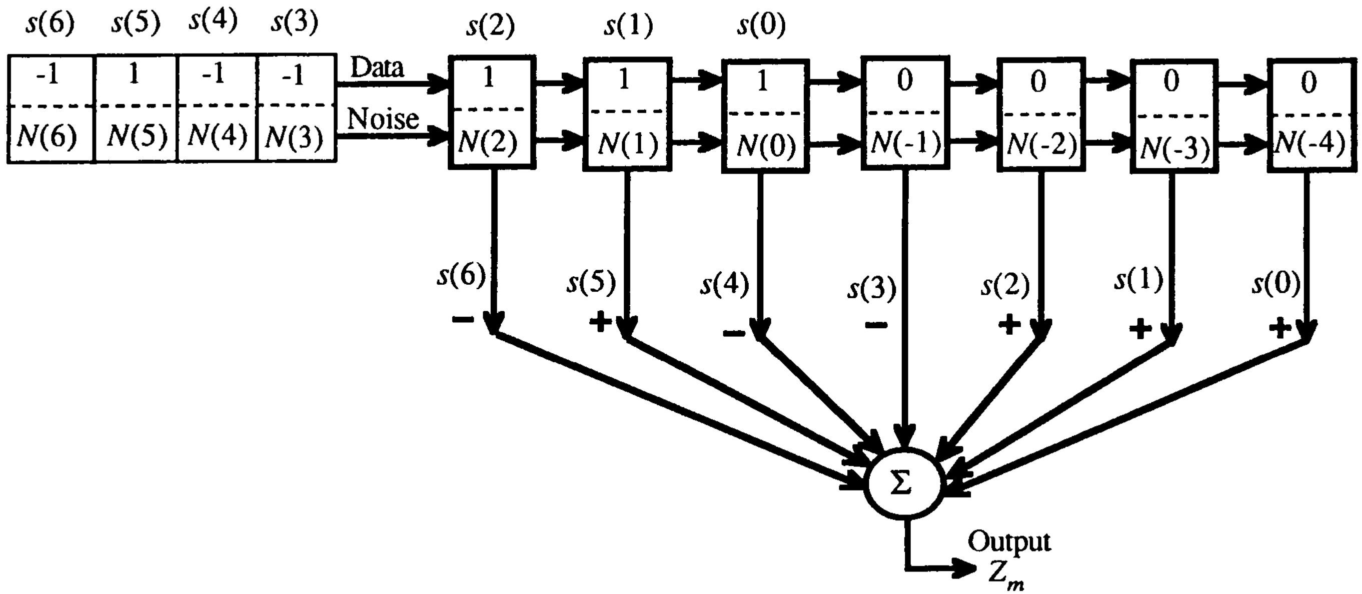

Figure 4.1. Autocorrelation in AWGN.

noise samples below it. The state of the registers in the figure corresponds to $m = 2$, and the amplitude of the encoding sequence, $s(m)$, is assumed to be unity. The first three samples have already entered the matched filter, and the remaining four are waiting to be clocked in. The matched filter being a linear system, the statistics of the output samples, Z_m, can be determined by superposition. In the absence of noise, the input is $s(m)$, and the output equals the ACS, R_m. However, for noise alone, the output of the matched filter consists of the addition or subtraction of seven independent and zero-mean Gaussian random variables, each having a variance of σ^2; thus the output samples have zero mean and variance, $7\sigma^2$. Note here that each of the seven registers of the matched filter contain noise samples because in a practical situation the matched filter continuously receives the noise samples prior to the arrival of the signal samples. Therefore, applying superposition, in the signal and AWGN case, the output Z_m is Gaussian with mean R_m and variance $7\sigma^2$.

Mathematically, the general expression for the output in the noise-only case for a matched filter of length M in Figure 4.1 can be written as

$$Z_m = \sum_{i=0}^{M-1} N(i+m-M+1)s^*(i) \tag{4.1}$$

Denoting $\sigma_o^2 = \mathrm{Var}\{Z_m\}$, the variance of Z_m can be found from

$$\sigma_o^2 = \sum_{i=0}^{M-1} \mathrm{Var}\{N(i+m-M+1)\}|s(i)|^2 \tag{4.2}$$

Since for the real binary case $s^2(i) = 1$, and $\mathrm{Var}\{N(\bullet)\} = \sigma^2$, it can be concluded from (4.2) that in the noise-only case the output samples of a matched filter of length M are Gaussian with zero mean and variance, σ_o^2, where

$$\sigma_o^2 = M\sigma^2 \tag{4.3}$$

Therefore, for an arbitrary input sequence of length, M, in AWGN, the matched filtered output samples, Z_m, are Gaussian with mean R_m and variance $M\sigma^2$, and its pdf is given by

$$f_{Z_m}(z_m) = \frac{1}{\sqrt{2\pi M\sigma^2}} \exp\left[- \frac{(z_m - R_m)^2}{2M\sigma^2} \right] \tag{4.4}$$

It can be noted from Figure 4.1 that the matched filtered output samples which are separated by less than the length, M, of the matched filter are not independent; they are correlated. This conclusion can be verified by considering the output, Z_m, for a few different values of m. For example, Z_2 contains noise samples $N(2)$, $N(1)$, ..., $N(-4)$; and Z_3 contains noise samples $N(3)$, $N(2)$, ..., $N(-3)$. Since both Z_2 and Z_3 contain the common noise samples $N(2)$, $N(1)$, ..., $N(-3)$, they are correlated. The implication of this observation is later explored in this chapter when a theoretical analysis is performed on the quadrature receiver for the signal plus AWGN case.

4.2 Output of the Golay Type I Decoder for a Complementary Coded Sequence in AWGN

In this section, the statistics of the samples out of the Golay type I decoder for a complementary coded sequence in the presence of the AWGN samples is determined. To see that an identical result as in (4.3) is obtained when a complementary coded subsequence is matched filtered in AWGN using a Golay type I decoder in Figure 2.3, consider the matched filtering of the direct subsequence $s^D(m)$ of length M. In the absence of noise, the ACS is R_m^D. In the noise-only case, each of the registers contains an independent zero-mean Gaussian sample with variance σ^2, and the output of the upper (or the lower) adder of the first section of the decoder is the addition or subtraction of 2^1 Gaussian random variables, each having a variance of σ^2. Therefore, the variance of the Gaussian samples at the output of the first stage adder is $2^1\sigma^2$. Similarly, the output of the adders of the second stage is addition or subtraction of two Gaussian random variables, each having a variance of $2^1\sigma^2$. Hence, the variance of the Gaussian samples at the output of the second stage adder is $2^2\sigma^2$. Reasoning in this way it can be concluded that the variance of the zero-mean Gaussian samples at the output of the N-th stage adder is $2^N\sigma^2$. Now note that the length, M, of a complementary code subsequence and the number of stages, N, in a Golay type I decoder are related by (2.15). Consequently, the variance of the zero-mean output samples is $M\sigma^2$. Therefore, in the signal plus AWGN case, the pdf of the output samples is given by

$$f_{Z_m^D}(z_m^D) = \frac{1}{\sqrt{2\pi M\sigma^2}}\exp\left[-\frac{\left(z_m^D - R_m^D\right)^2}{2M\sigma^2}\right]. \tag{4.5}$$

Note the expected similarity between (4.4) and (4.5) despite using matched filters having different structures. Identical results would be obtained by using the complement subsequence. Thus, on adding the direct and complement subsequences the m-th sample of the resulting sequence is Gaussian with mean R_m and variance $2M\sigma^2$, where it is emphasized that M is the length of each of the subsequences, and the total number of chips in the complementary coded signal is $2M$. In contrast, the total length of the PN sequence was denoted by M. The purpose in this section has been to show that identical results are obtained whether one uses the Golay type I filter or the discrete matched filter of the preceding section.

4.3 Output of the Quadrature Receiver for a Binary Phase Coded Signal in AWGN

In this section, the expression for the output sample, A_m, of the quadrature receiver shown in Figure 1.8 and its statistics for an arbitrary binary phase coded waveform in AWGN is determined. It was shown for the noise-free case in Chapter 1 that the output samples, A_m, from the quadrature processor in Figure 1.8 are the magnitudes of the ACS of the input encoding sequence that modulated the RF signal. The binary coding sequence, (3.10) and (3.11) for the signal plus AWGN case without target scintillation and fading can be written as

$$x(m) = \cos(\gamma + \phi_m) + N_c(m)\cos\gamma - N_s(m)\sin\gamma \tag{4.6}$$

$$y(m) = \sin(\gamma + \phi_m) + N_c(m)\sin\gamma + N_s(m)\cos\gamma \tag{4.7}$$

where $N_c(m)$ and $N_s(m)$ are the m-th zero-mean Gaussian quadrature samples having variance σ^2. The output of the matched filter due to the first term of (4.6) and (4.7) can be directly written from (1.13) and (1.14). Using (4.1) for the remaining noise terms yields

$$I(m) = R_m \cos\gamma + N_I(m)\cos\gamma - N_Q(m)\sin\gamma \tag{4.8}$$

$$Q(m) = R_m \sin\gamma + N_I(m)\sin\gamma + N_Q(m)\cos\gamma \tag{4.9}$$

In (4.8) and (4.9), N_I(m) and N_Q(m) are zero-mean Gaussian random variables, and as discussed in the Section 4.1, the variance of each of these is σ_o^2 as in (4.3). Substituting (4.8) and (4.9) in (1.5) yields the following simple result [see Appendix A4.1]

$$A_m = \sqrt{[R_m + N_I(m)]^2 + N_Q^2(m)} \tag{4.10}$$

Since $N_I(m)$ and $N_Q(m)$ are independent, A_m has the well known Rician pdf

$$f_{A_m}(a_m) = \frac{a_m}{\sigma_o^2}\exp\left[-\frac{a_m^2 + R_m^2}{2\sigma_o^2}\right] I_0\left(\frac{R_m a_m}{\sigma_o^2}\right) \tag{4.11}$$

where,

$\sigma_o^2 = M\sigma^2,$

M = length of the sequence, and

R_m = Noise-free ACS of the input sequence.

In (4.11), $I_0(x)$ is the zero-order modified Bessel function defined as

$$I_0(x) = \frac{1}{2\pi}\int_0^{2\pi} \exp(x\cos\alpha)\, d\alpha \tag{4.12}$$

Note that for $R_m = 0$ in (4.10), as expected, (4.11) reduces to a Rayleigh pdf.

Having found the pdf of A_m, an attempt is made in the following to analytically determine the average PSLR and ISLR defined in (3.13) and (3.15). Consider the PSLR, which can be written as

$$\text{PSLR} = \mathrm{E}\left\{\frac{\text{Max}\{A_m\};\ m = \text{sidelobes}}{A_m;\ m = \text{mainlobe}}\right\} \tag{4.13}$$

The immediate difficulty in evaluating the PSLR by analytical methods arises due to the correlations among the A_m's as discussed in Section 4.1. As a consequence of the correlations, there does not seem to be a convenient and tractable expression for the joint pdf of the random variables in the numerator. In addition, the correlation between the numerator and denominator makes it all the more difficult to evaluate (4.12) by analytical methods. Similar difficulty arises in evaluating the ISLR by analytical methods. It should be noted that the above analytical attempt was made for the simplest case of a biphase coded signal in AWGN without target fluctuation and fading. The complexity of the problem, therefore, requires that these quantities of interest be determined by Monte Carlo simulations.

The pdf of the output samples in (4.11), nevertheless, provides an alternative method to partly verify the results and the correctness of the simulation methodology. It was mentioned in Chapter 3 that the PSLR and ISLR are related to the probabilities of detection and false alarm. In the following, a closed form expression is provided to calculate these two probabilities for a given threshold V_T. The probability of detecting the mainlobe peak, P_D, is

$$P_D = \int_{V_T}^{\infty} f_{A_m}(a_m)da_m \text{ ; } m = \text{mainlobe peak} \tag{4.14}$$

Substituting (4.11) in (4.14) a compact expression of P_D can be found to be

$$P_D = Q\left(\frac{|R_m|}{\sqrt{M}\sigma}, \frac{V_T}{\sqrt{M}\sigma}\right); m = \text{mainlobe peak} \tag{4.15}$$

where, Q(a,b) is Marcum's Q-function and is defined by [23, p. 332]

$$Q(a,b) = \int_{b}^{\infty} u \, exp\left[-\frac{a^2+u^2}{2}\right] I_0(au)\, du \tag{4.16}$$

Efficient and highly accurate methods of evaluating Q(a,b) are available [24]. Similarly, the probability of false alarm at the m-th sidelobe, P_{F_m}, is also given by the integral in (4.14). consequently,

$$P_{F_m} = Q\left(\frac{|R_m|}{\sqrt{M}\sigma}, \frac{V_T}{\sqrt{M}\sigma}\right); \; m = \text{sidelobe} \tag{4.17}$$

The expressions in (4.15) and (4.17) are identical, but care should be taken to use the appropriate value of R_m for a given value of m. Thus, at least for the signal plus AWGN case, P_D and P_{F_m} obtained from simulations can be verified by comparing with the values obtained from computing (4.15) and (4.17).

4.4 Output of the Quadrature Receiver for a Complementary Coded Signal in AWGN

Similar to (4.6) and (4.7) the quadrature samples in this case are

$$x^D(m) = \cos(\gamma + \phi_m^D) + N_c^D(m)\cos\gamma - N_s^D(m)\sin\gamma \tag{4.18}$$

$$y^D(m) = \sin(\gamma + \phi_m^D) + N_c^D(m)\sin\gamma + N_s^D(m)\cos\gamma \tag{4.19}$$

$$x^C(m) = \cos(\gamma + \phi_m^C) + N_c^C(m)\cos\gamma - N_s^C(m)\sin\gamma \tag{4.20}$$

$$y^C(m) = \sin(\gamma + \phi_m^C) + N_c^C(m)\sin\gamma + N_s^C(m)\cos\gamma \tag{4.21}$$

Also, there is no correlation among the noise samples. Referring to Figure 2.5, after matched filtering

$$I^D(m) = R_m^D \cos\gamma + N_I^D(m)\cos\gamma - N_Q^D(m)\sin\gamma \tag{4.22}$$

$$Q^D(m) = R_m^D \sin\gamma + N_I^D(m)\sin\gamma + N_Q^D(m)\cos\gamma \tag{4.23}$$

$$I^C(n) = R_m^C \cos\gamma + N_Q^C(m)\cos\gamma - N_Q^C(m)\sin\gamma \tag{4.24}$$

$$Q^C(m) = R_m^C \sin\gamma + N_I^C(m)\sin\gamma + N_Q^C(m)\cos\gamma \tag{4.25}$$

In (4.22) to (4.25), $N_I^D(m)$, $N_Q^D(m)$, $N_I^C(m)$, and $N_Q^C(m)$ are independent zero-mean Gaussian random variables having variance as in (4.3), where M is the length of each of the subsequences – direct, or complement. It can be shown that [see Appendix A4.2]

$$A_m = \sqrt{\left(R_m^D + R_m^C + N_I^D(m) + N_I^C(m)\right)^2 + \left(N_Q^D(m) + N_Q^C(m)\right)^2} \tag{4.26}$$

The similarity between (4.10) and (4.26) is worth noticing. Interestingly enough, for complementary codes also, A_m has a Rician pdf, because in (4.26) the first term inside the parentheses is a Gaussian random variable with mean $R_m^D + R_m^C$ and variance $2\sigma_o^2$, and the second term is also a Gaussian random variable with zero mean and the same variance $2\sigma_o^2$, and these two Gaussian random variables are also independent. Thus the Rician pdf of A_m is

$$f_{A_m}(a_m) = \frac{a_m}{2\sigma_o^2} \exp\left[-\frac{a_m^2 + \left(R_m^D + R_m^C\right)^2}{4\sigma_o^2}\right] I_0\left(\frac{\left(R_m^D + R_m^C\right)a_m}{2\sigma_o^2}\right) \tag{4.27}$$

Recall that at the mainlobe, $R_m^D + R_m^C = 2R_m^D$. Therefore, in terms of Marcum's Q-function, the probability of detecting the mainlobe is

$$P_D = Q\left(\frac{2R_m^D}{\sqrt{2M}\sigma}, \frac{V_T}{\sqrt{2M}\sigma}\right) \quad : m = \text{mainlobe peak} \tag{4.28}$$

Also, since at any of the sidelobes, $R_m^D + R_m^C = 0$, and $I_0(0) = 1$, (4.27) reduces to a Rayleigh pdf given by

$$f_{A_m}(a_m) = \frac{a_m}{2\sigma_o^2} \exp\left[-\frac{a_m^2}{4\sigma_o^2}\right] \tag{4.29}$$

Integrating the above from the threshold V_T to infinity yields the closed form expression for the probability of false alarm at any of the sidelobes as

$$P_F = \exp\left[-\frac{V_T^2}{4M\sigma^2}\right] \quad : m = \text{sidelobes} \tag{4.30}$$

In the above, the subscript m has been dropped from P_{F_m}, because the probability of false alarm at any of the sidelobes has the same value; this is an interesting result.

4.5 Output of the Quadrature Receiver for Frank Coded Signal in AWGN

In the Frank coded case also, the quadrature samples $x(m)$ and $y(m)$ are given by (4.6) and (4.7) respectively. Performing correlations with the Frank sequence $s^*(m)$ results in

$$I(m) = \sum_{i=0}^{m} \cos(\gamma + \phi_{i+m-M+1})s^*(i) + \sum_{i=0}^{M-1} N_c(i+m-M+1)\cos\gamma\, s^*(i)$$
$$- \sum_{i=0}^{M-1} N_s(i+m-M+1)\sin\gamma\, s^*(i) \tag{4.31}$$

$$Q(m) = \sum_{i=0}^{m} \sin(\gamma + \phi_{i+m-M+1})s^*(i) + \sum_{i=0}^{M-1} N_c(i+m-M+1)\sin\gamma\, s^*(i)$$
$$+ \sum_{i=0}^{M-1} N_s(i+m-M+1)\cos\gamma\, s^*(i) \tag{4.32}$$

Now substituting the Frank signal $s^*(i) = \cos\phi_i - j\sin\phi_i$ in (4.31) and (4.32), using (1.5), recognizing R_m from (1.3), denoting $N_c(i+m-M+1) = N_c(\bullet)$ and $N_s(i+m-M+1) = N_s(\bullet)$, and collecting the real and imaginary parts yields

$$A_m = \left| R_m\cos\gamma + \sum_{i=0}^{M-1} \begin{matrix} N_c(\bullet)\cos\gamma\cos\phi_i - N_s(\bullet)\sin\gamma\cos\phi_i \\ + N_c(\bullet)\sin\gamma\sin\phi_i + N_s(\bullet)\cos\gamma\sin\phi_i \end{matrix} \right.$$

$$\left. + jR_m\sin\gamma + j\sum_{i=0}^{M-1} \begin{matrix} -N_c(\bullet)\cos\gamma\sin\phi_i + N_s(\bullet)\sin\gamma\sin\phi_i \\ + N_c(\bullet)\sin\gamma\cos\phi_i + N_s(\bullet)\cos\gamma\cos\phi_i \end{matrix} \right| \tag{4.33}$$

Each of the summations in (4.33) contains four noise terms. For convenience, denote these noise summation terms by

$$N_I(m) = \sum_{i=0}^{M-1} \begin{array}{l} N_c(\bullet)\cos\gamma\cos\phi_i - N_s(\bullet)\sin\gamma\cos\phi_i \\ + N_c(\bullet)\sin\gamma\sin\phi_i + N_s(\bullet)\cos\gamma\sin\phi_i \end{array} \tag{4.34}$$

and

$$N_Q(m) = \sum_{i=0}^{M-1} \begin{array}{l} -N_c(\bullet)\cos\gamma\sin\phi_i + N_s(\bullet)\sin\gamma\sin\phi_i \\ + N_c(\bullet)\sin\gamma\cos\phi_i + N_s(\bullet)\cos\gamma\cos\phi_i \end{array} \tag{4.35}$$

It may initially appear that since $N_I(m)$ and $N_Q(m)$ each contain the same noise terms $N_c(\bullet)$ and $N_s(\bullet)$, they may not be independent. However, it can be shown that due to the presence of orthogonal terms, $N_I(m)$ and $N_Q(m)$ are uncorrelated zero-mean Gaussian random variables [see Appendix A4.4]. In addition, it can be shown that [see Appendix A4.5]

$$\mathrm{Var}\{N_I(m)\} = M\sigma^2 \tag{4.36}$$

$$\mathrm{Var}\{N_Q(m)\} = M\sigma^2 \tag{4.37}$$

As before, in (4.36) and (4.37) M is the length of the Frank sequence, and σ^2 is the variance of the AWGN samples. Therefore, (4.33) reduces to

$$A_m = \sqrt{[R_m\cos\gamma + N_I(m)]^2 + [R_m\sin\gamma + N_Q(m)]^2} \tag{4.38}$$

Since in the RHS of (4.38), $N_I(m)$ and $N_Q(m)$ are independent zero-mean Gaussian random variables having equal variance, A_m can be recognized to be another representation of a Rician random variable [23, pp. 328-334] having the same pdf as in

(4.11) which was derived earlier for binary phase coding. Note the two alternate forms of the Rician random variables in (4.10) and (4.38). Therefore, the expressions for P_D and P_{F_m} in (4.15) and (4.17) derived for the binary case are directly applicable to the Frank codes as well.

The correctness of the above derived expressions for P_D and P_{F_m} using a quadrature receiver for binary phase coding (PN sequence), complementary coding, and Frank coding have been verified by the results obtained through simulations. The results presented in this chapter are restricted to non-hybrid codes and the AWGN case. It has not been found possible to derive convenient expressions for P_D and P_{F_m} after including the effect of target fluctuation and fading. The complexity of the problem necessitates the use of simulation methods which are described for non-hybrid coding methods in the next chapter.

CHAPTER 5

Performance of Non-hybrid Codes

In this chapter the resolution performance results of non-hybrid pulse compression techniques using the statistical radar system models described in Chapter 3 are presented. These results have been obtained through Monte Carlo simulations using the LabVIEW graphical programming language developed by National Instruments, Inc., Austin, Texas. The number of iterations for each simulation was chosen to ensure that upon repeating the simulation several times the PSLR and ISLR values did not differ by more than 0.5 dB. After presenting simulation results for individual coding techniques, a comparison among them is made.

5.1 Results for PN Sequence Coded Waveforms

In the first simulation, a 15-chip PN sequence was used. The plot of the PSLR versus the ENR is shown in Figure 5.1. The data points in this figure and all subsequent figures have been connected by spline interpolation to obtain smooth curves. In order to obtain satisfactory results, 200000 iterations had to be used. The abbreviation of various statistical models used in the figure are the same as mentioned in Section 3.4. It can be observed from Figure 5.1 that the AWGN-only model has the smallest PSLR than any other model. Now consider including the effects of Swerling I and Swerling II target fluctuation models. For small ENR the S2 model has smaller PSLR than the S1 model.

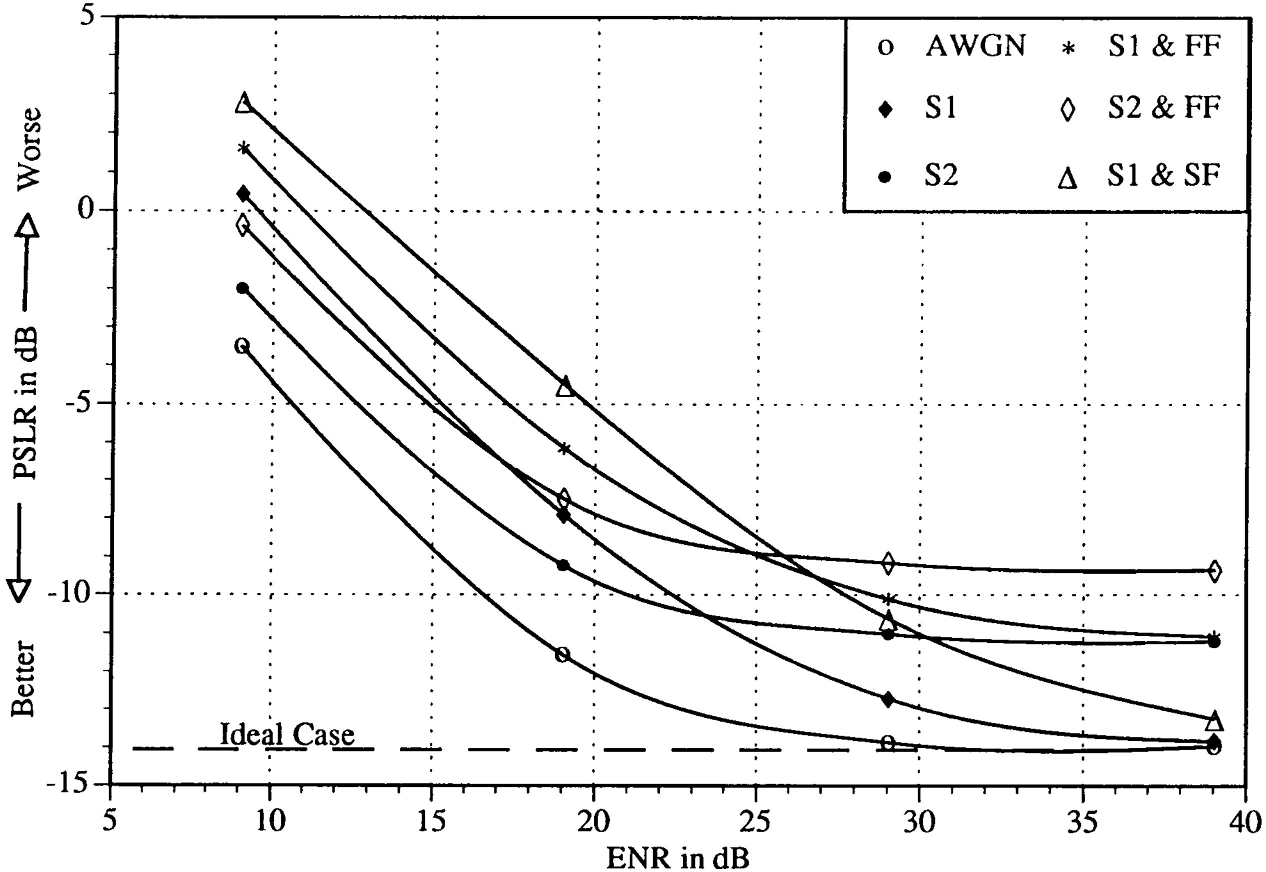

Figure 5.1. Impact of Noise, Target Scintillation, and Fading on the PSLR of a 15-chip PN Sequence Coded Waveform.

On the lower end of the ENR scale, results were obtained only until the resulting PSLR was about 0 dB, because for an ENR smaller than this the peak sidelobe becomes greater than the detection mainlobe causing excessive false alarm and the radar system gets highly degraded to be of any practical use. As the ENR is increased, a crossover of the PSLR curves occurs, and for an ENR of greater than 23.5 dB the PSLR of the S1 model becomes smaller than of the S2 model. It should be pointed out that similar crossover between the detection performance curves for S1 and S2 target fluctuation models have been reported for uncoded waveforms [1, p. 48]. Now consider the effect of including channel fading. Although combining the effects of target fluctuation and fading is generally a non-linear operation, the preceding observations do give some qualitative insight about what should be expected when the two Swerling target fluctuation models are combined with the slow or fast channel fading models. Compared to the Swerling I model alone, a Swerling I target model combined with slow fading, shown as "S1 & SF" in the figure, should intuitively perform better at larger ENR than at smaller ENR, as is confirmed by the simulation results. Similarly, compared to the Swerling II model alone, the Swerling II target model combined with fast fading, shown as "S2 & FF" in the figure can be seen to perform better at smaller ENR than at larger ENR. Along the same line of reasoning, the curve for Swerling I target fluctuation model combined with fast channel fading (S1 & FF) should be in between "S1 & SF" and "S2 & FF", as is actually the case.

The plot of ISLR versus the ENR for the 15-chip PN sequence code is shown in Figure 5.2. In this case also, the AWGN-only model results has the best performance, and the behavior for other models is basically similar to what was observed for the PSLR. However, compared to Figure 5.1, the crossovers of various curves in Figure 5.2 occur at different values of the ENR.

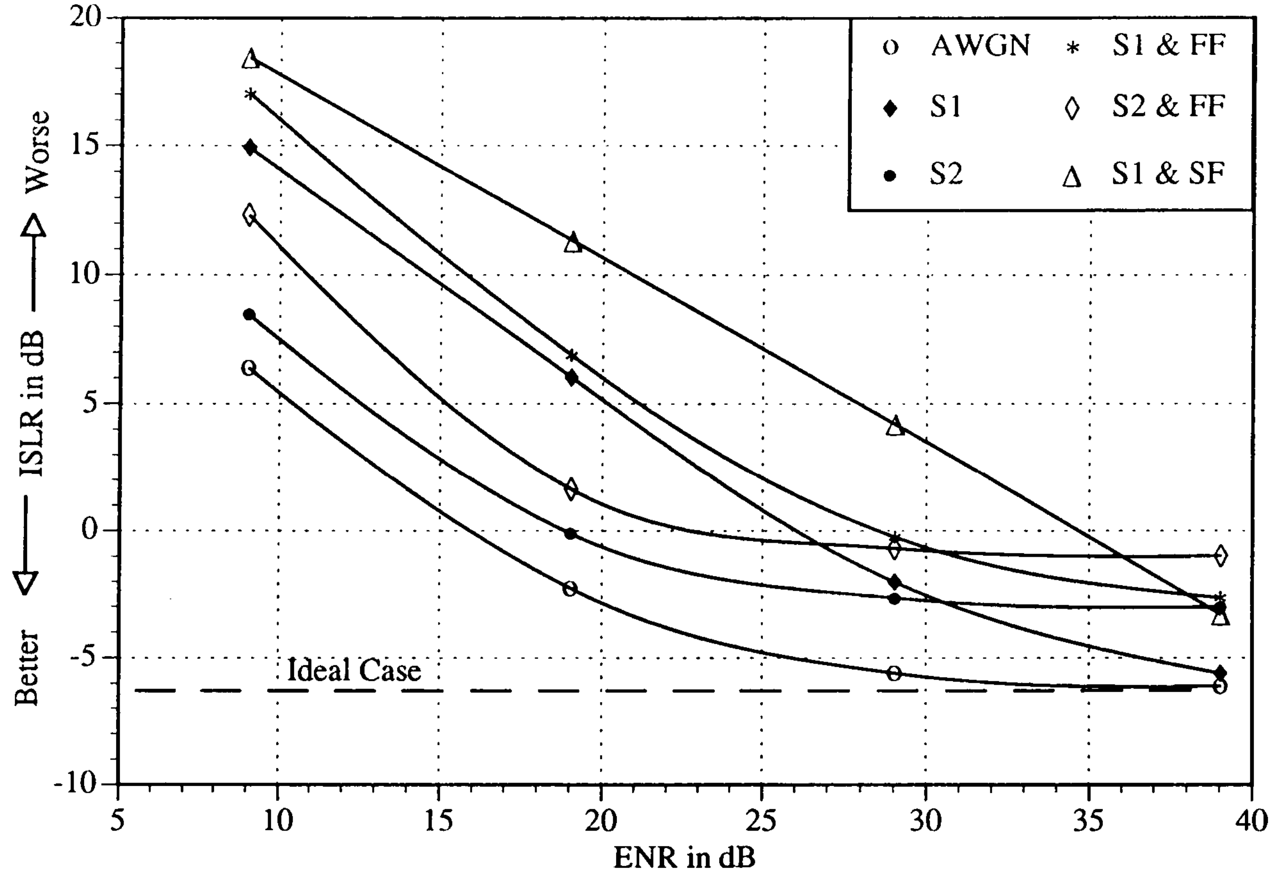

Figure 5.2. Impact of Noise, Target Scintillation, and Fading on the ISLR of a 15-chip PN Sequence Coded Waveform.

Next, a longer PN sequence coded waveform consisting of 255 chips was used, and the results obtained are shown in Figures 5.3 and 5.4. In this case 50,000 iterations were required to obtain satisfactory results. The shape of the PSLR and ISLR curves for this longer PN sequence is very similar to the curves for the 15-chip sequence.

The above data obtained using two different codelengths can now be used to investigate the effect of codelength on the resolution performance of PN sequence coded waveforms. It is well known that in an ideal situation (in the absence of noise, target fluctuation, and fading), a longer PN sequence has smaller PSLR. For example, the PLSR and ISLR of a 15-chip PN sequence are –13.98 dB and –6.2 dB, whereas for a 255-chip code, the PSLR and ISLR are –25.85 dB and –6.1 dB respectively. However, as far as the PSLR is concerned, a comparison of the influence of statistical models on 15- and 255-chip PN sequence coded waveforms has yielded a surprising conclusion in this investigation. Figure A5.1 in Appendix 5 shows the effect of AWGN on the PSLR of 15- and 255-chip coded waveforms. Notice that at large ENR, which is equivalent to low noise level, the 255-chip coded waveform has significantly smaller PSLR than that of a 15-chip coded waveform, as expected before. However, increasing the noise, which is equivalent to decreasing the ENR, causes a faster degradation in the PLSR of the 255-chip coded waveform than the PSLR of the 15-chip coded waveform, and at an ENR of 20 dB a crossover occurs. As shown in the figure, the smaller codelength has a marginally better PSLR for the ENR values of less than 20 dB. This observation may suggest that it is better to use a shorter PN sequence. However, a peak power limited radar transmitter using a shorter codelength may not be able to provide sufficient energy for reliable detection, and in such a situation, a tradeoff between resolution and detectability would be desirable. A comparison of the ISLR of the two codelengths in AWGN is shown in

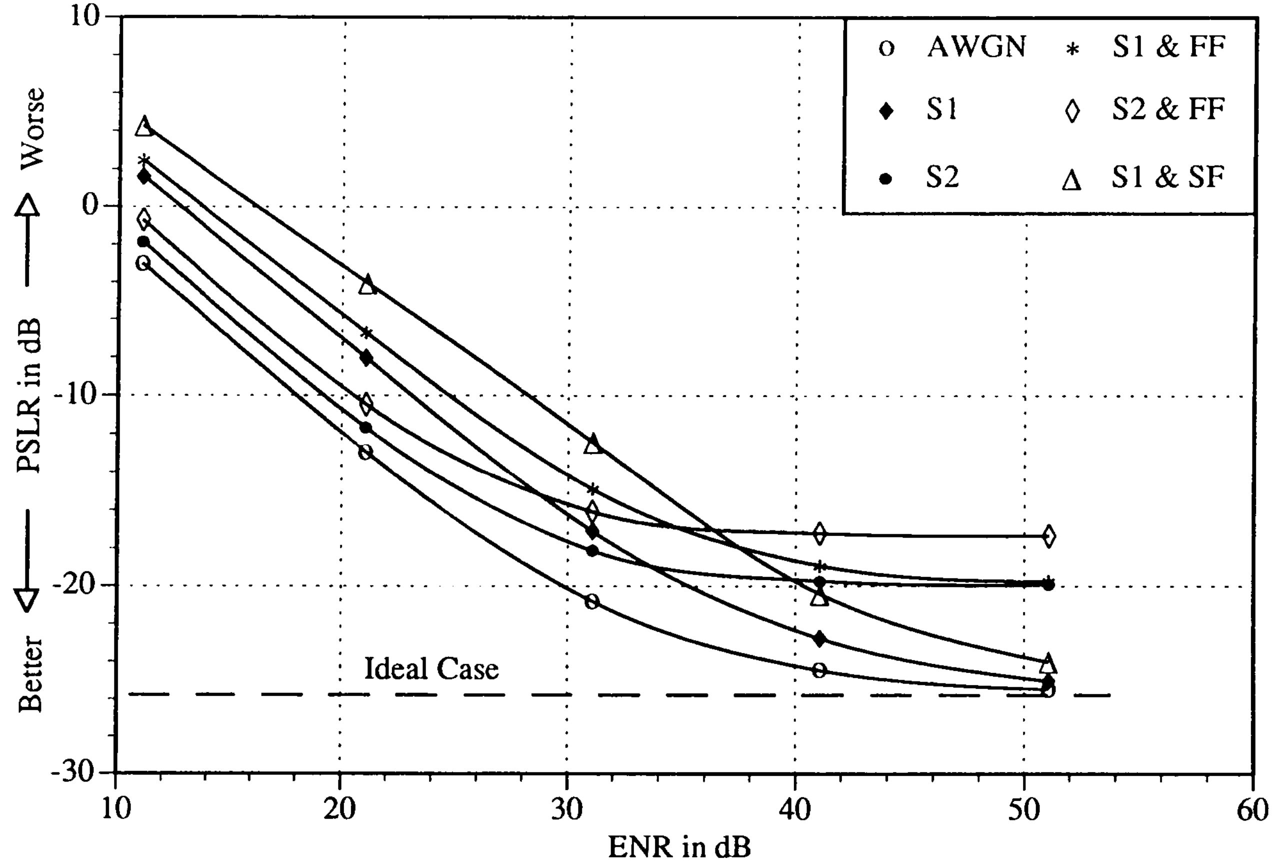

Figure 5.3. Impact of Noise, Target Scintillation, and Fading on the PSLR of a 255-chip PN Sequence Coded Waveform.

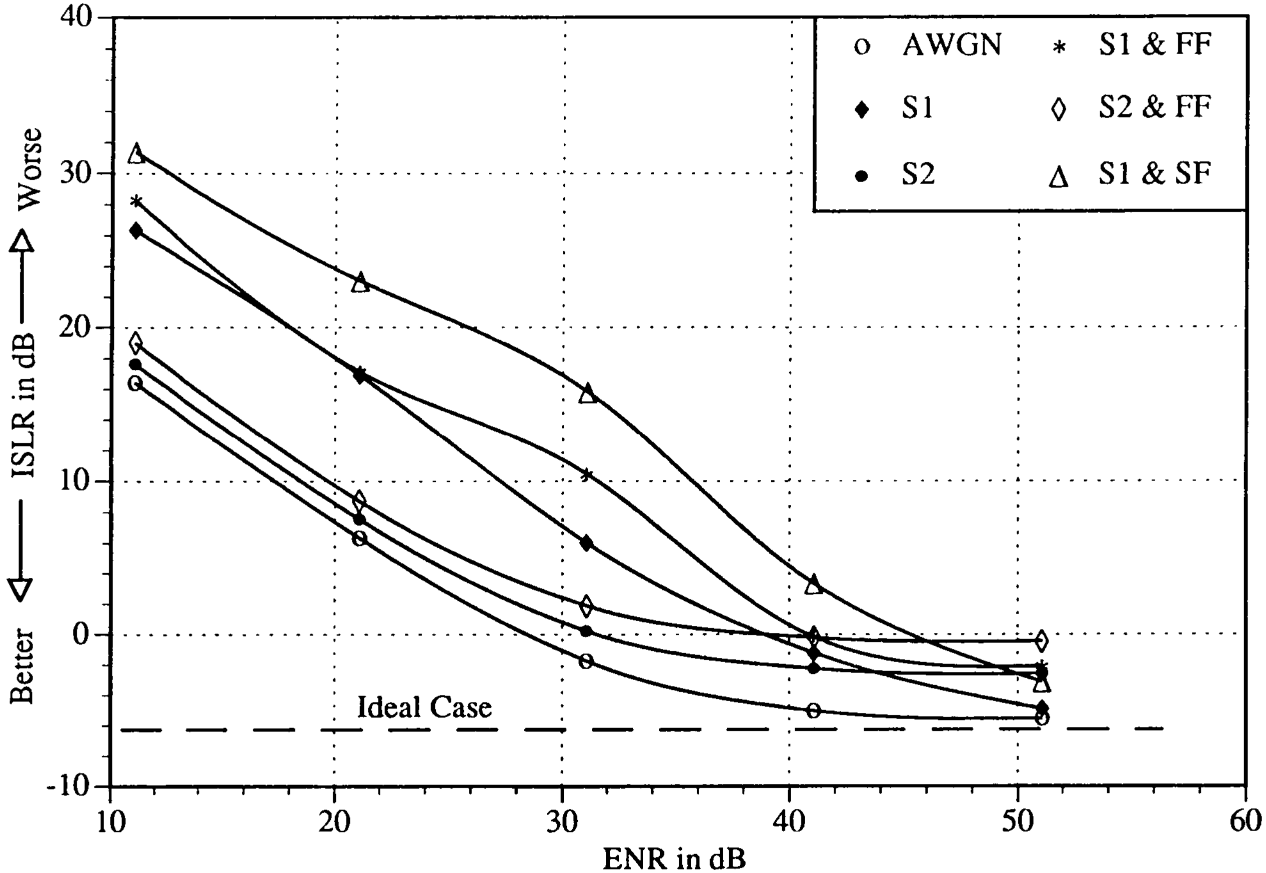

Figure 5.4. Impact of Noise, Target Scintillation, and Fading on the ISLR of a 255-chip PN Sequence Coded Waveform.

Figure A5.2 which shows that the ISLR of the smaller codelength is always smaller than the ISLR obtained from using the longer codelength; this is in line with the previously known trend for the ideal case. For the remaining five statistical models, similar conclusion can be drawn from Figures A5.3 – A5.12.

5.2 Results for Frank Coded Waveforms

In this case also, first a smaller Frank coded waveform having only 16-chips was used. The data obtained from simulations are plotted in Figures 5.5 and 5.6. The values shown were obtained from 200,000 iterations. It is observed from both figures that the AWGN-only model has the smallest PSLR and ISLR. The general shapes of the PSLR curves are similar to what was observed for the PN sequence coded waveforms in the preceding section. The ISLR values for different models in Figure 5.6 at the higher and lower ends of the ENR bear similar relationships to what was observed for the PN sequence coded waveforms. However, there are two crossovers between the "S1" and "S1 & FF" curves at 14 dB and 24 dB, and this is somewhat different from the characteristic curves for the PN sequence coded waveforms.

Next, a 256-chip Frank coded waveform was used in the simulation. The results are plotted in Figures 5.7 and 5.8. The values shown were obtained from 50,000 iterations. In both figures, except for the crossover locations for the "S1" and "S1 & FF" curves, which occur at 27 dB and 41 dB, the PSLR and ISLR characteristics are similar to that of the 16-chip Frank coded waveform used before.

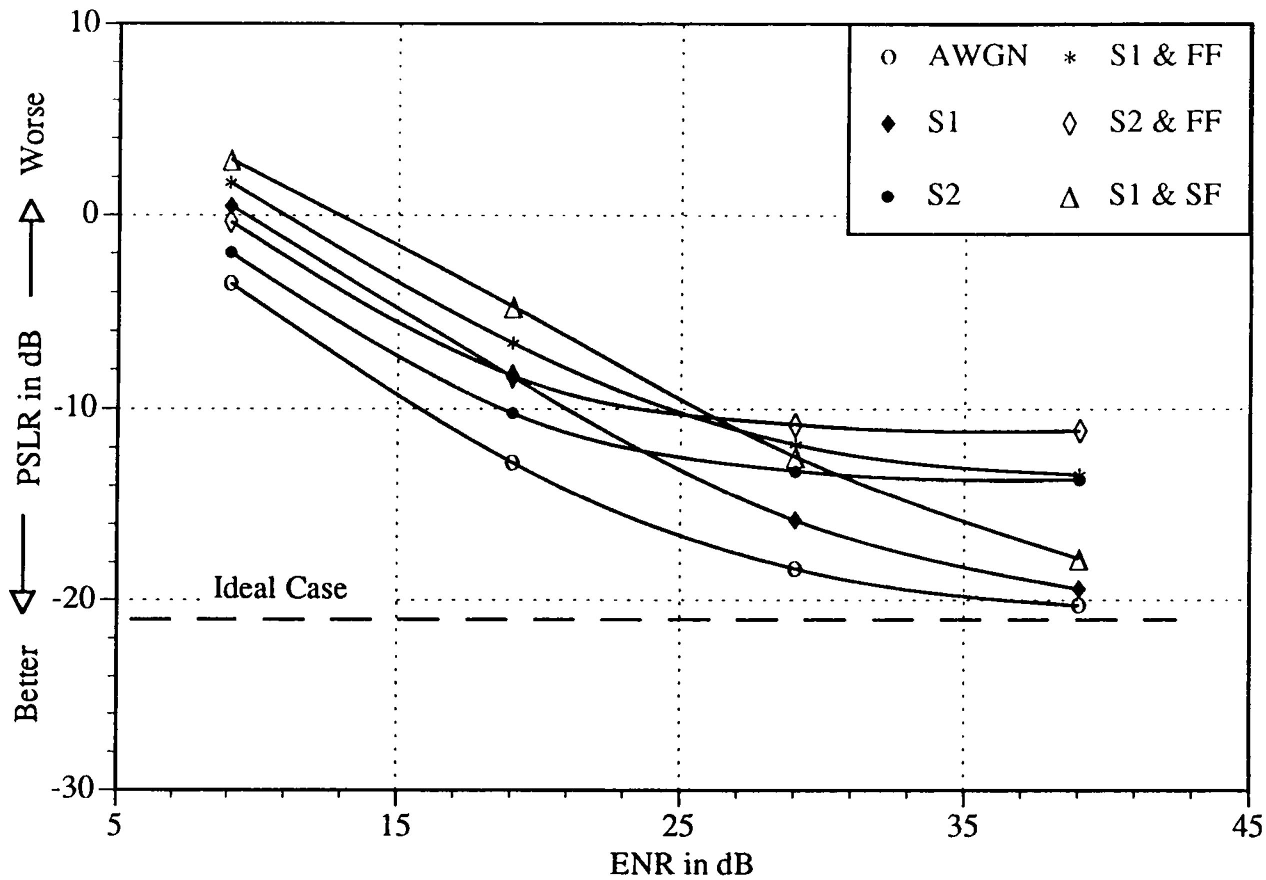

Figure 5.5. Impact of Noise, Target Scintillation, and Fading on the PSLR of a 16-chip Frank Coded Waveform.

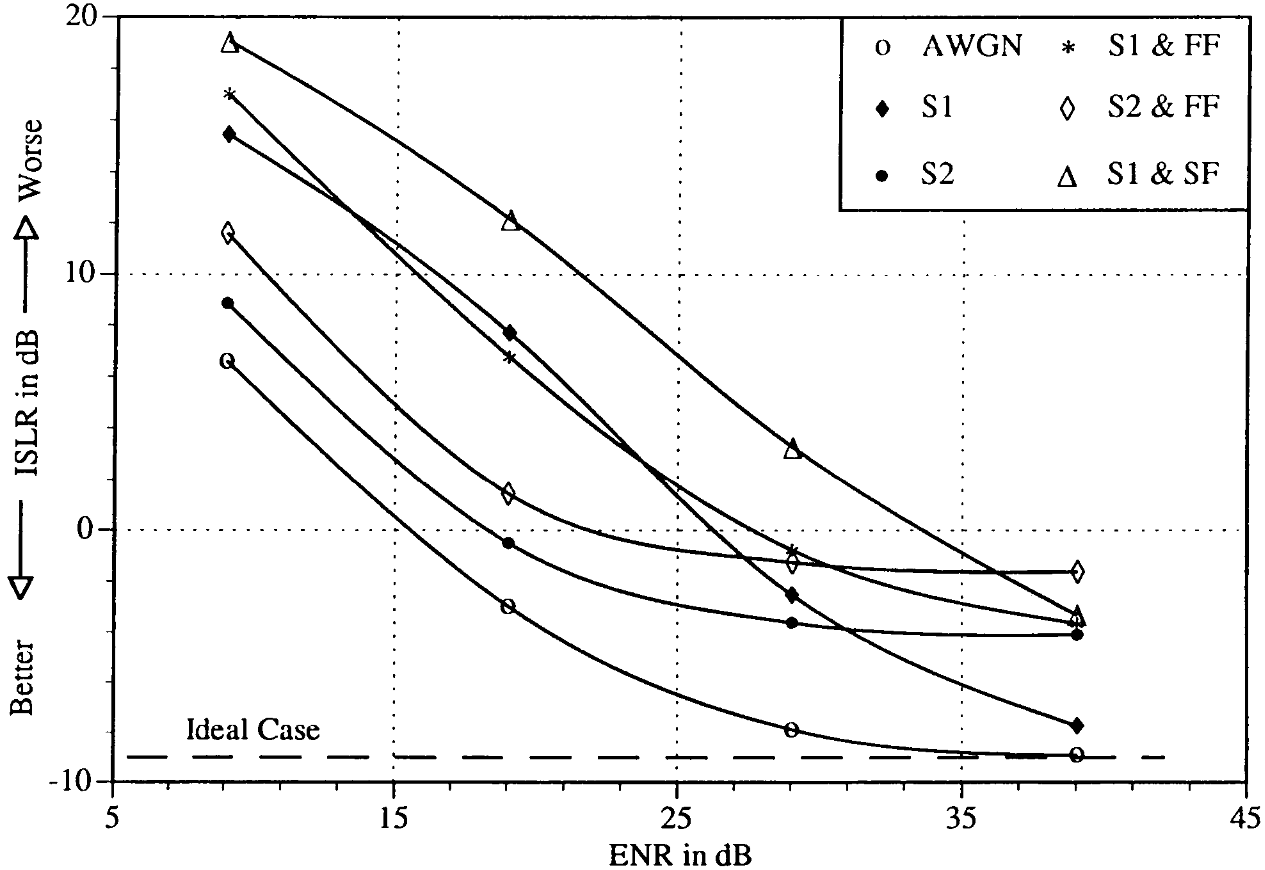

Figure 5.6. Impact of Noise, Target Scintillation, and Fading on the ISLR of a 16-chip Frank Coded Waveform.

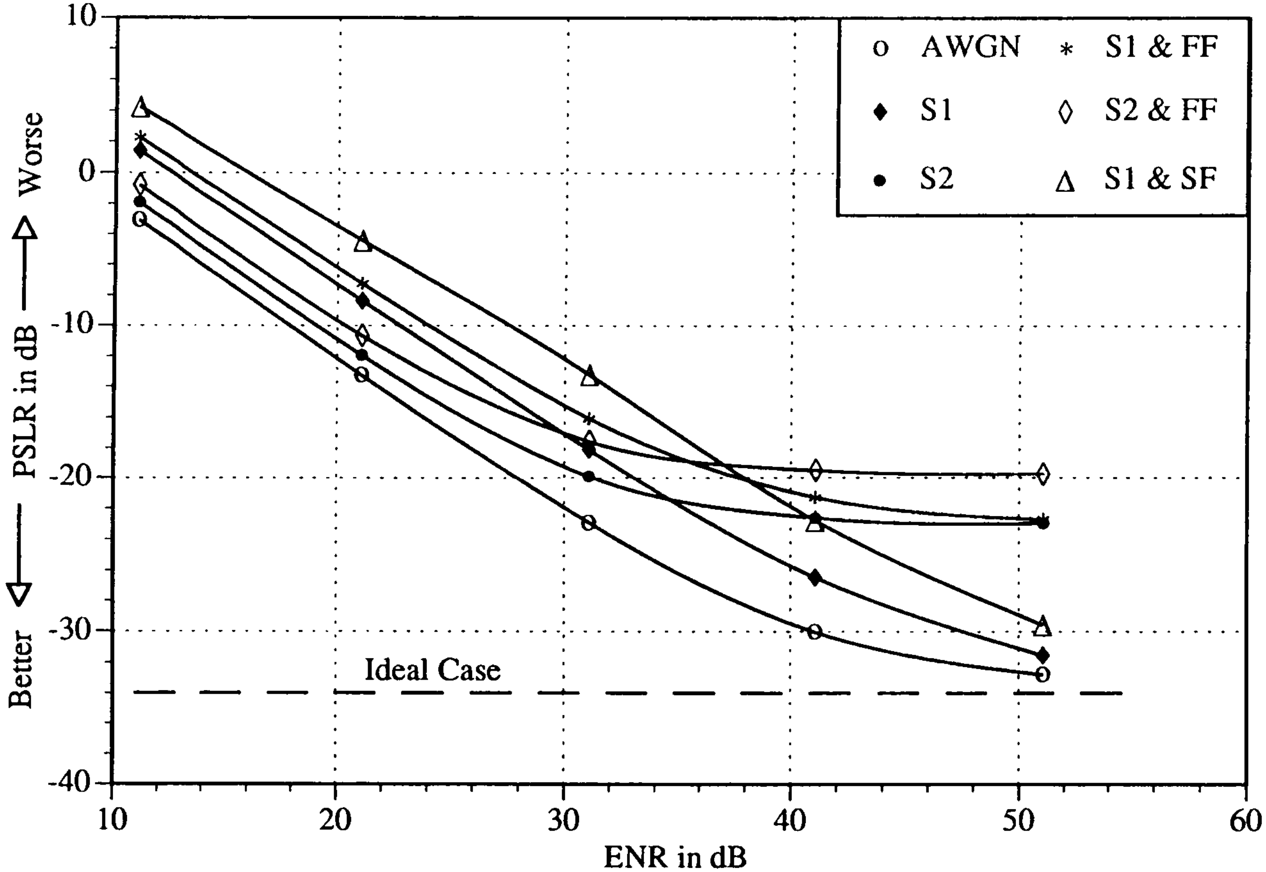

Figure 5.7. Impact of Noise, Target Scintillation, and Fading on the PSLR of a 256-chip Frank Coded Waveform.

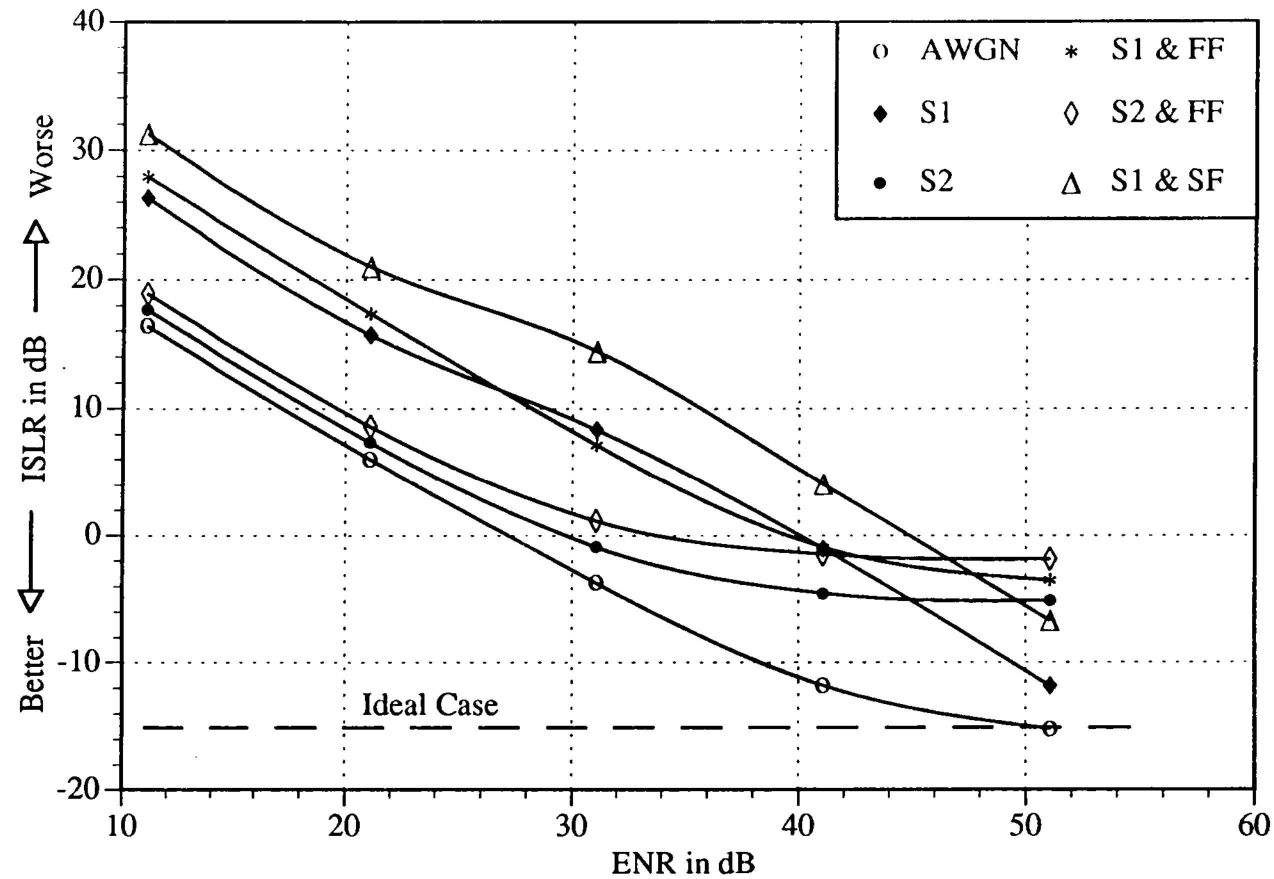

Figure 5.8. Impact of Noise, Target Scintillation, and Fading on the ISLR of a 256-chip Frank Coded Waveform.

The effect of codelength on the resolution performance is now investigated. Under ideal condition, the PLSR and ISLR of a 16-chip Frank coded sequence are known to be −21.07 dB and −9.03 dB, whereas for a 256-chip code, the PSLR and ISLR are −33.97 dB and −15.02 dB respectively. Therefore, the PSLR and ISLR of the Frank code in ideal conditions improve with an increase in the codelength. In order to investigate the effect of codelengths, the PSLR and ISLR for the two codes using each statistical model have been plotted in Figures A5.13-A5.24. It can be seen from the plots for each of the models that the PSLR for the longer codelength is significantly smaller than the PSLR for the shorter codelength at large ENR, but as the ENR is reduced, a crossover takes place and the situation reverses at smaller ENR. At the lower end of the ENR the PSLR for the shorter codelength is about 3 dB smaller than the PSLR for the longer codelength. The effect of codelength on the ISLR follows similar trend except for the S1, S1 & FF, and S1 & SF models, and suggests that the Swerling I target model always causes the ISLR of the longer Frank sequence to be worse than the ISLR of the shorter Frank sequence.

5.3 Results for Complementary Coded Waveforms

In this case, first a smaller complementary coded waveform having only 2x8-chips was used. The data obtained from 200,000 iterations are plotted in Figures 5.9 and 5.10. Notice the almost linear PSLR characteristics of the AWGN and S1 models in Figure 5.9, whereas the PSLR characteristics of these two models for the PN sequence and Frank coded waveforms were non-linear. These two characteristics can be expressed as

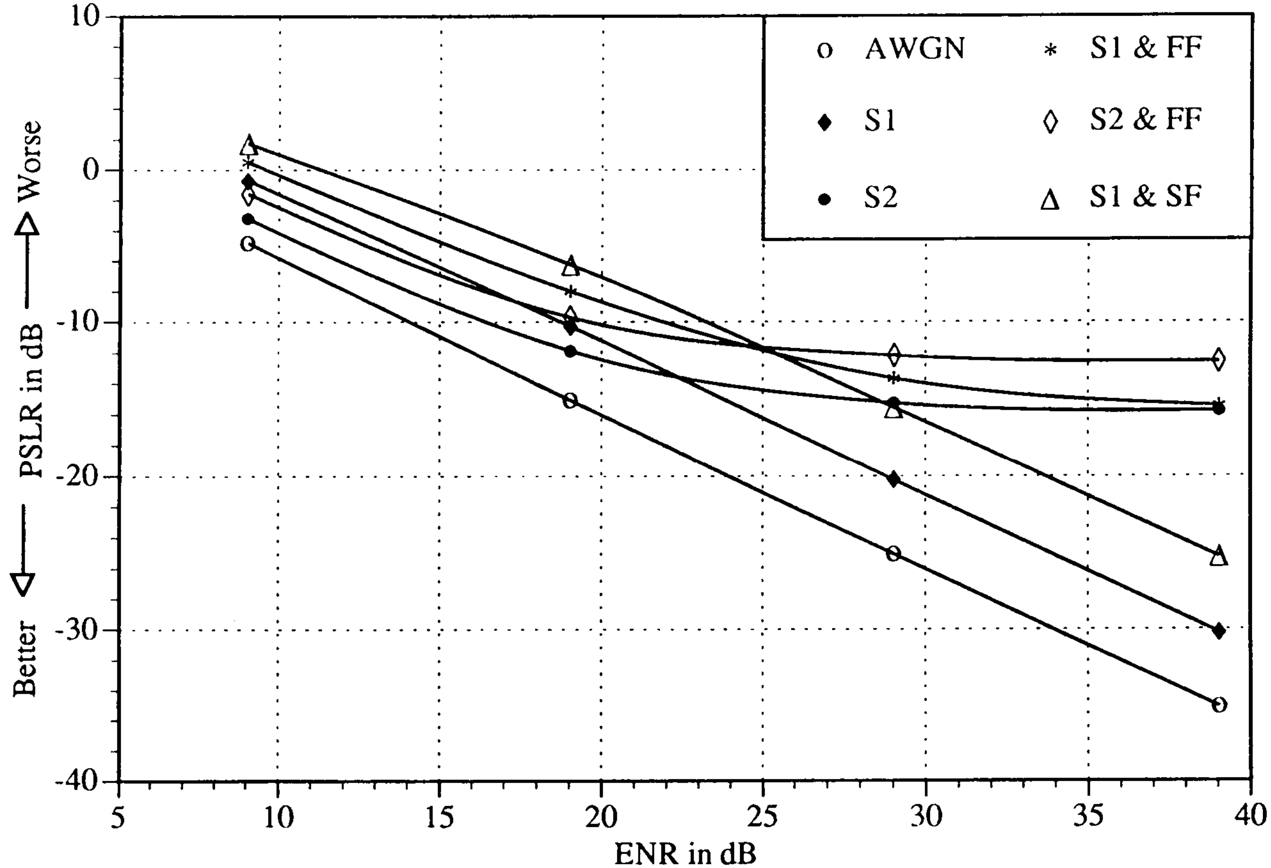

Figure 5.9. Impact of Noise, Target Scintillation, and Fading on the PSLR of a 2x8-chip Complementary Coded Waveform.

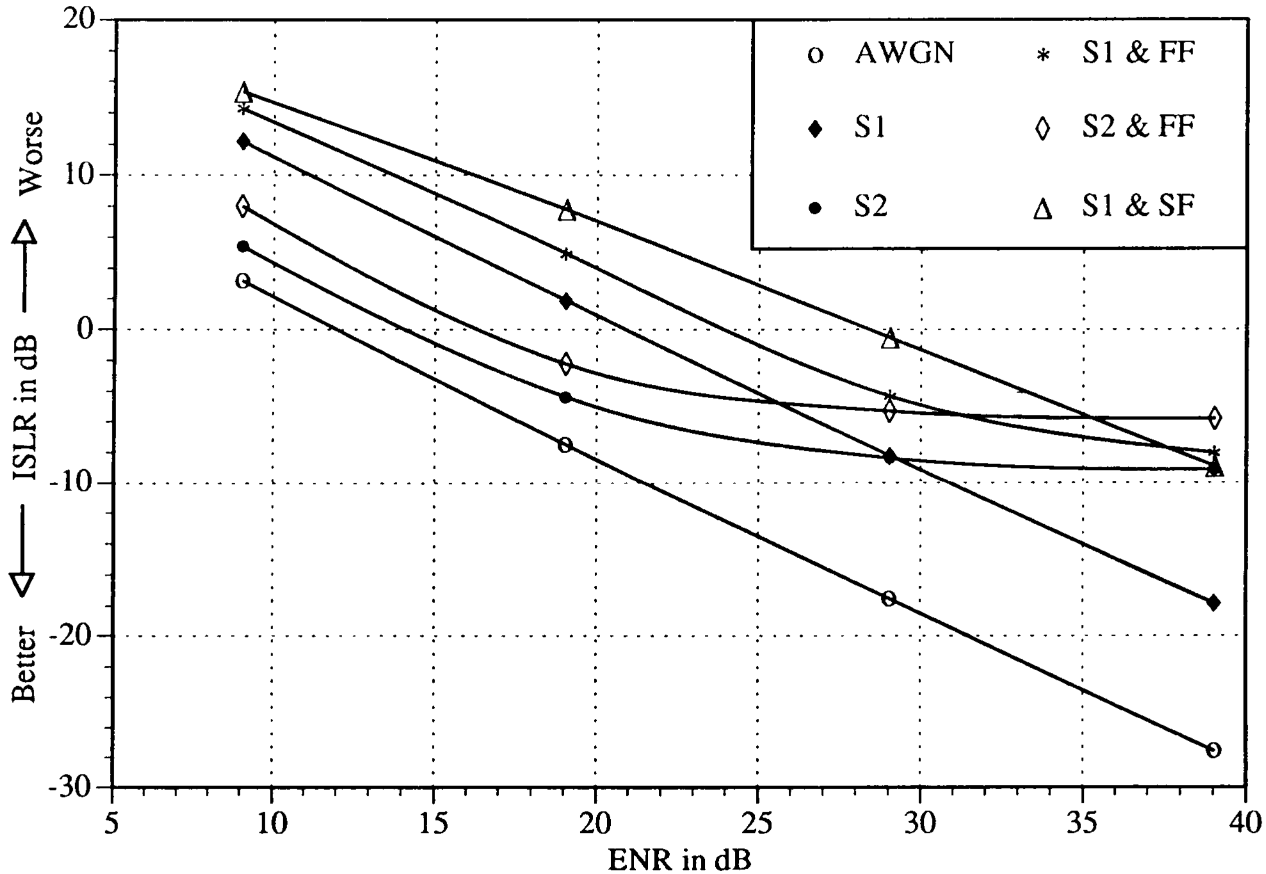

Figure 5.10. Impact of Noise, Target Scintillation, and Fading on the ISLR of a 2x8-chip Complementary Coded Waveform.

$$\mathrm{PSLR}_{(2x8)} = \begin{cases} -\mathrm{ENR} + 4.22, & \mathrm{AWGN}; \\ -\mathrm{ENR} + 8.27, & \mathrm{S1}. \end{cases} \tag{5.1}$$

In (5.1) PSLR and ENR are in dB. Also observe the -1 slope of these two linear characteristics. The remaining four curves bear the same qualitative relationship as found in the case of PN sequence and Frank coded waveforms. Now consider Figure 5.10 which shows the ISLR characteristics of six statistical models. In this case also, the AWGN and S1 characteristics are linear with a slope of -1, and can be expressed as

$$\mathrm{ISLR}_{(2x8)} = \begin{cases} -\mathrm{ENR} + 12.2, & \mathrm{AWGN}; \\ -\mathrm{ENR} + 21.1, & \mathrm{S1}. \end{cases} \tag{5.2}$$

Next, a 2x128-chip complementary coded waveform was used in the simulation. The results are plotted in Figures 5.11 and 5.12. Except in the region of 17 dB < ENR < 27 dB where the "S1" and "S1 & FF" models have identical ISLR values, the PSLR and ISLR characteristics in both the figures are qualitatively similar to the characteristics of the 2x8-chip complementary coded waveform discussed before. Also, the linear equations of the PSLR and ISLR for AWGN and S1 models can be expressed as

$$\mathrm{PSLR}_{(2x128)} = \begin{cases} -\mathrm{ENR} + 7.45, & \mathrm{AWGN}; \\ -\mathrm{ENR} + 11.9, & \mathrm{S1}. \end{cases} \tag{5.3}$$

and

$$\mathrm{ISLR}_{(2x128)} = \begin{cases} -\mathrm{ENR} + 24.4, & \mathrm{AWGN}; \\ -\mathrm{ENR} + 32.8, & \mathrm{S1}. \end{cases} \tag{5.4}$$

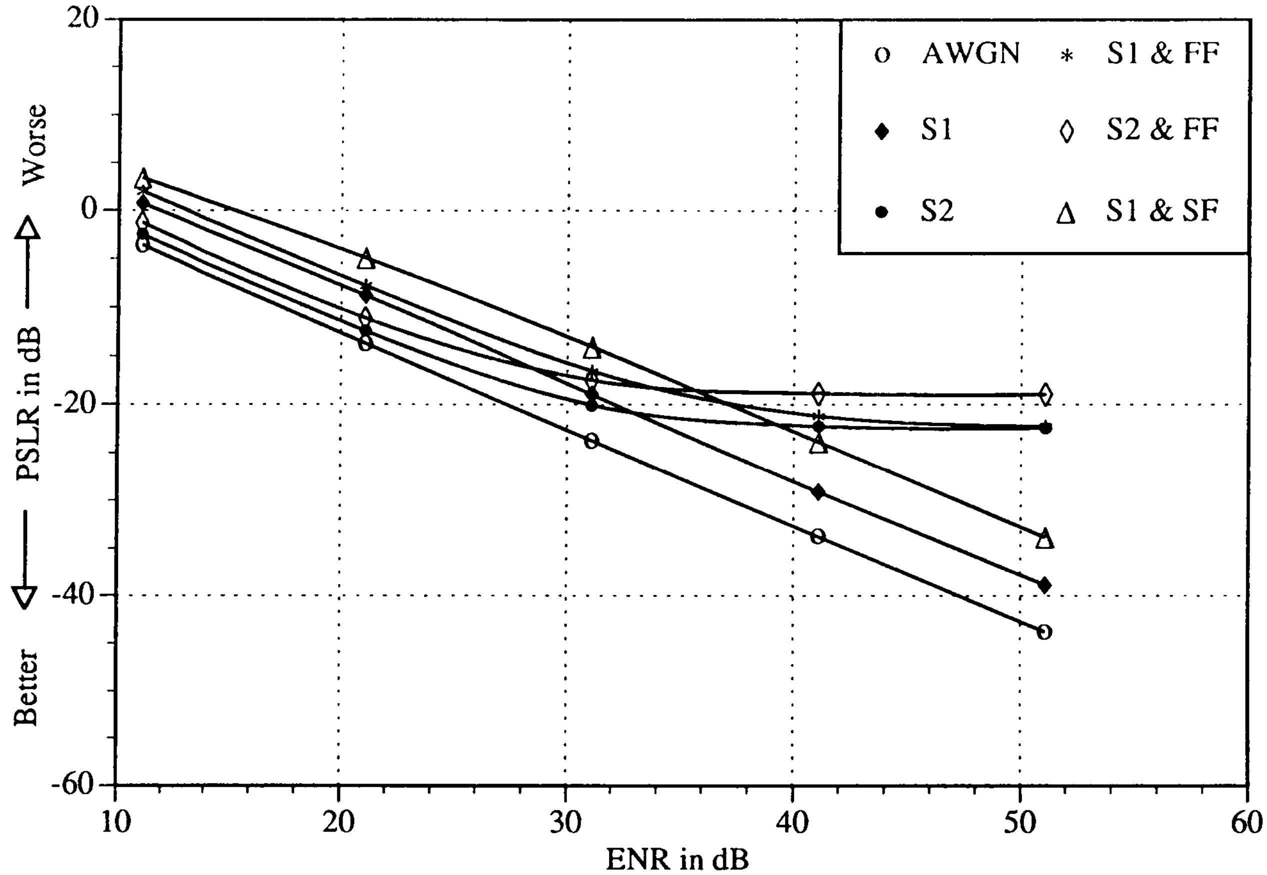

Figure 5.11. Impact of Noise, Target Scintillation, and Fading on the PSLR of a 2x128-chip Complementary Coded Waveform.

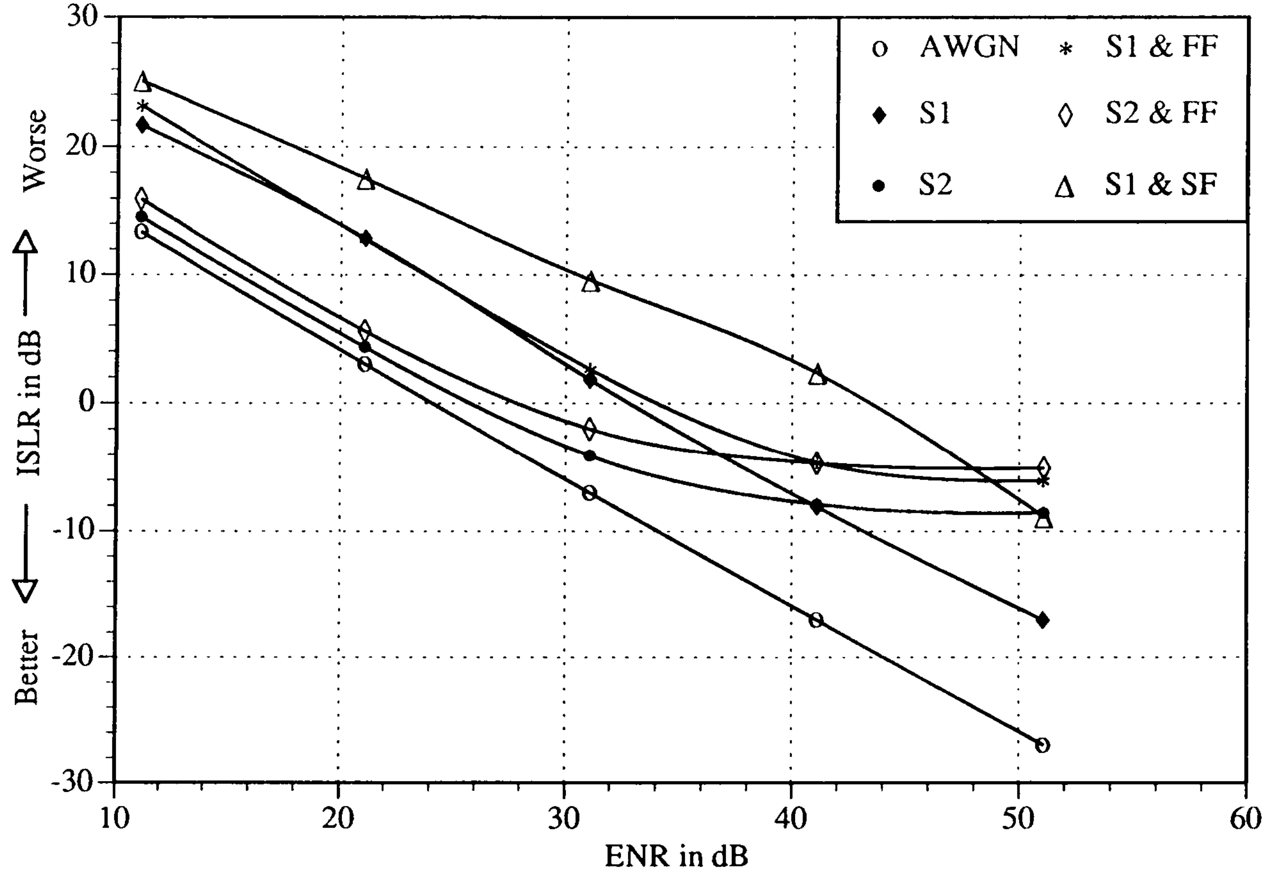

Figure 5.12. Impact of Noise, Target Scintillation, and Fading on the ISLR of a 2x128-chip Complementary Coded Waveform.

In order to investigate the effect of the number of chips used, the PSLR and ISLR for the two codelengths for each model have been plotted in Figures A5.25-A5.36. Figures A5.25-A5.28, or (5.1) – (5.4), indicate that the longer sequence suffers more degradation in AWGN and S1 models than the shorter sequence. The difference in the degradation is about 3.4 dB for the PSLR, and 12 dB for the ISLR. Recall that during investigation of the effect of codelength on the PSLR of PN sequence and Frank codes, crossovers of the PSLR curves for AWGN and S1 models were noticed. However, no such crossover is observed for complementary codes because of the linear PSLR and ISLR characteristics for AWGN and S1 models. Crossovers of the PSLR curves do occur in the case of S2, S1 & FF, and S2 & FF models as can be seen from Figures A5.29, A5.31, and A5.33 respectively. Each of these three models showing crossover of the PSLR characteristics contains a common attribute — all of them contain chip-to-chip Rayleigh variation of the amplitude whether such a variation is caused by Swerling II target fluctuation or by fast fading. Since in the absence of chip-to-chip Rayleigh amplitude variations the PSLR of the longer code is found to to be worse than the shorter code, and after including the effect of chip-to-chip amplitude variation crossovers occur, it can be concluded that a chip-to-chip Rayleigh variation in any form is more detrimental to the PSLR of a shorter code than to the PSLR of a longer code. There is no crossover of the ISLR characteristics for any of the models; the ISLR of the shorter sequence is always found to be smaller than the ISLR of the longer sequence.

5.4 Comparison of the Performance of Coding Techniques

In the preceding sections the effects of various statistical models on individual coding techniques were studied. In this section, a comparative performance of the three coding methods is discussed. First, the shorter sequences listed in Table 3.1 are compared. The PSLR and ISLR of the shorter codes for the six chosen models are shown in Figures A5.37–A5.48 in Appendix 5. As can be observed from these figures, the complementary coded waveform has the smallest PSLR and ISLR for all of the models, and it clearly outperforms the other two codes. In all cases, the Frank coded waveform has a better PSLR performance than the complementary coded waveform. However, as summarized in Table 5.1 which grades the three codes from the best to the worst on the basis of the ISLR performance for each of the models in different ENR regions, there are a few limited regions for S1, S2, and S1 & SF models in which the ISLR performance of the PN sequence coded waveform has been found to be marginally better than the Frank coded waveform, though the difference is not very significant.

Similar plots for the longer sequences listed in Table 3.2 are shown in Figures A5.49–A5.60 in Appendix 5. In order to highlight some of the interesting observations, the results are summarized in Table 5.2. As shown in the table, the PN sequence coded waveform has the worst performance for any of the models. Recall that while comparing the performance of shorter sequences, the complementary coded waveform was found to be the best, but this is not true for the longer sequence. The longer complementary coded sequence performs the best only for AWGN, S1, S1&SF models. As shown in Table 5.2, above certain ENR values for S2, S1&FF, and S2&FF models, the Frank coded waveform has marginally smaller PSLR than the complementary coded waveform. It is

Table 5.1. A Comparison of the ISLR Performance of 15/16-chip Codes.

Model	ENR Region	Best	Average	Worst
AWGN	Entire	CC	FR	PN
S1	< 27 dB	CC	PN	FR
	> 27 dB	CC	FR	PN
S2	< 15 dB	CC	PN	FR
	> 15 dB	CC	FR	PN
S1&FF	Entire	CC	FR	PN
S2&FF	Entire	CC	FR	PN
S1&SF	< 23 dB	CC	PN	FR
	> 23 dB	CC	FR	PN

interesting to note that each of these three models include chip-to-chip Rayleigh amplitude variation, whether it is caused by Swerling II target fluctuation or by fast channel fading. This suggests that at large ENR values any chip-to-chip amplitude variation causes more serious degradation to the PSLR of a longer complementary coded waveform, than to the PSLR of a longer Frank coded waveform.

The results for ISLR performance are summarized in Table 5.3, which shows that the complementary coded waveform has the best performance. The Frank coded waveform generally performs better than the PN sequence coded waveform, except for in

Table 5.2. A Comparison of the PSLR Performance of 255/256-chip Codes.

Model	ENR Region	Best	Average	Worst
AWGN	Entire	CC	FR	PN
S1	Entire	CC	FR	PN
S2	< 33 dB	CC	FR	PN
	> 33 dB	FR	CC	PN
S1&FF	< 41 dB	CC	FR	PN
	> 41 dB	FR	CC	PN
S2&FF	< 30 dB	CC	FR	PN
	> 30 dB	FR	CC	PN
S1&SF	Entire	CC	FR	PN

the limited ENR regions for the S1, S1&FF, and S1&SF models. Note that each of these three models include scan-to-scan Rayleigh amplitude variation. It can thus be concluded that in certain regions any chip-to-chip amplitude variation causes more serious degradation to the ISLR of a longer Frank polyphase coded waveform, than to the ISLR of a longer binary PN sequence coded waveform.

Table 5.3. A Comparison of the ISLR Performance of 255/256-chip Codes.

Model	ENR Region	Best	Average	Worst
AWGN	Entire	CC	FR	PN
S1	< 25 dB	CC	FR	PN
	25<ENR<42	CC	PN	FR
	> 42 dB	CC	FR	PN
S2	Entire	CC	FR	PN
S1&FF	< 13 dB	CC	FR	PN
	13<ENR<22	CC	PN	FR
	> 22 dB	CC	FR	PN
S2&FF	Entire	CC	FR	PN
S1&SF	< 36 dB	CC	FR	PN
	36<ENR<44	CC	PN	FR
	> 44 dB	CC	FR	PN

5.5 Summary of Results

The quantitative and qualitative results presented in this chapter can be summarized as follows.

1. At low ENR, a scan-to-scan amplitude variation, such as Swerling I target fluctuation or slow fading, causes greater resolution degradation for all of the codes than a chip-to-chip amplitude variation.

2. In contrast, at high ENR, a chip-to-chip amplitude variation, such as Swerling II target fluctuation or fast fading, causes greater resolution degradation for all of the codes than a scan-to-scan amplitude variation.
3. At low ENR, the PSLR of a shorter PN sequence coded waveform is marginally better than the PSLR of a longer PN sequence coded waveform, but the situation significantly reverses at higher ENR. The ISLR of a shorter PN sequence coded waveform is always better than the ISLR of a longer PN sequence coded waveform.
4. A shorter Frank coded waveform has marginally better PSLR at low ENR than a longer Frank coded waveform, but a longer codelength at higher ENR has a significantly better PSLR than a longer codelength. A scan-to-scan Rayleigh amplitude variation in any form is more detrimental to the ISLR of longer Frank coded waveform to a shorter Frank coded waveform. In the absence of a scan-to-scan amplitude variation, the ISLR of a shorter Frank coded waveform is always better than that of a longer Frank coded waveform.
5. In the absence of chip-to-chip Rayleigh variation, the PSLR of a shorter complementary coded waveform is always better than the PSLR of a longer complementary coded waveform. A chip-to-chip Rayleigh variation in any form is more detrimental to the PSLR of a shorter complementary coded waveform than to the PSLR of a longer complementary coded waveform, and for such models, a longer complementary coded waveform exhibits better PSLR at higher ENR than the shorter complementary coded waveform. The ISLR of the shorter complementary coded waveform always happens to be smaller than the ISLR of the longer complementary coded waveform.
6. A comparison of the three coding methods using shorter sequences shows that the complementary coded waveform has the best, and the PN sequence coded waveform

has the worst performance for any of the models. The Frank coded sequence performs in between these two.

7. A comparison of the three coding methods using longer sequences suggests that the PSLR of the PN sequence coded waveform is the worst. The PSLR of the longer complementary coded sequence is the best for models that do not include chip-to-chip Rayleigh amplitude variations. A chip-to-chip amplitude variation causes more serious degradation to the PSLR of a longer complementary coded waveform than to the PSLR of a longer Frank coded waveform; this causes the PSLR of the Frank coded waveform to be marginally better than the PSLR of the complementary coded waveform in a few small regions of ENR values. However, for the most part, the complementary coded waveform does have a better PSLR than the Frank coded waveform.
8. Among the longer codes, the complementary coded waveform has the best ISLR performance. The Frank coded waveform generally performs better than the PN sequence coded waveform, except in the limited ENR regions for the models which include scan-to-scan Rayleigh amplitude variations. Any scan-to-scan amplitude variation causes more serious degradation to the ISLR of a longer Frank polyphase coded waveform than to the ISLR of a longer binary PN sequence coded waveform.

Quantitative and qualitative performance results of non-hybrid coded waveforms were presented in this chapter. As will be seen, the conclusions arrived at in this chapter, to a great extent, are precursors of the results for hybrid coded radar signals presented in the next chapter.

CHAPTER 6

Performance of Hybrid Codes

In this chapter the resolution performance results of hybrid pulse compression techniques for the statistical radar system models described in Chapter 3 are presented. Hybrid codes, which employ a combination of phase coding and frequency stepping, were briefly discussed in Chapter 2. In the case of non-hybrid coded waveforms it was assumed that either there was no Doppler shift, or if there was a Doppler shift, the frequencies of the IF oscillator was assumed to have been suitably adjusted. The processing applied to hybrid coded waveforms includes two additional ideas. First, the Doppler shift of the received waveform is determined, but to extract the Doppler shift the sequences must be repeated in time. Second, a phase compensation is applied to offset the additional phase terms which result due to transmission of the subsequences at different instants of time. These additional ideas and the processing algorithm for hybrid codes are introduced in the next section, and after presenting simulation results for individual coding techniques, a comparison among them is made.

6.1 Algorithm for Processing of Hybrid Coded Waveforms

The signal processing algorithm for detection of hybrid coded waveforms is described in this section. The mathematical details related to the development of the algorithm can be found in [16]. Referring to Figure 2.7, the equation of the transmitted hybrid coded waveform can be written as

$$s(t) = \sum_{k=0}^{K-1} \sum_{n=0}^{N-1} \sum_{p=0}^{L-1} u_p(t-pT_r-nT_{dk}-T_{fk})\cos[2\pi(f_{RF}+f_k)t + \theta_k] \tag{6.1}$$

where

K = Number of frequency steps

N = Number of repetitions

L = Number of subsequences in a code ($L = 1$ for a PN sequence, and $L = 2$ for a complementary code pair)

$u_p(t)$ = A phase coded subsequence.

T_r = Transmission delay between the subsequences.

The equation for the p-th subsequence of the delayed echo due to a constant velocity target is therefore

$$r(t) = u_p(t-pT_r-nT_{dk}-T_{fk}-\tau)\cos[2\pi(f_{RF}+f_k+f_{dk})t - 2\pi(f_{RF}+f_k)\tau + \theta_k] \tag{6.2}$$

where

$\tau = \frac{2R}{c}$ is the round-trip time delay to the target, and

$f_{dk} = -(f_{RF}+f_k)\dot{\tau}$ is the Doppler shift due to the k-th frequency, where the dot indicates the time derivative.

The received signal, $r(t)$, is processed by a quadrature receiver similar to the one shown in Figure 1.8. In the case of frequency stepping, the center frequencies of the video signal are f_{ok} instead of a single frequency, f_o. The center frequency, f_{ok} is related to the expected value of the Doppler shift. The video signal centered at f_{ok} is sampled once every chip-time to generate the quadrature samples as shown in Step 1 in Figure 6.1. In the next step, these quadrature samples are correlated with the encoding sequence to obtain the $I(k,n,p,m)$ and $Q(k,n,p,m)$ samples. Note that for the PN sequence coded waveform, L=1 and the index p has a single value , which results in a three-dimensional matrix for $I(\bullet)$ and $Q(\bullet)$. However, for the complementary coded pair, L = 2 and p = 0,1 which results in a four-dimensional data matrix. Using these I- and Q-samples, the complex sample matrix, $w(k,n,p,m)$, is generated as shown in Step 3. In the next step, an N-point FFT is performed on each of the sequences along the n-axis to extract the Doppler information. This FFT translates the N time-samples obtained from repeating the subsequence into their corresponding frequency samples. The resulting frequency bin width along the n-axis is

$$f_{bk} = \frac{1}{NT_{dk}} \tag{6.3}$$

If the Doppler shift is a multiple of f_{bk}, the corresponding frequency sample will occupy the correct single frequency bin. Step 5 is very important in realizing the benefit of frequency stepping. In this step, the samples from $w1(k,n,p,m)$ are multiplied by $\exp[-j2\pi n f_{bk}(pT_r+T_{fk})]$ to apply phase correction to compensate for the Doppler induced phase errors resulting from known transmission delays, T_r and T_{fk}. Step 6 is applicable only to the complementary coded waveform in which case corresponding samples from the subsequences are added. Since Step 4 had converted the time-samples into frequency samples, Step 7 translates the matrix back into the time-samples by taking K-point IFFT along the k-axis. Therefore, the delay bin-width, $\Delta\tau$,becomes

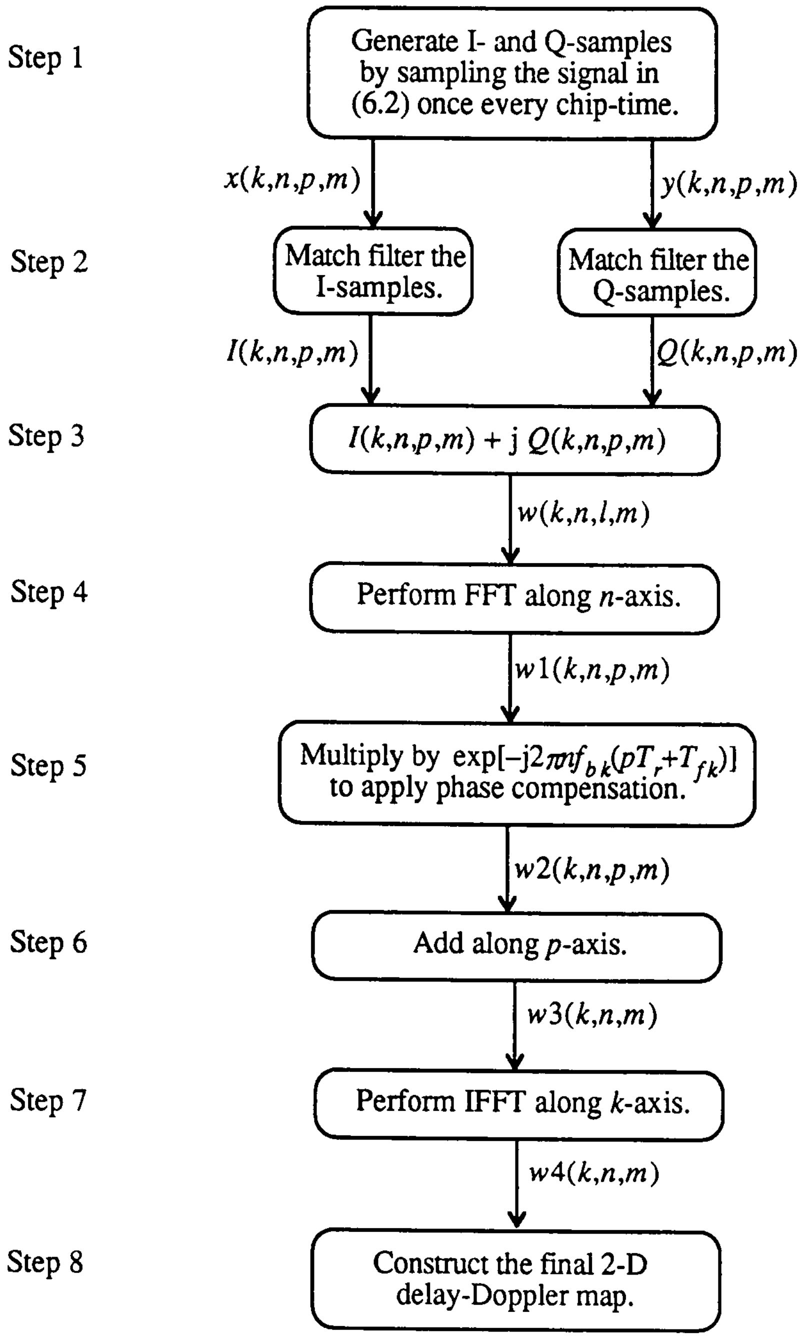

Figure 6.1. Algorithm for Detection of Hybrid Coded Waveforms.

$$\Delta\tau = \frac{1}{K\,\Delta f} \tag{6.4}$$

where, for linear frequency stepping, Δf is the frequency increment. In the final step, a two-dimensional delay-Doppler map showing $\Delta\tau$ versus f_{bk} is constructed. Such maps for the PN sequence and complementary coded waveforms for the parameter values chosen in the simulation are shown in Figure 6.2 for a noise-free situation. Due to the chosen value of the Doppler shift the decoded samples fall in the third row. The leading blank bins are due to the assumed delay τ of the echo. More will be said about these maps in the following sections.

The target and/or channel fading models were incorporated into the above algorithm by appropriately multiplying random Rayleigh samples to the quadrature samples $x(k,n,p,m)$ and $y(k,n,p,m)$. Independent Gaussian samples were then added to these quadrature samples prior to matched filtering. The results obtained are presented in the following sections.

6.2 Results for PN Sequence Coded Waveform

A 15-chip PN sequence with eight repetitions and eight frequency steps was used for simulation. Therefore, as mentioned for this waveform in Table 3.3, $M = 15, L = 1$, $N = 8$, and $K = 8$. The final delay-Doppler map in Figure 6.2(a), which depends on the parameters used in the simulation, shows the location of the decoded samples as dots for the noise-free case. The blank bins indicate zero values in the noise-free case. The

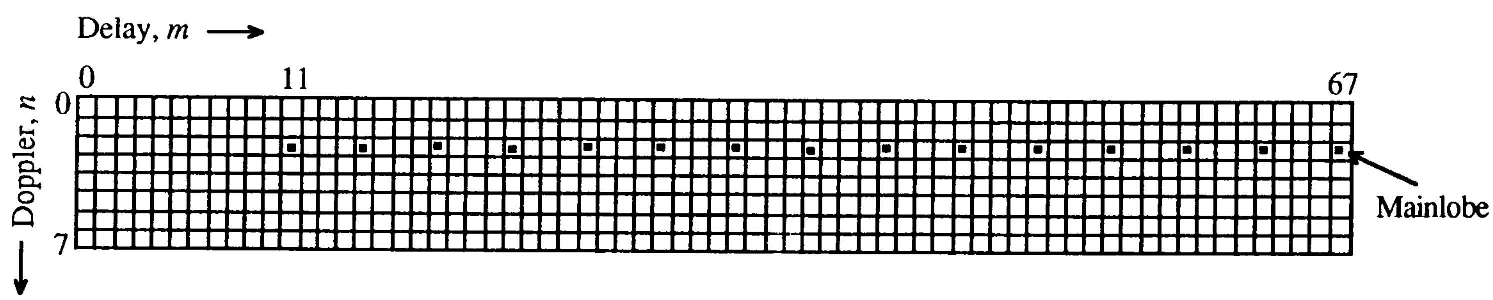

(a)

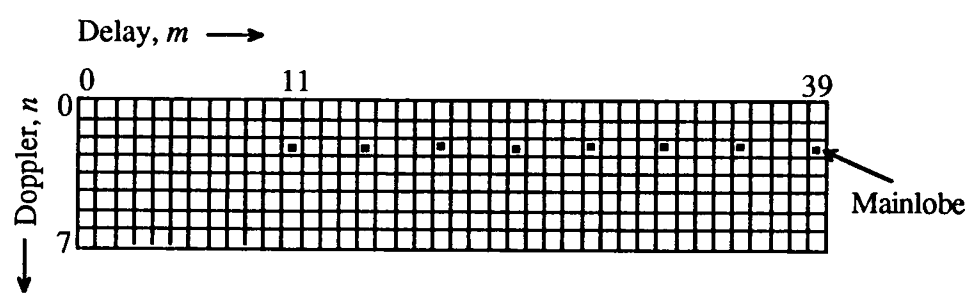

(b)

Figure 6.2. The Final Delay-Doppler Maps for Coded Waveforms in a Noise-free environment.
(a) PN Sequence. (b) Complementary Code.

mainlobe occurs at m = 67, and the sidelobe samples are separated by four samples because eight frequency steps were used. When noise is added, each of these cells contains a non-zero value. The PSLR or ISLR were calculated using all of the sidelobe samples for m = 11 through m = 66 in the third row. The plot of the PSLR versus the ENR is shown in Figure 6.3. In order to obtain satisfactory results, 15000 iterations had to be used for each data point requiring 10 computer-days on Macintosh IIx. The bulk of the simulation time was consumed in performing FFT and correlations. It can be observed from Figure 6.3 that the at small ENR values, the qualitative characteristics of the PSLR plot are similar to the ones found for non-hybrid PN sequence coded waveforms in Chapter 5. However, the difference in the PSLR is only 5 dB. Also, at smaller ENR values crossovers do occur as in the case of non-hybrid waveforms, but at much larger ENR values each of the models results in almost the same PSLR, and the difference between any two models becomes negligible. In any case, the hybrid coded PN sequence waveforms generally retain their non-hybrid PSLR characteristics. Each of the models at large ENR almost approaches the ideal PSLR value of -13.979 dB.

The plot of ISLR versus the ENR for the 15-chip PN sequence code is shown in Figure 6.4. In this case also, the AWGN-only model results has the best performance, and the behavior for other models is qualitatively similar to what was observed for the PSLR.

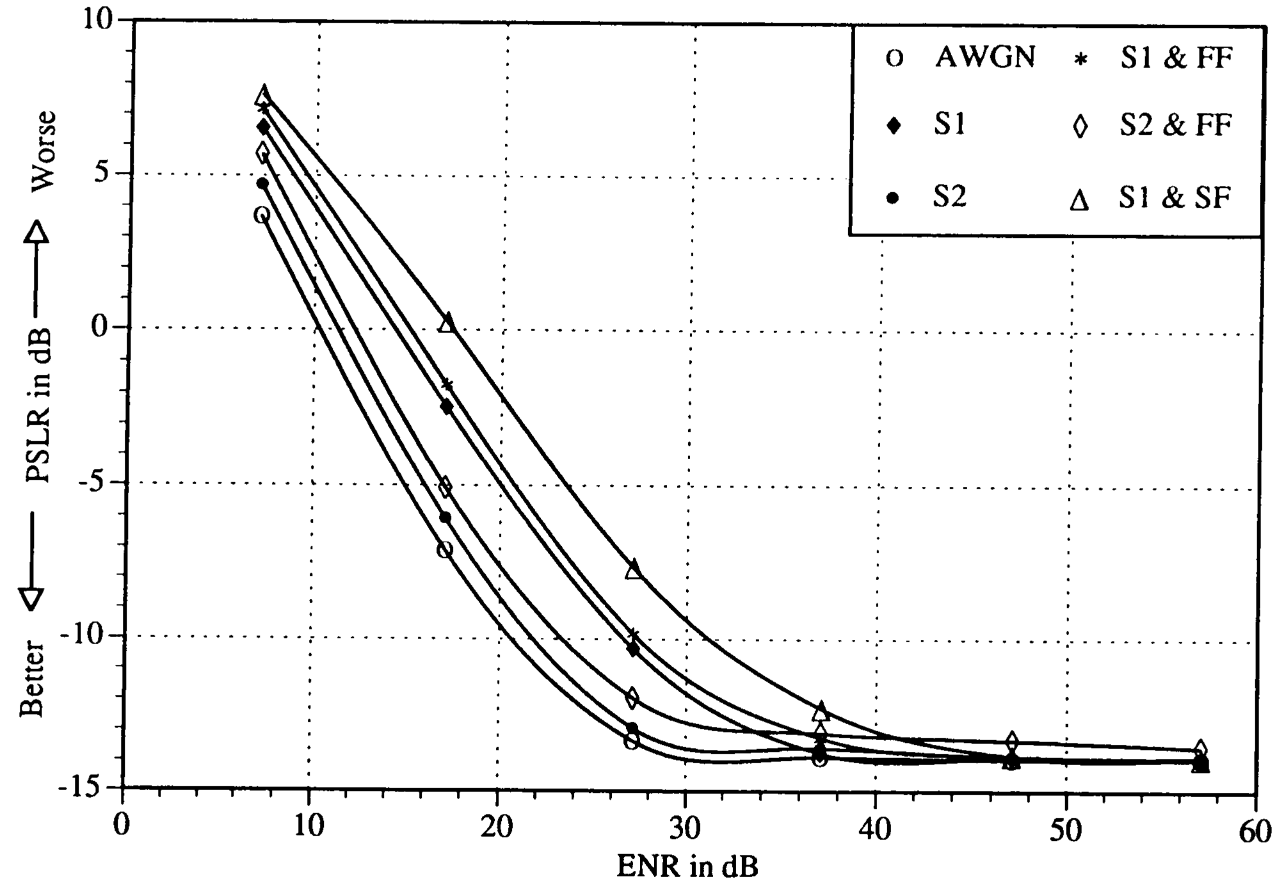

Figure 6.3. Impact of Noise, Target Scintillation, and Fading on the PSLR of a Hybrid 15-chip PN Sequence Coded Waveform.

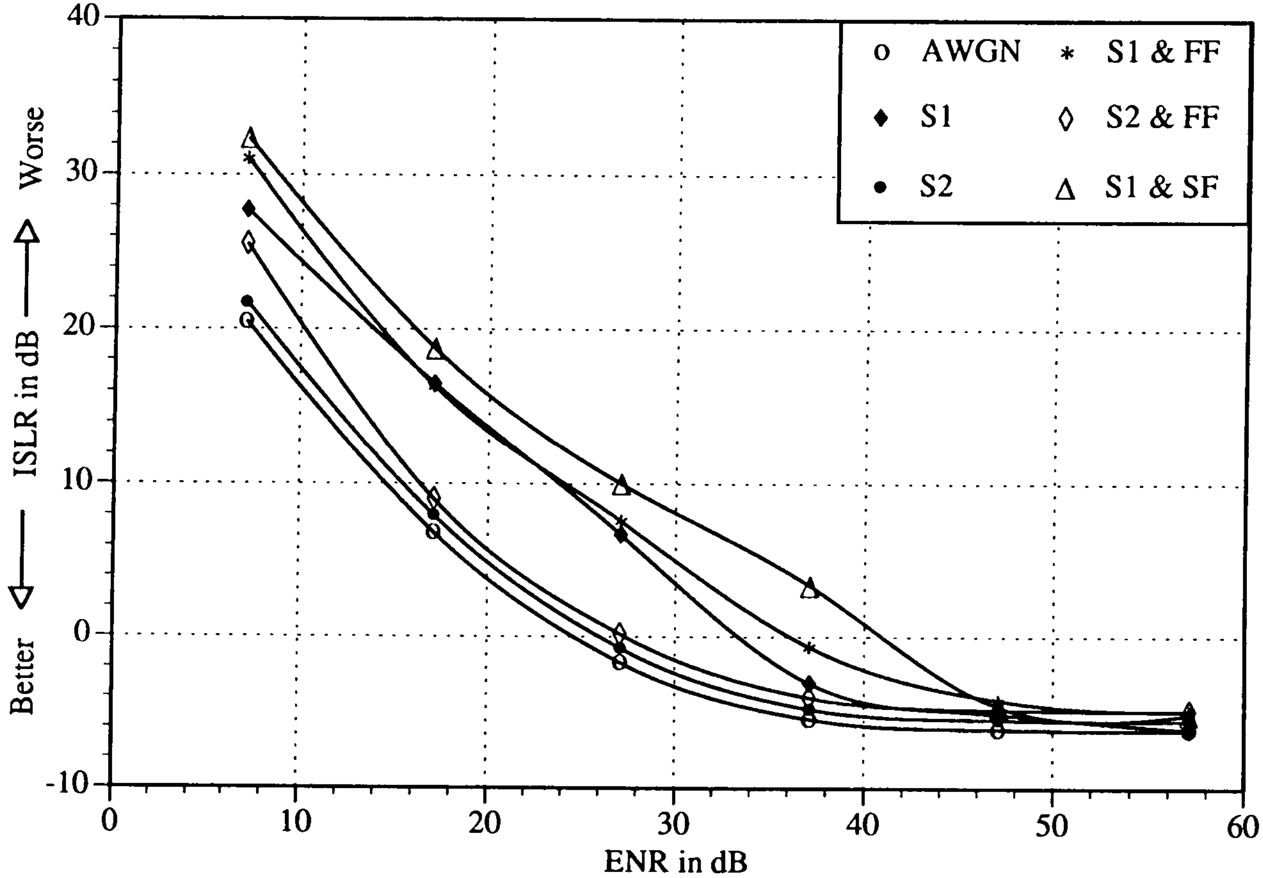

Figure 6.4. Impact of Noise, Target Scintillation, and Fading on the ISLR of a Hybrid 15-chip PN sequence Coded Waveform.

6.3 Results for Complementary Coded Waveform

In this case, a complementary coded waveform having 2x8-chips, eight subsequence repetitions, and eight frequency steps has been used. Thus the same number of subsequence repetitions and frequency steps have been used as in the case of the hybrid PN sequence coded waveform in the preceding section. The final delay-Doppler map for the parameters used in the simulation is shown in Figure 6.2(b) in which the third row contains the decoded samples for the noise-free case. The mainlobe occurs at $m = 39$, and the sidelobe samples are separated by four samples. The sidelobe locations have shown by dots, but for complementary code these values are zero for noise-free situation. The PSLR or ISLR were calculated using all of the sidelobe samples for $m = 11$ through $m = 38$ in the third row. The data obtained from 15,000 iterations are plotted in Figures 6.5 and 6.6. Notice the linear PSLR characteristics of the AWGN and S1 models in Figure 6.5, and recall that the PSLR characteristics of these two models for non-hybrid complementary codes were also found to be linear. These two characteristics for the hybrid code under consideration can be written as

$$\mathrm{PSLR}_{(2x8x8x8)} = \begin{cases} -\mathrm{ENR} + 9.46, & \text{AWGN;} \\ -\mathrm{ENR} + 13.03, & \text{S1.} \end{cases} \tag{6.5}$$

In (6.5) the PSLR and ENR are in dB, and the subscripts to the PSLR stand for (LxMxNxK). Also observe the same -1 slope of these two linear characteristics. A comparison of (6.5) with the results for 2x8-chip and 2x128-chip non-hybrid complementary coded waveforms in (5.1) and (5.3) illustrates the similarity between non-hybrid and hybrid coded waveforms. It was concluded from (5.1) and (5.3) that the PLSR of the longer code was not as good as the PLSR of the shorter code. The PSLR of

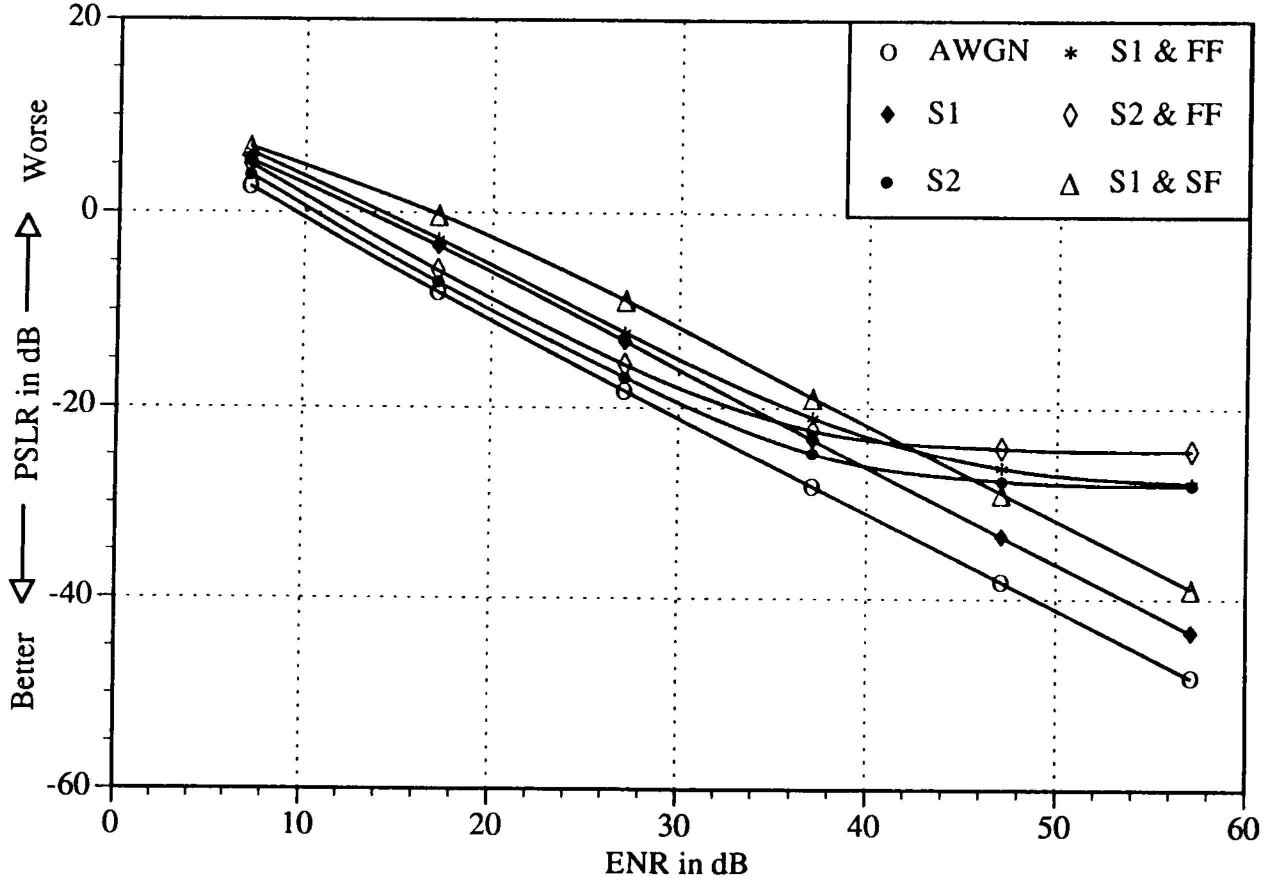

Figure 6.5. Impact of Noise, Target Scintillation, and Fading on the PSLR of a Hybrid 2x8-chip Complementary Coded Waveform.

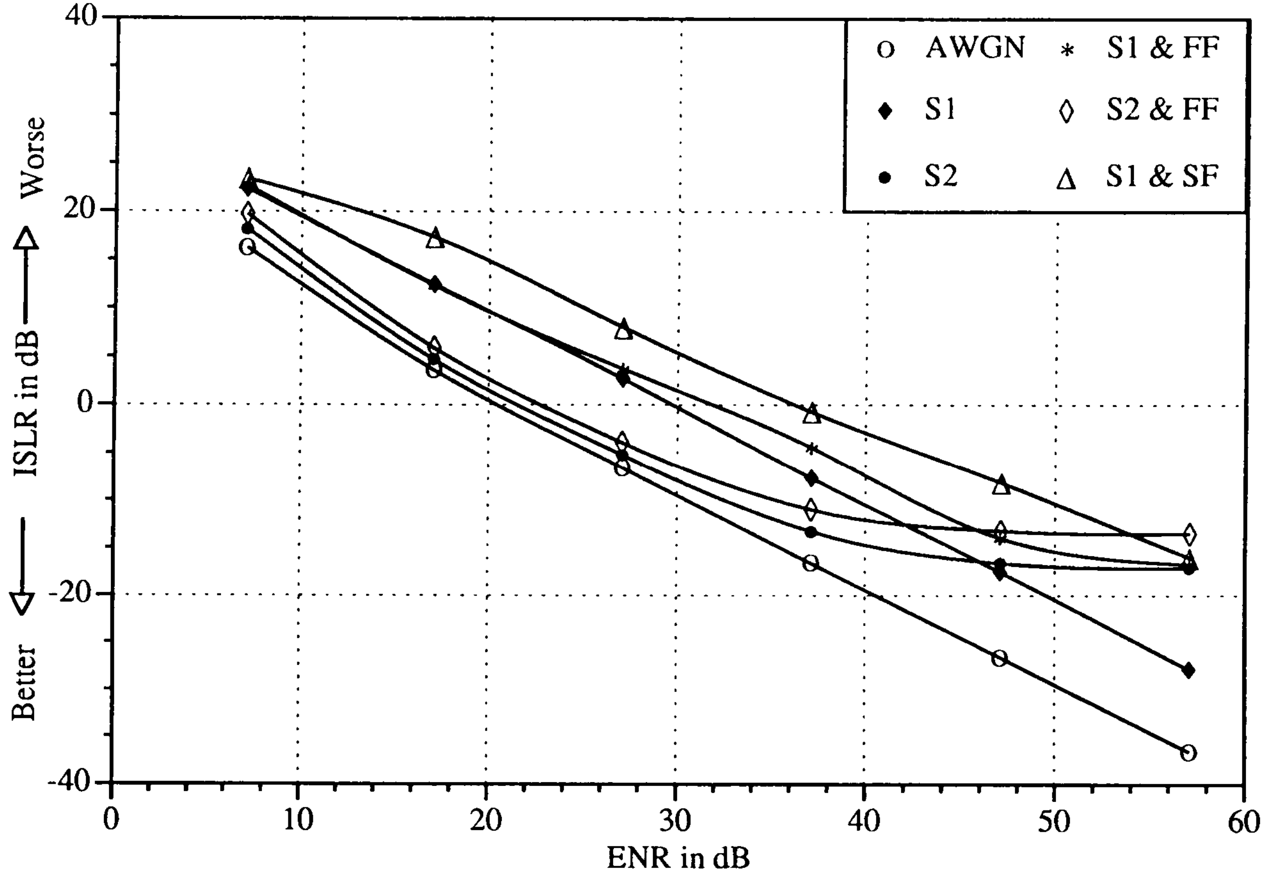

Figure 6.6. Impact of Noise, Target Scintillation, and Fading on the ISLR of a Hybrid 2x8-chip Complementary Coded Waveform.

the 2x8x8x8-chip hybrid waveform clearly indicates the same trend. Note that the hybrid waveform used here contains 1024 chips, and from the observed trend it appears possible that a 2x512-chip complementary coded waveform will have an identical PSLR performance as a 2x8x8x8-chip hybrid waveform. However, due to the enormous computer time needed, this comparison was not tried. The remaining four curves bear the same qualitative relationship as found in the case of non-hybrid complementary coded waveforms.

Now consider Figure 6.6 which shows the ISLR characteristics of six statistical models. In this case also, the AWGN and S1 characteristics are linear with a slope of -1, and can be expressed as

$$ISLR_{(2x8x8x8)} = \begin{cases} -ENR + 22.23, & \text{AWGN;} \\ -ENR + 29.61, & \text{S1.} \end{cases} \tag{6.6}$$

Equation (6.6) should be compared with the results for non-hybrid codes in (5.2) and (5.4) to see the similarity. The remaining four curves bear the same qualitative relationship for these statistical models as found in the case of non-hybrid complementary coded waveforms.

6.4 Comparison of the Performance of Hybrid Coding Techniques

In the preceding sections, the effects of various statistical models on individual coding techniques were studied. In this section, comparative performance of the two hybrid coding methods are compared. The PSLR and ISLR of the two hybrid codes for the six chosen models are compared in Figures A6.1–A6.12 in Appendix 6. As can be observed from these figures, the hybrid complementary coded waveform always has smaller PSLR and ISLR for all of the models, and it clearly outperforms the hybrid PN sequence codes.

6.5 Summary of Results

The quantitative and qualitative results presented in this chapter provide the following additional conclusions.

1. In general, statistical models qualitatively affect the hybrid coded waveforms in the same way as they affect the non-hybrid coded waveforms.
2. The variation in the PSLR of the hybrid PN sequence coded waveform for a given ENR is not more than 5 dB using any of the models. At higher end of the ENR scale, the difference in the PSLR of the hybrid PN sequence code is negligible regardless of the model used. In contrast, the choice of statistical models has relatively greater impact on the PSLR and ISLR of the hybrid complementary coded waveform, especially at large ENR values. This observation, to a lesser extent, applies to the ISLR as well.
3. The hybrid complementary coded waveform has better PSLR and ISLR performance than the hybrid PN sequence coded waveform.

CHAPTER 7

Conclusions

The objective of this paper has been to determine the effect of a wide class of operating conditions on coded radar waveforms. Three efficient non-hybrid coding methods – PN sequence, Frank, and complementary codes – were used for this purpose. Two sequences were used for each of these three non-hybrid coding methods – a shorter sequence, and a relatively longer sequence. In addition, frequency-stepped hybrid waveforms employing PN sequences and complementary codes were also used in the investigation. Exhaustive numerical results for resolution performance in terms of PSLR and ISLR were presented for six different situations which included various combinations of AWGN; Swerling I and Swerling II target fluctuations; and slow and fast channel fading. Extensive discussions on the results highlighting major trends as well as minor exceptions were presented at the end of the preceding two chapters. A few general conclusions are, however, summarized in the following paragraphs.

It is concluded from the results that for all of the coding methods, non-hybrid and hybrid, at a low noise level a chip-to-chip amplitude variation is more detrimental to the resolution performance than a scan-to-scan amplitude variation. In contrast, at a high noise level a scan-to-scan amplitude variation causes more degradation to the resolution performance than a chip-to-chip amplitude variation. These observations suggest that it is important to a radar designer to consider the ENR together with the expected target fluctuation and/or channel fading characteristics to achieve the desired values of PSLR and

ISLR. The use of an appropriate target and/or channel model is highly desirable to optimize the radar system design and to avoid misleading results.

From the study of the effect of codelength of non-hybrid waveforms, it has been concluded that at a high noise level, shorter Frank and PN sequence codes have better resolution performance than the corresponding longer codes. However, this generalization does not hold true for complementary codes for AWGN and scan-to-scan amplitude variations, in which case, regardless of the noise level, a longer code always performs worse than a shorter code. These observations are contrary to the well-known rule in an ideal noise-free situation in which the ACS of a longer PN or Frank code is known to have better PSLR and ISLR.

Among non-hybrid coding methods, complementary codes generally outperform the Frank and PN sequence codes, and the PN sequence codes have generally been found to demonstrate the worst resolution performance. In general, the statistical models qualitatively affect the hybrid coded waveforms in much the same way as they affect the non-hybrid coded waveforms, with the hybrid complementary coded waveforms having better resolution performance than the hybrid PN sequence coded waveforms.

Although a few valuable analytical results have been derived in Chapter 4, it is pertinent to mention that the end-results were obtained through time-consuming computer simulations. This can be thought of as a limitation of this research. For a problem of this complexity, it does not appear possible to obtain closed form results. However, the theoretical derivation of the expected values of PSLR and ISLR, where the mainlobe and sidelobe samples are correlated Rician random variables, provides a challenging opportunity for future work. An important finding of this investigation that the expected values of PLSR and ISLR depend on the ENR suggests that the final analytical result, if ever derived, should be some function of the ENR.

This comprehensive study has yielded several valuable new results which will supplement to the body of the existing knowledge in the radar area and will help select appropriate coding schemes under a variety of operating conditions. As a consequence, this will help design efficient radars with improved resolution under a constrained power budget. Furthermore, due to many similarities between radar and data communication problems, the results, in part, may also be valuable to the researchers in the latter area.

LIST OF REFERENCES

LIST OF REFERENCES

[1] M. I. Skolnik, *Introduction to Radar Systems,* Second Edition, McGraw Hill, Inc., New York, NY, 1980.

[2] M. J. E. Golay, "Complementary Series", *IEEE Transaction on Information Theory*, Vol. IT-7, pp. 82-87, April 1961.

[3] R. Sivaswamy, "Self-Clutter Cancellation and Ambiguity Properties of Subcomplementary Sequences," *IEEE Transaction on Aerospace and Electronic Systems*, Vol. AES-18, No. 2, pp. 163-181, March 1982.

[4] J. L. Eaves and E. K. Reedy, *Principles of Modern Radar,* Van Nostrand Reinhold Company, New York, NY, 1987.

[5] F. E. Nathanson, *Radar Design Principles*, McGraw Hill, Inc.,Second Edition, New York, NY, 1991.

[6] D. B. Koch, "Compensation Techniques for Radar Waveform Utilizing Complementary Phase Coding," *Proc. of the Southeastcon 90,* Vol. III, pp. 885-888, New Orleans, LA, April 1990.

[7] D. B. Koch, and W. H. Tranter, "Processing Considerations for Hybrid Waveforms Utilizing Complementary Phase Coding and Linear Freqeuency Stepping," *Proc. of the IEEE International Radar Conference*, pp. 606-611, Arlington, VA, May 1990.

[8] R. S. Robertson, M. Autry, and C. Brenneise, "A Ka-band Instrumentation Radar with One Foot Range Resolution," *Proc. of the IEEE National Radar Conference*, pp. 1-5, March 1991.

[9] N. Levanon, *Radar Principles*, John Wiley & Sons, Inc., New York, NY, 1988.

[10] B. L. Lewis, F. F. Kretschmer, Jr., and W. W. Shelton, *Aspects of Radar Signal Processing*, Artech House, Inc., Norwood, MA, 1986.

[11] P. Swerling, "Detection of Fluctuating Pulsed Signals in the Presence of Noise," *IRE Transaction on Information Theory*, Vol. IT-3, No. 3, pp. 175-178, September 1957.

[12] R. S. Berkowitz, *Modern Radar: Analysis, Evaluation, and System Design*, John Wiley & Sons, Inc., New York, NY, 1965.

[13] C. E. Cook, "Pulse Compression, Key to More Efficient Radar Transmission,"*Proc. of the IRE*, Vol. 48, No. 3, pp. 310-316, March 1960.

[14] C. C. Tseng, and C. L. Liu, "Complementary Sets of Sequences," *IEEE Transaction on Information Theory*, Vol. IT-18, No. 5, pp. 644-652, September 1972.

[15] R. Sivaswamy, "Digital and Analog Subcomplementary Sequences for Pulse Compression," *IEEE Transaction on Aerospace and Electronic Systems*, Vol. AES-14, pp. 343-350, March 1978.

[16] G. W. Zeoli, "Comment on 'Self-Clutter Cancellation and Ambiguity Properties of Subcomplementary Sequences'," *IEEE Transaction on Aerospace and Electronic Systems*, Vol. AES-19, No. 5, pp. 780-781, September 1983.

[17] R. Sivaswamy, "On 'Comment on Self-Clutter Cancellation and Ambiguity Properties of Subcomplementary Sequences'," *IEEE Transaction on Aerospace and Electronic Systems*, Vol. AES-22, No. 1, page 97, January 1986.

[18] G. W. Zeoli, "Author's Reply," *IEEE Transaction on Aerospace and Electronic Systems*, Vol. AES-22, No. 1, pp. 97-98, January 1986.

[19] D. B. Koch, "Analysis of a Generalized Coding/Decoding Method Using FIR Digital Filters for Radar Waveform Design," *Proc. of the 22nd Southeastern Symposium on System Theory*, Vol. III, pp. 885-888, Cookeville, TN, March 1990.

[20] R. L. Frank, "Polyphase Codes with Good Nonperiodic Correlation Properties," *IEEE Transaction on Information Theory*, Vol. 9, pp. 43-45, January 1963.

[21] B. Sklar, *Digital Communications: Fundamentals and Applications*, Prentice Hall, New Jersey, NJ, 1988.

[22] R. E. Blahut, *Principles and Practice of Information Theory*, Addison-Wesley, Reading, MA, 1987.

[23] H. Urkowitz, *Signal Theory and Random Process*, Artech House, Inc., Dedham, MA, 1983.

[24] P. E. Cantrell, and A. K. Ojha, "Comparison of Generalized Q-function Algorithms," *IEEE Transaction on Information Theory*, vol. IT-33, pp. 591-596, July 1987.

[25] A. Papoulis, *Probability, Random Variables, and Stochastic Processes*, McGraw Hill, Inc., New York, NY, 1984.

APPENDICES

Appendix 1

Consider the processing of a coded waveform consisting of M chips by the quadrature receiver in Figure 1.8 of Chapter 1. The phase of the received signal in (1.7) has been set to zero, and will be used as a reference. If θ_{RF} is an arbitrary phase difference between the received signal and the local oscillator of the down converter, then,

$$r_1(t) = 2\cos[(\omega_{RF} - \omega_{IF} + \omega_o)t + \theta_{RF}]\cos\left(\omega_{RF}t + \phi_m\right)$$

$$= \cos[(2\omega_{RF} - \omega_{IF} + \omega_o)t + \theta_{RF} + \phi_m] + \cos[(\omega_{IF} - \omega_o)t - \theta_{RF} + \phi_m] \quad \text{(A1.1)}$$

The first term in the right hand side (RHS) in the above expression is filtered out by the bandpass filter resulting in

$$r_2(t) = \cos[(\omega_{IF} - \omega_o)t - \theta_{RF} + \phi_m] \quad \text{(A1.2)}$$

The in-phase component is given by

$$x_1(t) = r_2(t) \times 2\cos(\omega_{IF}t + \theta_{IF})$$

$$= 2\cos[(\omega_{IF} - \omega_o)t - \theta_{RF} + \phi_m]\cos(\omega_{IF}t + \theta_{IF})$$

$$= \cos[(2\omega_{IF} - \omega_o)t + \theta_{IF} - \theta_{RF} + \phi_m] + \cos(\omega_o t + \theta_{RF} + \theta_{IF} - \phi_m) \quad \text{(A1.3)}$$

In the above, θ_{IF} also is an arbitrary phase. The first term is filtered out by the low pass filter resulting in

$$x_2(t) = \cos(-\omega_o t - \theta_{RF} - \theta_{IF} + \phi_m) \tag{A1.4}$$

This video signal $x_2(t)$ is sampled once every chip time at $t = t_0 + mT_c$. Therefore,

$$x(m) = \cos[-\omega_o(t_0 + mT_c) - \theta_{RF} - \theta_{IF} + \phi_m]$$

$$= \cos[-(\omega_o t_0 + \theta_{RF} + \theta_{IF}) + \phi_m] \tag{A1.5}$$

The second line of (A1.5) results from Assumption 2 of Section 1.5 which requires that each chip contain an integer number of cycles of the video signal, due to which $m\omega_0 T_c = 2\pi mn$. For the sake of brevity, the total phase inside the parenthesis in the second line in (A1.5) has be lumped together and inclusive of the negative sign has been denoted by γ in (1.10). It is worth noting here that the restriction imposed by Assumption 2 ensures that for each of the samples, γ is a constant unknown value. A better feel for this can be obtained by observing the waveform relationship of Figure 1.9. Consequently,

$$x(m) = \cos\left(\gamma + \phi_m\right) \tag{A1.6}$$

Similarly, for the quadrature component,

$$y_1(t) = r_2(t) \times [-2\sin(\omega_{IF}t + \theta_{IF})]$$

$$= -2\cos[(\omega_{IF} - \omega_o)t - \theta_{RF} + \phi_m]\sin(\omega_{IF}t + \theta_{IF})$$

$$= -\sin[(2\omega_{IF} - \omega_o)t + \theta_{IF} - \theta_{RF} + \phi_m] - \sin(\omega_o t + \theta_{RF} + \theta_{IF} - \phi_m) \quad \text{(A1.7)}$$

$$y_2(t) = \sin(-\omega_o t - \theta_{RF} - \theta_{IF} + \phi_m) \quad \text{(A1.8)}$$

$$y(m) = \sin[-(\omega_o t_0 + \theta_{RF} + \theta_{IF}) + \phi_m] \quad \text{(A1.9)}$$

$$y(m) = \sin\left(\gamma + \phi_m\right) \quad \text{(A1.10)}$$

Appendix 2

Table 2A.1. Peak Sidelobe Ratio (PSLR) and Integrated Sidelobe Ratio (ISLR) of the Shifted PN Sequence

Sequence	Autocorrelation Sequence	PSL	ISL
1 1 1 1 -1 -1 -1 1 -1 -1 1 1 -1 1 -1	-1, 0, -1, 0, 3, 0, 1, -2, -1, -4, -1, 0, -1, 0, 15, ...	4/15	70/225
-1 1 1 1 1 -1 -1 -1 1 -1 -1 1 1 -1 1	-1, 2, -1, 0, 3, 0, -1, 0, -1, -4, -1, 0, -3, 0, 15, ...	4/15	86/225
1 -1 1 1 1 1 -1 -1 -1 1 -1 -1 1 1 -1	-1, 2, -1, -2, 1, 2, -1, 0, -3, -2, 1, 0, -3, 0, 15, ...	3/15	76/225
-1 1 -1 1 1 1 1 -1 -1 -1 1 -1 -1 1 1	-1, 0, 1, 0, 1, 4, -1, 0, -5, -2, -1, -2, -1, 0, 15, ...	5/15	110/225
1 -1 1 -1 1 1 1 1 -1 -1 -1 1 -1 -1 1	1, -2, 1, 0, -1, 2, -3, 2, -3, 0, -1, -2, 1, -2, 15, ...	3/15	86/225
1 1 -1 1 -1 1 1 1 1- 1 -1 -1 1 -1 -1	-1, -2, 1, 0, -3, 0, -3, 2, -1, 2, -1, -2, 1, 0, 15, ...	3/15	78/225
-1 1 1 -1 1 -1 1 1 1 1 -1 -1 -1 1 -1	1, -2, 1, 2, -3, 0, -3, 2, -1, 2, -3, -2, 1, -2, 15, ...	3/15	110/225
-1 -1 1 1 -1 1 -1 1 1 1 1 -1 -1 -1 1	-1, 0, 3, 2, -3, -2, -3, 2, 1, 2, -3, -4, -1, 0, 15, ...	4/15	134/225
1 -1 -1 1 1 -1 1 -1 1 1 1 1 -1 -1 -1 *	-1, 0, 1, 2, -1, -2, -1, 0, 1, 0, -3, -2, -1, 0, 15, ...	3/15	54/225
-1 1 -1 -1 1 1 -1 1 -1 1 1 1 1 -1 -1	1, 0, -1, 2, -1, -4, 1, -2, 3, 0, -3, 0, -1, -2, 15, ...	4/15	100/225
-1 -1 1 -1 -1 1 1 -1 1 -1 1 1 1 1 -1	1, 0, -3, 0, -1, -2, -1, 0, 1, 0, -1, 2, -1, -2, 15, ...	3/15	54/225
-1 -1 -1 1 -1 -1 1 1 -1 1 -1 1 1 1 1	-1, -2, -3, -2, -1, -2, 1, -2, 1, 0, 1, 2, 1, 0, 15, ...	3/15	72/225
1 -1 -1 -1 1 -1 -1 1 1 -1 1 -1 1 1 1	1, 0, -1, -4, 1, -2, 1, -2, 1, -2, 3, 0, -1, -2, 15, ...	4/15	94/225
1 1 -1 -1 -1 1 -1 -1 1 1 -1 1 -1 1 1	1, 2, -1, -2, -1, 0, 3, -4, -1, 0, 1, 0, -3, -2, 15, ...	4/15	102/225
1 1 1 -1 -1 -1 1 -1 -1 1 1 -1 1 -1 1	1, 0, 1, -2, 1, 0, 3, -4, -1, -2, 1, -2, -1, -2, 15, ...	4/15	94/225

A2.1 Proof: $A_m = \left| R_m^D + R_m^C \right|$

Correlations of the direct and complement quadrature samples in (2.19)–(2.22) with appropriate reference sequences are performed using (1.4). The resulting output sequences are

$$I^D(m) = \sum_{i=0}^{m} \cos\left(\gamma + \phi^D_{M-1+i-m}\right) s^{D^*}(i) \tag{A2.1}$$

$$Q^D(m) = \sum_{i=0}^{m} \sin\left(\gamma + \phi^D_{M-1+i-m}\right) s^{D^*}(i) \tag{A2.2}$$

$$I^C(m) = \sum_{i=0}^{m} \cos\left(\gamma + \phi^C_{M-1+i-m}\right) s^{C^*}(i) \tag{A2.3}$$

$$Q^C(m) = \sum_{i=0}^{m} \sin\left(\gamma + \phi^C_{M-1+i-m}\right) s^{C^*}(i) \tag{A2.4}$$

From Figure 2.5

$$I(m) = I^D(m) + I^C(m) \tag{A2.5}$$

$$Q(m) = Q^D(m) + Q^C(m) \tag{A2.6}$$

Substituting (A2.1) and (A2.3) in (A2.5), and (A2.2) and (A2.4) in (A2.6) yields

$$I(m) = \sum_{i=0}^{m} \cos\left(\gamma+\phi^{D}_{M-1+i-m}\right)s^{D^*}(i) + \sum_{i=0}^{m} \cos\left(\gamma+\phi^{C}_{M-1+i-m}\right)s^{C^*}(i) \qquad \text{(A2.6)}$$

$$Q(m) = \sum_{i=0}^{m} \sin\left(\gamma+\phi^{D}_{M-1+i-m}\right)s^{D^*}(i) + \sum_{i=0}^{m} \sin\left(\gamma+\phi^{C}_{M-1+i-m}\right)s^{C^*}(i) \qquad \text{(A2.7)}$$

Inserting (A2.6) and (A2.7) in (1.5) and applying Euler's identity gives

$$A_m = \left|\sum_{i=0}^{m} \exp\left[j\left(\gamma+\phi^{D}_{M-1+i-m}\right)\right]s^{D^*}(i) + \sum_{i=0}^{m} \exp\left[j\left(\gamma+\phi^{C}_{M-1+i-m}\right)\right]s^{C^*}(i)\right| \qquad \text{(A2.8)}$$

Equation (A2.8) further gets simpified to

$$A_m = \left|\exp(j\gamma)\right|\left|\sum_{i=0}^{m} \exp\left(j\phi^{D}_{M-1+i-m}\right)s^{D^*}(i) + \sum_{i=0}^{m} \exp\left(j\phi^{D}_{M-1+i-m}\right)s^{C^*}(i)\right| \qquad \text{(A2.9)}$$

Note that $|\exp(j\gamma)| = 1$, and from (2.7), (2.8) and (1.3) the first and second summation terms can be recognized to be R^D_m and R^C_m respectively. Therefore, (A2.9) reduces to

$$A_m = \left| R^D_m + R^C_m \right| \qquad \text{(A2.10)}$$

This completes the proof.

Appendix 3

A3.1 Expression for the Quadrature Samples in the Noise-only Case

Consider the quadrature receiver in Figure 1.8. In the noise-only case, $r(t) = n(t)$. Using the narrowband representation of the noise as

$$n(t) = n_c(t)\cos(\omega_{RF}\,t) - n_s(t)\sin(\omega_{RF}\,t) \tag{A3.1}$$

and applying trigonometric identities, the expressions for the signals at various points in Figure 1.8 are:

$$r_1(t) = 2\cos[(\omega_{RF} - \omega_{IF} + \omega_o)t + \theta_{RF}] \times [n_c(t)\cos\omega_{RF}\,t - n_s(t)\sin\omega_{RF}\,t] \tag{A3.2}$$

$$r_2(t) = n_c(t)\cos[(\omega_{IF} - \omega_o)t - \theta_{RF}] - n_s(t)\sin[(\omega_{IF} - \omega_o)t - \theta_{RF}] \tag{A3.3}$$

$$x_1(t) = r_2(t) \times 2\cos(\omega_{IF}t + \theta_{IF}) \tag{A3.4}$$

$$x_2(t) = n_c(t)\cos(\omega_c t + \theta_{IF} + \theta_{RF}) + n_s(t)\sin(\omega_c t + \theta_{IF} + \theta_{RF}) \tag{A3.5}$$

Sampling the above analog in-phase signal at $t_m = t_0 + mT_c$, recognizing that $\omega_o T_c$ is an integer multiple of 2π, and substituting γ from (1.10), the equation for the in-phase sample becomes

$$x(m) = n_c(t_0 + mT_c)\cos\gamma - n_s(t_0 + mT_c)\sin\gamma \tag{A3.6}$$

In (A3.6), $n_c(t_0 + mT_c)$ and $n_s(t_0 + mT_c)$ are the m-th Gaussian samples with zero mean and variance, σ^2, because they are samples from zero-mean stationary Gaussian process. In addition, being samples of the quadrature components, they are uncorrelated, and hence statistically independent as well. For convenience, denoting the m-th noise samples in (A3.6) as

$$N_c(m) = n_c(t_0 + mT_c) \tag{A3.7}$$

and

$$N_s(m) = n_s(t_0 + mT_c) \tag{A3.8}$$

yields (3.8).

Similarly, for the quadrature component,

$$y_1(t) = r_2(t) \times [-2\sin(\omega_{IF}t + \theta_{IF})] \tag{A3.9}$$

$$y_2(t) = -n_c(t)\sin(\omega_o t + \theta_{IF} + \theta_{RF}) + n_s(t)\cos(\omega_o t + \theta_{IF} + \theta_{RF}) \tag{A3.10}$$

$$y(m) = n_c(t_0 + mT_c)\sin\gamma + n_s(t_0 + mT_c)\cos\gamma \tag{A3.11}$$

$$y(m) = N_c(m)\sin\gamma + N_s(m)\cos\gamma \tag{A3.12}$$

A3.2 Generating Rayleigh Distributed Samples from Uniformly Distributed Samples

If U is a random variable uniformly distributed between 0 and 1, then a random variable R having a distribution function $F_R(r)$ can be obtained from [25, p. 104]

$$u = F_R(r) \tag{A3.13}$$

Consider R being a Rayleigh random variable with parameter σ^2. Then the pdf of R is

$$f_R(r) = \frac{r}{\sigma^2}\exp\left[-\frac{r^2}{2\sigma^2}\right] \tag{A3.14}$$

Therefore, from (A3.13)

$$u = \int_0^r \frac{x}{\sigma^2}\exp\left[-\frac{x^2}{2\sigma^2}\right]\mathrm{d}x \tag{A3.15}$$

Substituting $y = x^2/2\sigma^2$ in (A3.15) simplifies it to

$$u = \int_0^{\frac{r^2}{2\sigma^2}} \exp[-y]\mathrm{d}y \tag{A3.16}$$

Evaluating the integral in (A3.16) yields

$$u = 1 - \exp\left[-\frac{r^2}{2\sigma^2}\right] \tag{A3.17}$$

From (A3.17), R in terms U is given by

$$R = \sigma\sqrt{-2\ln(1-U)} \tag{A3.18}$$

Appendix 4

A4.1 Proof of (4.10)

From (1.5),

$$A_m = \sqrt{I^2(m) + Q^2(m)} \tag{A4.1}$$

Substituting (4.8) and (4.9) in (A4.1)

$$A_m^2 = \left[(R_m + N_I(m))\cos\gamma - N_Q(m)\sin\gamma\right]^2 + \left[(R_m + N_I(m))\sin\gamma + N_Q(m)\cos\gamma\right]^2 \tag{A4.2}$$

On squaring and simplifying

$$\begin{aligned} A_m^2 = {} & (R_m + N_I(m))^2\cos^2\gamma + N_Q^2(m)\sin^2\gamma - 2(R_m + N_I(m))N_Q\sin\gamma\cos\gamma \\ & + (R_m + N_I(m))^2\sin^2\gamma + N_Q^2(m)\cos^2\gamma + 2(R_m + N_I(m))N_Q\sin\gamma\cos\gamma \end{aligned} \tag{A4.3}$$

Using the trigonometric identity, $\sin^2\theta + \cos^2\theta = 1$, the above expression yields (4.10).

A4.2 Proof of (4.26)

From Figure 2.5

$$A_m = \left|\left(I^D(m) + I^C(m)\right) + j\left(Q^D(m) + Q^C(m)\right)\right| \tag{A4.4}$$

Substituting (4.22) - (4.25) in (A4.4) yields

$$A_m = \Big|\left(R_m^D + R_m^C\right)\cos\gamma + \left(N_I^D(m) + N_I^C(m)\right)\cos\gamma - \left(N_Q^D(m) + N_Q^C(m)\right)\sin\gamma$$

$$+ j\Big[\left(R_m^D + R_m^C\right)\sin\gamma + \left(N_I^D(m) + N_I^C(m)\right)\sin\gamma + \left(N_Q^D(m) + N_Q^C(m)\right)\cos\gamma\Big]\Big|$$

(A4.5)

Simplifying the above by trigonometric identities yields the following simple expression for the magnitudes of the final decoded samples, A_m.

$$A_m = \sqrt{\left(R_m^D + R_m^C + N_I^D(m) + N_I^C(m)\right)^2 + \left(N_Q^D(m) + N_Q^C(m)\right)^2} \quad \text{(A4.6)}$$

A4.3 The Rician pdf

This is not a new derivation, but has been provided for the sake of a ready reference. Let R be a non-random constant value, and N_c, and N_s be two independent zero mean Gaussian random variables with variance σ^2. It is desired to determine the pdf of A, where A is given by

$$A = \sqrt{(R + N_c)^2 + N_s^2} \quad \text{(A4.7)}$$

Denote

$$X = R + N_c \quad \text{(A4.8)}$$

Clearly, X is a Gaussian random variable with mean R and variance σ^2. Since N_c and N_s are independent, X and N_s are also independent. Therefore, their joint pdf can be written as the product of their individual pdf's. Hence,

$$f(x,n_s) = \frac{1}{2\pi\sigma^2}\exp\left[\frac{(x - R)^2 + n_s^2}{2\sigma^2}\right] \tag{A4.9}$$

To find the pdf of A, use the following transformation.

$$R + N_c = A\cos\theta, \tag{A4.10}$$

$$N_s = A\sin\theta \tag{A4.11}$$

The above transformation is a two random variable to two random variable transformation, and yields the joint pdf of A in (A4.7) and θ as

$$f(a,\theta) = \frac{a}{2\pi\sigma^2}\exp\left[\frac{a^2 - 2aR\cos\theta + R^2}{2\sigma^2}\right] \tag{A4.12}$$

Taking the marginal of the joint pdf in (A4.12) over θ finally yields the Rician pdf of A as

$$f_A(a) = \frac{a}{\sigma^2}\exp\left[-\frac{a^2 + R^2}{2\sigma^2}\right] I_0\left(\frac{Ra}{\sigma^2}\right) \tag{A4.13}$$

where, $I_0(x)$ is the zero-order modified Bessel function given by

$$I_0(x) = \frac{1}{2\pi}\int_0^{2\pi} \exp(x\cos\theta)\, d\theta \tag{A4.14}$$

A4.4 Independence of $N_I(m)$ and $N_Q(m)$

To show the independence of $N_I(m)$ and $N_Q(m)$, consider the terms inside the summation in (4.34) and (4.35), and denote them as

$$\begin{aligned} X_i &= N_c(\bullet)\cos\gamma\cos\phi_i - N_s(\bullet)\sin\gamma\cos\phi_i \\ &\quad + N_c(\bullet)\sin\gamma\sin\phi_i + N_s(\bullet)\cos\gamma\sin\phi_i \end{aligned} \tag{A4.15}$$

and

$$\begin{aligned} Y_i = &\quad -N_c(\bullet)\cos\gamma\sin\phi_i + N_s(\bullet)\sin\gamma\sin\phi_i \\ &\quad + N_c(\bullet)\sin\gamma\cos\phi_i + N_s(\bullet)\cos\gamma\cos\phi_i \end{aligned} \tag{A4.16}$$

Now determine the correlation coefficient, ρ_{xy}, defined as

$$\rho_{xy} = \frac{\mathrm{E}\{X_i Y_i\}}{\sigma_x \sigma_y} \tag{A4.17}$$

If $\mathrm{E}\{X_i Yi\}$ in (A4.17) evaluates to zero, X_i and Y_i are uncorrelated. $\mathrm{E}\{X_i Yi\}$ is determined as follows from (A4.15) and (A4.16).

$$
\begin{aligned}
\mathrm{E}\{X_i\,Y_i\} = \mathrm{E}\{&[N_c(\bullet)\cos\gamma\cos\phi_i - N_s(\bullet)\sin\gamma\cos\phi_i \\
&+ N_c(\bullet)\sin\gamma\sin\phi_i + N_s(\bullet)\cos\gamma\sin\phi_i] \\
&\times[-N_c(\bullet)\cos\gamma\sin\phi_i + N_s(\bullet)\sin\gamma\sin\phi_i \\
&+ N_c(\bullet)\sin\gamma\cos\phi_i + N_s(\bullet)\cos\gamma\cos\phi_i]\}
\end{aligned}
\qquad \text{(A4.18)}
$$

On simplifying the above,

$$
\begin{aligned}
\mathrm{E}\{X_i\,Y_i\} =& -\mathrm{E}\{N_c^2(\bullet)\}\cos^2\gamma\sin\phi_i\cos\phi_i + \mathrm{E}\{N_c(\bullet)N_s(\bullet)\}\sin\gamma\cos\gamma\sin\phi_i\cos\phi_i \\
&+ \mathrm{E}\{N_c^2(\bullet)\}\sin\gamma\cos\gamma\cos^2\phi_i + \mathrm{E}\{N_c(\bullet)N_s(\bullet)\}\cos^2\gamma\cos^2\phi_i \\
&+ \mathrm{E}\{N_c(\bullet)N_s(\bullet)\}\sin\gamma\cos\gamma\sin\phi_i\cos\phi_i - \mathrm{E}\{N_s^2(\bullet)\}\sin^2\gamma\sin\phi_i\cos\phi_i \\
&- \mathrm{E}\{N_c(\bullet)N_s(\bullet)\}\sin^2\gamma\cos^2\phi_i - \mathrm{E}\{N_s^2\}(\bullet)\sin\gamma\cos\gamma\cos^2\phi_i \\
&- \mathrm{E}\{N_c^2(\bullet)\}\sin\gamma\cos\gamma\sin^2\phi_i + \mathrm{E}\{N_c(\bullet)N_s(\bullet)\}\sin^2\gamma\sin^2\phi_i \\
&+ \mathrm{E}\{N_c^2(\bullet)\}\sin^2\gamma\sin\phi_i\cos\phi_i + \mathrm{E}\{N_c(\bullet)N_s(\bullet)\}\sin\gamma\cos\gamma\sin\phi_i\cos\phi_i \\
&- \mathrm{E}\{N_c(\bullet)N_s(\bullet)\}\cos^2\gamma\sin^2\phi_i + \mathrm{E}\{N_s^2(\bullet)\}\sin\gamma\cos\gamma\sin^2\phi_i \\
&+ \mathrm{E}\{N_c(\bullet)N_s(\bullet)\}\sin\gamma\cos\gamma\sin\phi_i\cos\phi_i + \mathrm{E}\{N_s^2(\bullet)\}\cos^2\gamma\sin\phi_i\cos\phi_i
\end{aligned}
$$

(A4.19)

Since $N_c(\bullet)$ and $N_s(\bullet)$ have zero mean and are independent, $\mathrm{E}\{N_c(\bullet)N_s(\bullet)\} = 0$, and the cross terms in (A4.19) vanish. Substituting $\mathrm{E}\{N_c^2(\bullet)\} = \mathrm{E}\{N_c^2(\bullet)\} = \sigma^2$ in (A4.19) yields

$$
\begin{aligned}
\mathrm{E}\{X_i\,Y_i\} =& -\sigma^2\cos^2\gamma\sin\phi_i\cos\phi_i + \sigma^2\sin\gamma\cos\gamma\cos^2\phi_i \\
&- \sigma^2\sin^2\gamma\sin\phi_i\cos\phi_i - \sigma^2(\bullet)\sin\gamma\cos\gamma\cos^2\phi_i \\
&- \sigma^2\sin\gamma\cos\gamma\sin^2\phi_i + \sigma^2\sin^2\gamma\sin\phi_i\cos\phi_i \\
&+ \sigma^2\sin\gamma\cos\gamma\sin^2\phi_i + \sigma^2\cos^2\gamma\sin\phi_i\cos\phi_i
\end{aligned}
\qquad \text{(A4.20)}
$$

Then applying the trigonometric identity, $\sin^2\theta + \cos^2\theta = 1$, all of the terms in the RHS of the above equation vanish. This verifies that X_i and Y_i are uncorrelated, and being

Gaussian, they are independent as well. Thus (4.34) and (4.35) can, in general, be expressed as

$$N_I(m) = \sum_{i=0}^{M-1} X_i \tag{A4.21}$$

and

$$N_Q(m) = \sum_{i=0}^{M-1} Y_i \tag{A4.22}$$

where X_i and Y_i are independent zero-mean Gaussian random variables. Since X_i and Y_i are independent, $N_I(m)$ and $N_Q(m)$ in (A4.21) and (A4.22) are also independent. This completes the proof.

A4.5 Variance of $N_I(m)$ and $N_Q(m)$

It is well-known that if a_i are scalars and Z_i are independent zero-mean Gaussian random variables with variance, σ_i^2, then for a random variable Z defined as

$$Z = \sum_{i=0}^{M-1} a_i Z_i \tag{A4.23}$$

the variance is given by

$$\mathrm{Var}\{Z\} = \sum_{i=0}^{M-1} a_i^2 \sigma_i^2 \tag{A4.24}$$

To determine the variance of $N_I(m)$ and $N_Q(m)$, consider X in (A4.15) which represents the terms inside the summation in (4.34). Now focus on the four terms in the RHS in (A4.15). In order to apply (A4.24) to find the variance of the RHS in (A4.15), all of the four terms need to be independent, which on first look does not seem to be true. However, due to the independence of $N_c(\bullet)$ and $N_s(\bullet)$, the first two terms can be combined into a single zero-mean Gaussian random variable and applying (A4.24)

$$\mathrm{Var}\{N_c(\bullet)\cos\gamma\cos\phi_i - N_s(\bullet)\sin\gamma\cos\phi_i\} = \sigma^2\cos^2\phi_i \tag{A4.25}$$

Also, since $N_c(\bullet)$ and $N_s(\bullet)$ have zero mean

$$\mathrm{E}\{N_c(\bullet)\cos\gamma\cos\phi_i - N_s(\bullet)\sin\gamma\cos\phi_i\} = 0 \tag{A4.26}$$

Similarly, the third and fourth terms in the RHS of (A4.15) can also be combined into a single random variable and

$$\mathrm{Var}\{N_c(\bullet)\sin\gamma\sin\phi_i + N_s(\bullet)\cos\gamma\sin\phi_i\} = \sigma^2\sin^2\phi_i \tag{A4.27}$$

$$\mathrm{E}\{N_c(\bullet)\sin\gamma\sin\phi_i + N_s(\bullet)\cos\gamma\sin\phi_i\} = 0 \tag{A4.28}$$

Just as in the preceding section, it can be shown that

$$\mathrm{E}\{[N_c(\bullet)\cos\gamma\cos\phi_i - N_s(\bullet)\sin\gamma\cos\phi_4] \times [N_c(\bullet)\sin\gamma\sin\phi_i + N_s(\bullet)\cos\gamma\sin\phi_i]\} = 0 \tag{A4.29}$$

Hence, the two terms inside the brackets in (A4.29) are independent, and substituting (A4.25) and (A4.27) into (A4.24), the variance of X in (A4.15) evaluates to

$$\mathrm{Var}\{X\} = \sigma^2 \tag{A4.30}$$

Additionally, it can be verified that the mean of X is zero. Recall that X in (A4.15) is the same as the terms inside the summation for the expression of $N_I(m)$ in (4.34). Since $N_I(m)$ consists of the summation of M such independent zero-mean Gaussian random variables having variance of σ^2 from (A4.30),

$$\mathrm{Var}\{N_I(m)\} = M\sigma^2 \tag{A4.31}$$

and

$$\mathrm{E}\{N_I(m)\} = 0 \tag{A4.32}$$

Similarly, considering Y in (A4.16) it can be shown that

$$\mathrm{Var}\{N_Q(m)\} = M\sigma^2 \tag{A4.33}$$

and

$$\mathrm{E}\{N_Q(m)\} = 0 \tag{A4.34}$$

The independence of $N_I(m)$ and $N_Q(m)$ was shown in the preceding section.

Appendix 5

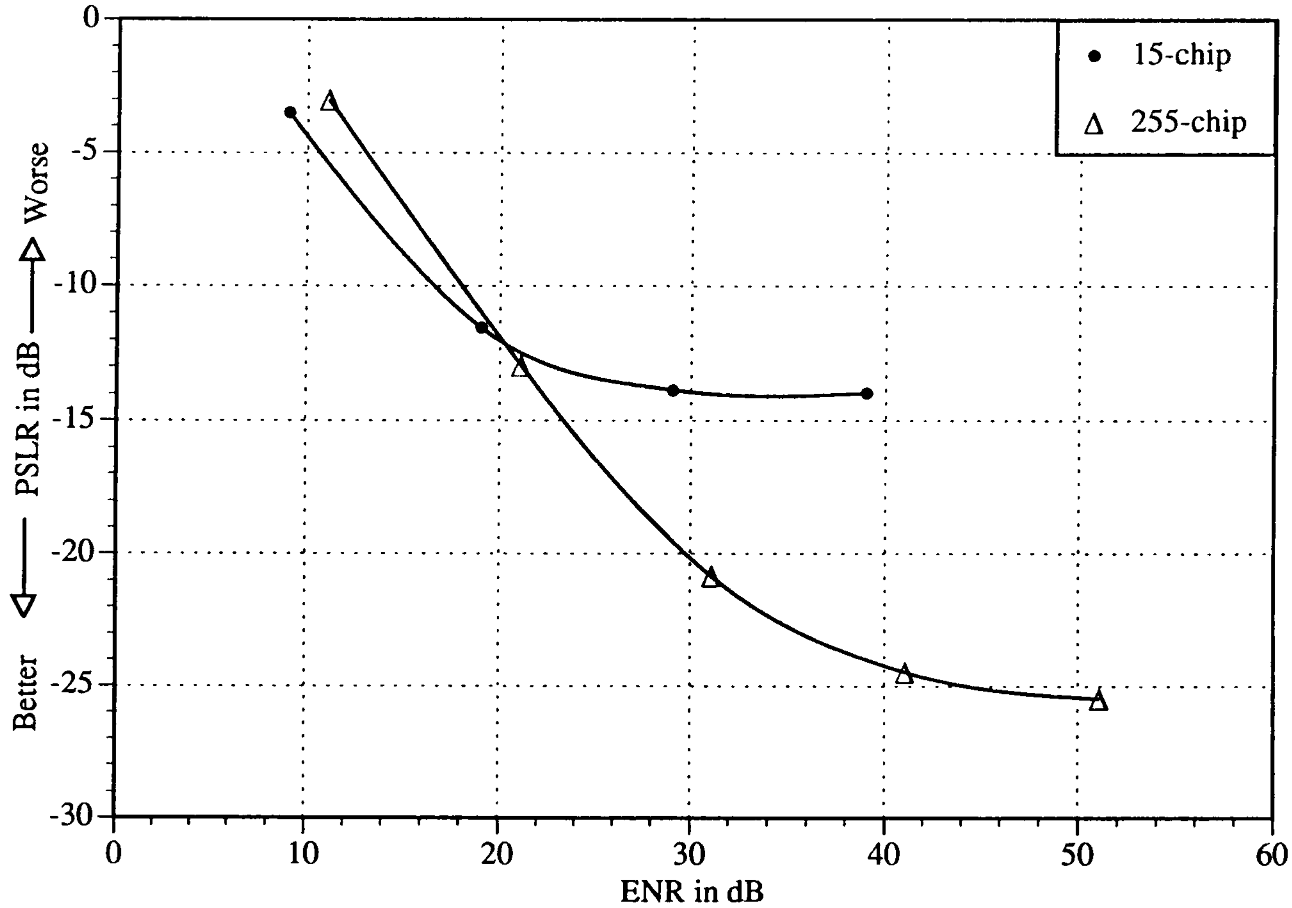

Figure A5.1. Effect of the Length of PN Sequence on PSLR in AWGN.

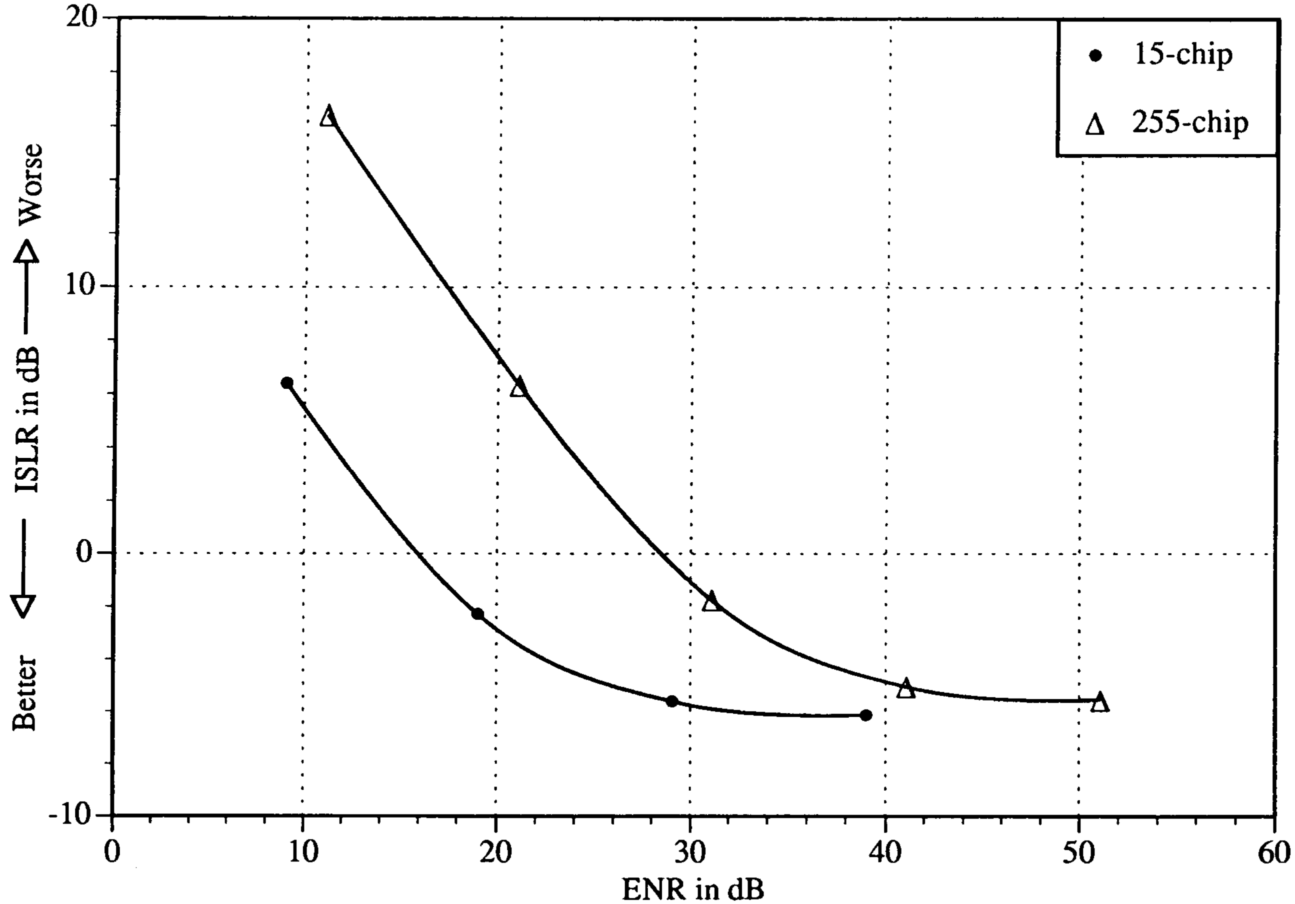

Figure A5.2. Effect of the Length of PN Sequence on ISLR in AWGN.

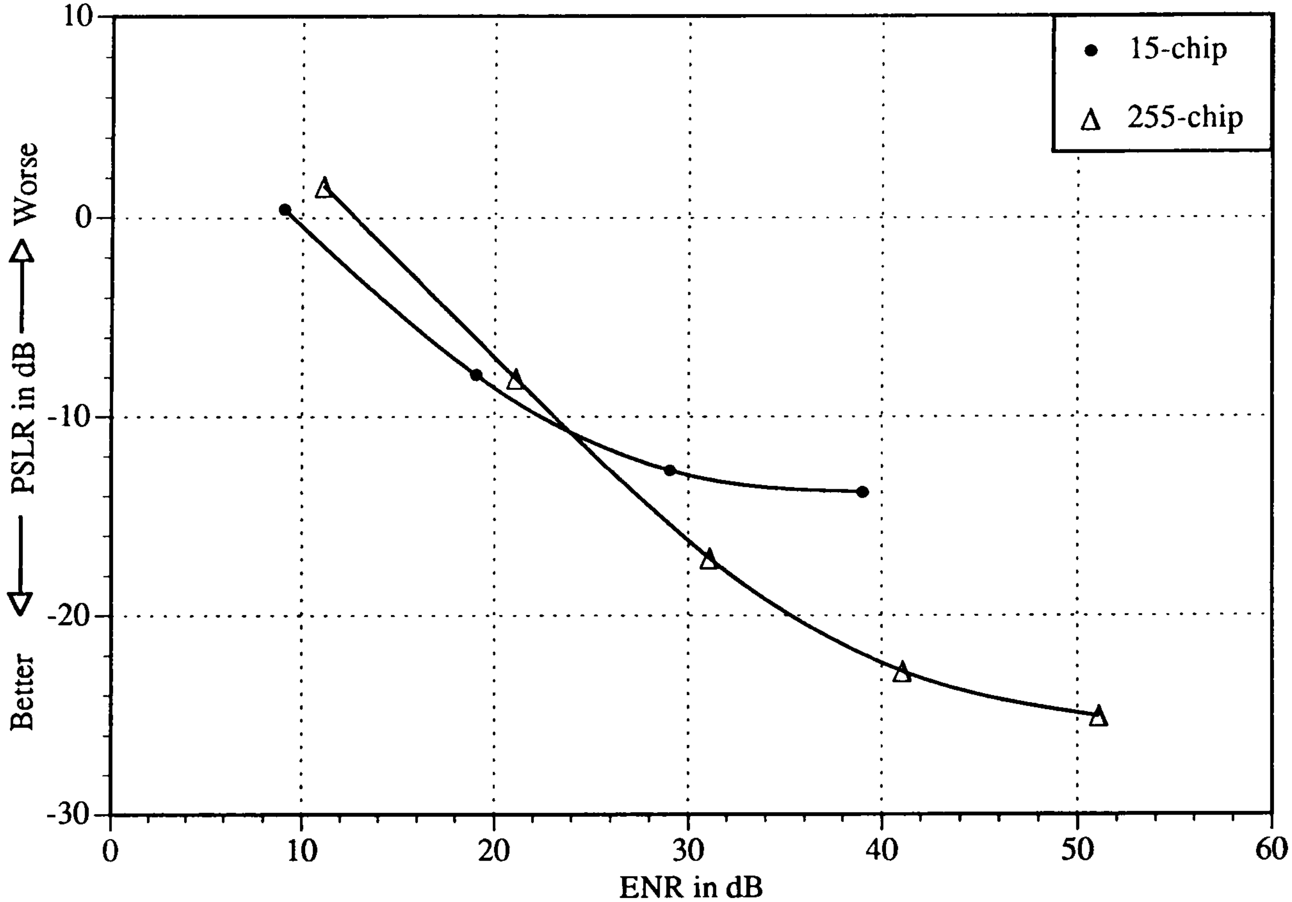

Figure A5.3. Effect of the Length of PN Sequence on the PSLR for Swerling I Target Fluctuation.

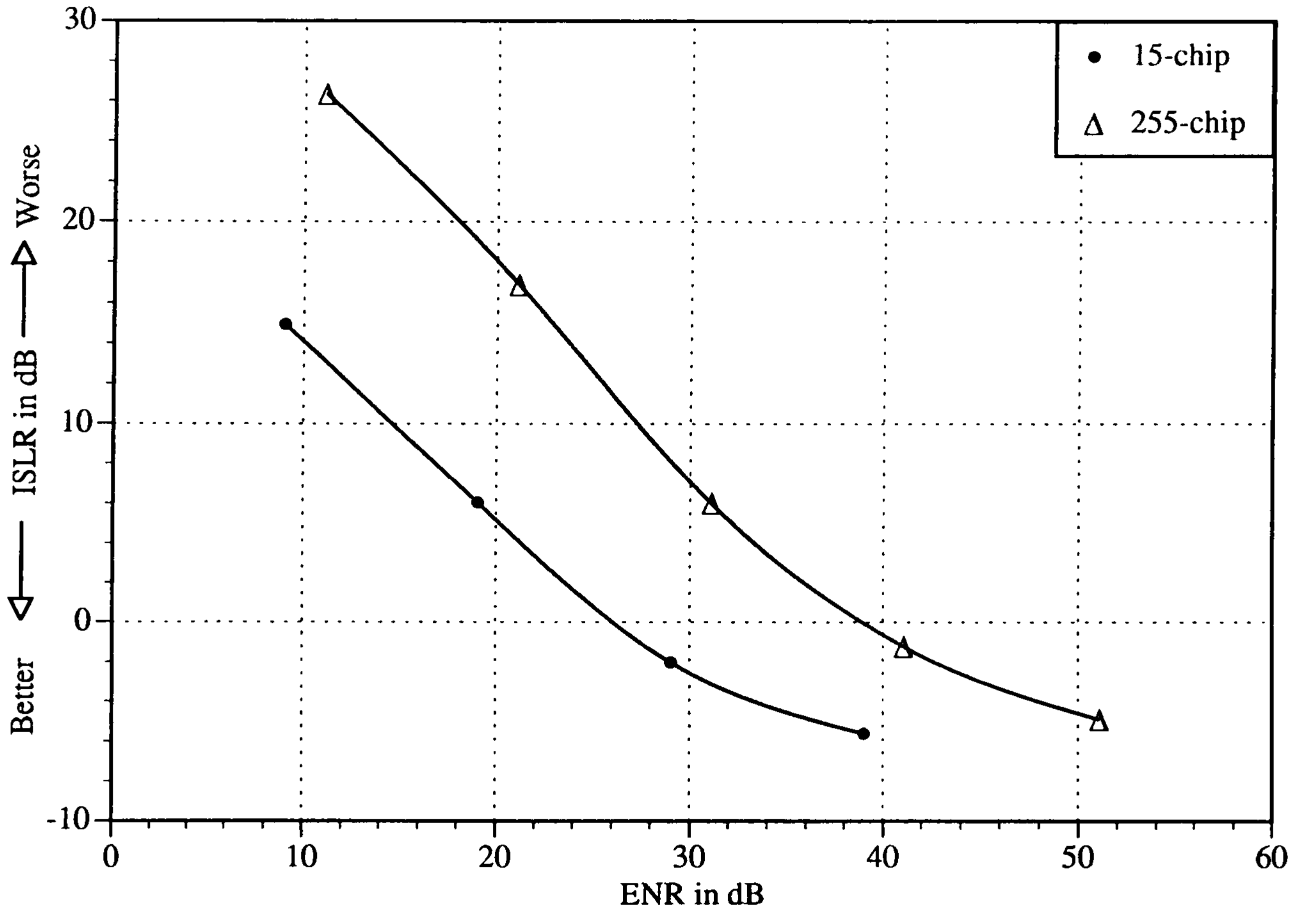

Figure A5.4. Effect of the Length of PN Sequence on the ISLR for Swerling I Target Fluctuation.

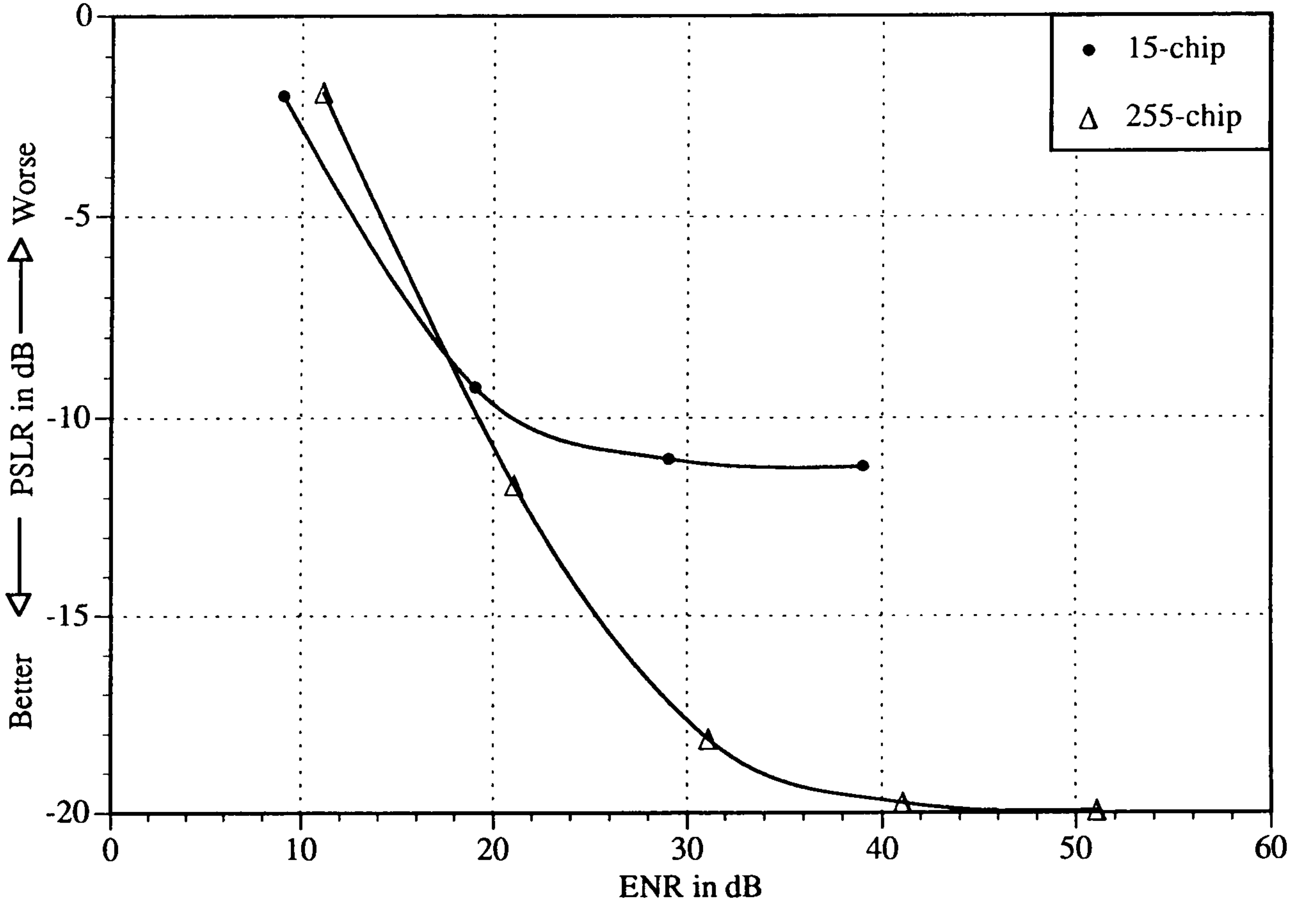

Figure A5.5. Effect of the Length of PN Sequence on the PSLR for Swerling II Target Fluctuation.

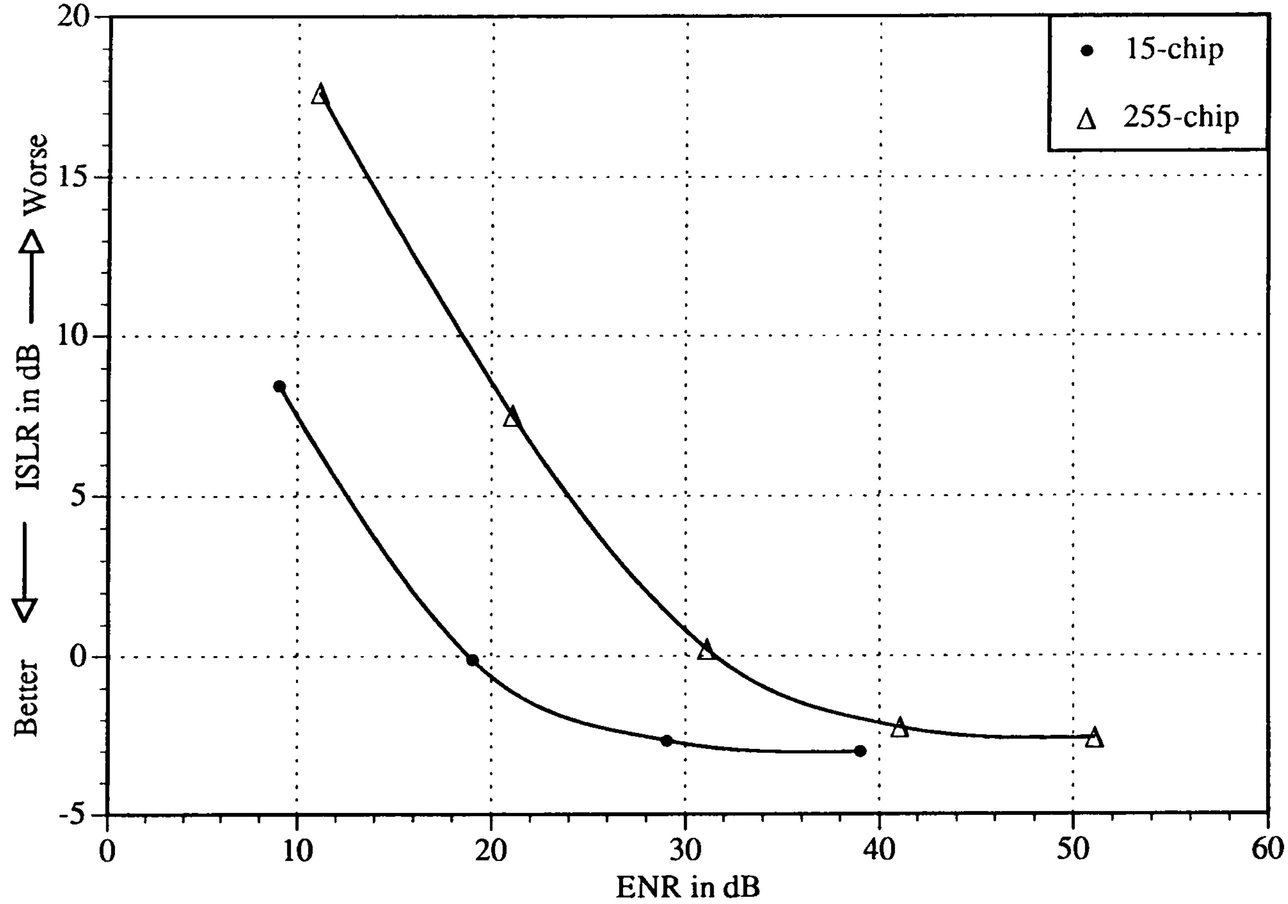

Figure A5.6. Effect of the Length of PN Sequence on the ISLR for Swerling II Target Fluctuation.

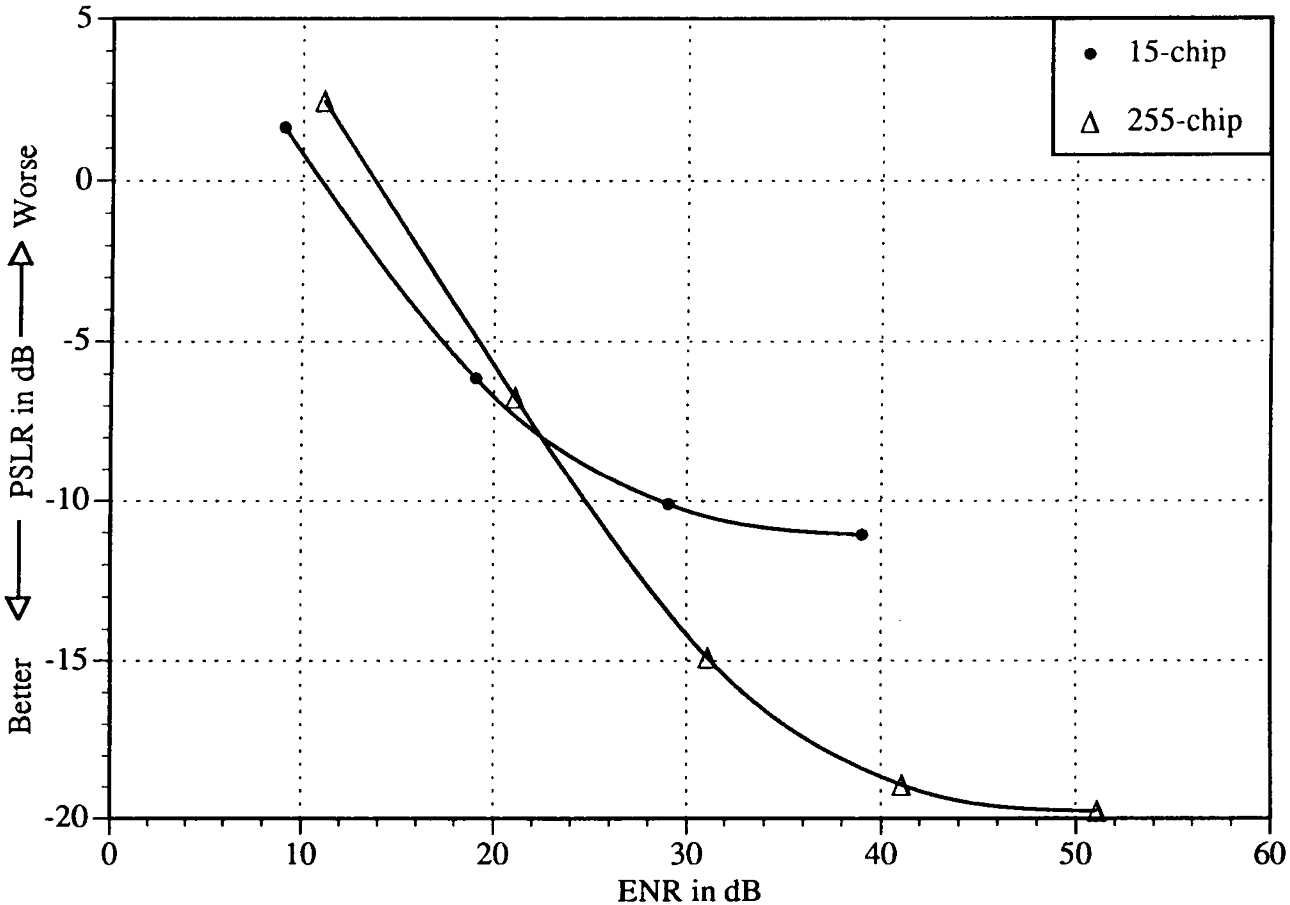

Figure A5.7. Effect of the Length of PN Sequence on the PSLR for Swerling I Target Fluctuation and Fast Fading.

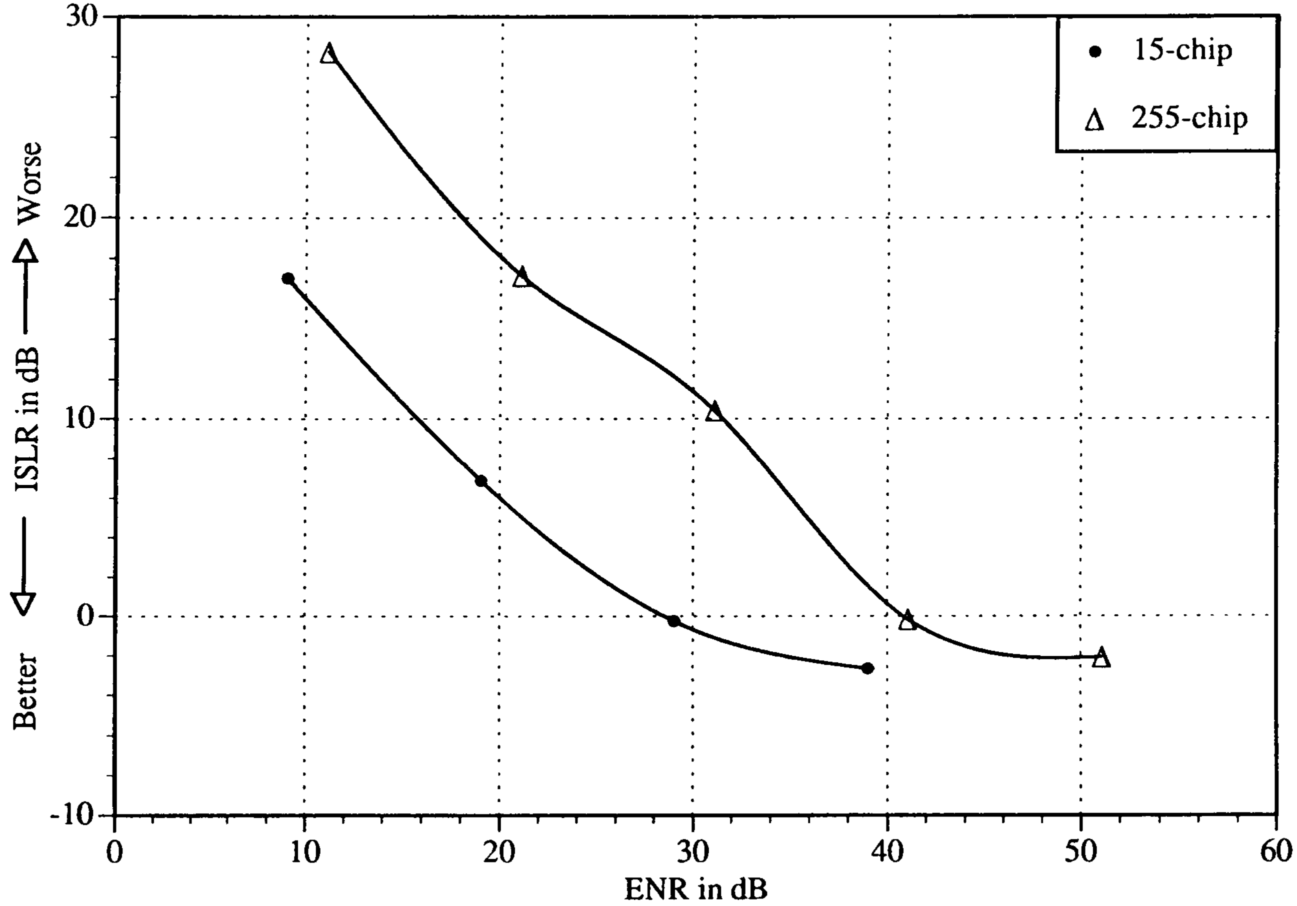

Figure A5.8. Effect of the Length of PN Sequence on the ISLR for Swerling I Target Fluctuation and Fast Fading.

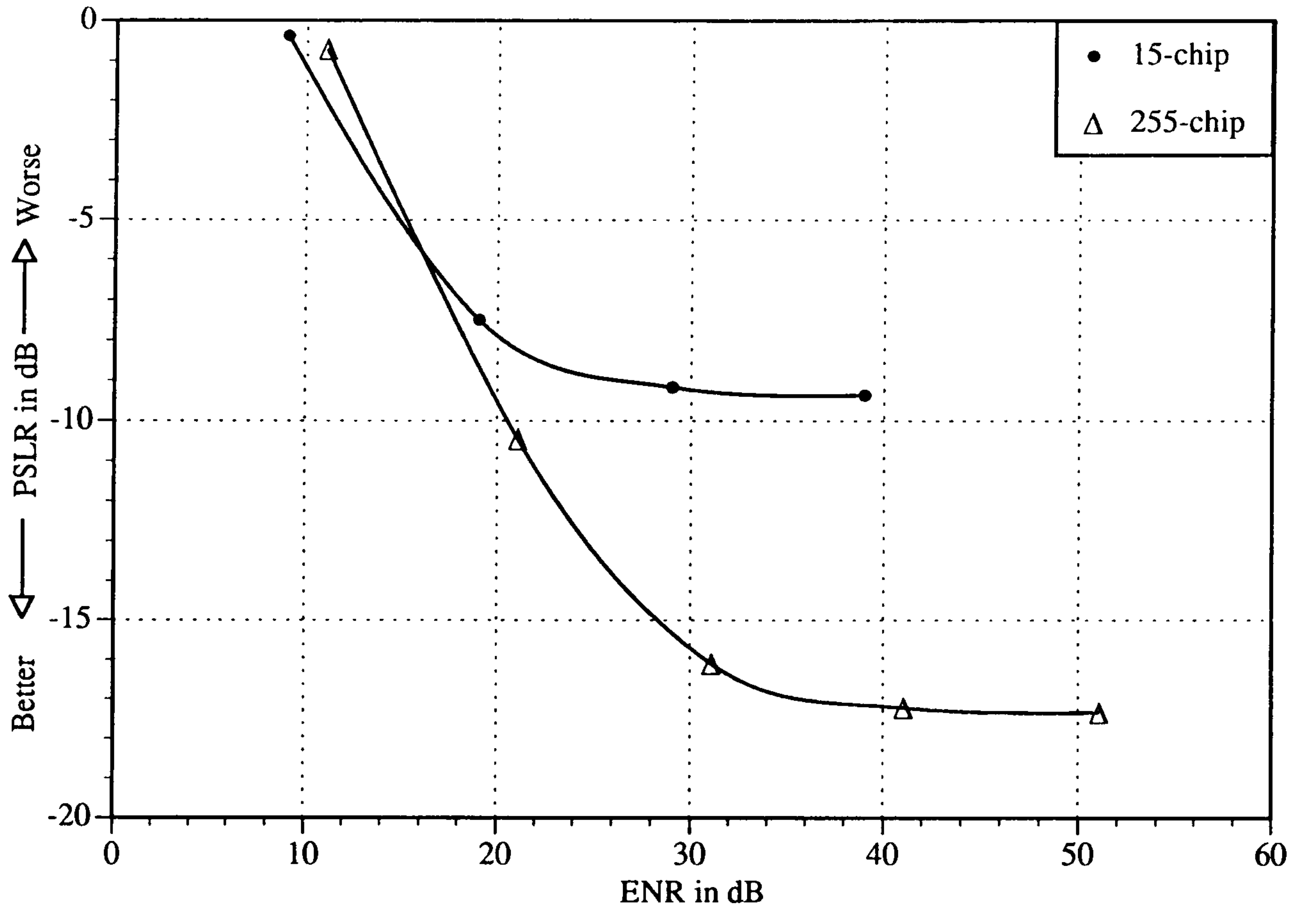

Figure A5.9. Effect of the Length of PN Sequence on the PSLR for Swerling II Target Fluctuation and Fast Fading.

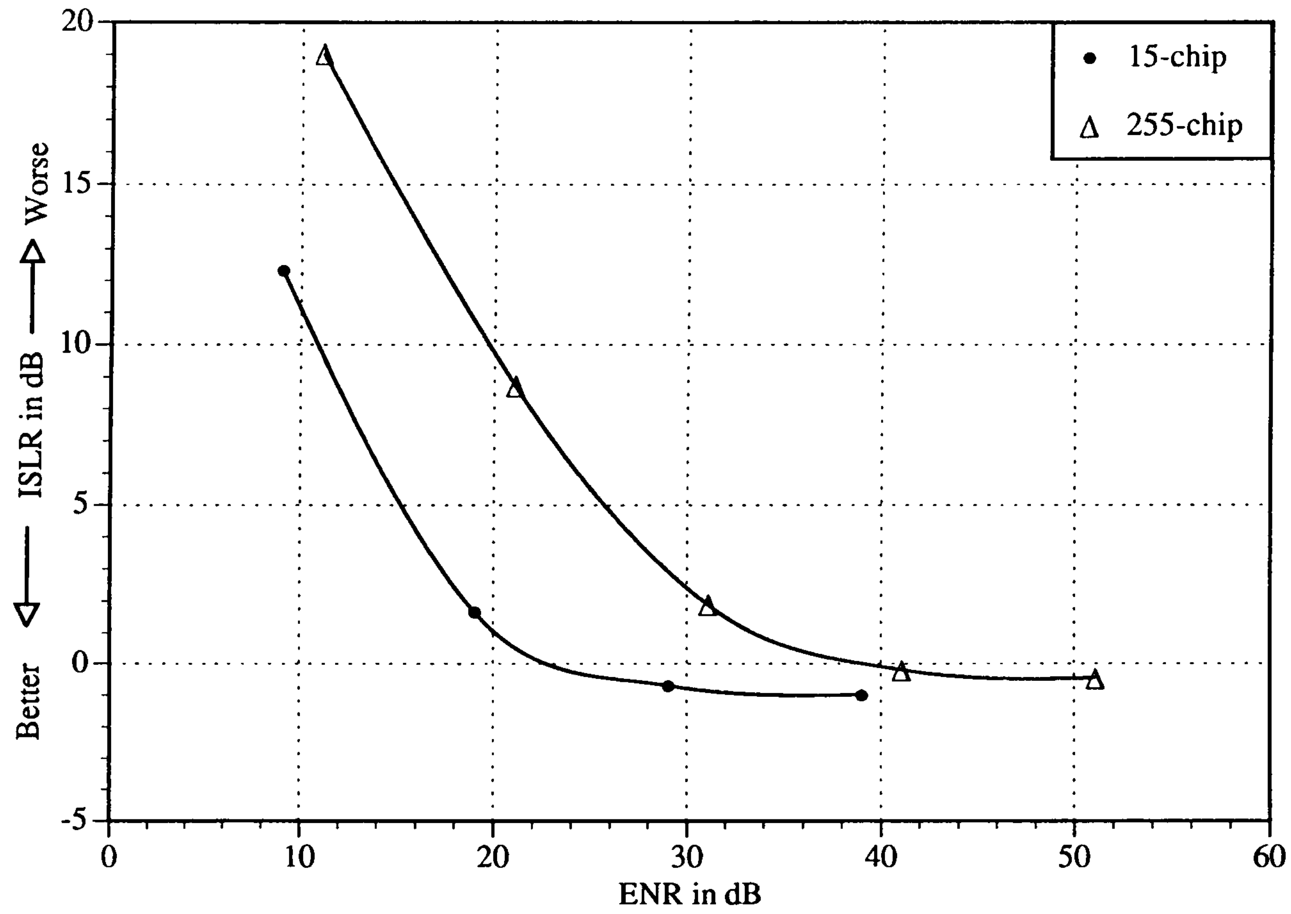

Figure A5.10. Effect of the Length of PN Sequence on the ISLR for Swerling II Target Fluctuation and Fast Fading.

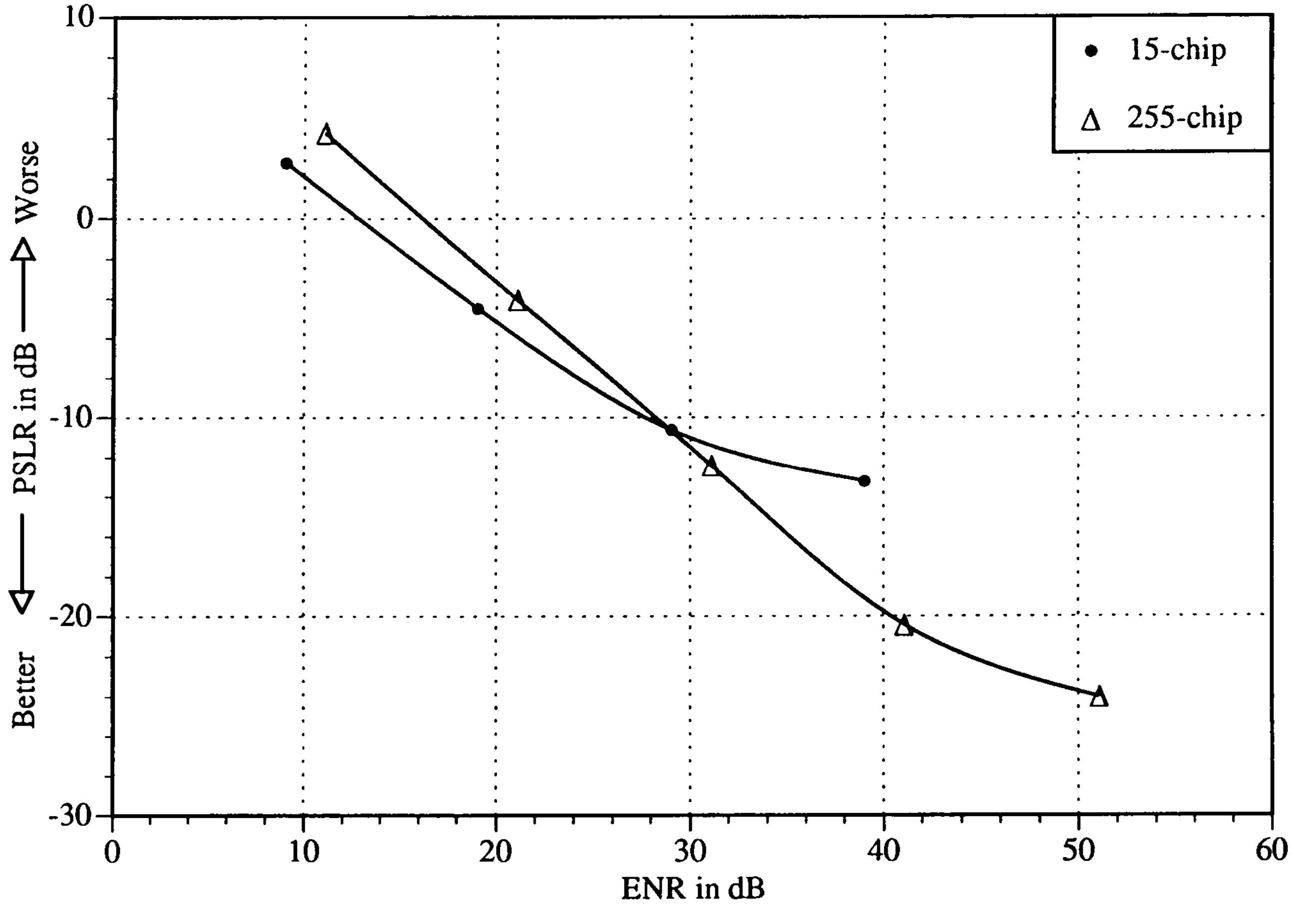

Figure A5.11. Effect of the Length of PN Sequence on the PSLR for Swerling I Target Fluctuation and Slow Fading.

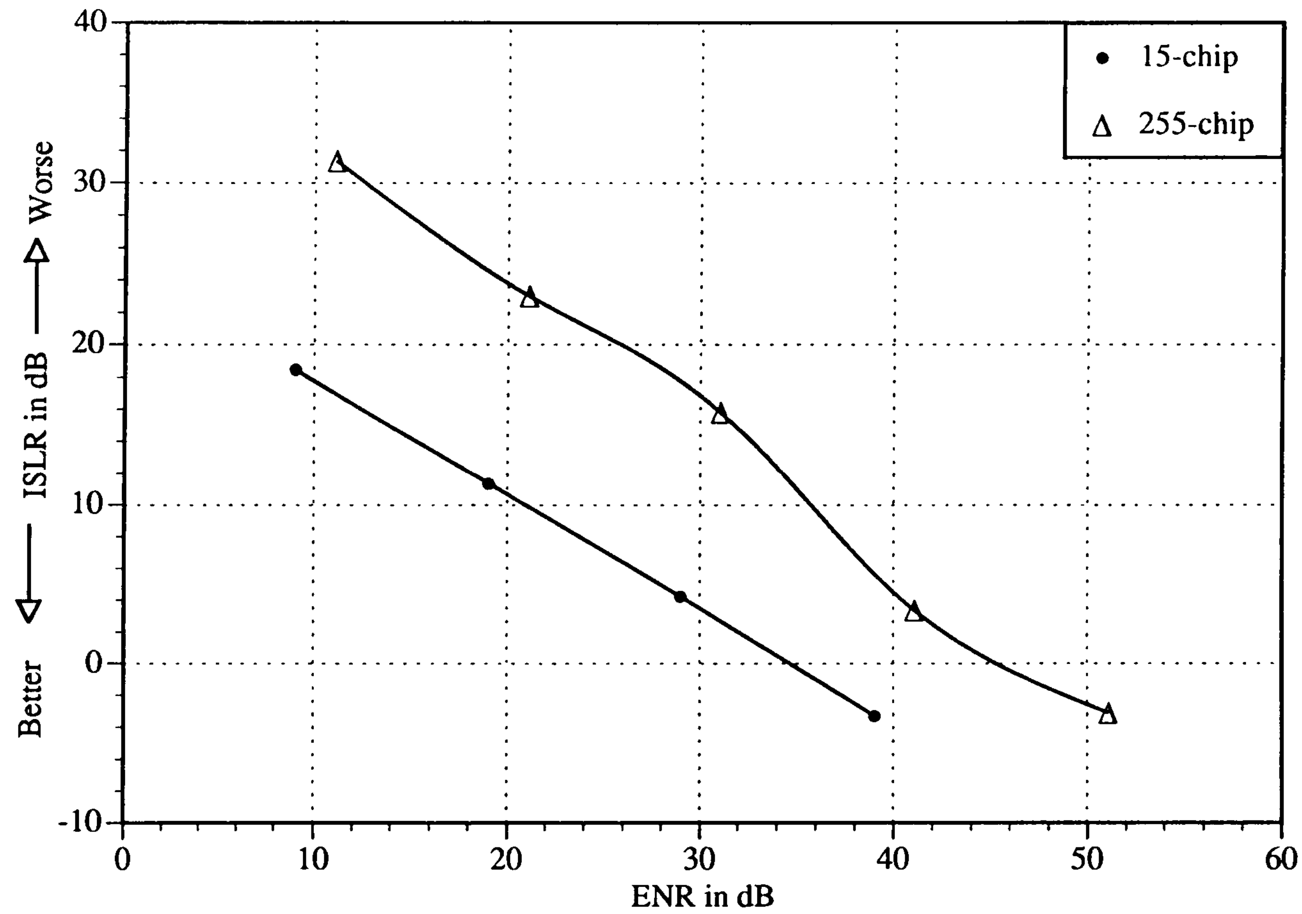

Figure A5.12. Effect of the Length of PN Sequence on the ISLR for Swerling I Target Fluctuation and Slow Fading.

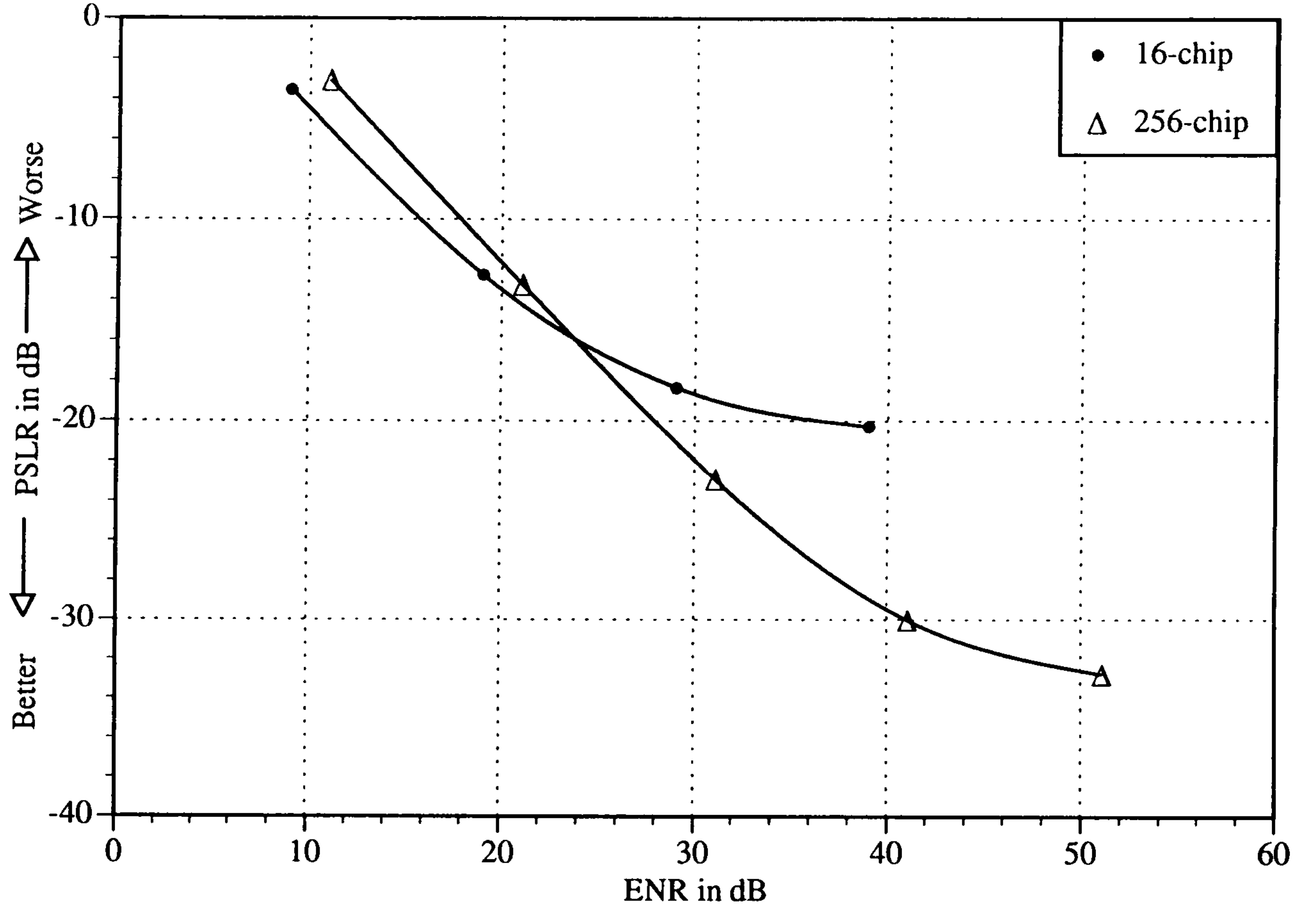

Figure A5.13. Effect of the Length of Frank Code on the PSLR in AWGN.

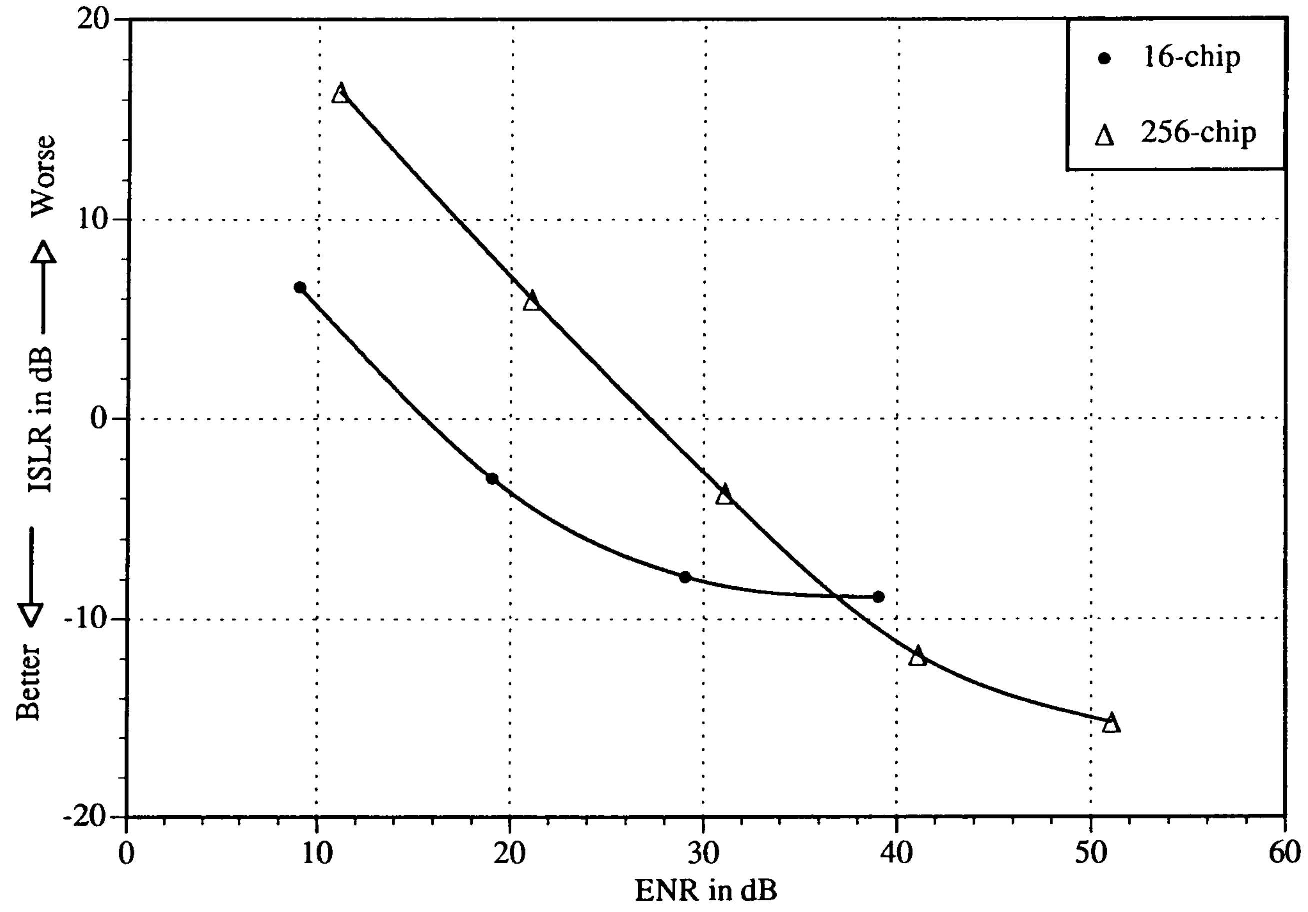

Figure A5.14. Effect of the Length of Frank Code on the ISLR in AWGN.

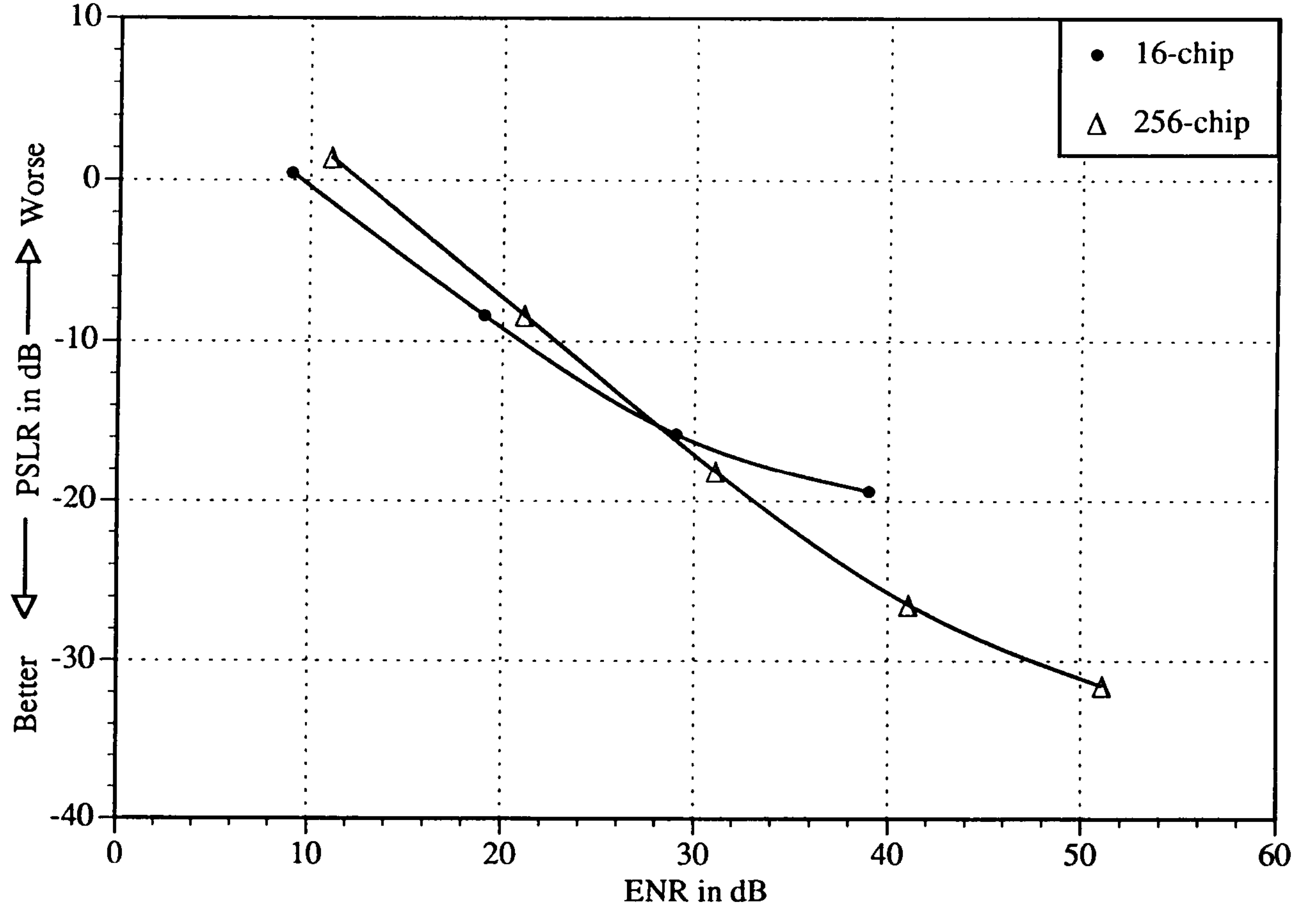

Figure A5.15. Effect of the Length of Frank Code on the PSLR for Swerling I Target Fluctuation.

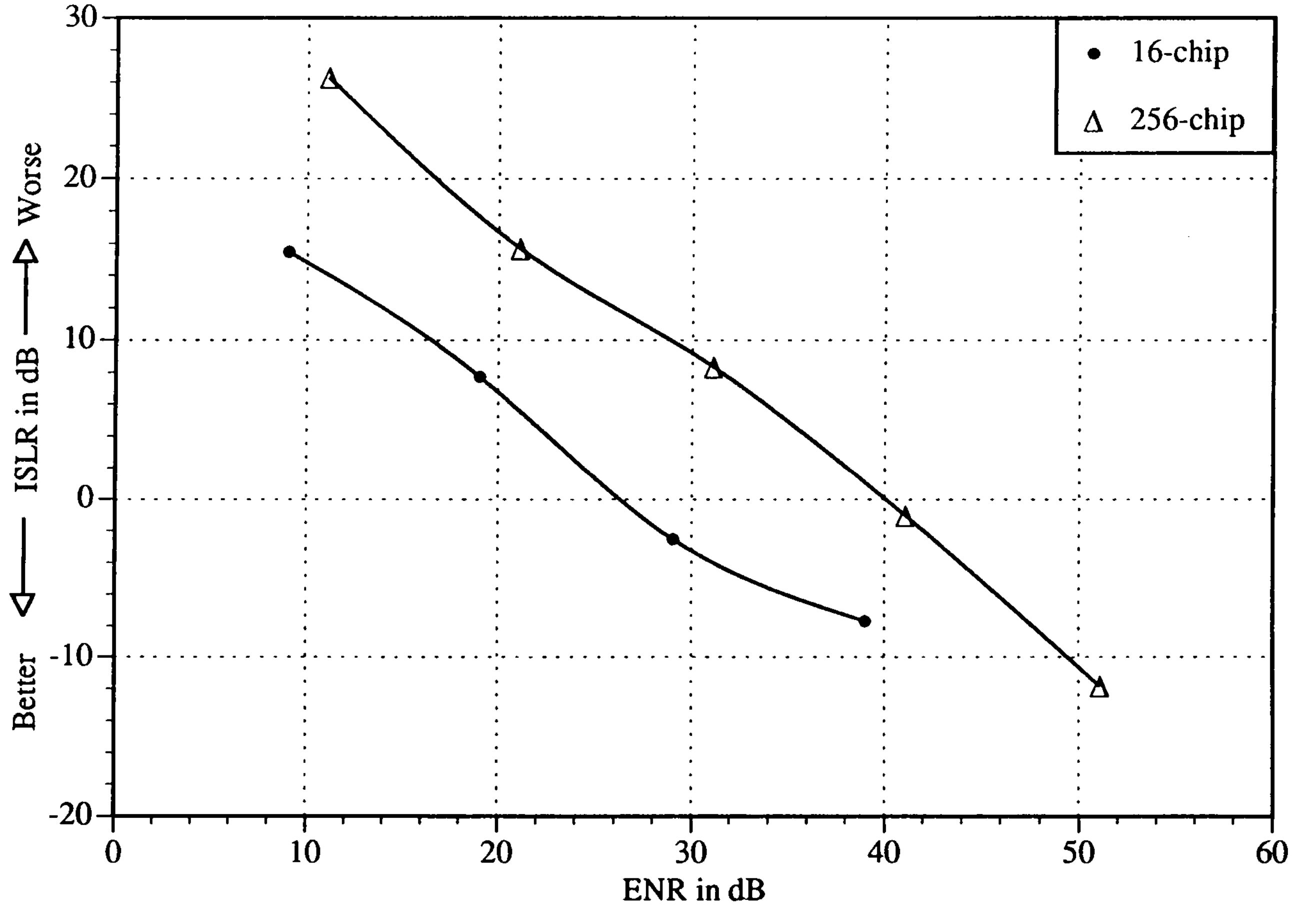

Figure A5.16. Effect of the Length of Frank code on the ISLR for Swerling I Target Fluctuation.

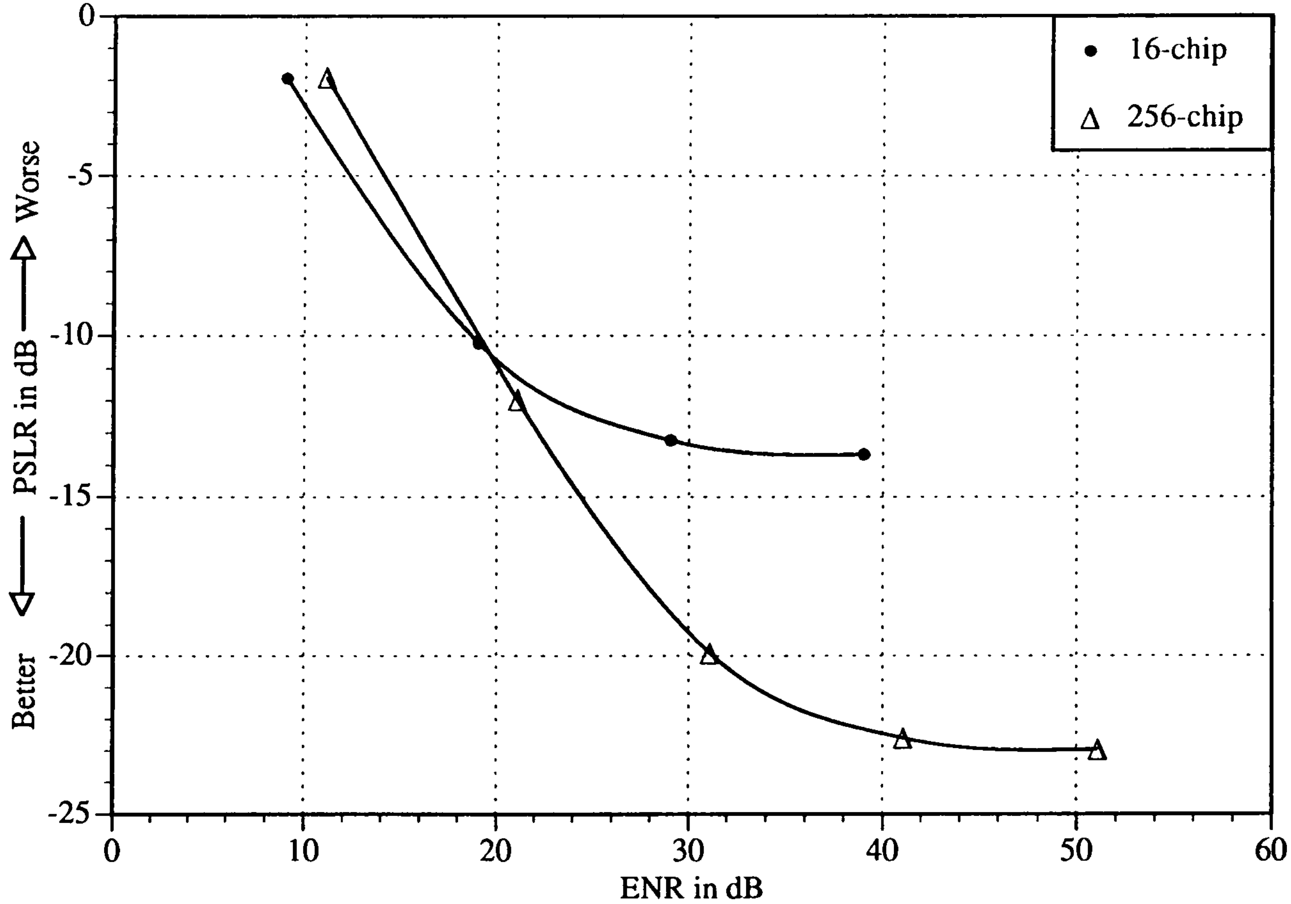

Figure A5.17. Effect of the Length of Frank Code on the PSLR for Swerling II Target Fluctuation.

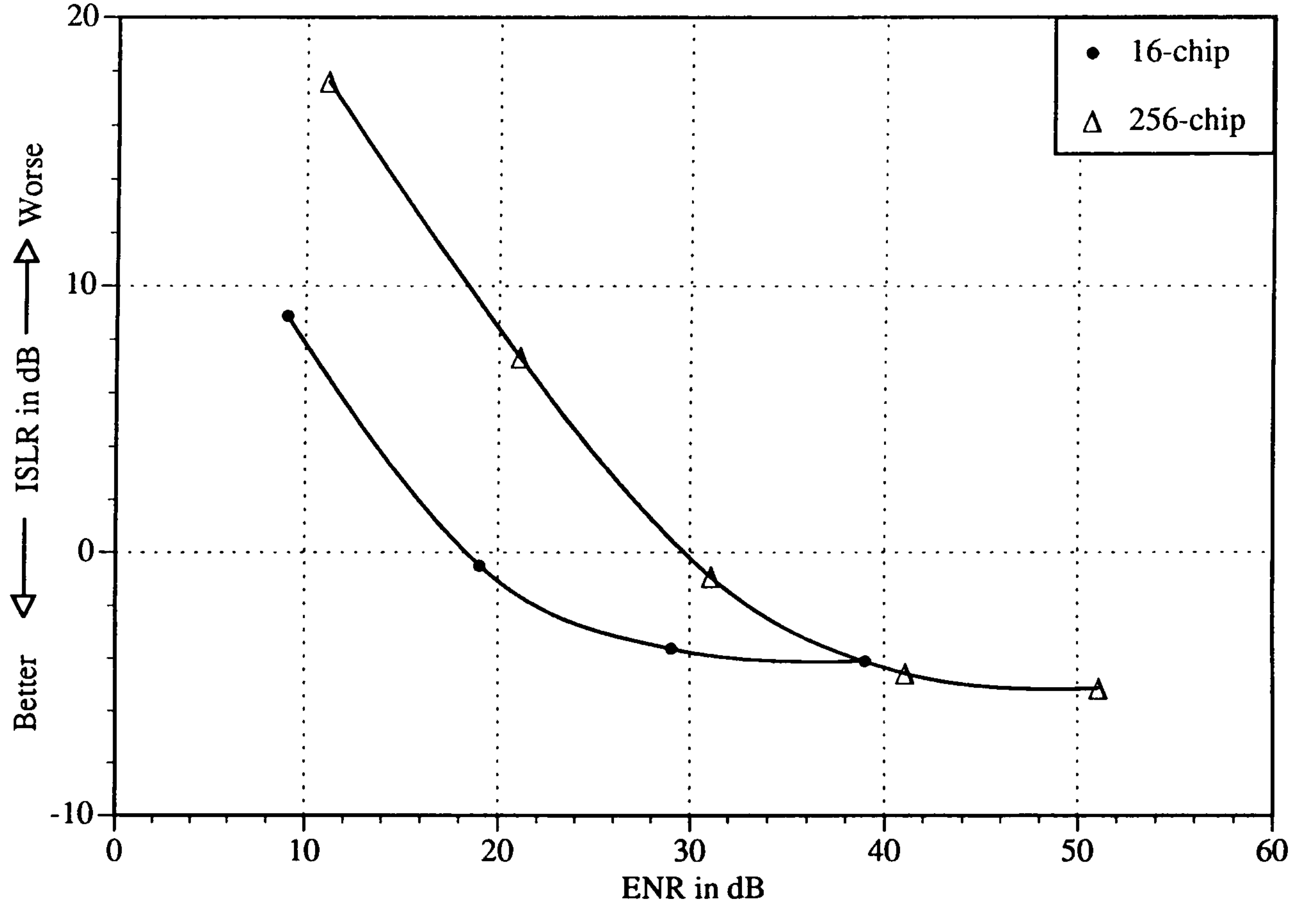

Figure A5.18. Effect of the Length of Frank Code on the ISLR for Swerling II Target Fluctuation.

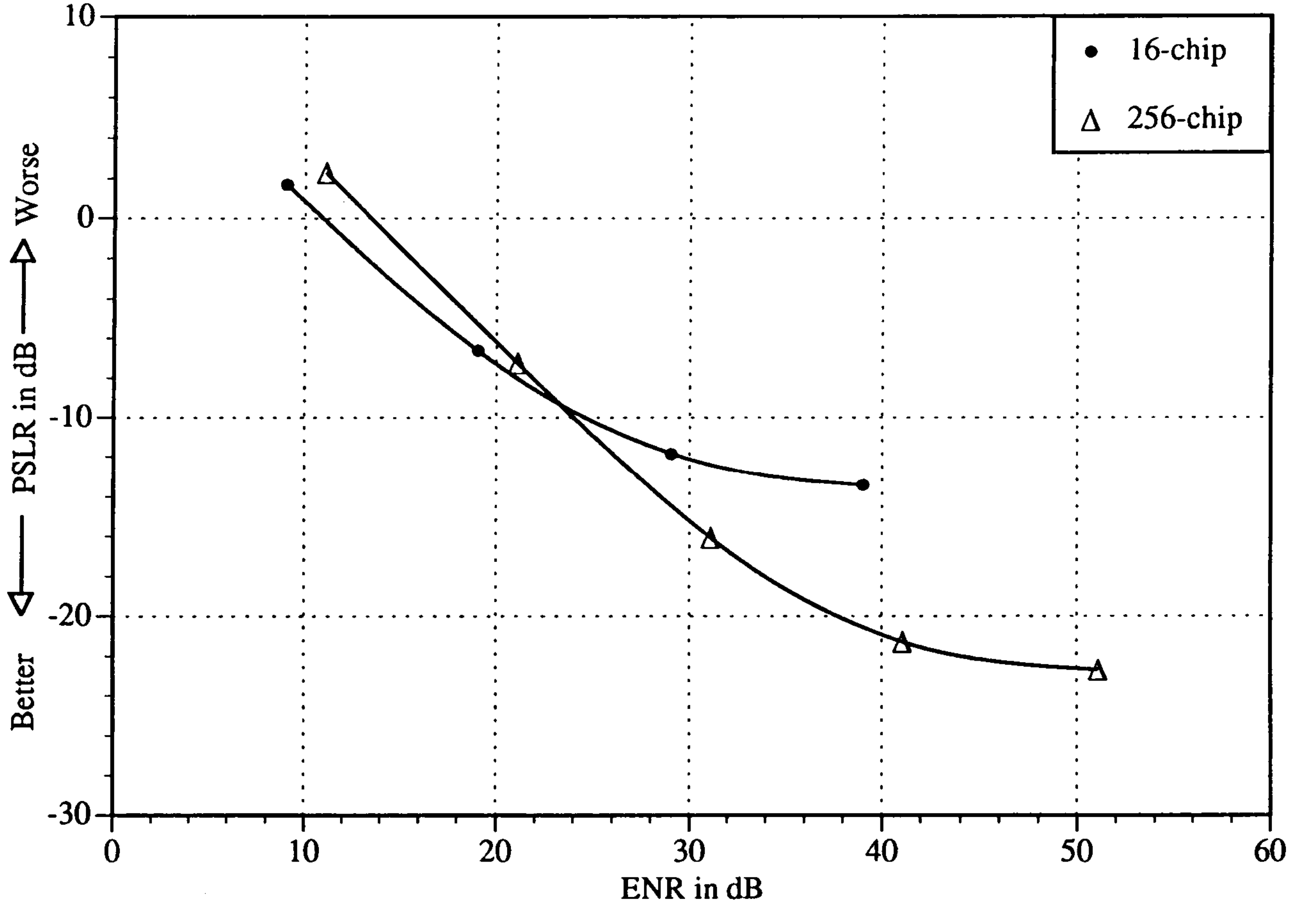

Figure A5.19. Effect of the Length of Frank Code on the PSLR for Swerling I Target Fluctuation and Fast Fading.

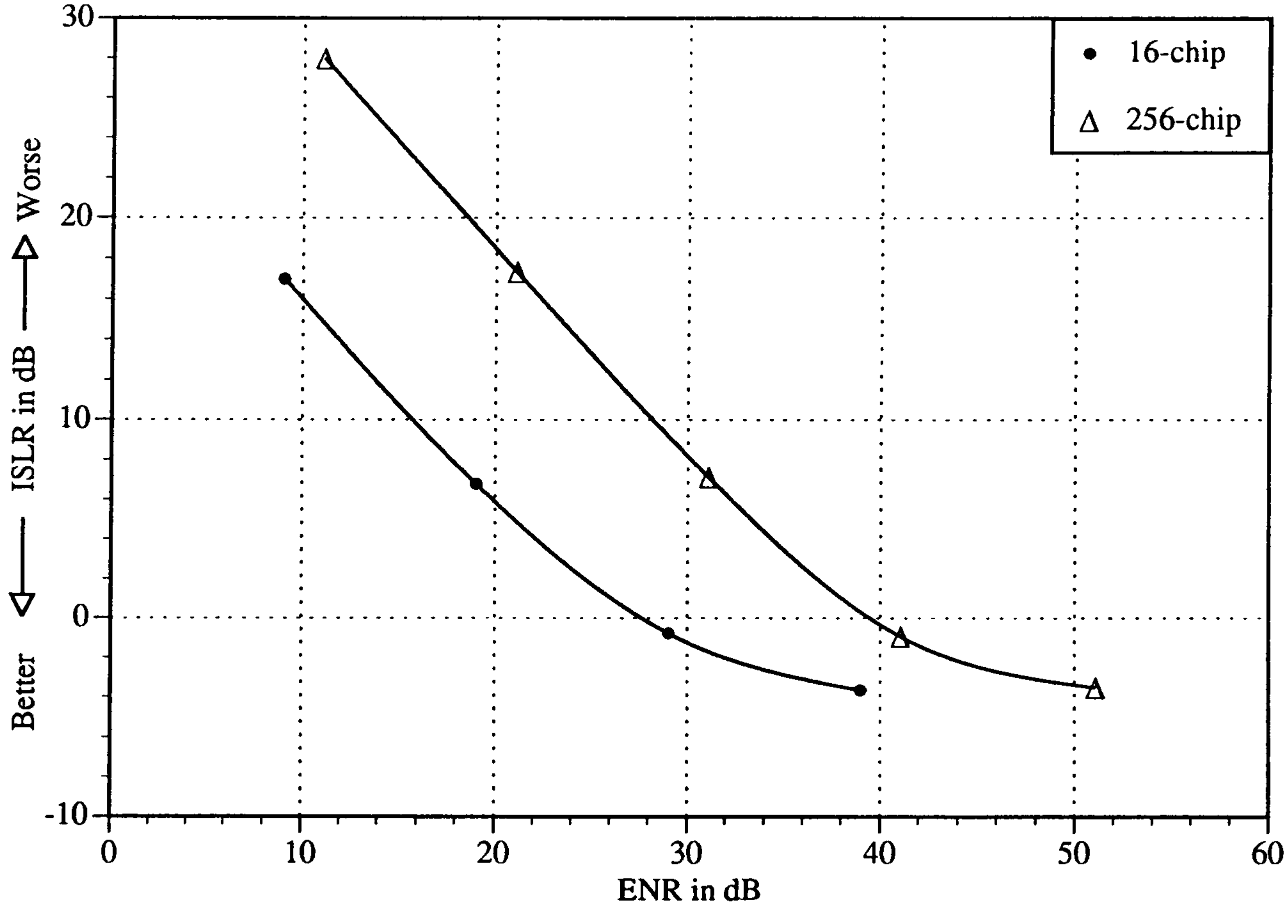

Figure A5.20. Effect of the Length of Frank Code on the ISLR for Swerling I Target Fluctuation and Fast Fading.

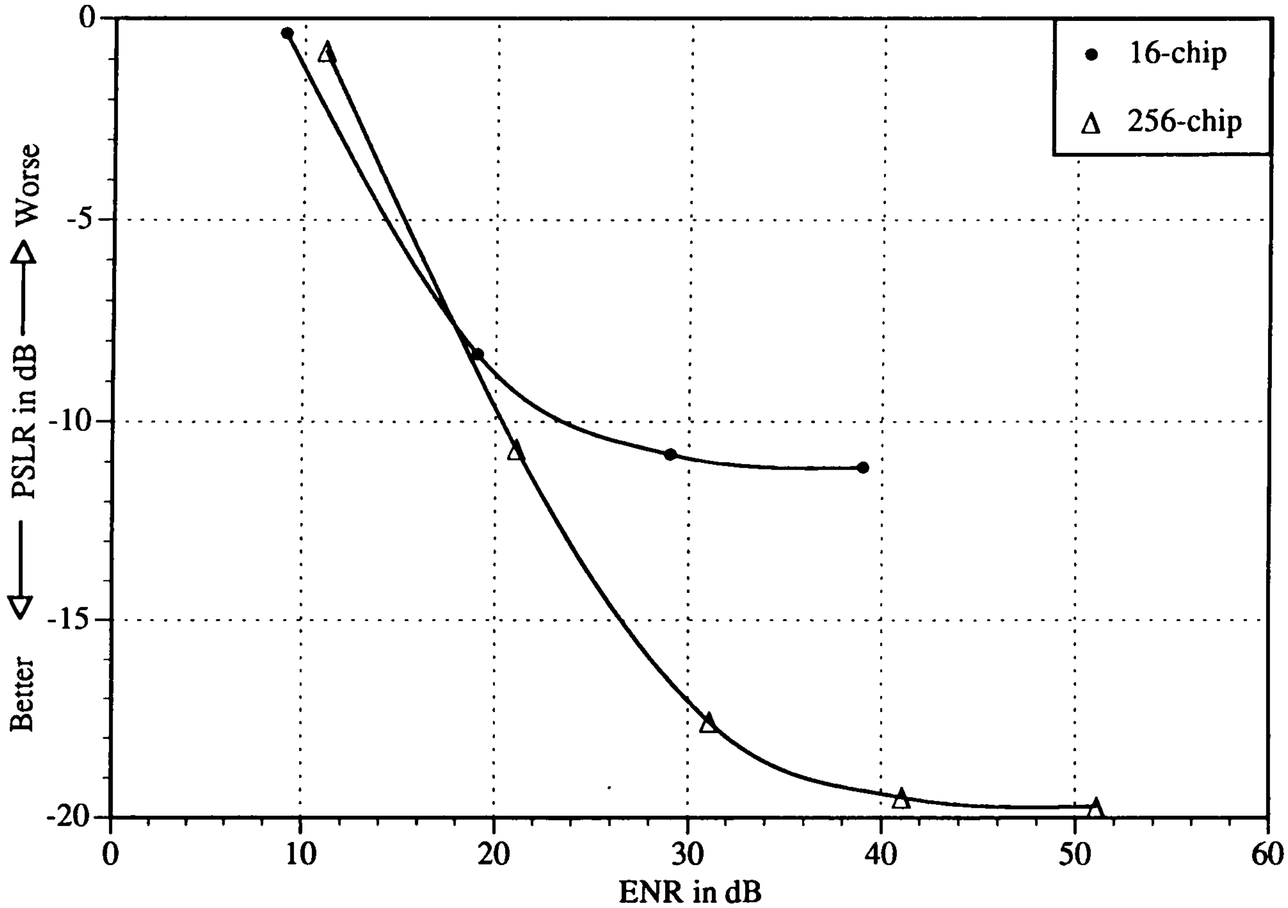

Figure A5.21. Effect of the Length of Frank Code on the PSLR for Swerling II Target Fluctuation and Fast Fading.

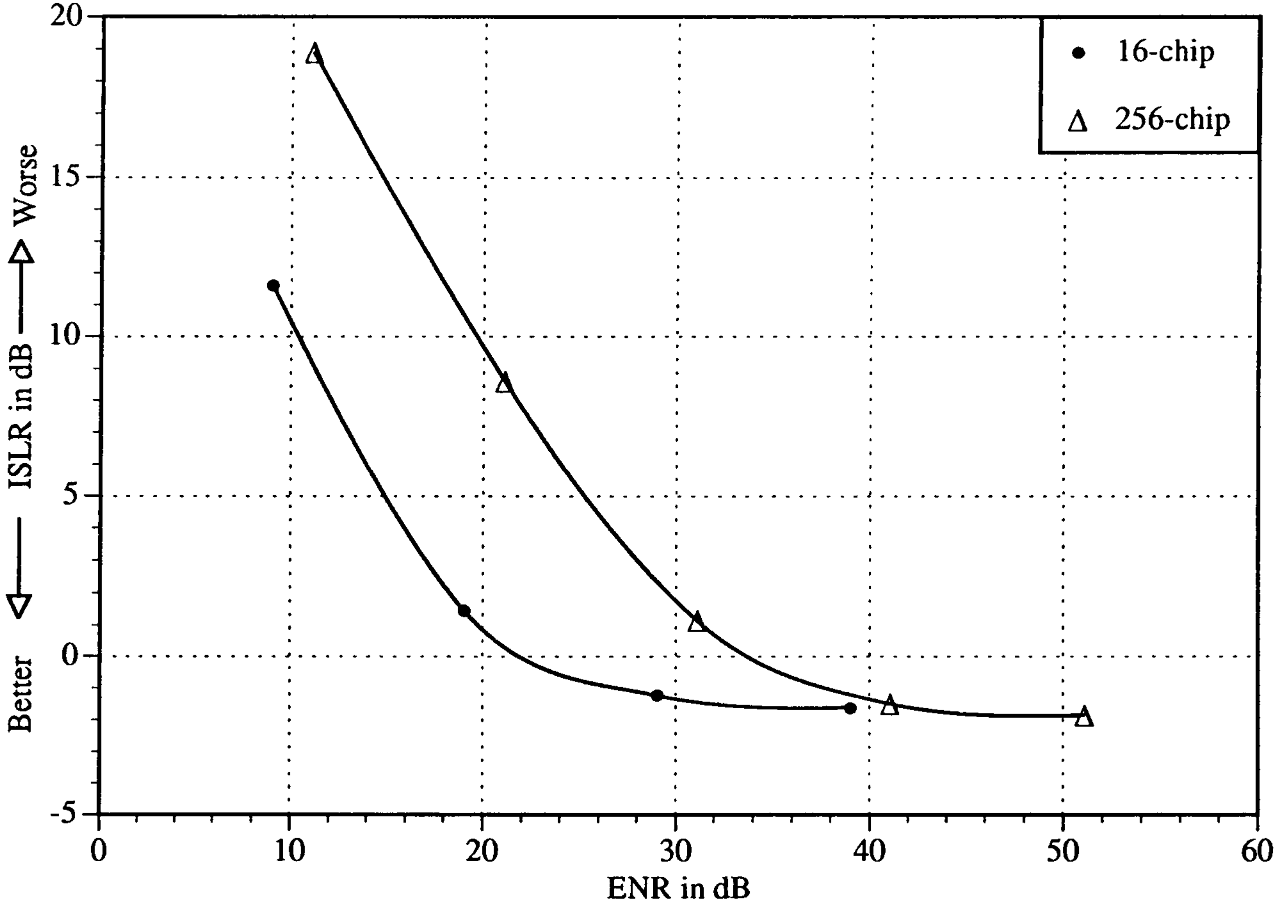

Figure A5.22. Effect of the Length of Frank Code on the ISLR for Swerling II Target Fluctuation and Fast Fading.

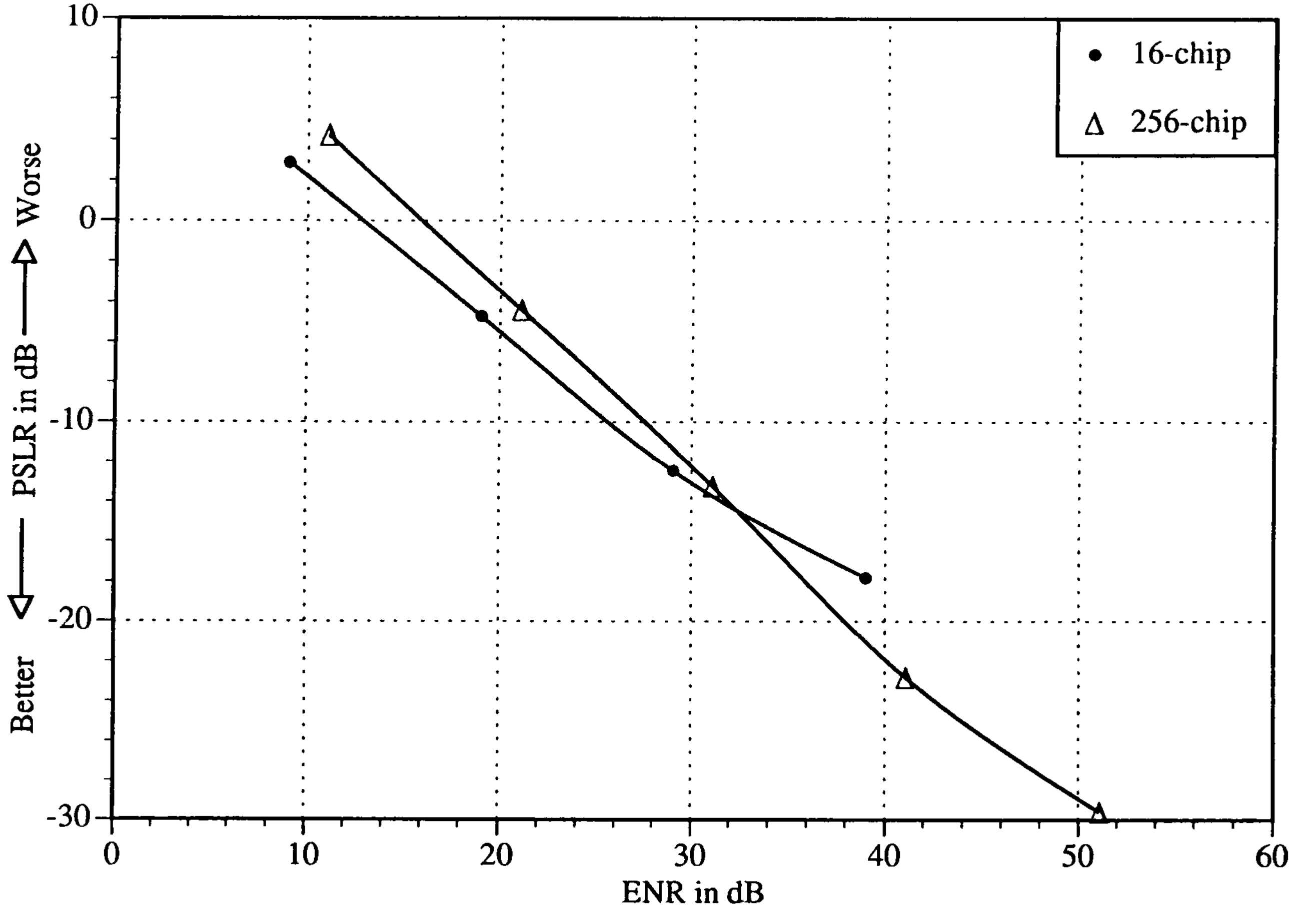

Figure A5.23. Effect of the Length of Frank Code on the PSLR for Swerling I Target Fluctuation and Slow Fading.

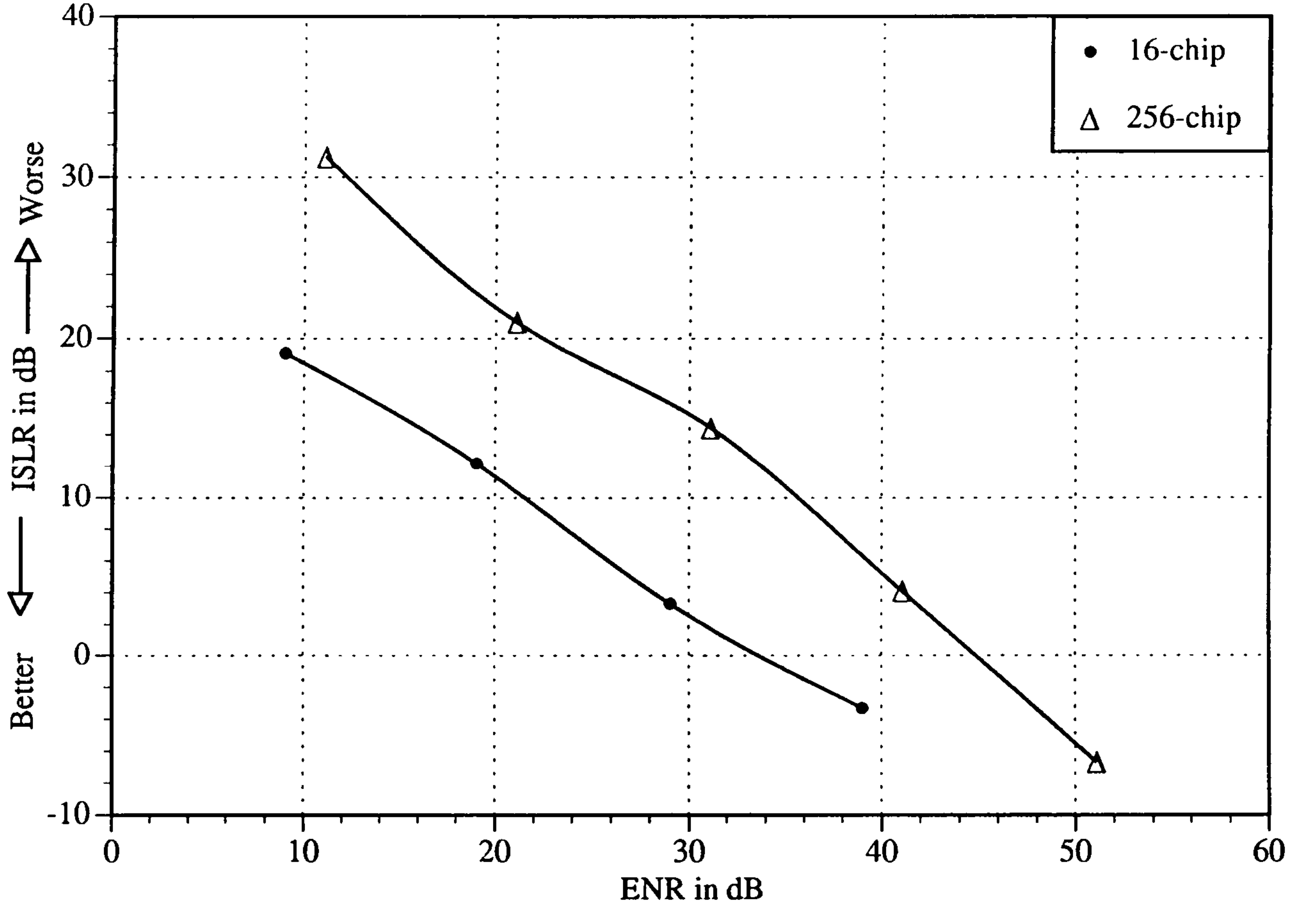

Figure A5.24. Effect of the Length of Frank Code on the ISLR for Swerling I Target Fluctuation and Slow Fading.

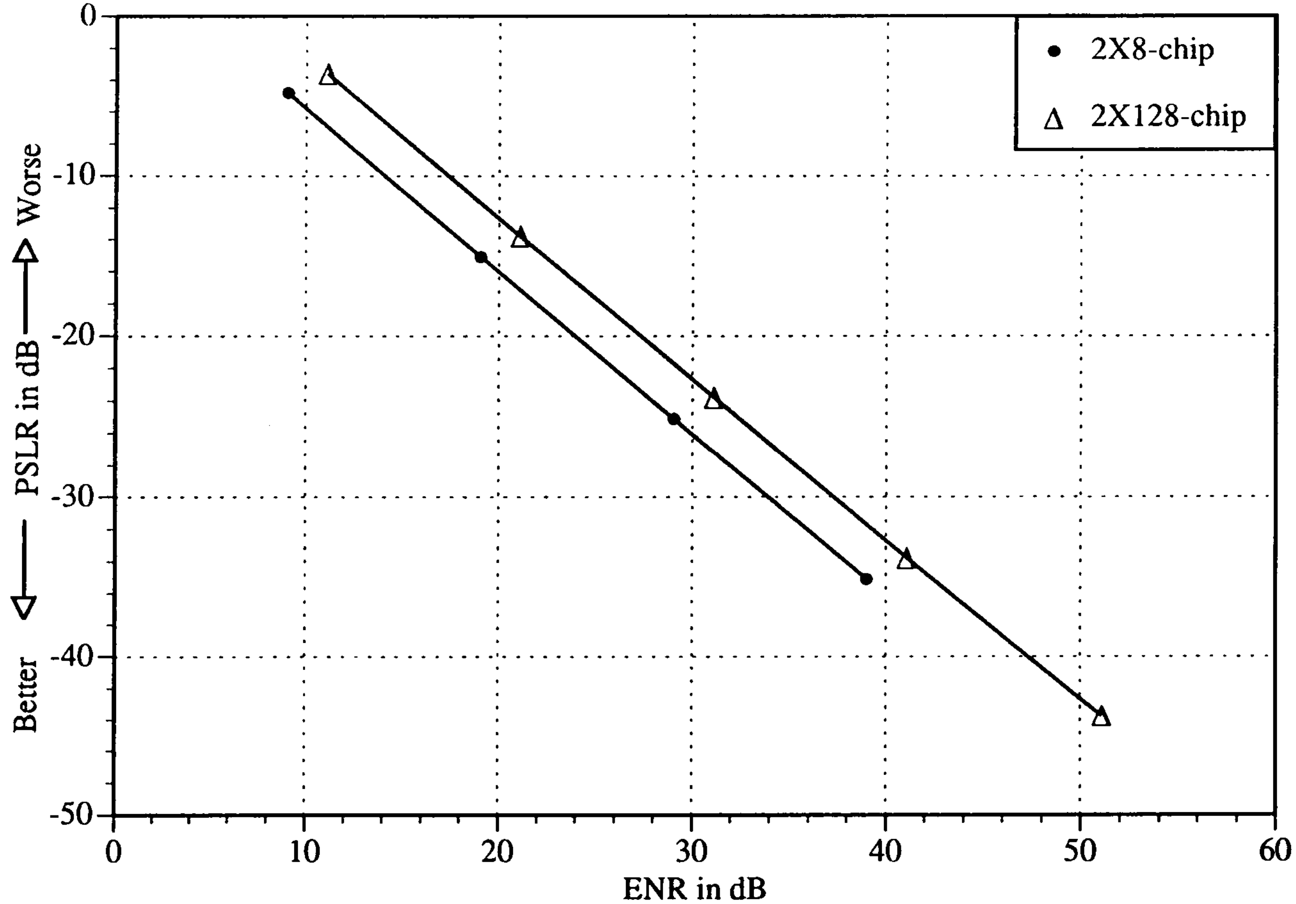

Figure A5.25. Effect of the Length of Complementary Code on the PSLR in AWGN.

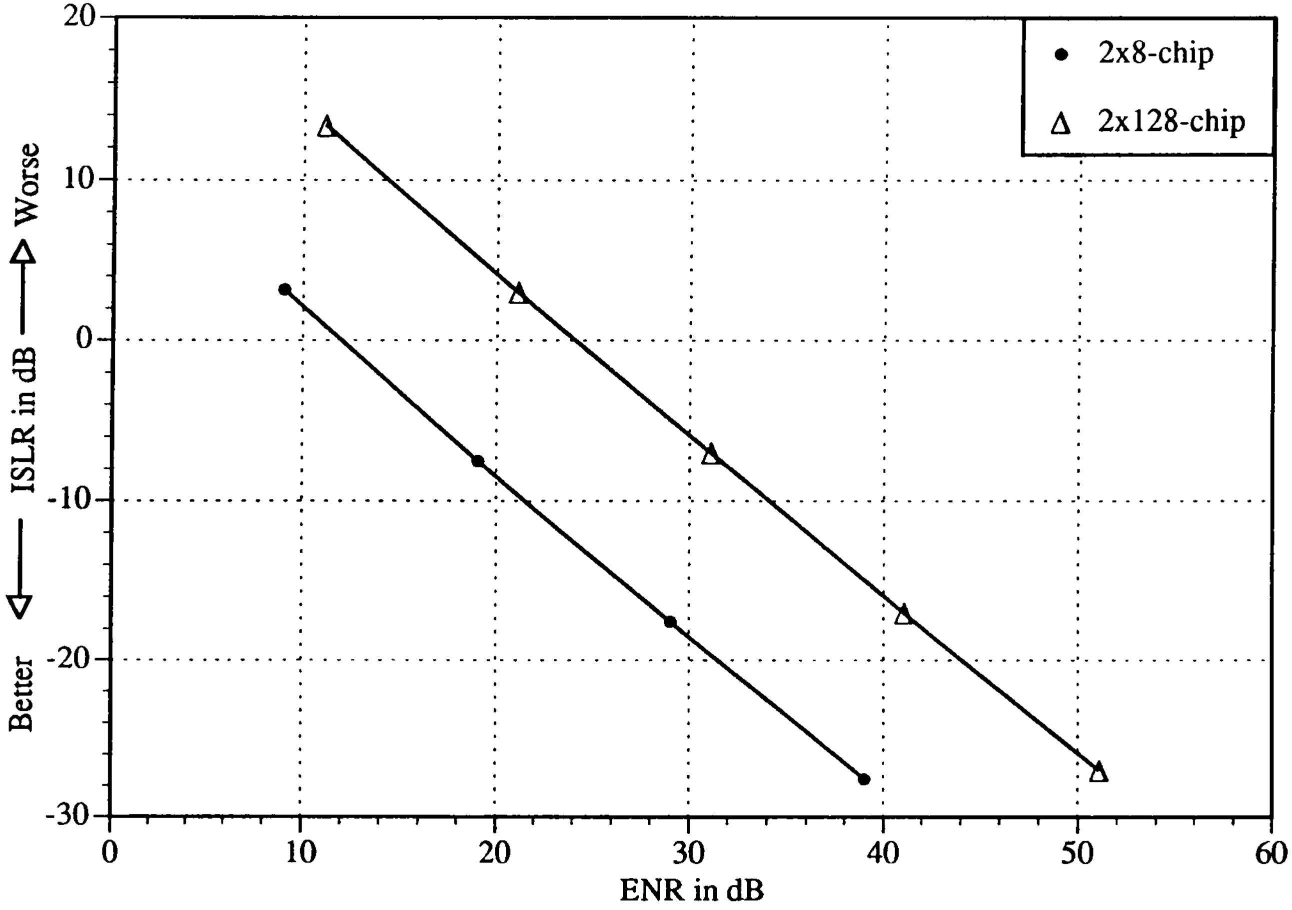

Figure A5.26. Effect of the Length of Complementary Code on the ISLR in AWGN.

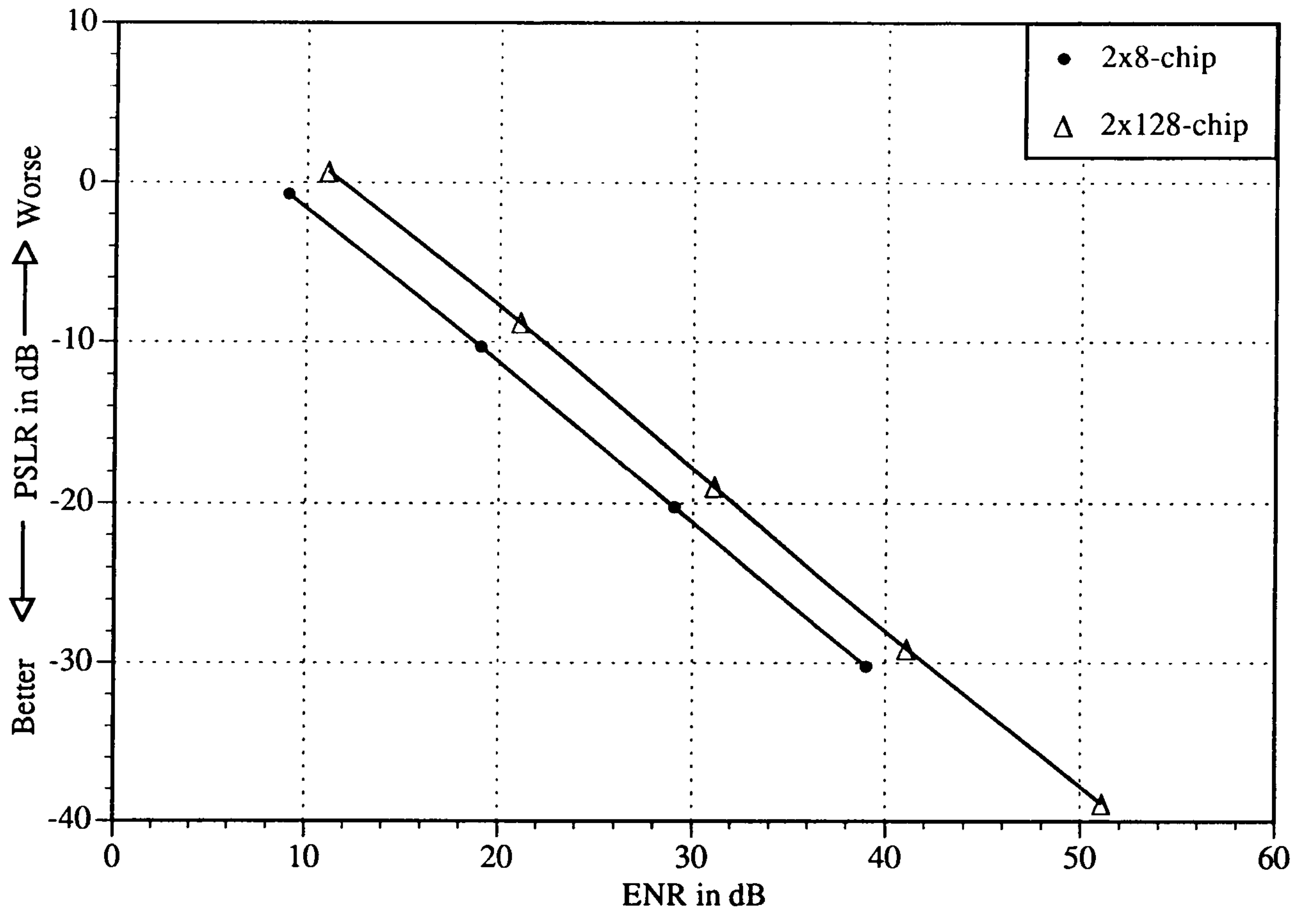

Figure A5.27. Effect of the Length of Complementary Code on the PSLR for Swerling I Target Fluctuation.

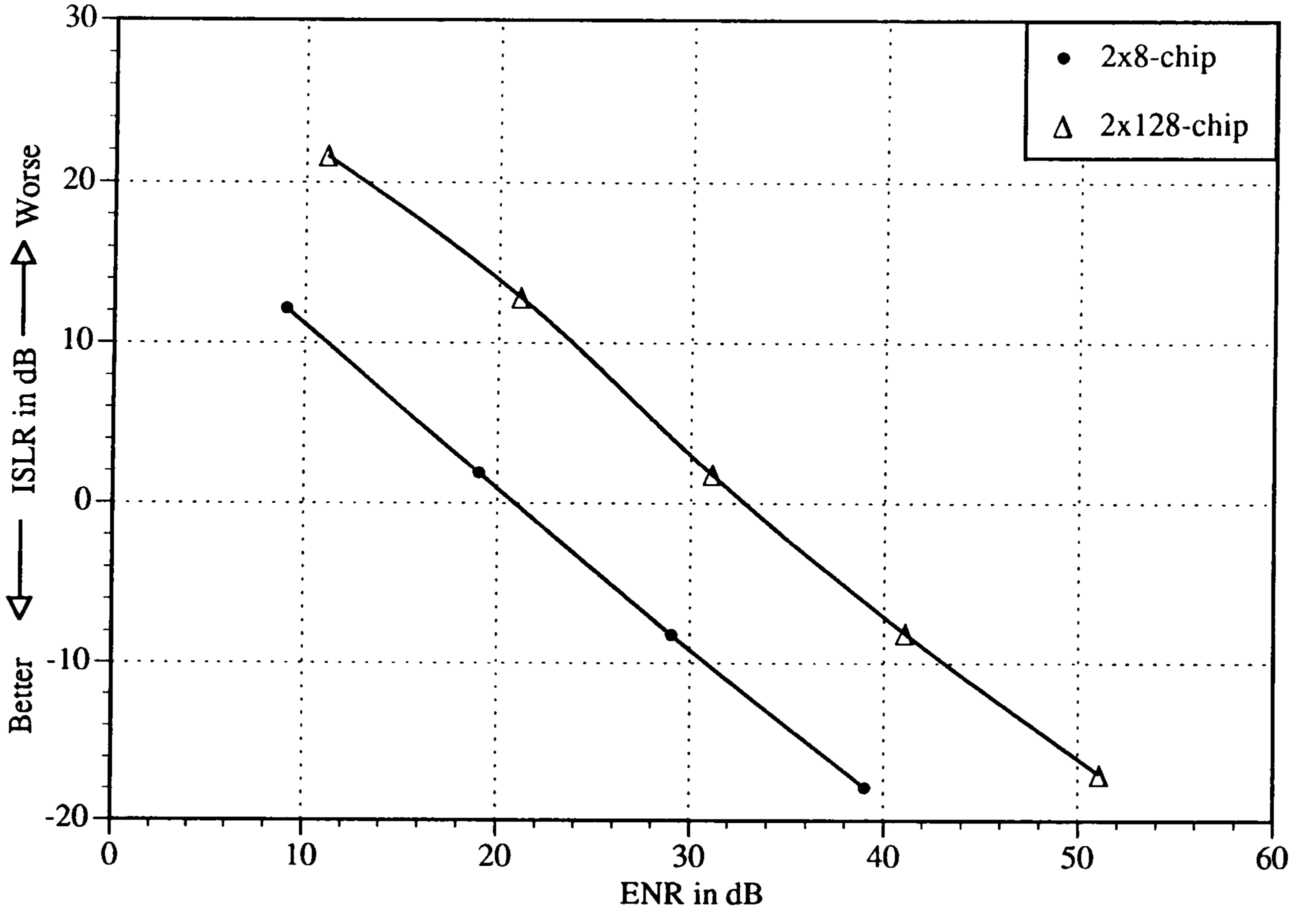

Figure A5.28. Effect of the Length of Complementary code on the ISLR for Swerling I Target Fluctuation.

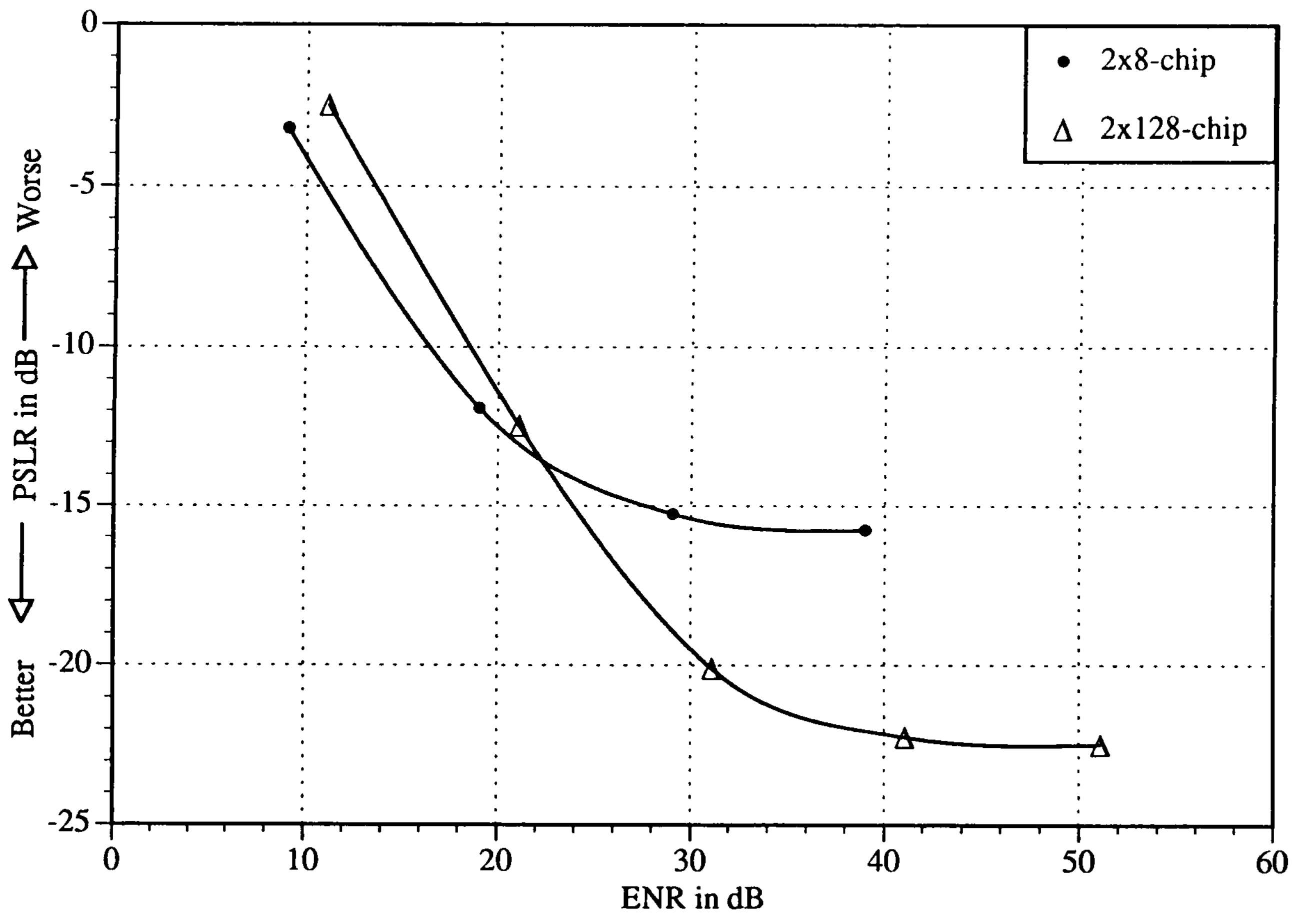

Figure A5.29. Effect of the Length of Complementary Code on the PSLR for Swerling II Target Fluctuation.

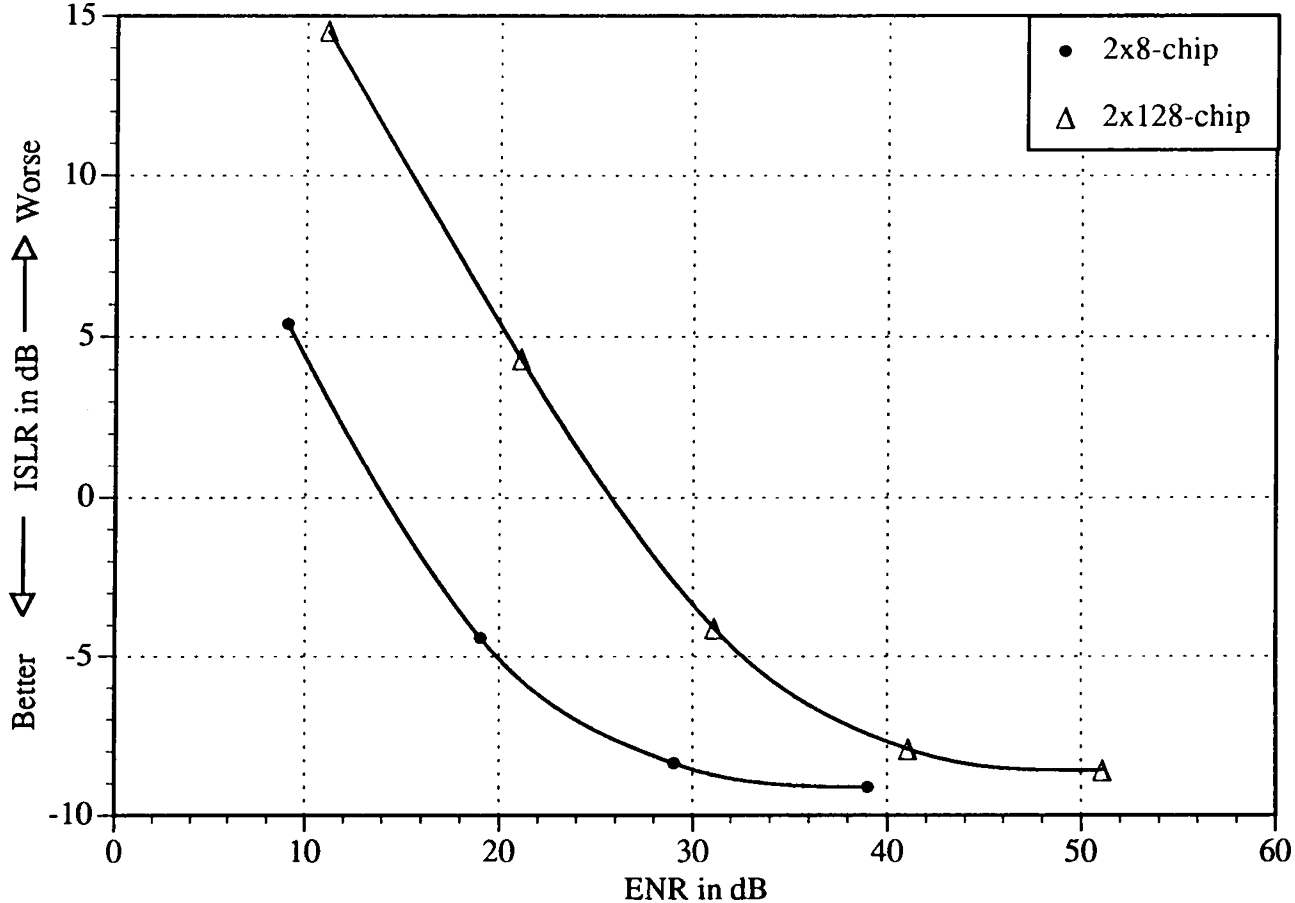

Figure A5.30. Effect of the Length of Complementary Code on the ISLR for Swerling II Target Fluctuation.

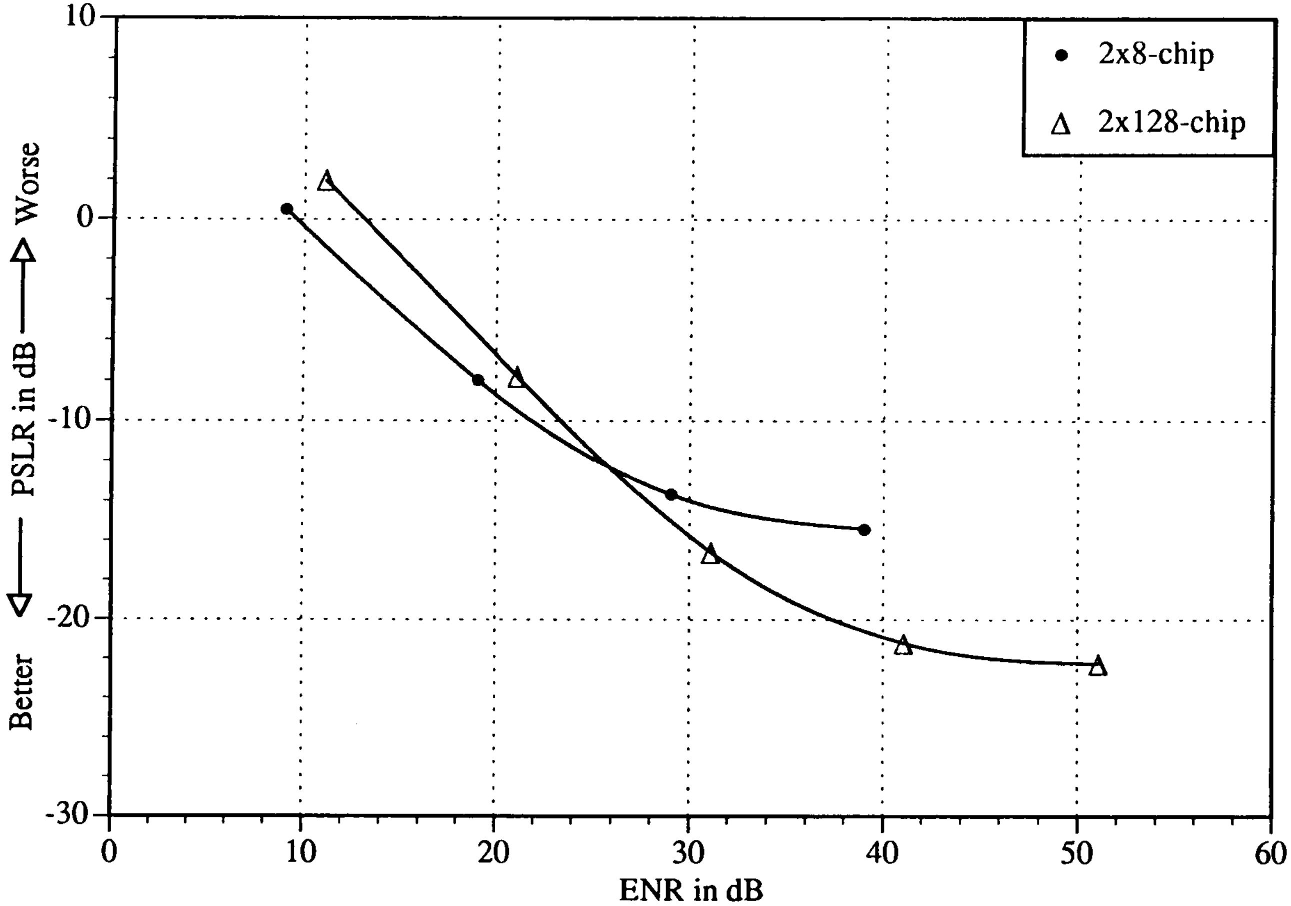

Figure A5.31. Effect of the Length of Complementary Code on the PSLR for Swerling I Target Fluctuation and Fast Fading.

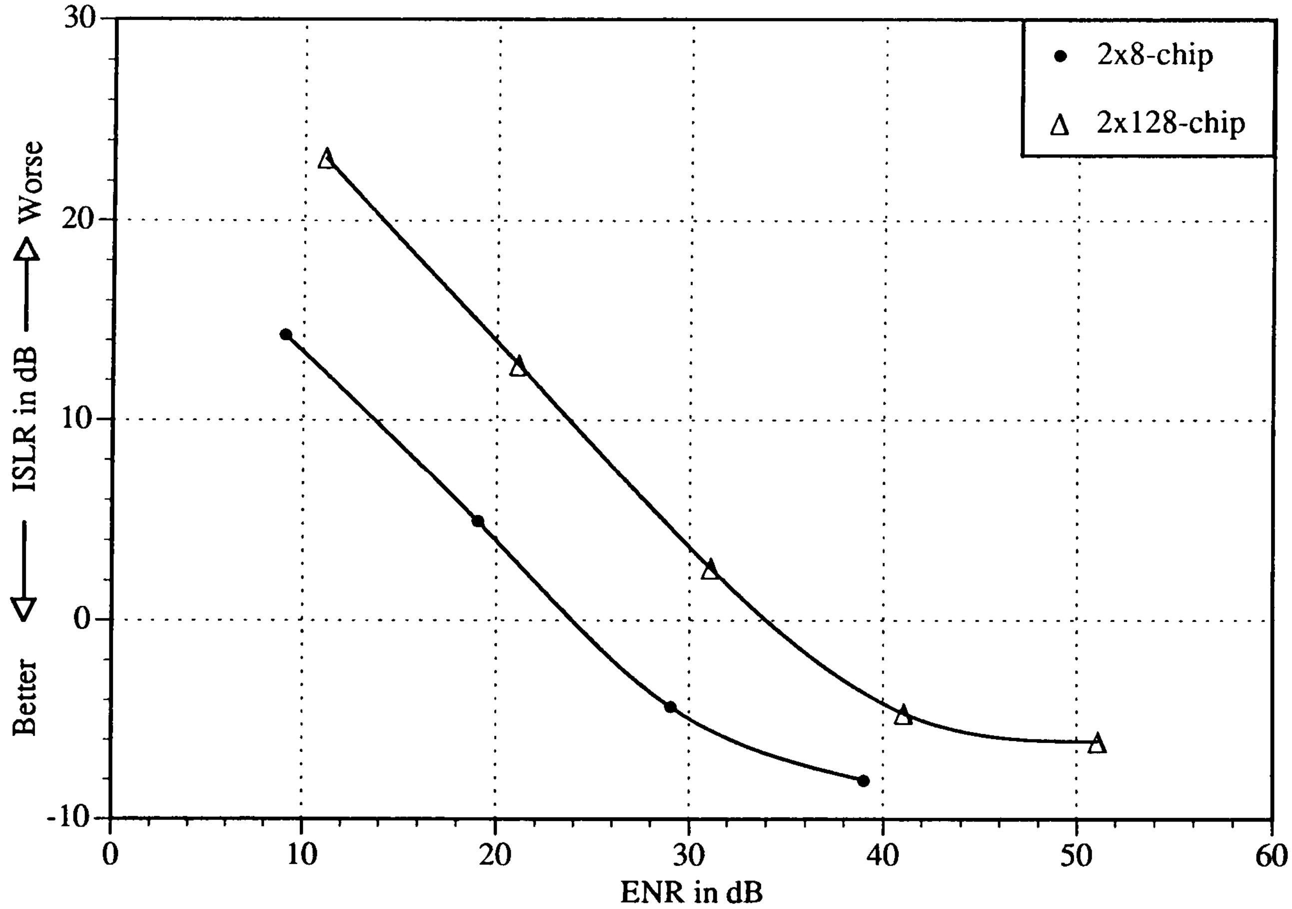

Figure A5.32. Effect of the Length of Complementary Code on the ISLR for Swerling I Target Fluctuation and Fast Fading.

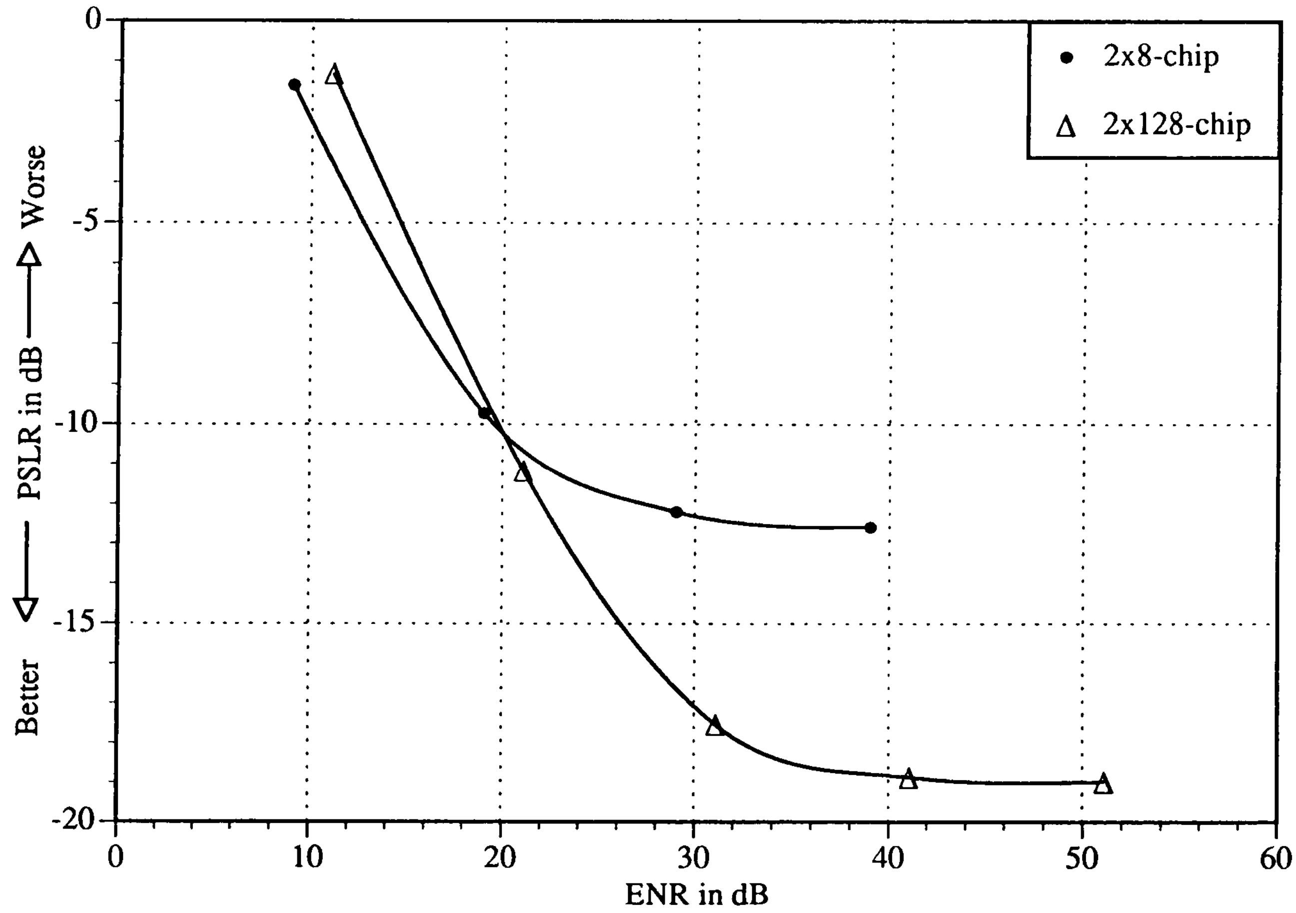

Figure A5.33. Effect of the Length of Complementary Code on the PSLR for Swerling II Target Fluctuation and Fast Fading.

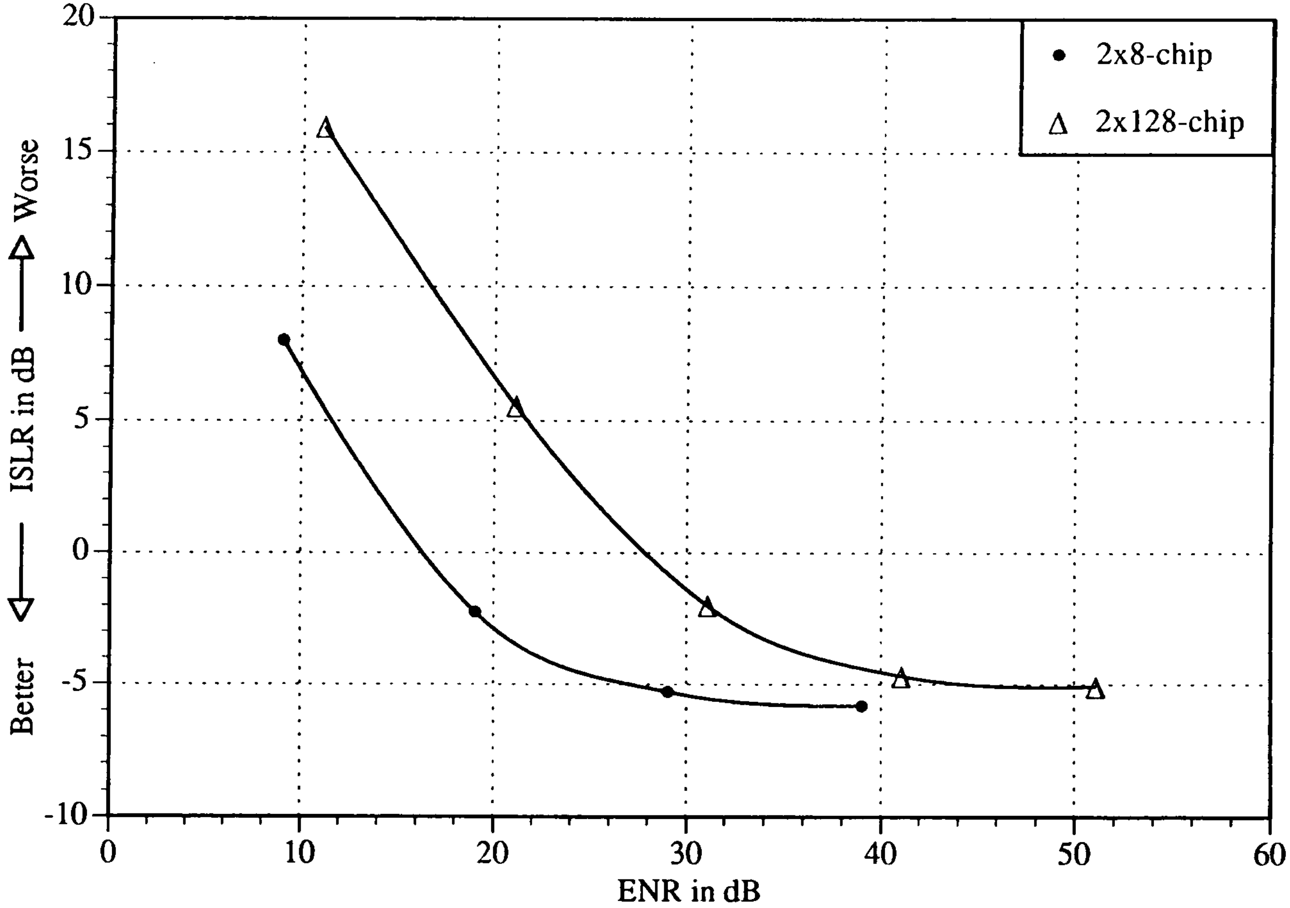

Figure A5.34. Effect of the Length of Complementary Code on the ISLR for Swerling II Target Fluctuation and Fast Fading.

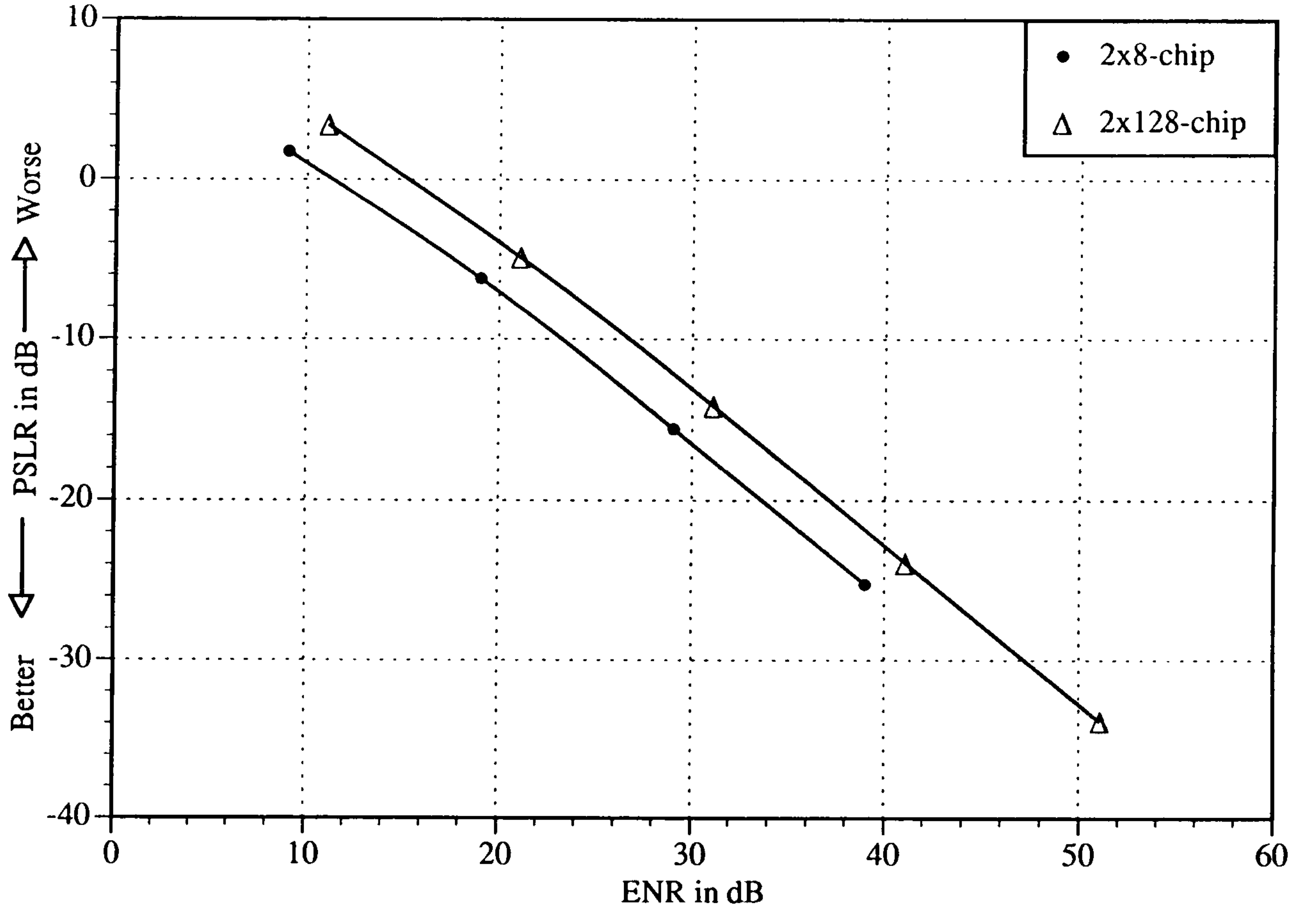

Figure A5.35. Effect of the Length of Complementary Code on the PSLR for Swerling I Target Fluctuation and Slow Fading.

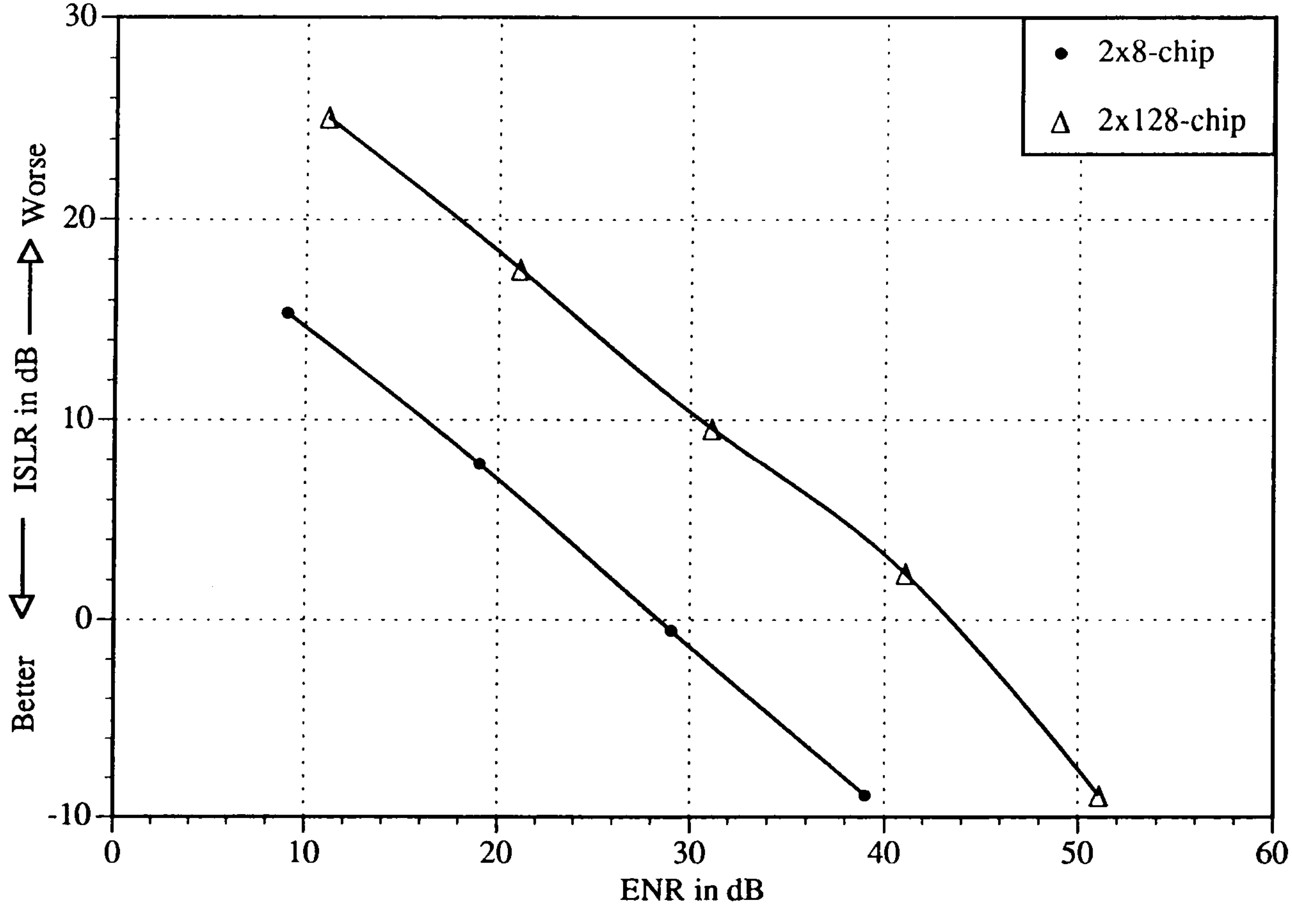

Figure A5.36. Effect of the Length of Complementary Code on the ISLR for Swerling I Target Fluctuation and Slow Fading.

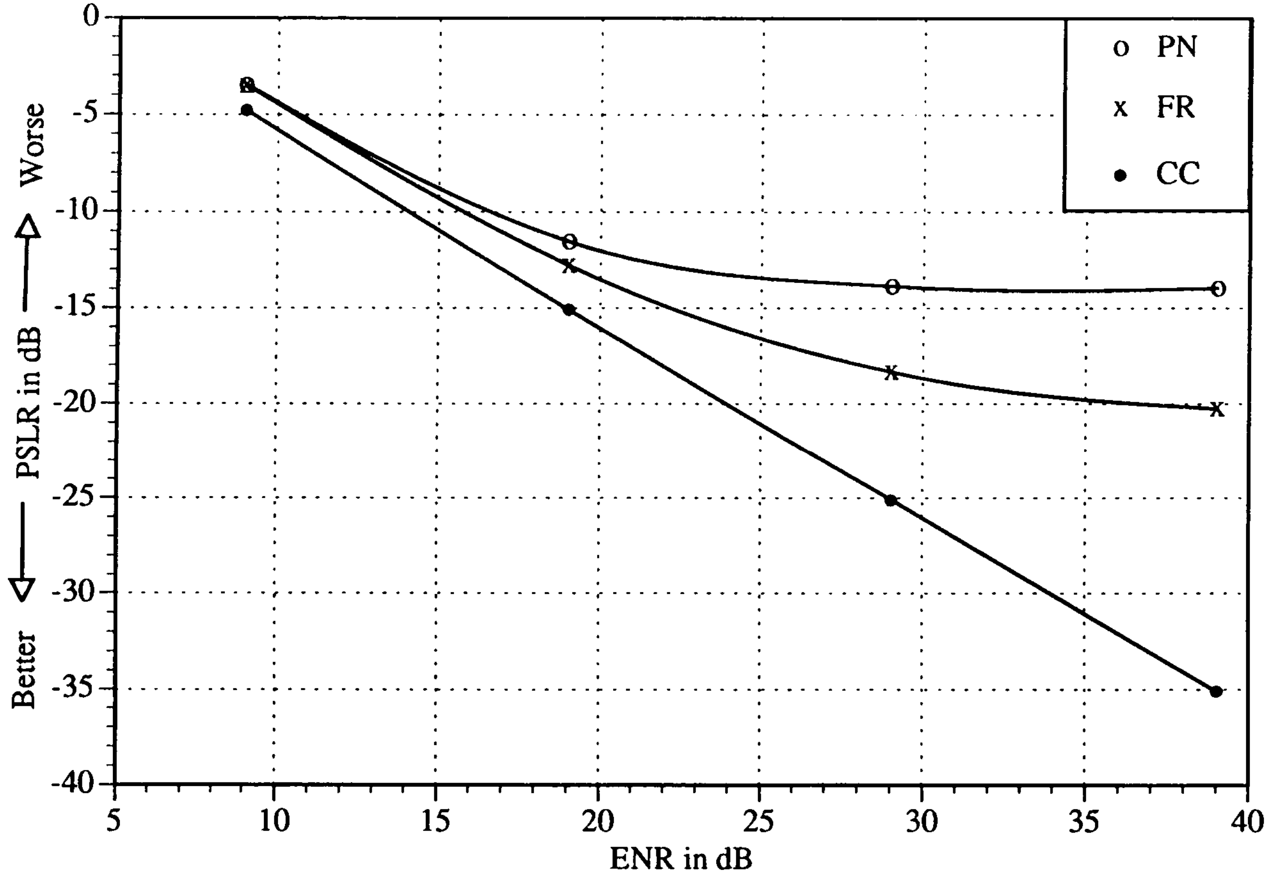

Figure A5.37. Comparison of the PSLR of 15/16-chip Codes in AWGN.

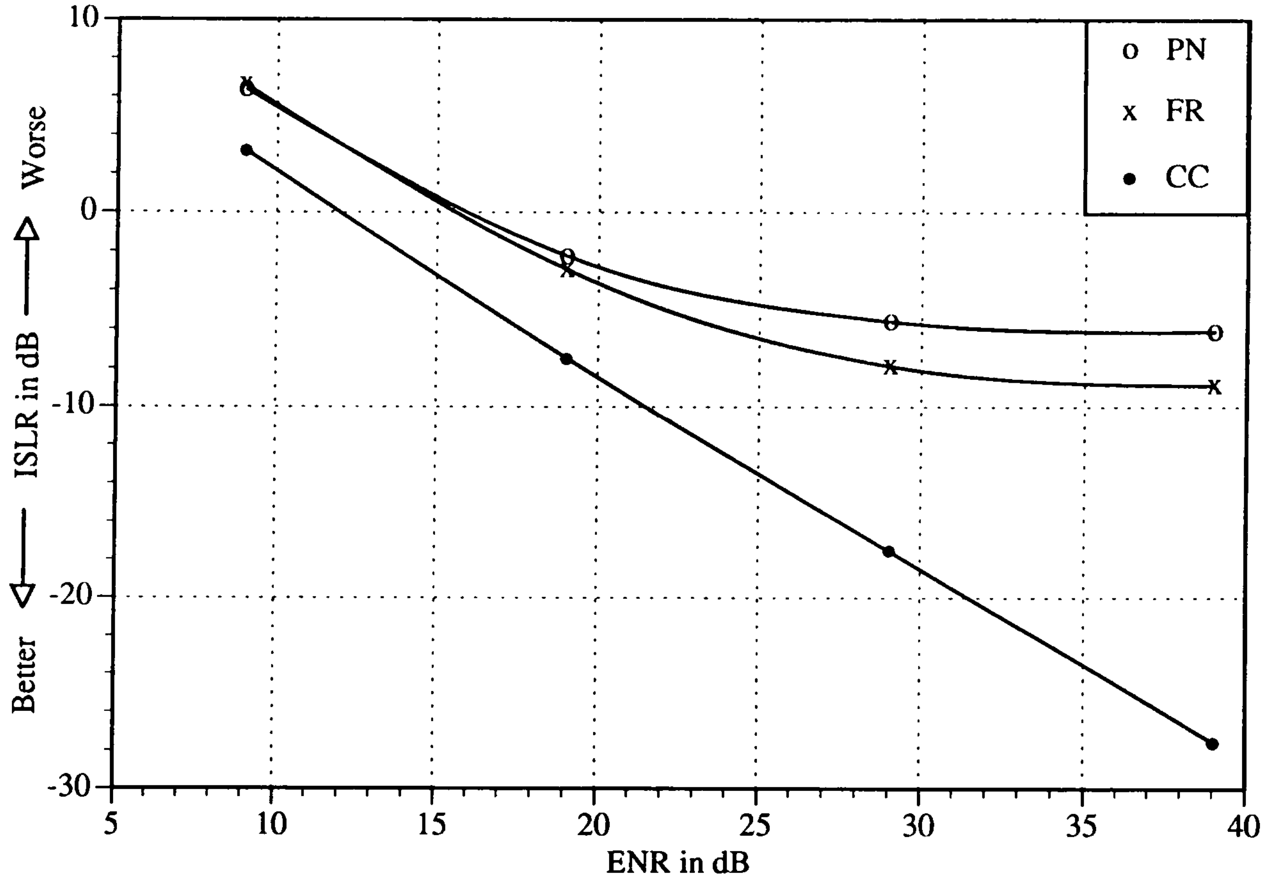

Figure A5.38. Comparison of the ISLR of 15/16-chip Codes in AWGN.

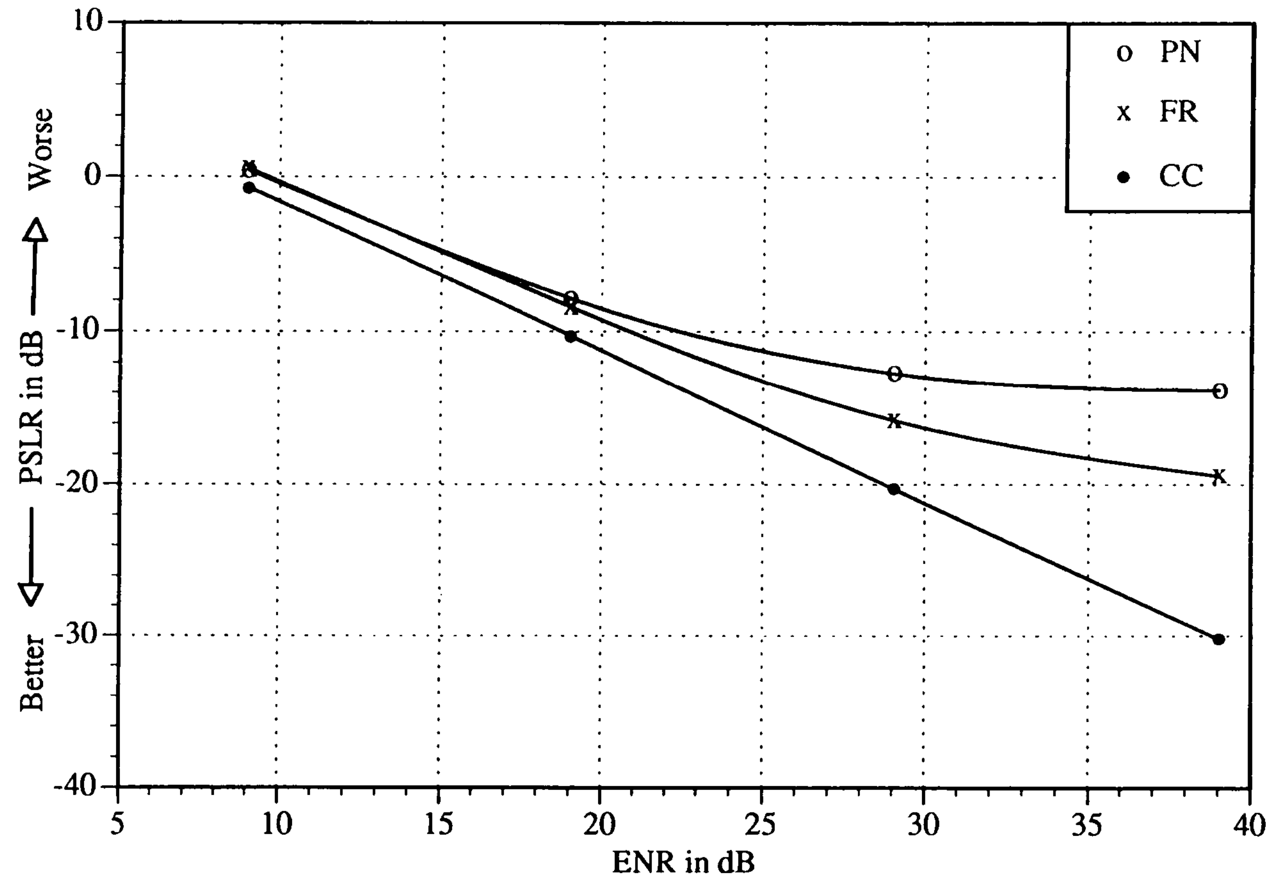

Figure A5.39. Comparison of the PSLR of 15/16-chip Codes in AWGN and Swerling I Target Fluctuation.

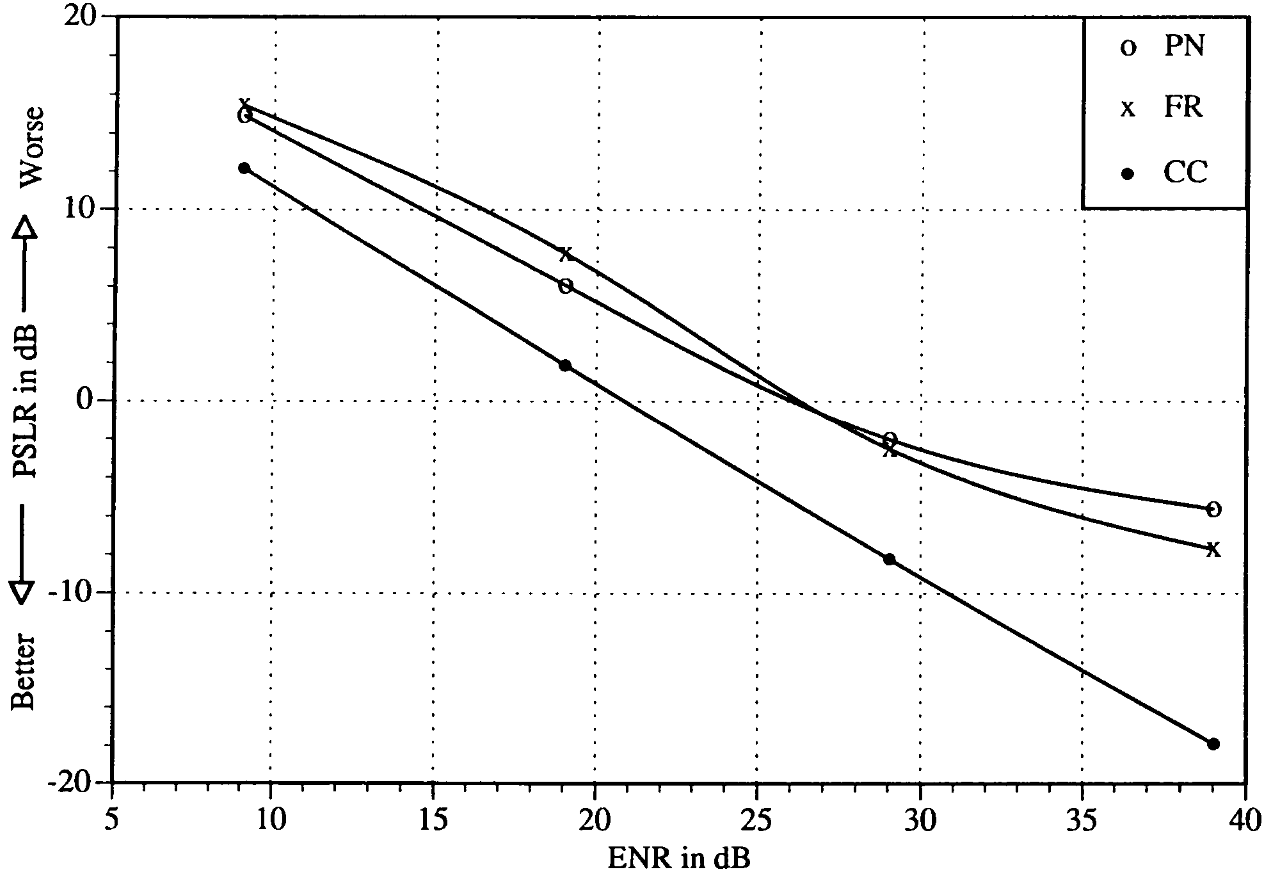

Figure A5.40. Comparison of the ISLR of 15/16-chip Codes in AWGN and Swerling I Target Fluctuation.

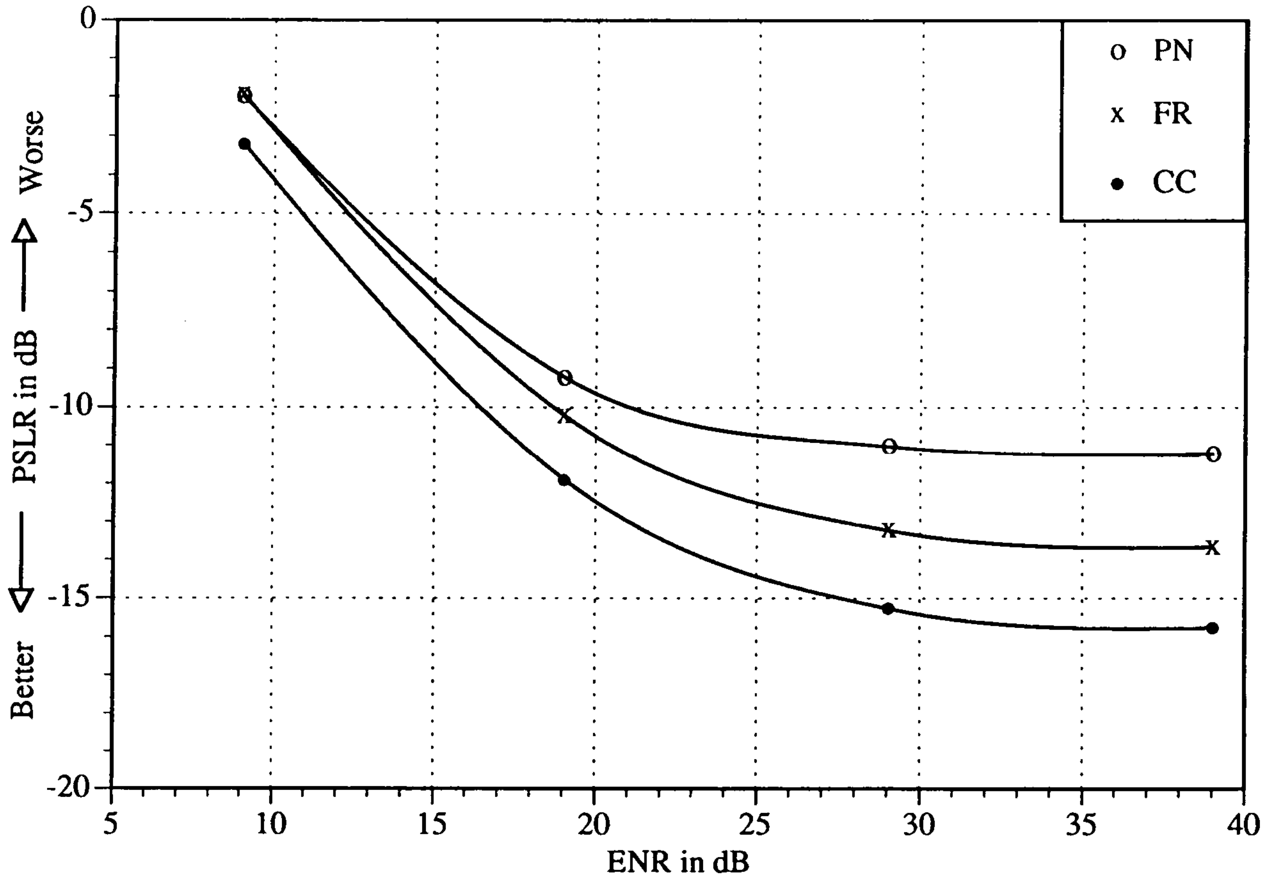

Figure A5.41. Comparison of the PSLR of 15/16-chip Codes in AWGN and Swerling II Target Fluctuation.

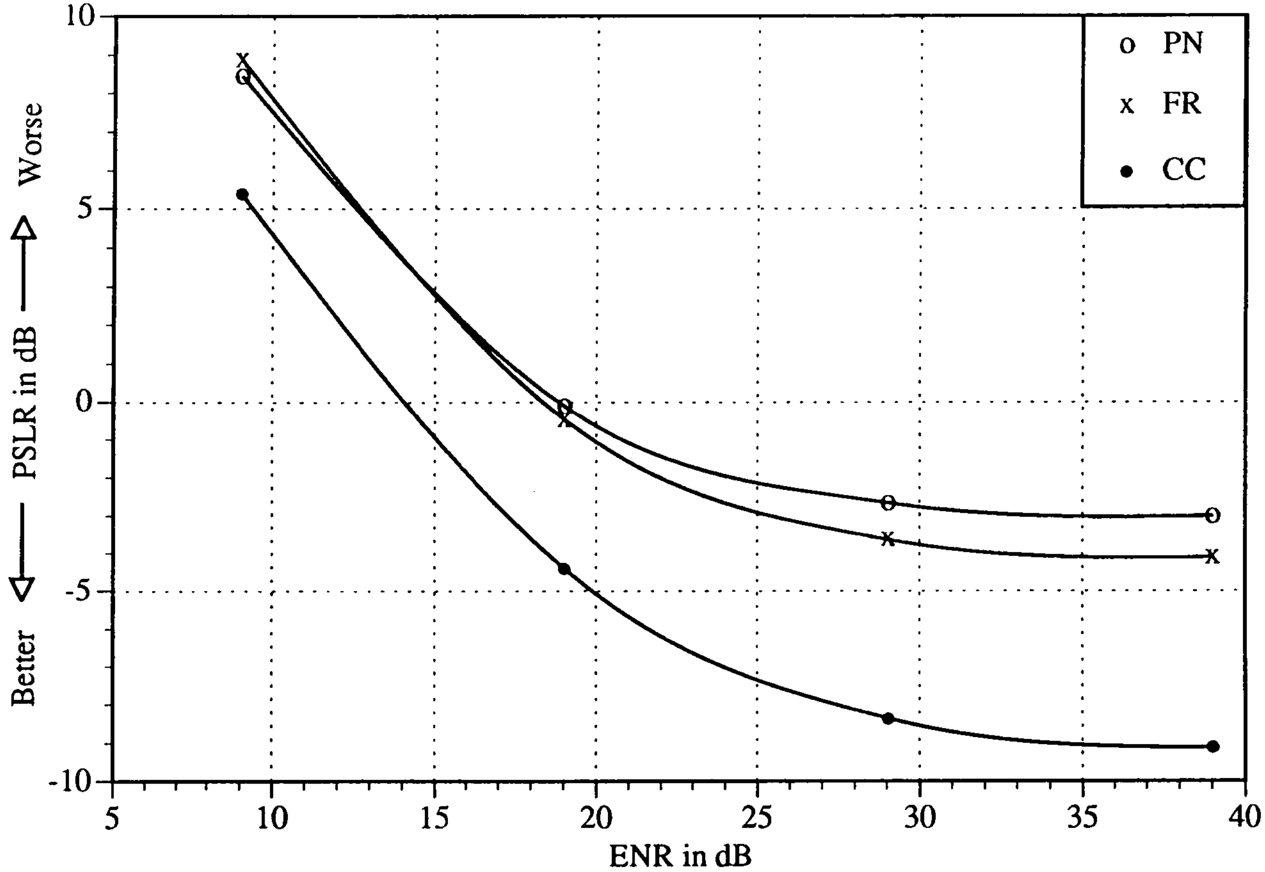

Figure A5.42. Comparison of the ISLR of 15/16-chip Codes in AWGN and Swerling II Target Fluctuation.

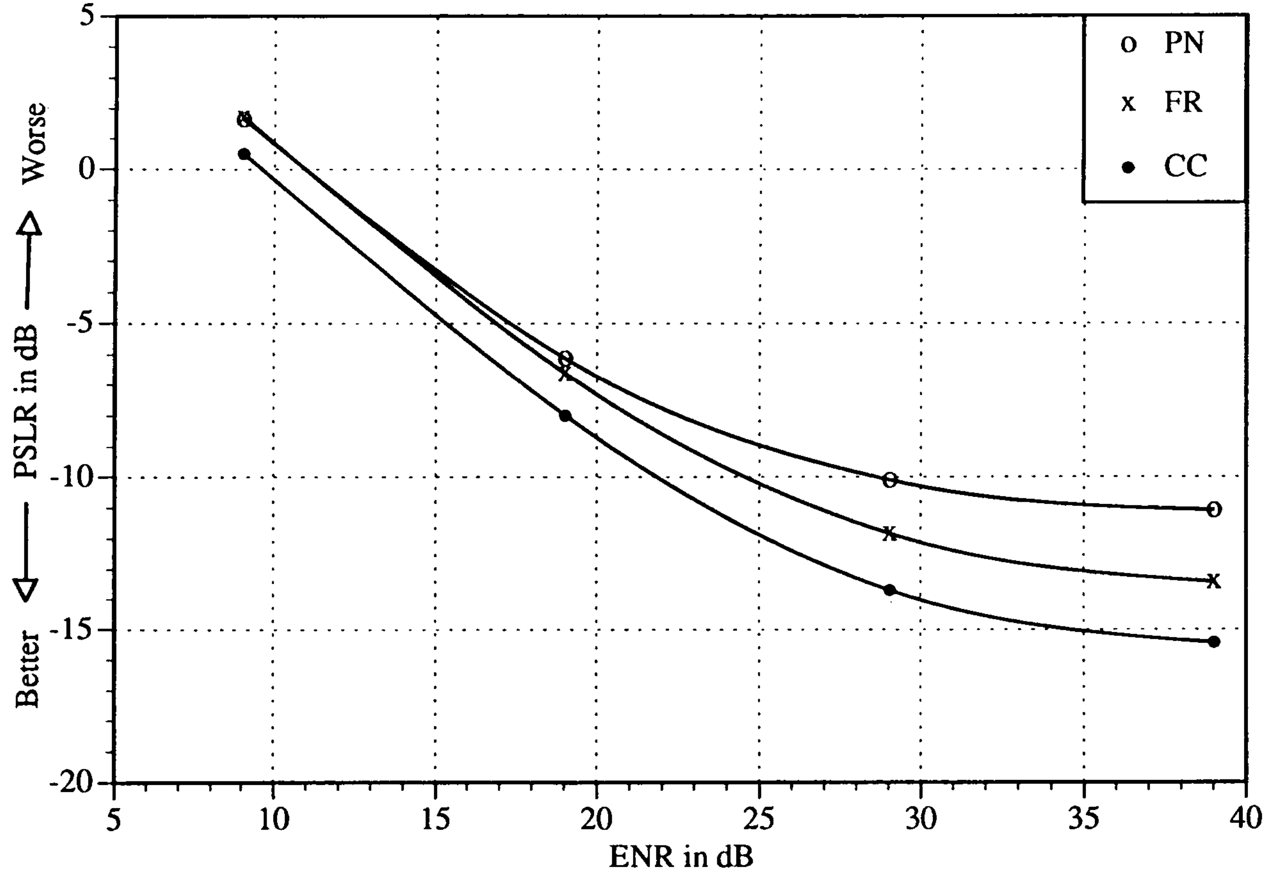

Figure A5.43. Comparison of the PSLR of 15/16-chip Codes in AWGN, Swerling I Target Fluctuation, and Fast Fading.

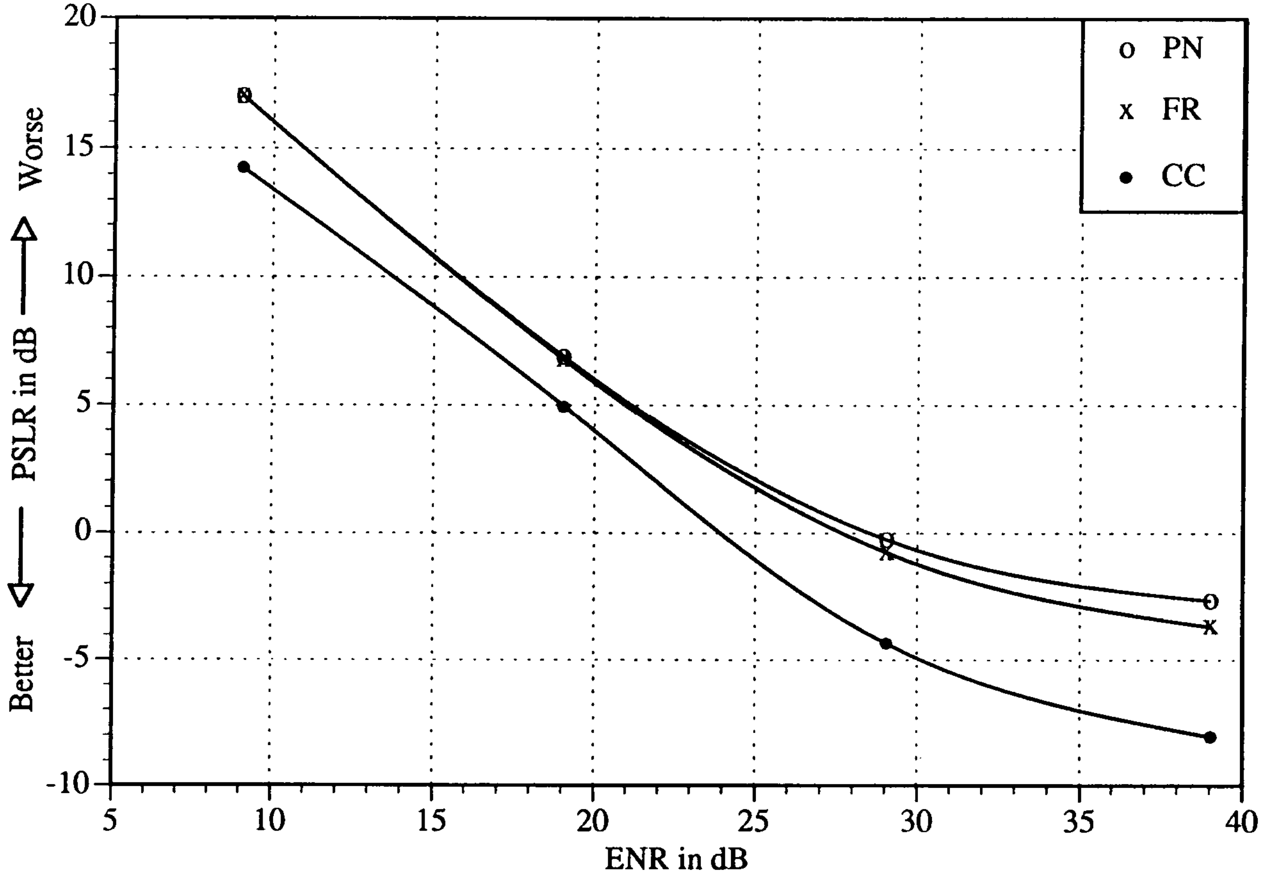

Figure A5.44. Comparison of the ISLR of 15/16-chip Codes in AWGN, Swerling I Target Fluctuation, and Fast Fading.

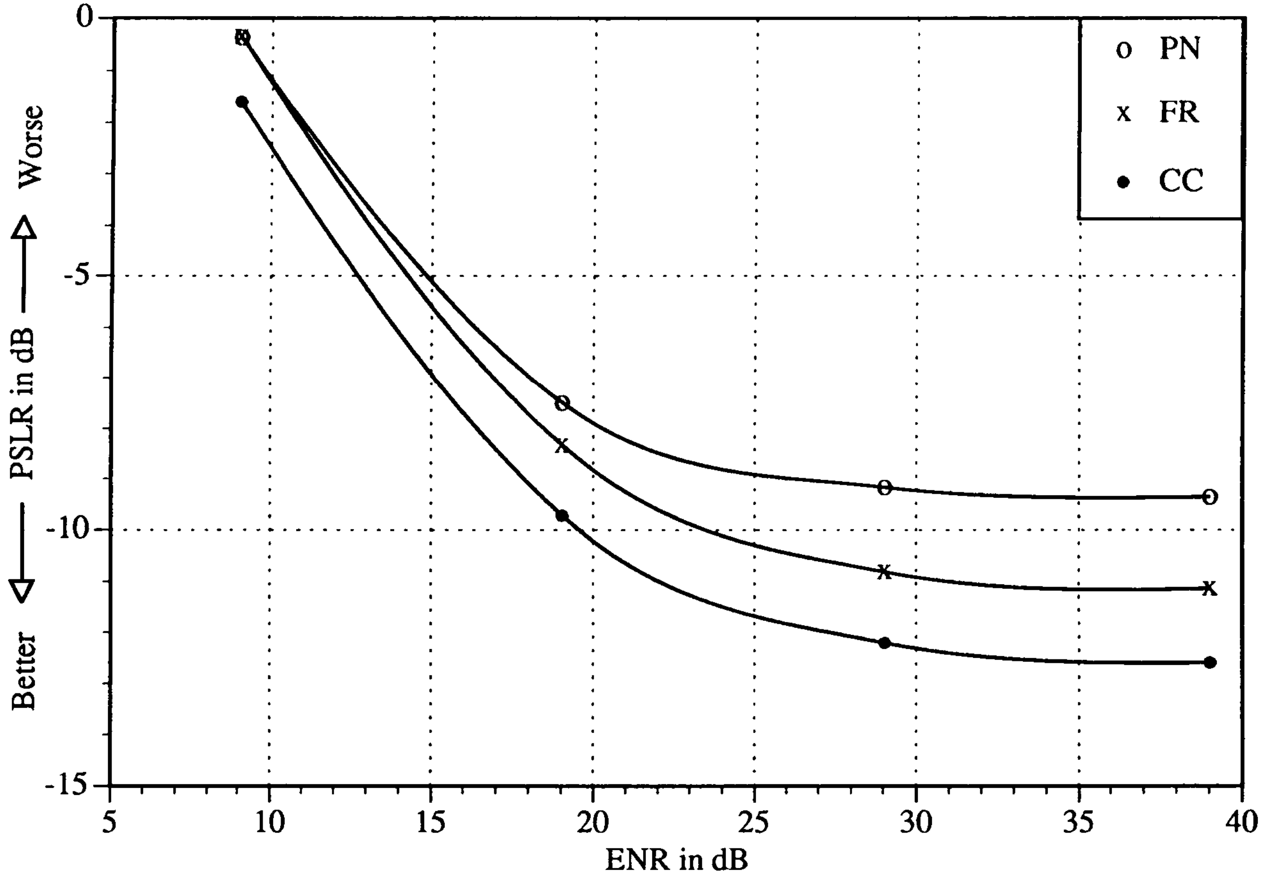

Figure A5.45. Comparison of the PSLR of 15/16-chip Codes in AWGN, Swerling II Target Fluctuation, and Fast Fading.

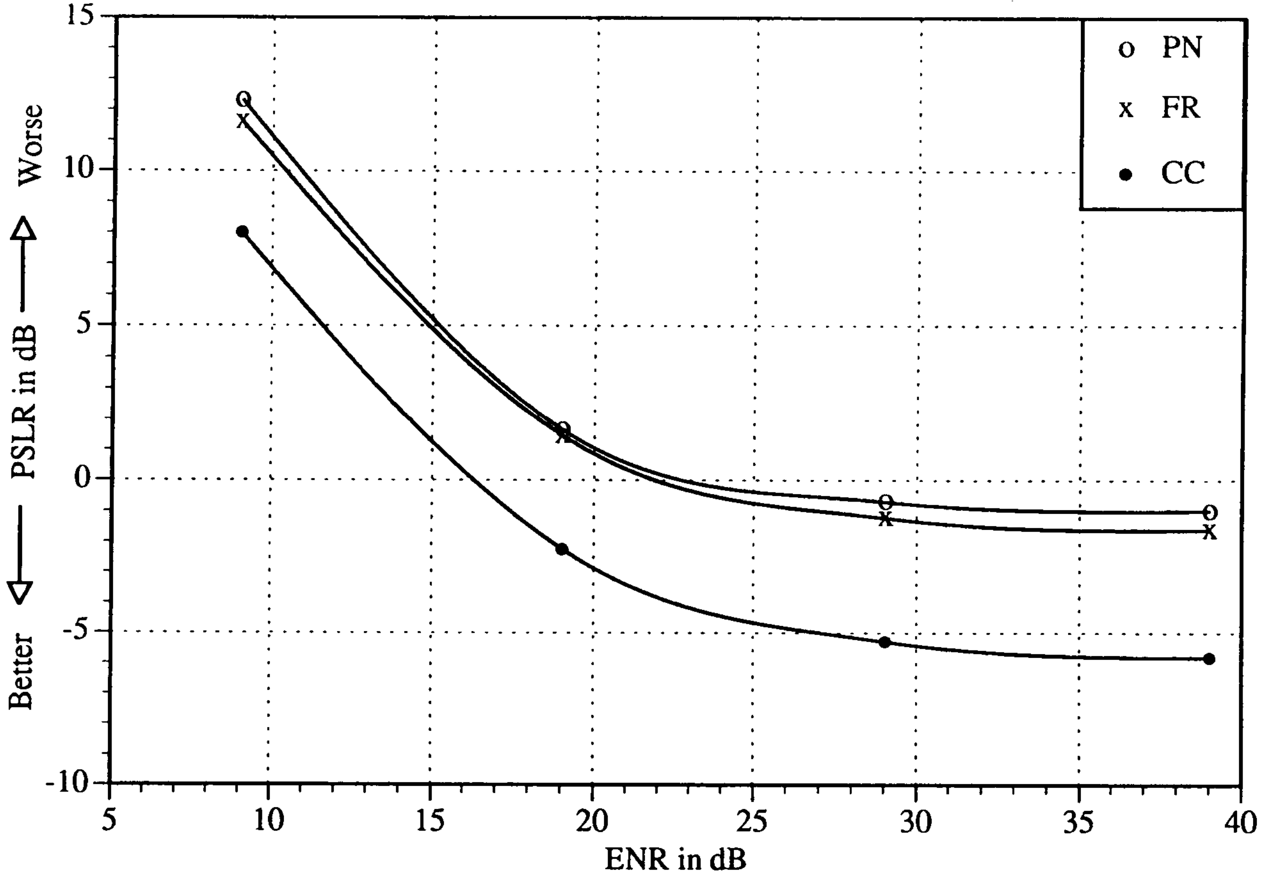

Figure A5.46. Comparison of the ISLR of 15/16-chip Codes in AWGN, Swerling II Target Fluctuation, and Fast Fading.

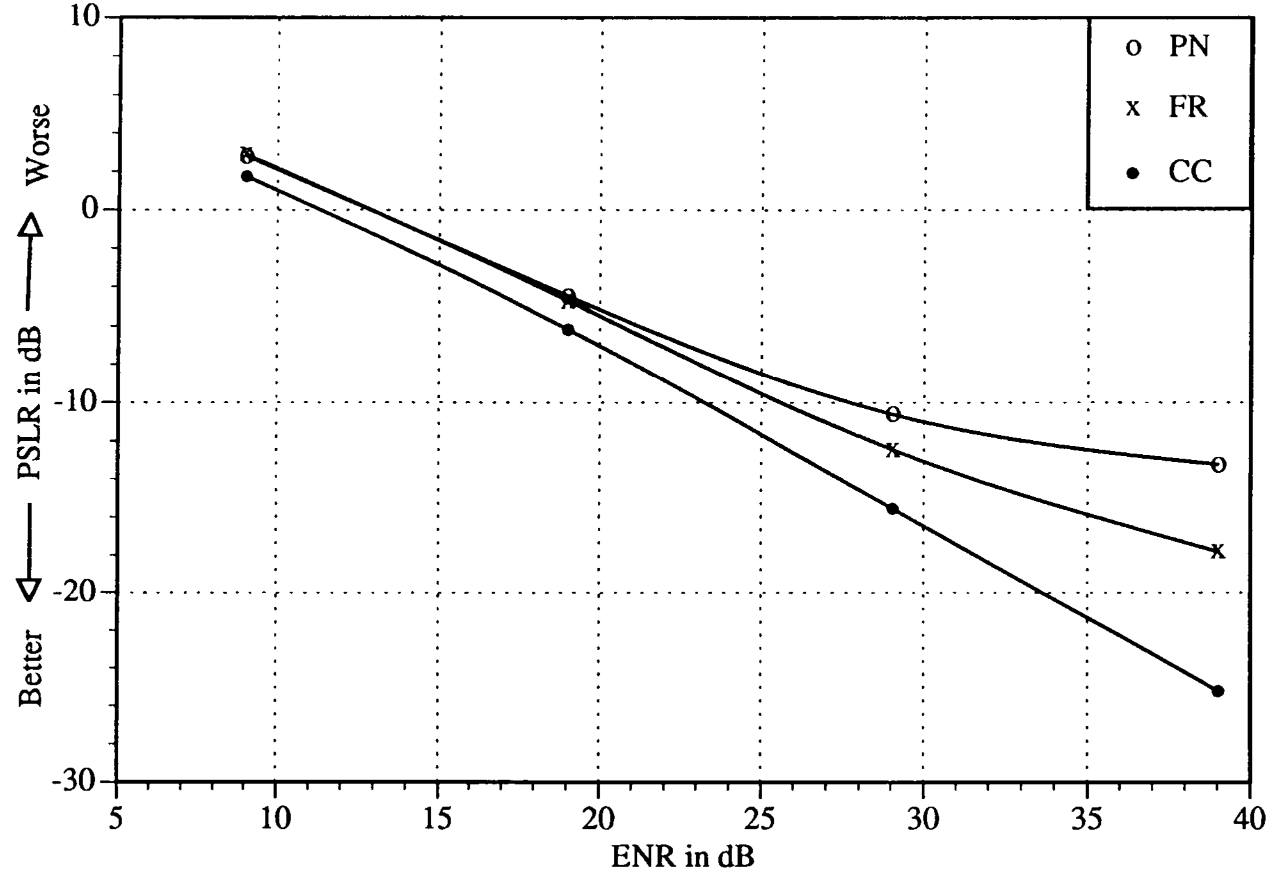

Figure A5.47. Comparison of the PSLR of 15/16-chip Codes in AWGN, Swerling I Target Fluctuation, and Slow Fading.

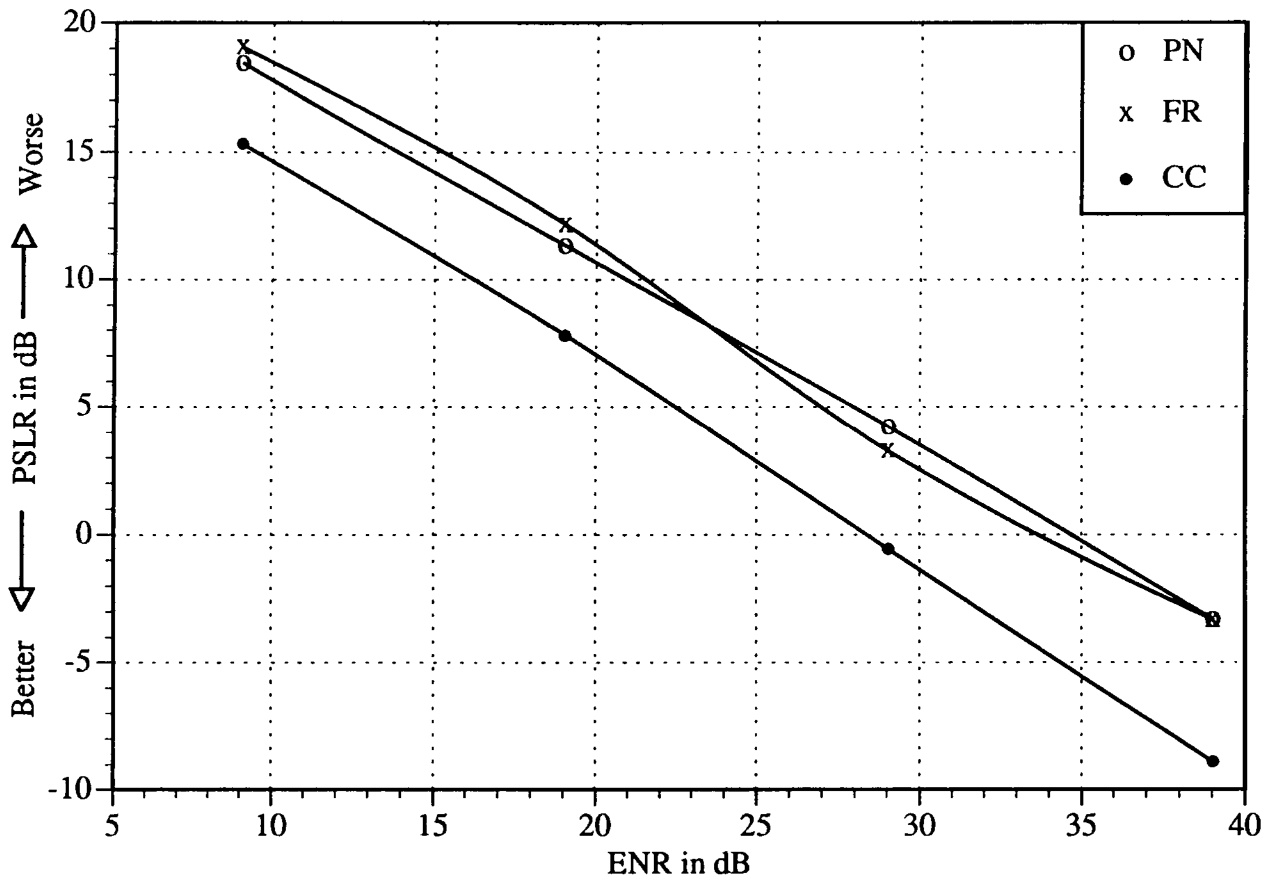

Figure A5.48. Comparison of the ISLR of 15/16-chip Codes in AWGN, Swerling I Target Fluctuation, and Slow Fading.

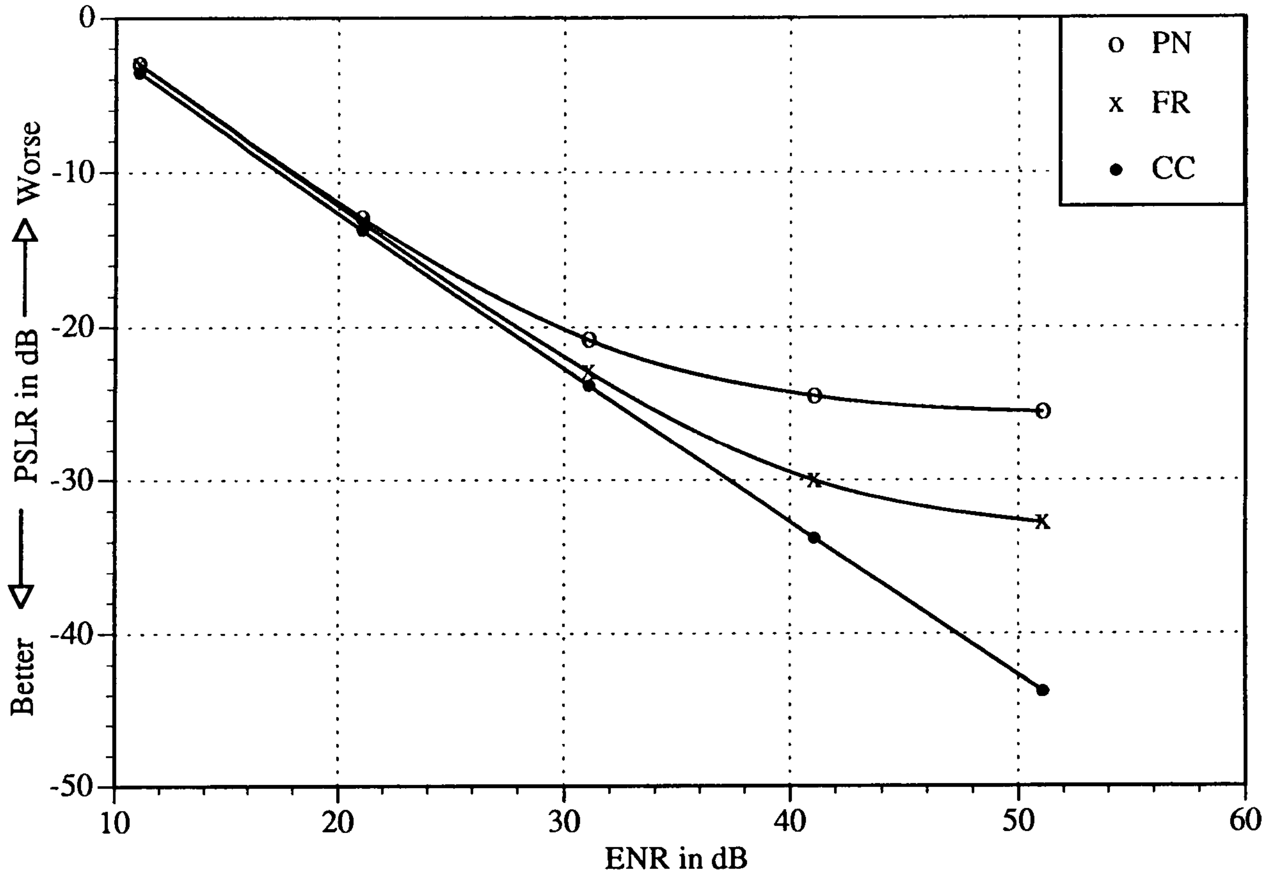

Figure A5.49. Comparison of the PSLR of 255/256-chip Codes in AWGN.

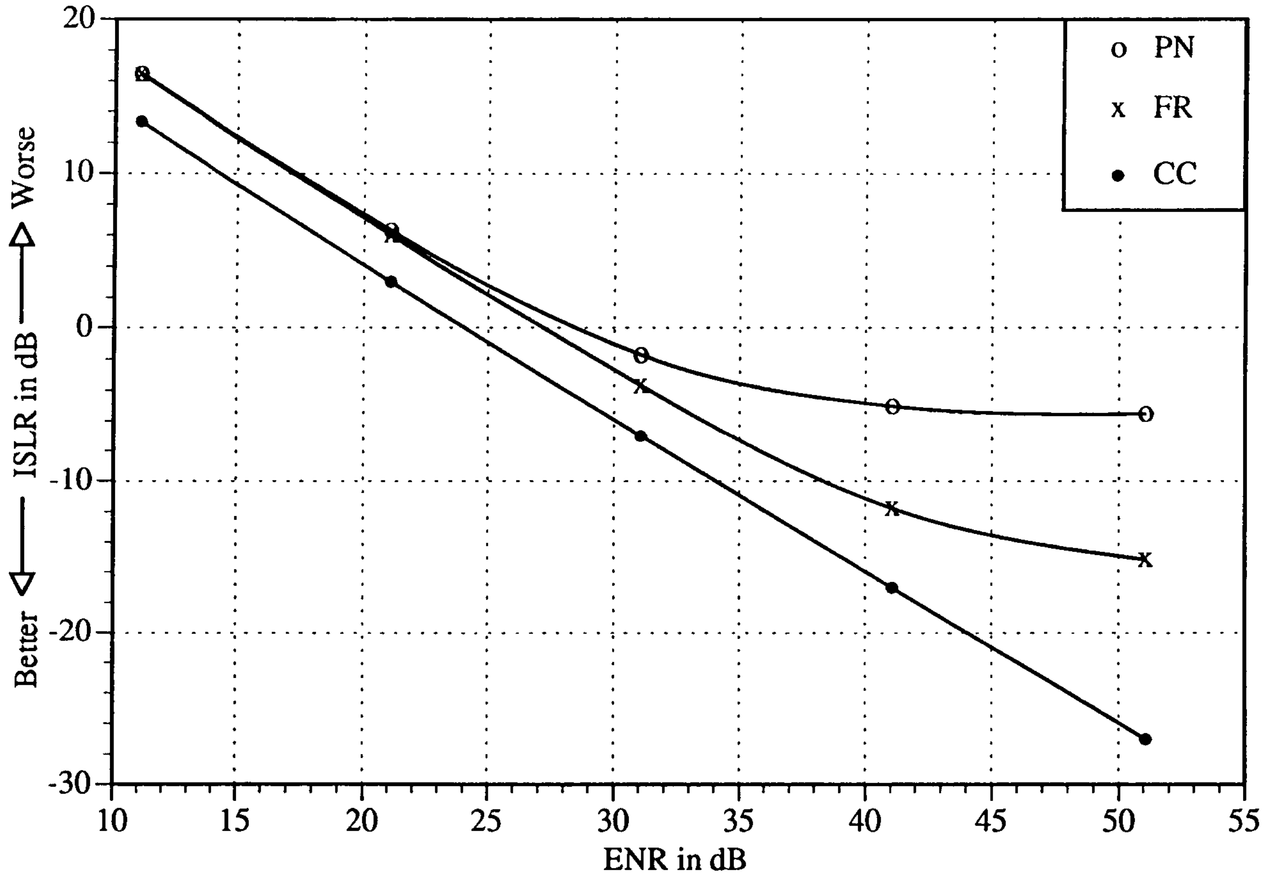

Figure A5.50. Comparison of the ISLR of 255/256-chip Codes in AWGN.

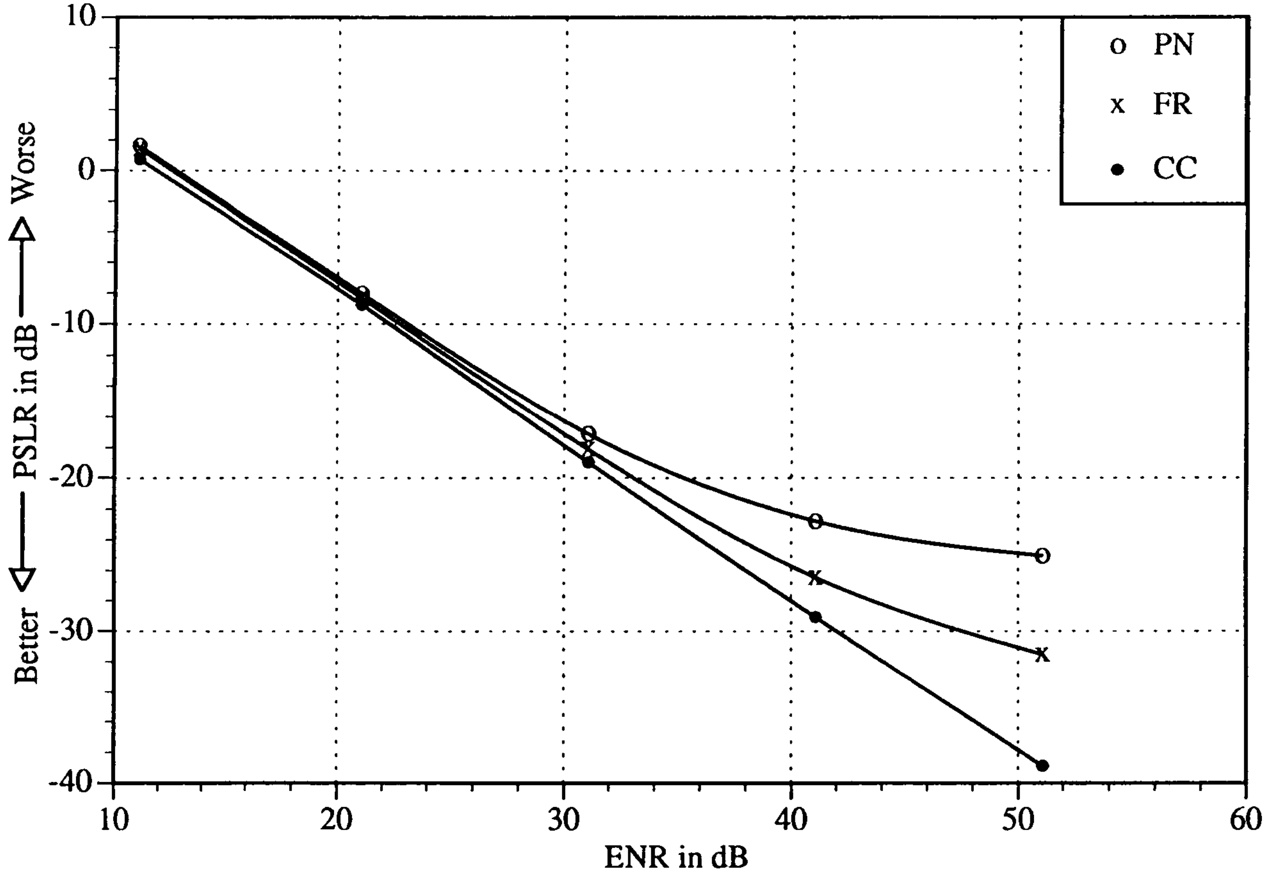

Figure A5.51. Comparison of the PSLR of 255/256-chip Codes in AWGN and Swerling I Target Fluctuation.

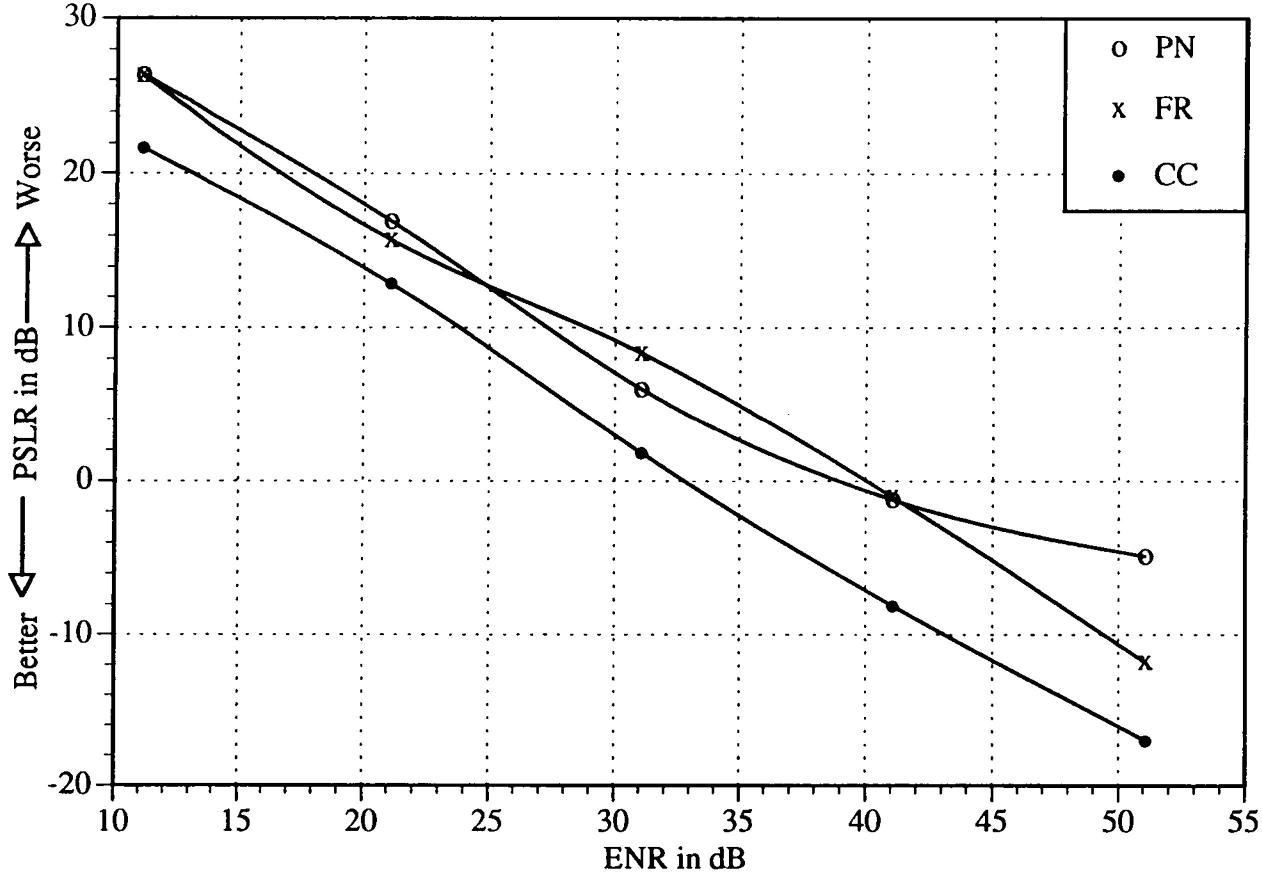

Figure A5.52. Comparison of the ISLR of 255/256-chip Codes in AWGN and Swerling I Target Fluctuation.

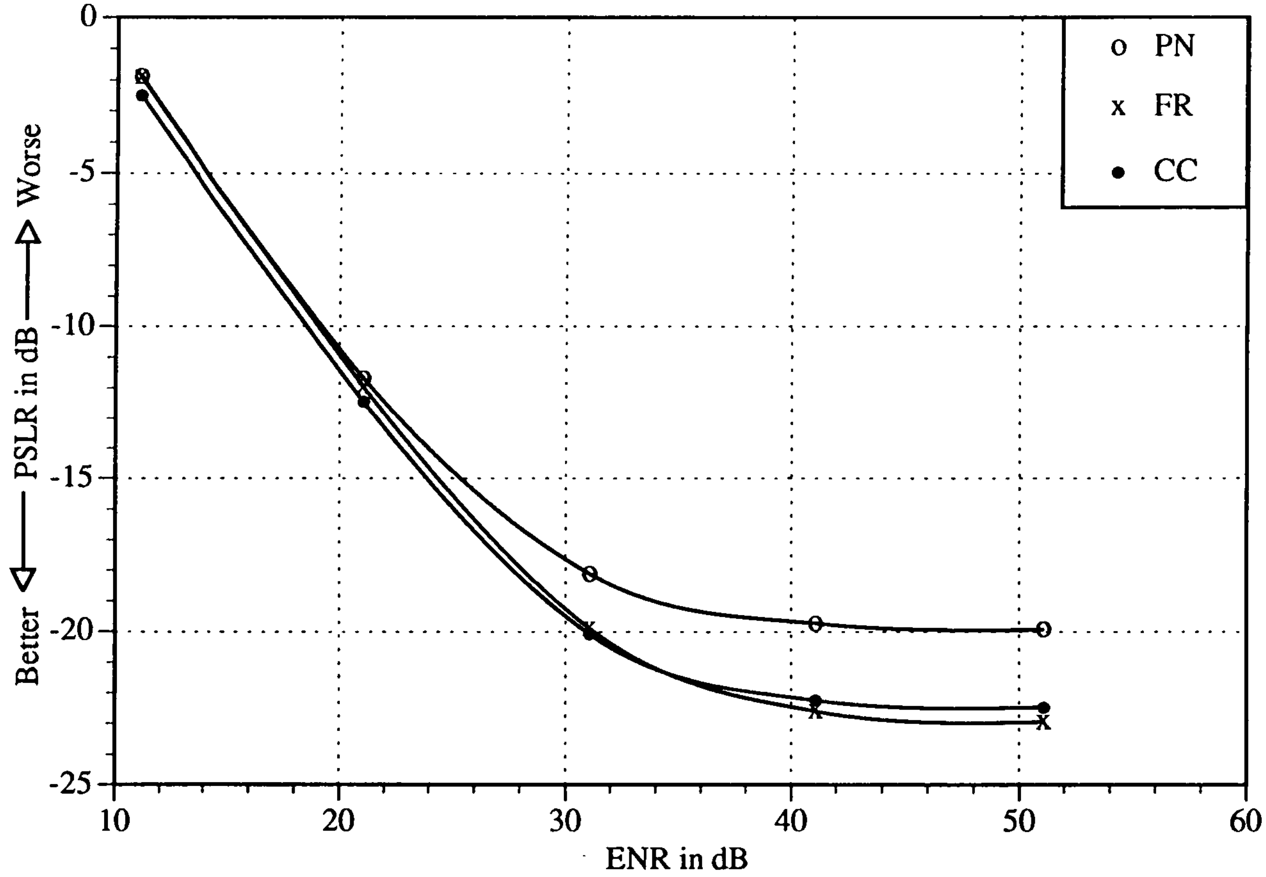

Figure A5.53. Comparison of the PSLR of 255/256-chip Codes in AWGN and Swerling II Target Fluctuation.

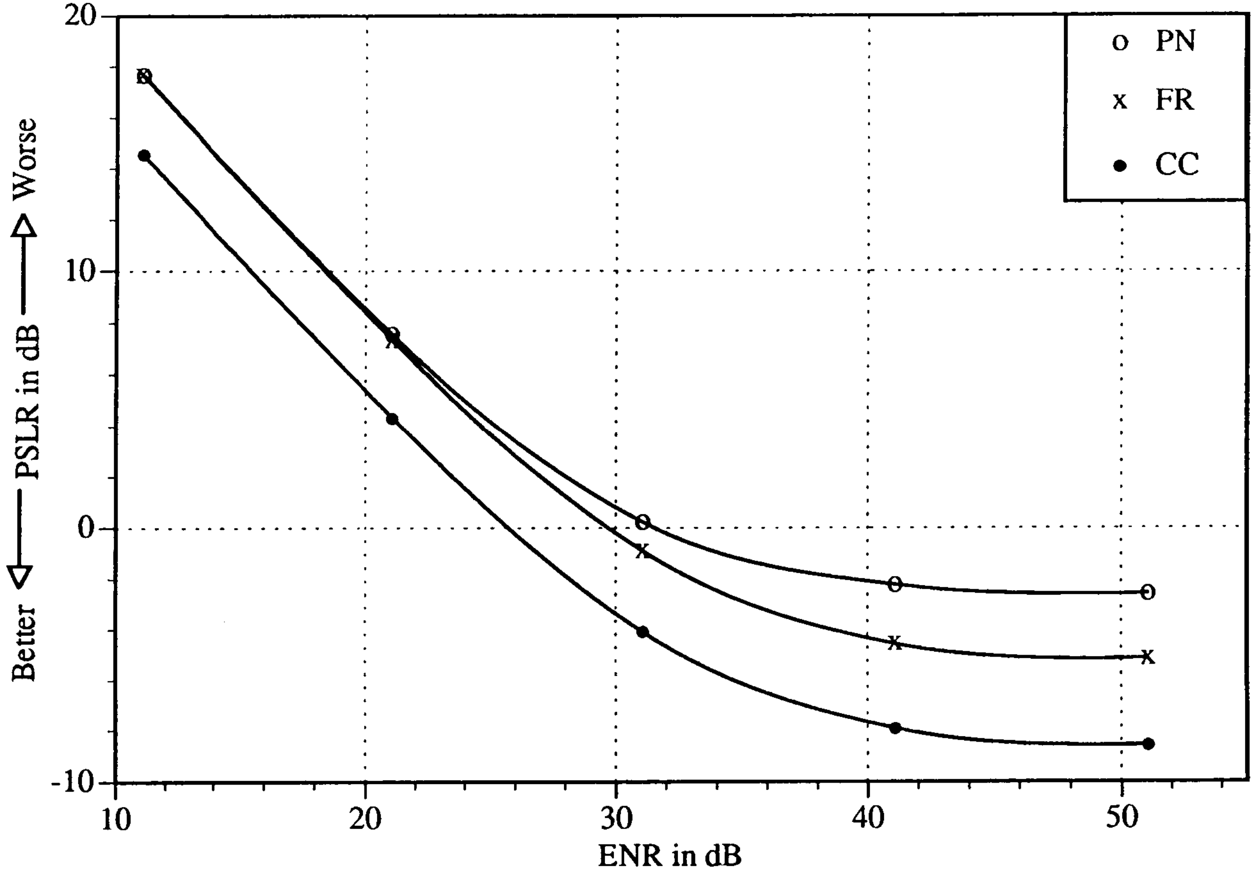

Figure A5.54. Comparison of the ISLR of 255/256-chip Codes in AWGN and Swerling II Target Fluctuation.

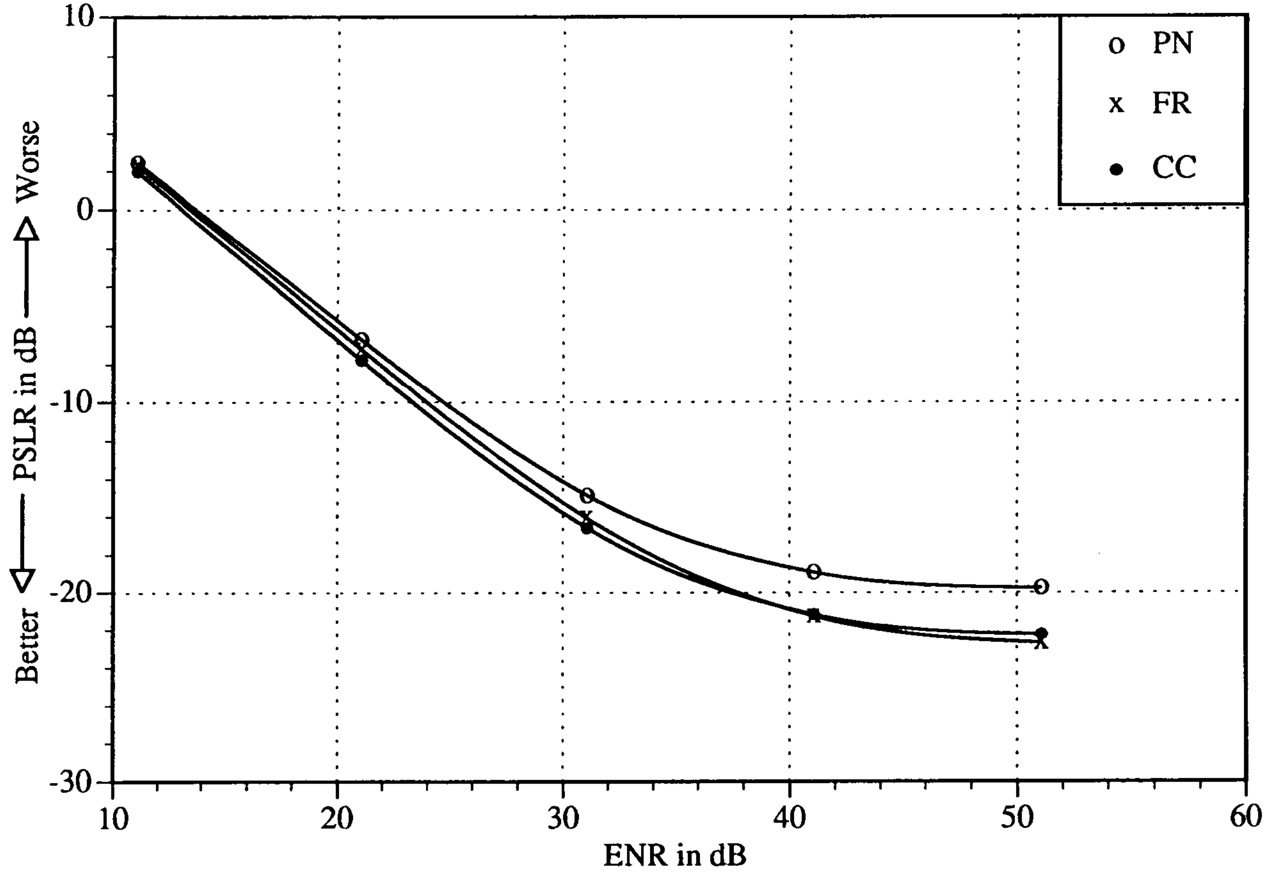

Figure A5.55. Comparison of the PSLR of 255/256-chip Codes in AWGN, Swerling I Target Fluctuation, and Fast Fading.

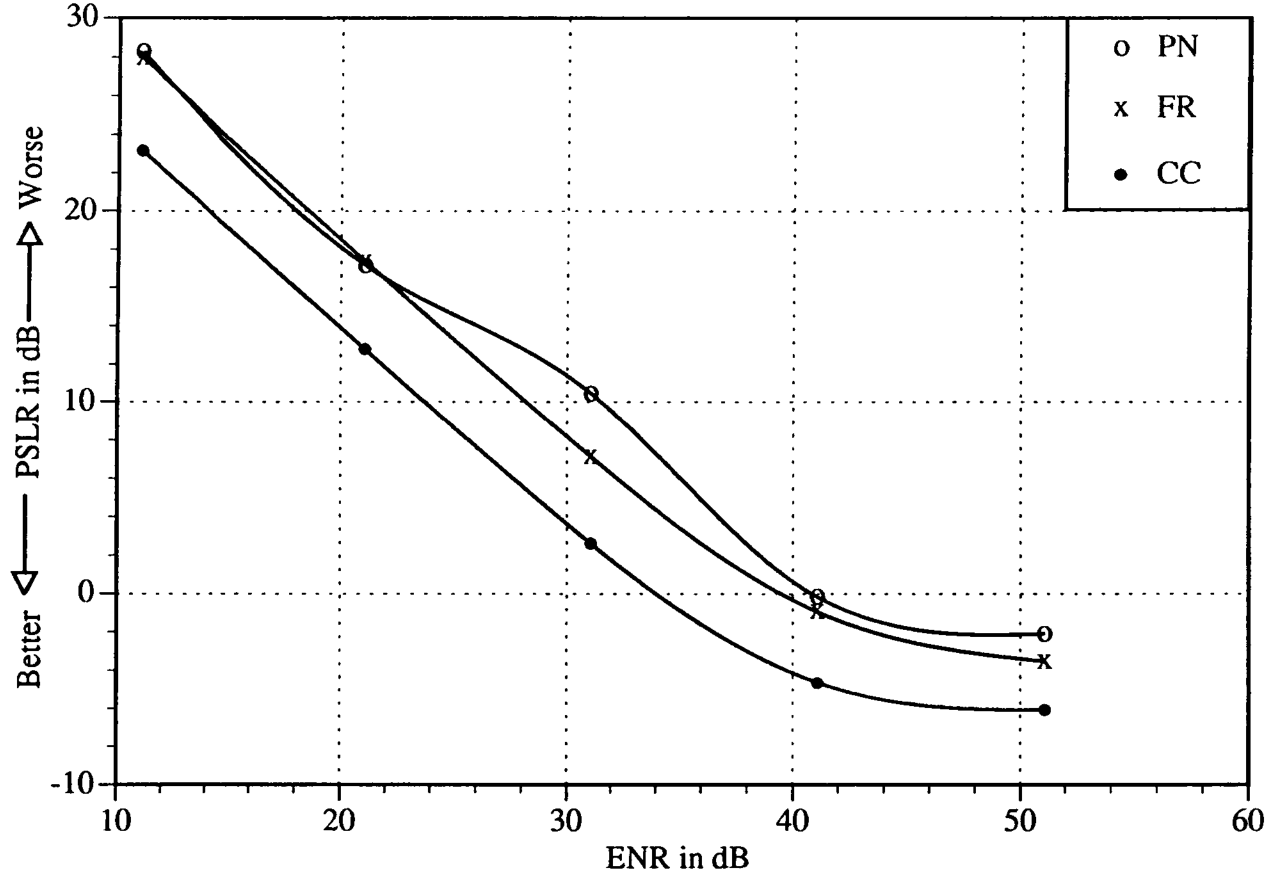

Figure A5.56. Comparison of the ISLR of 255/256-chip Codes in AWGN, Swerling I Target Fluctuation, and Fast Fading.

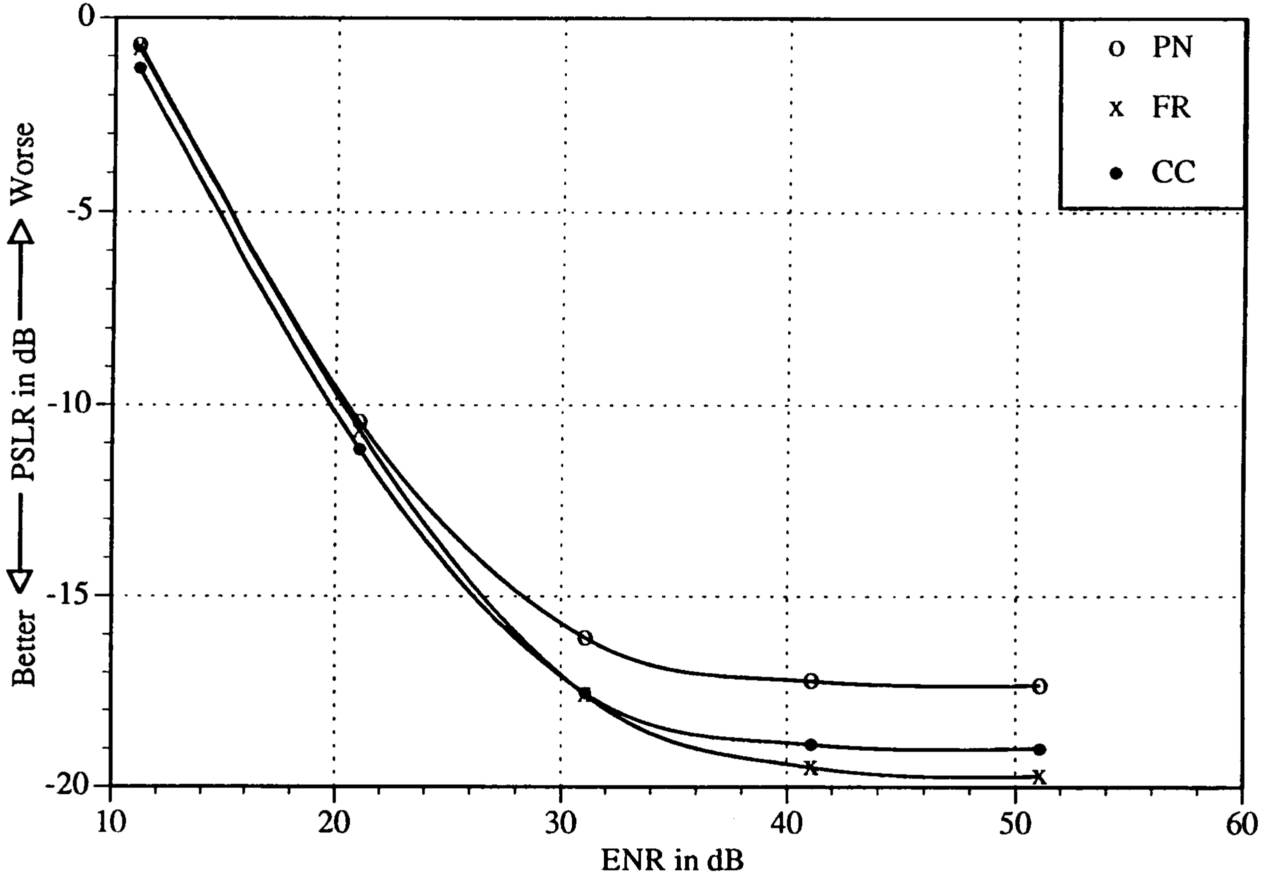

Figure A5.57. Comparison of the PSLR of 255/256-chip Codes in AWGN, Swerling II Target Fluctuation, and Fast Fading.

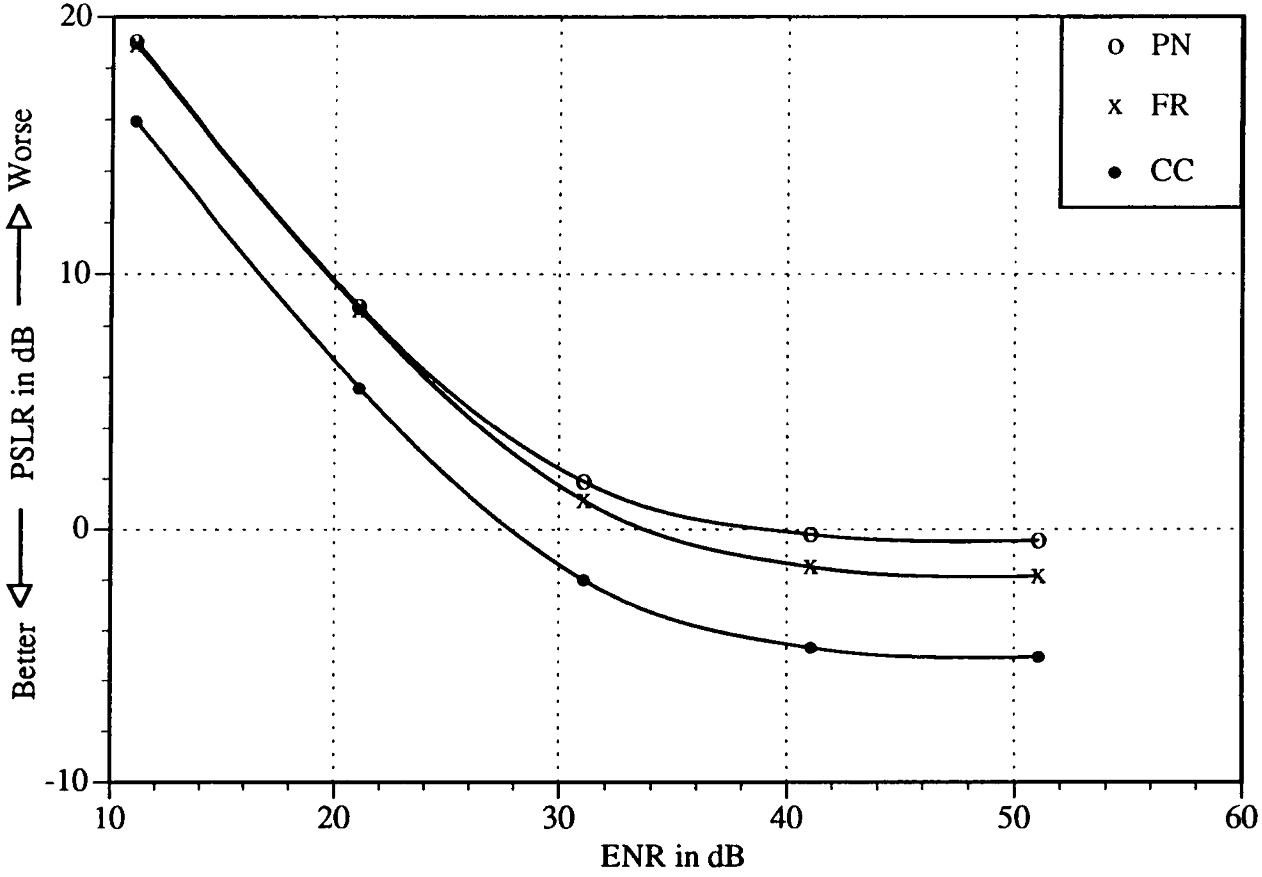

Figure A5.58. Comparison of the ISLR of 255/256-chip Codes in AWGN, Swerling II Target Fluctuation, and Fast Fading.

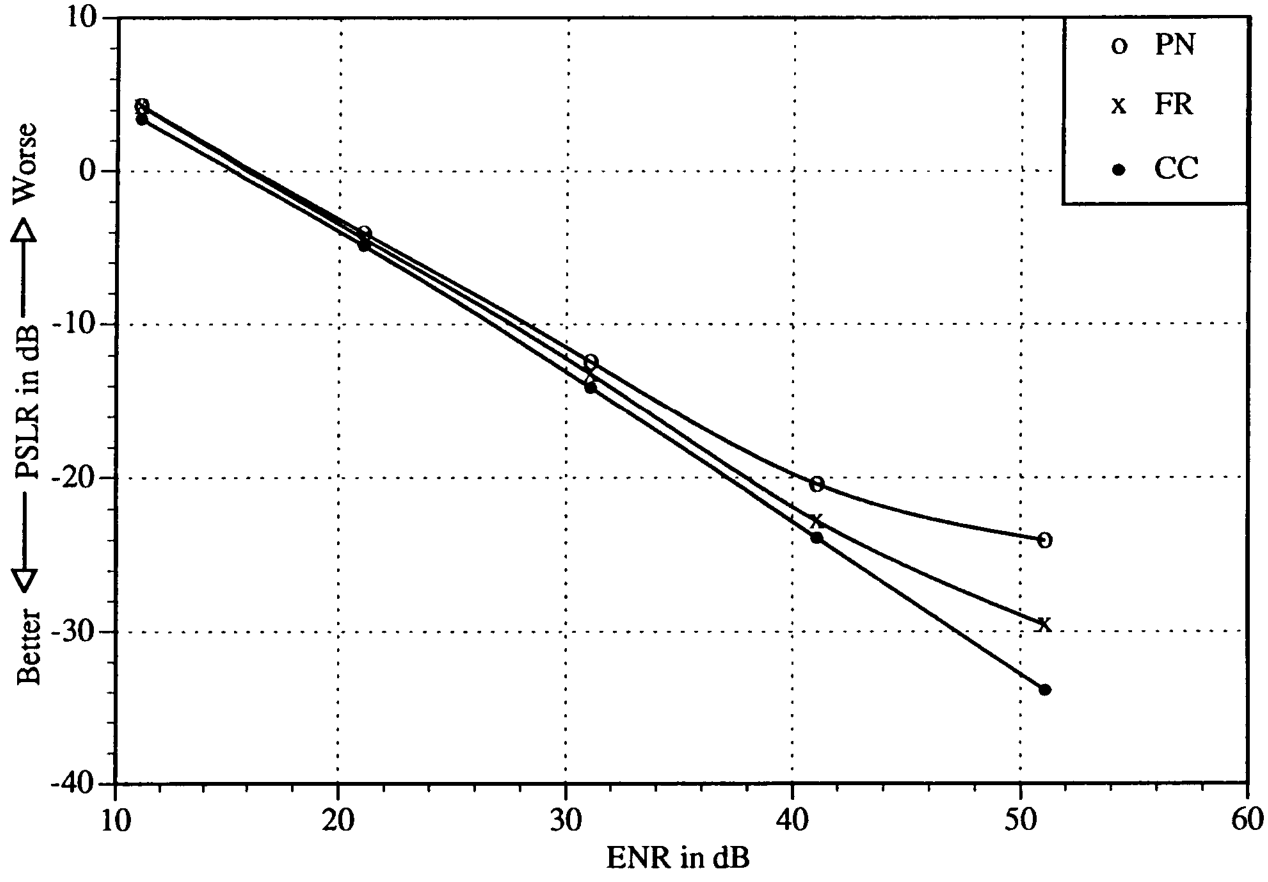

Figure A5.59. Comparison of the PSLR of 255/256-chip Codes in AWGN, Swerling I Target Fluctuation, and Slow Fading.

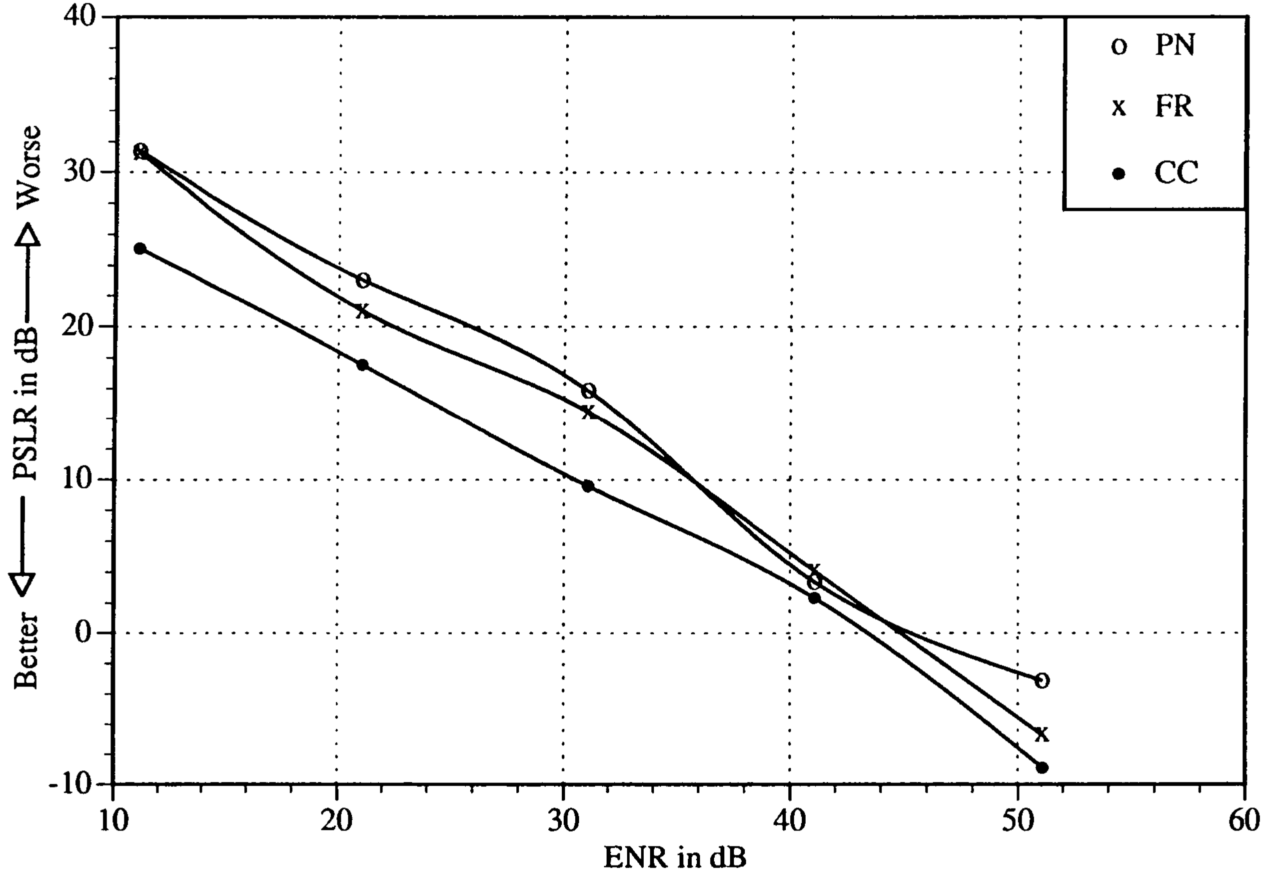

Figure A5.60. Comparison of the ISLR of 255/256-chip Codes in AWGN, Swerling I Target Fluctuation, and Slow Fading.

Appendix 6

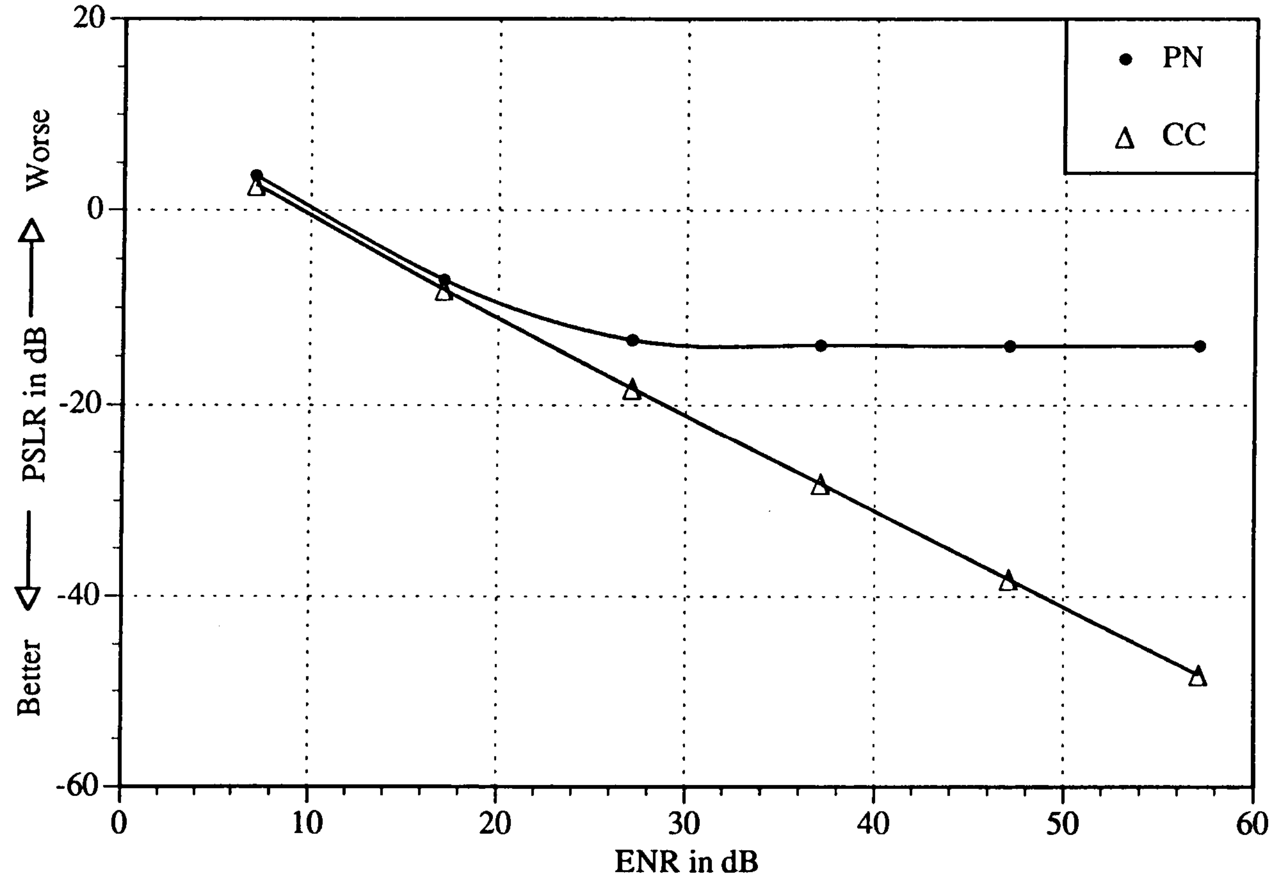

Figure A6.1. Comparison of the PSLR of Hybrid Coded Waveform in AWGN.

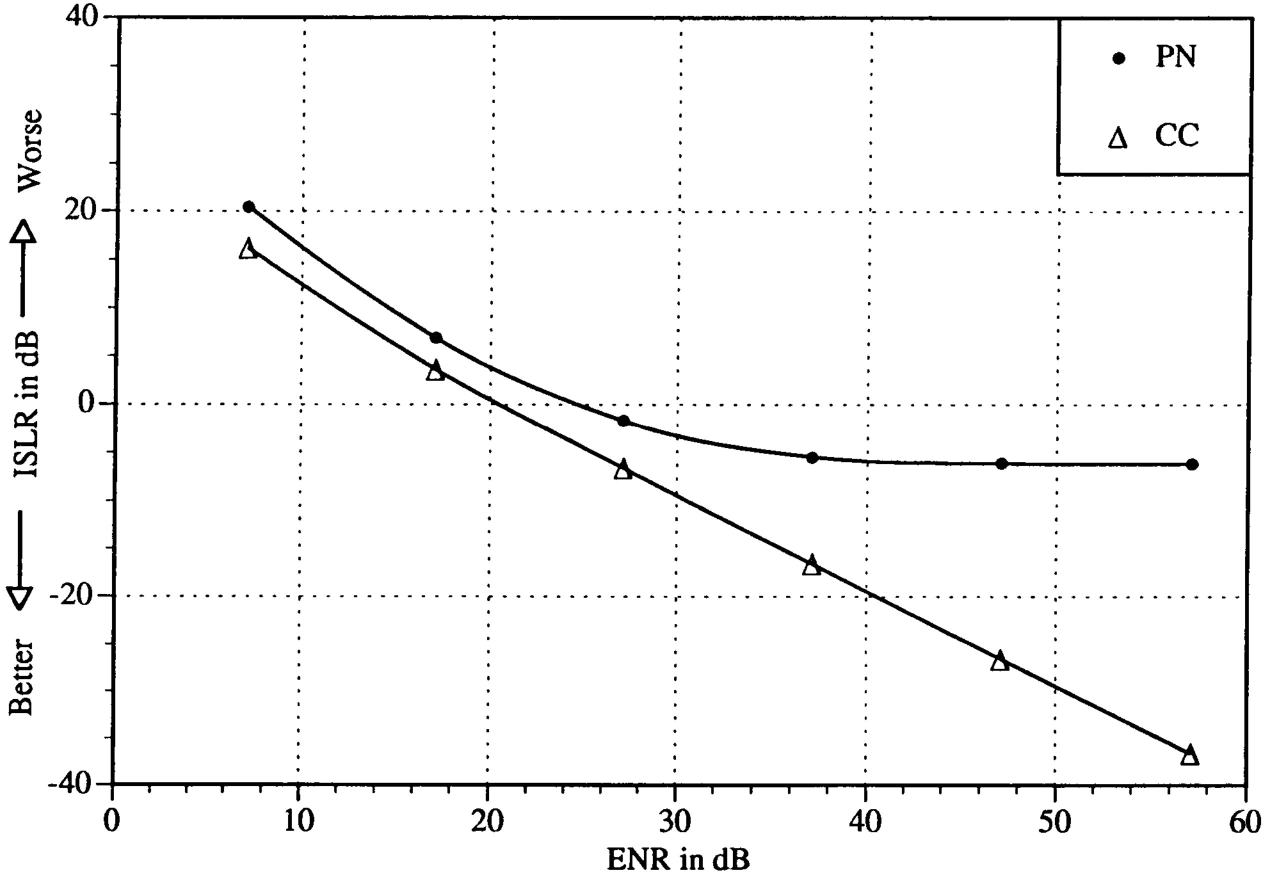

Figure A6.2. Comparison of the ISLR of Hybrid Coded Waveforms in AWGN.

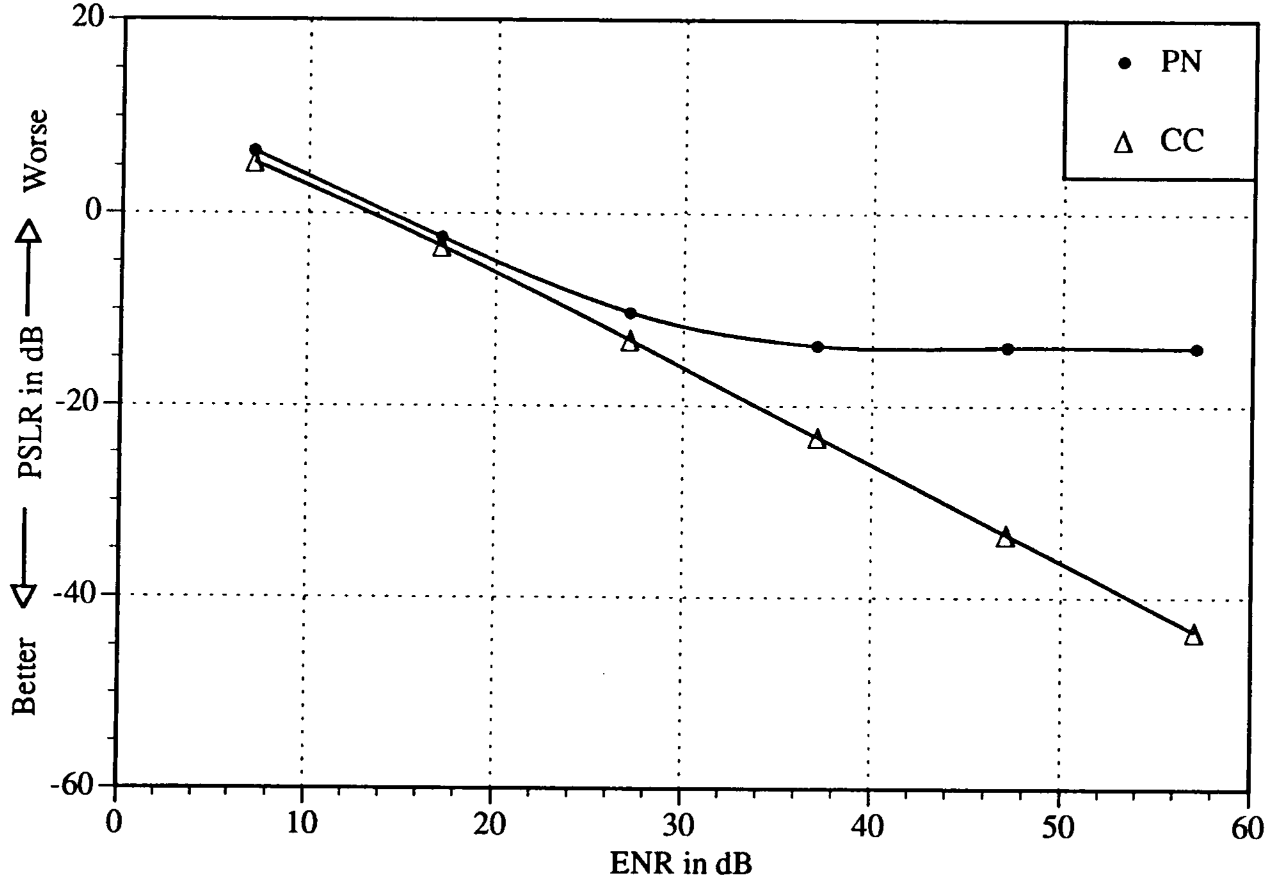

Figure A6.3. Comparison of the PSLR of Hybrid Coded Waveform in AWGN and Swerling I Target Fluctuation.

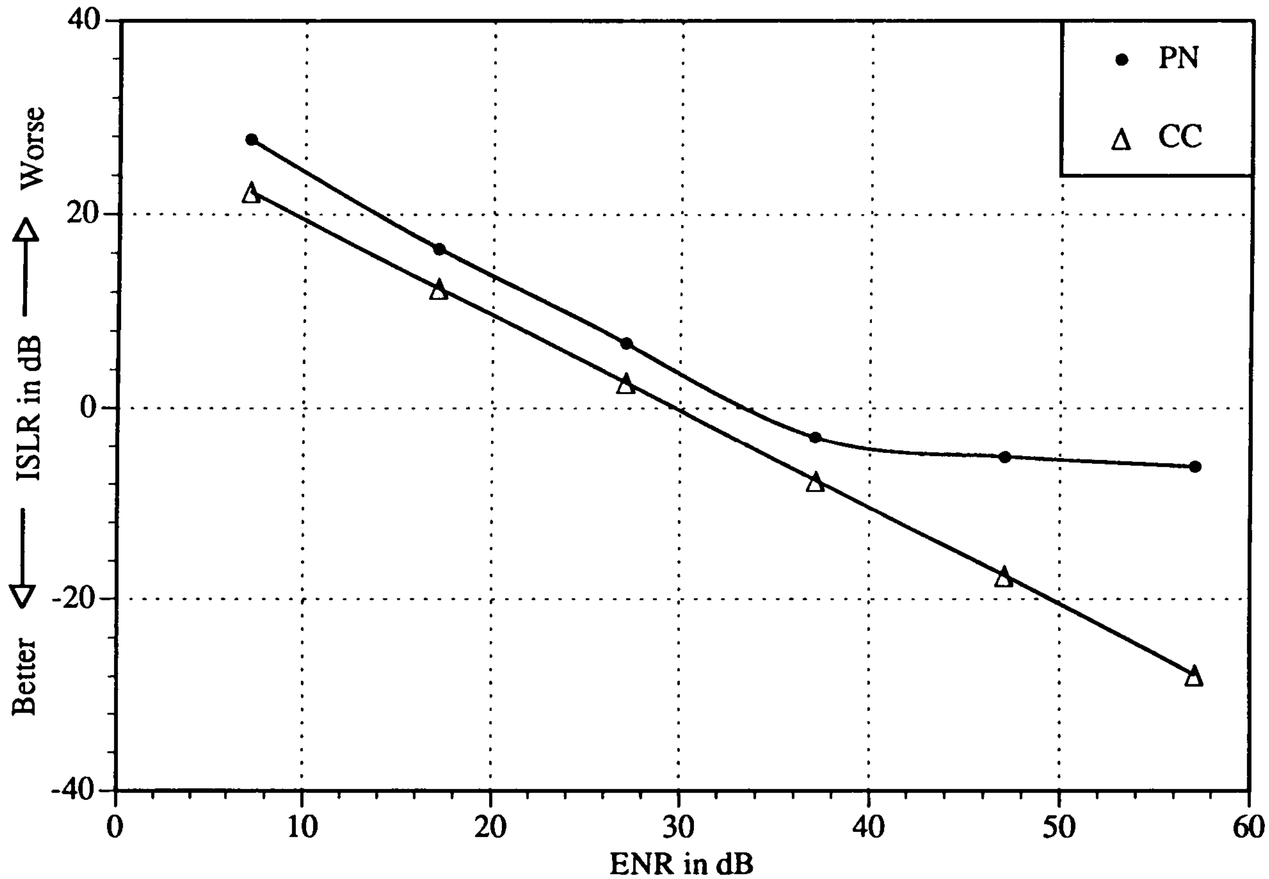

Figure A6.4. Comparison of the ISLR of Hybrid Coded Waveforms in AWGN and Swerling I Target Fluctuation.

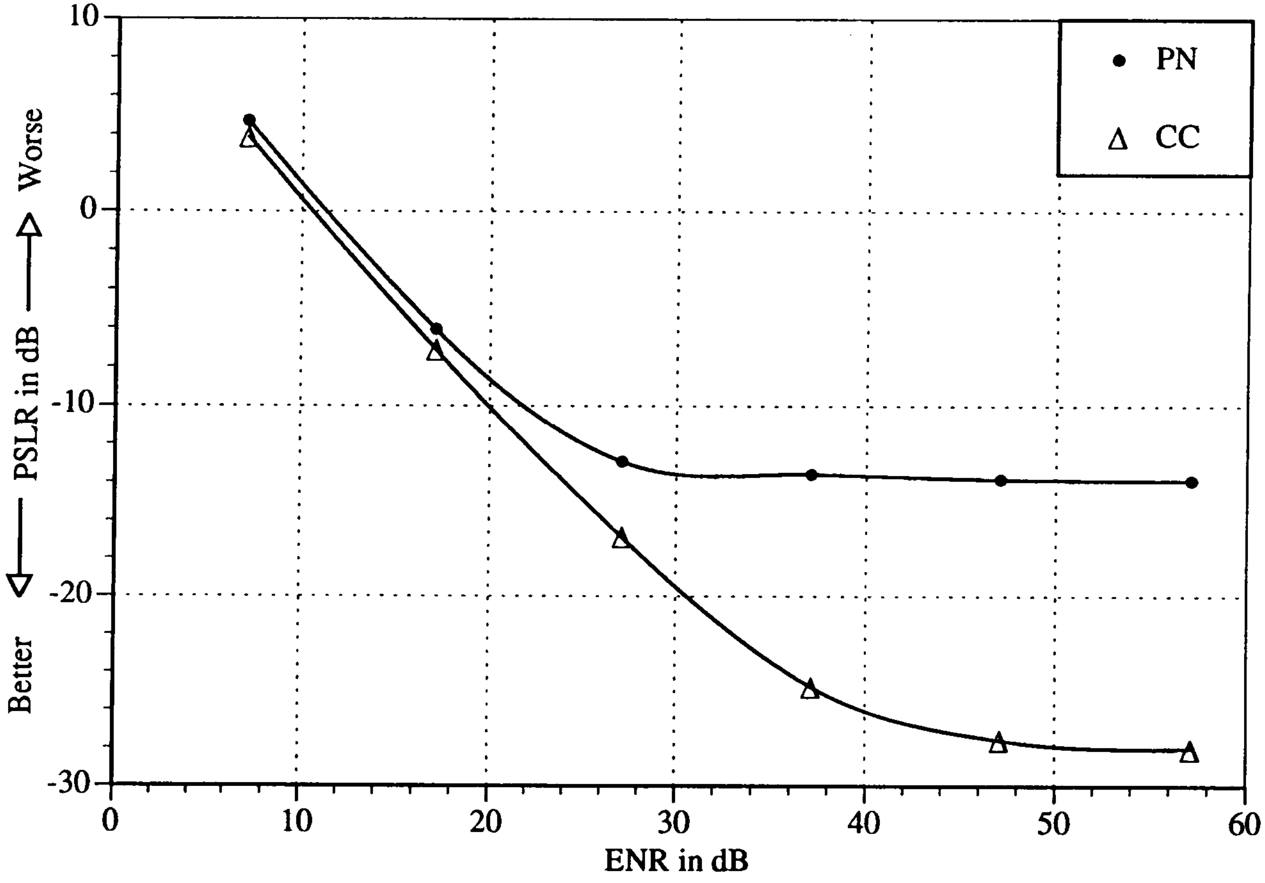

Figure A6.5. Comparison of the PSLR of Hybrid Coded Waveform in AWGN and Swerling II Target Fluctuation.

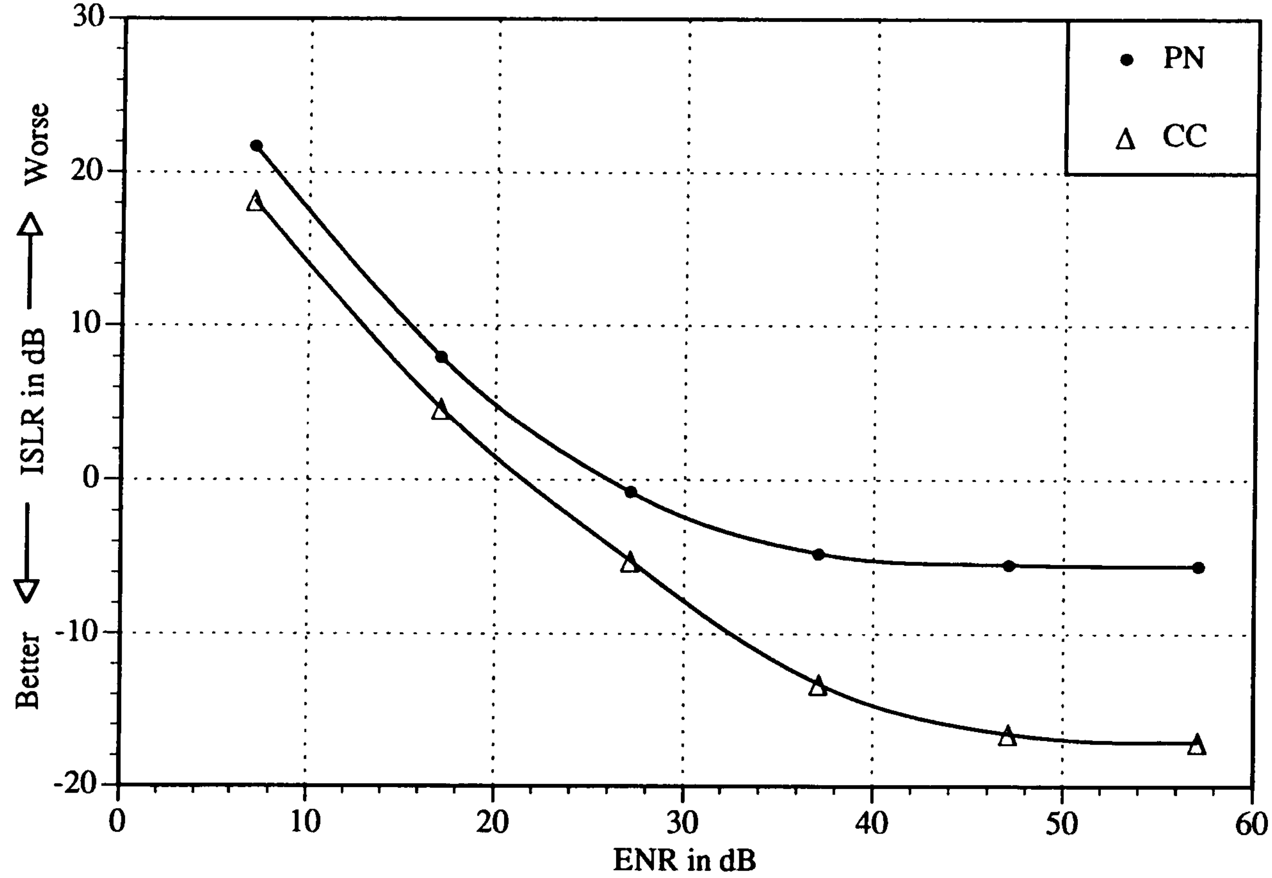

Figure A6.6. Comparison of the ISLR of Hybrid Coded Waveforms in AWGN and Swerling II Target Fluctuation.

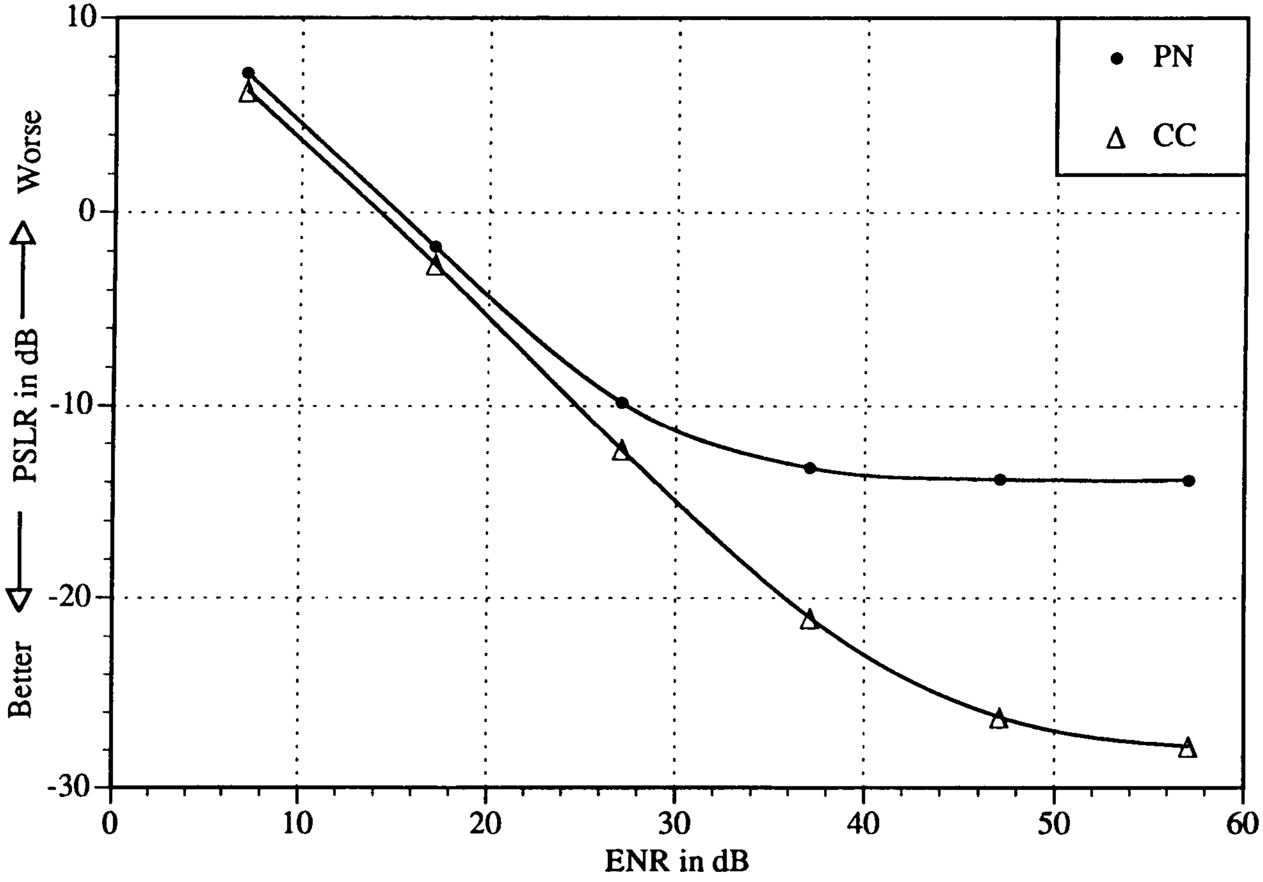

Figure A6.7. Comparison of the PSLR of Hybrid Coded Waveform in AWGN, Swerling I Target Fluctuation, and Fast Fading.

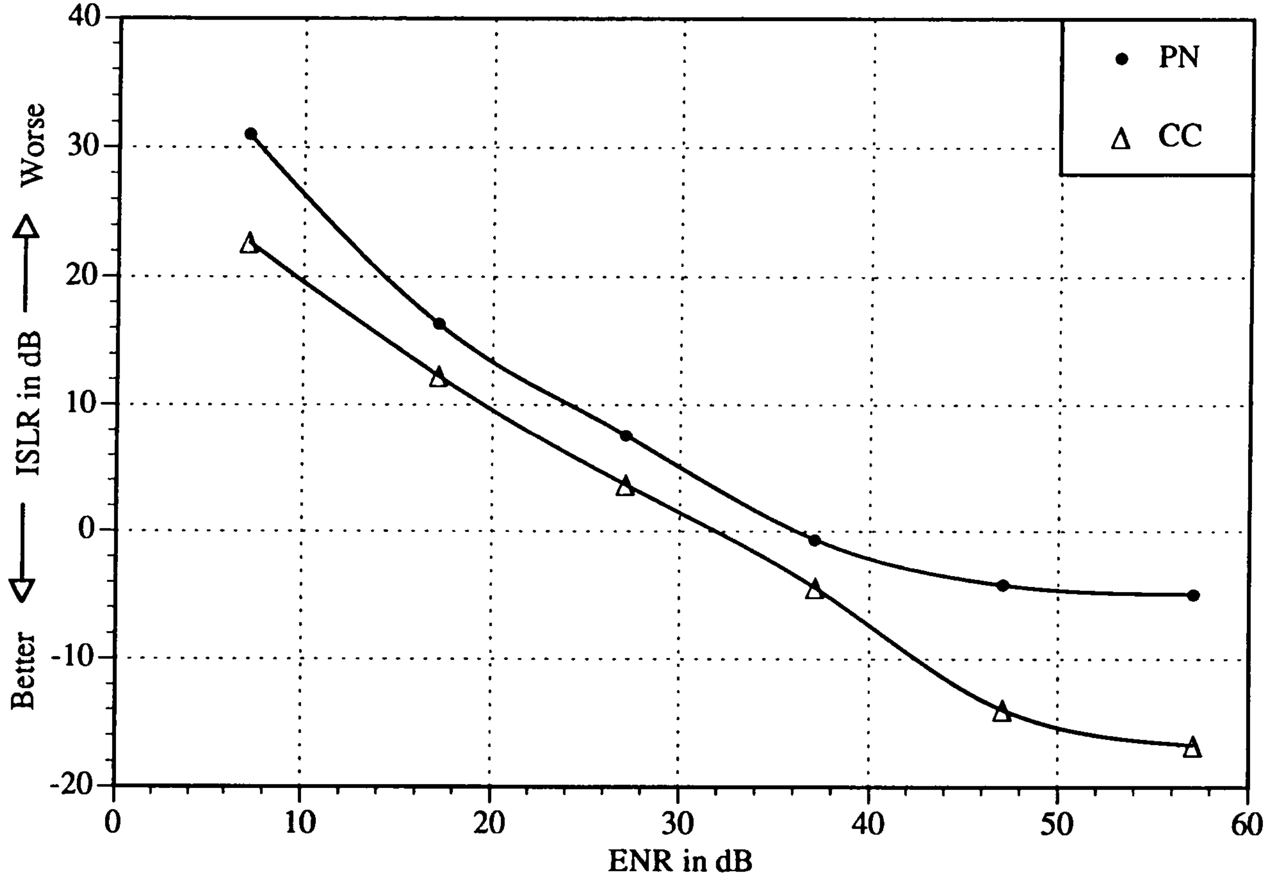

Figure A6.8. Comparison of the ISLR of Hybrid Coded Waveforms in AWGN, Swerling I Target Fluctuation, and Fast Fading.

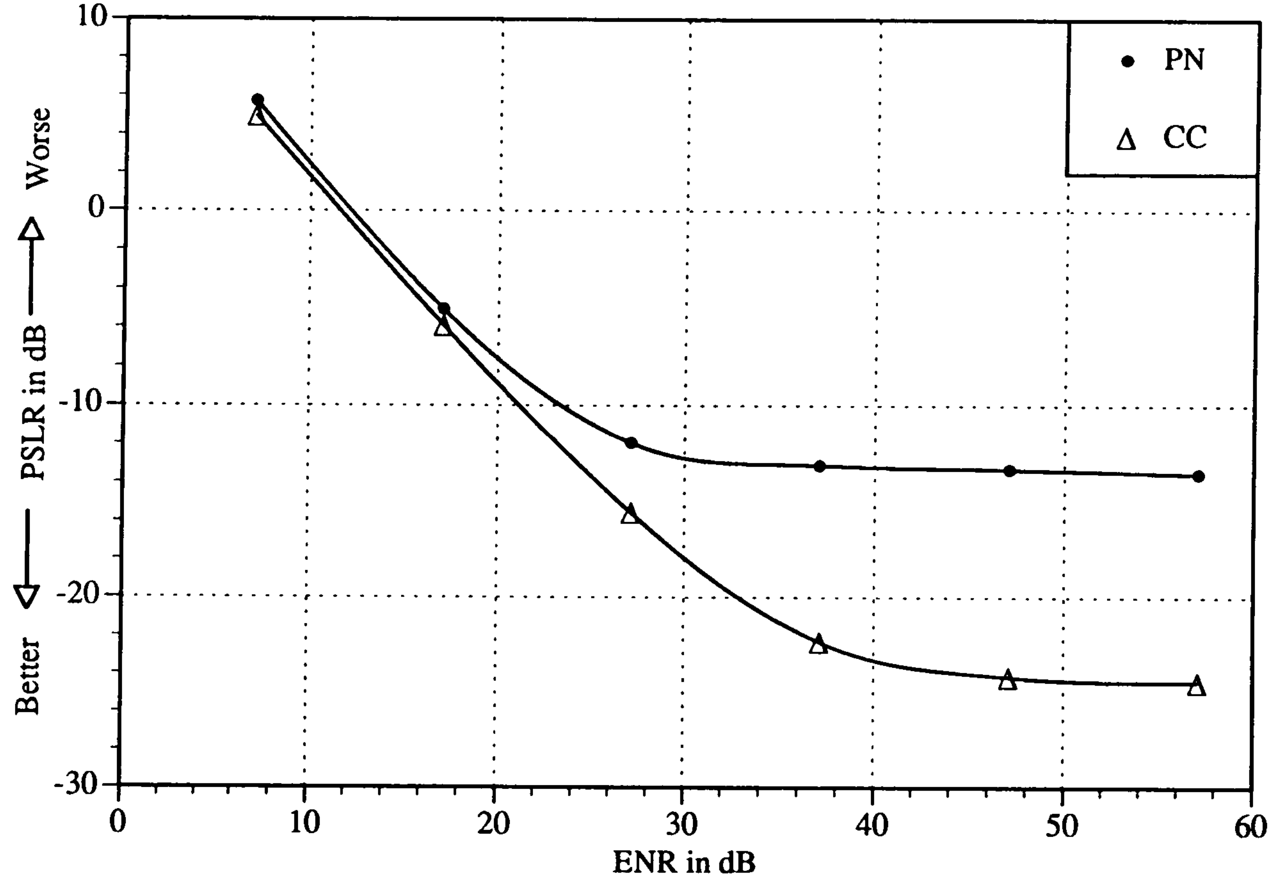

Figure A6.9. Comparison of the PSLR of Hybrid Coded Waveform in AWGN, Swerling II Target Fluctuation, and Fast Fading.

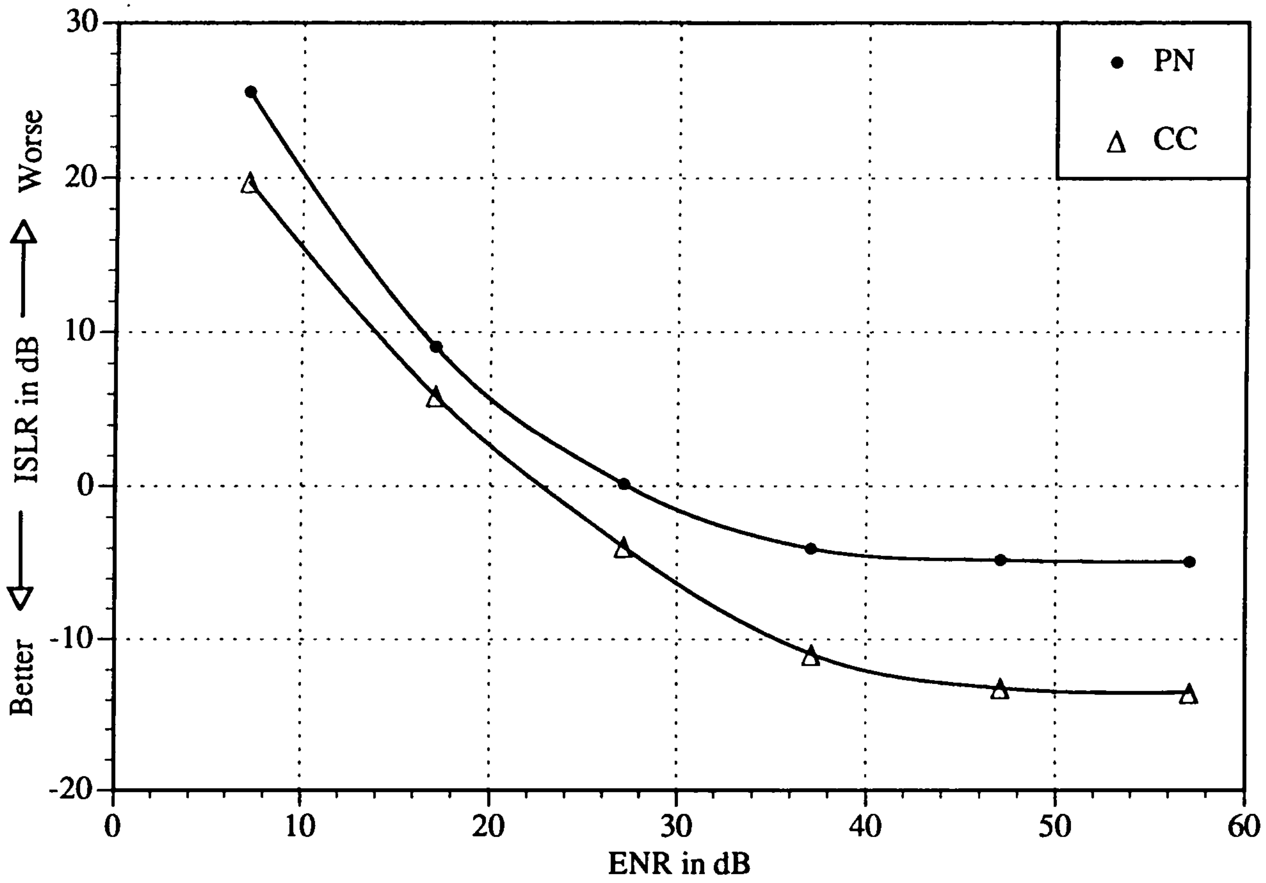

Figure A6.10. Comparison of the ISLR of Hybrid Coded Waveforms in AWGN, Swerling II Target Fluctuation, and Fast Fading.

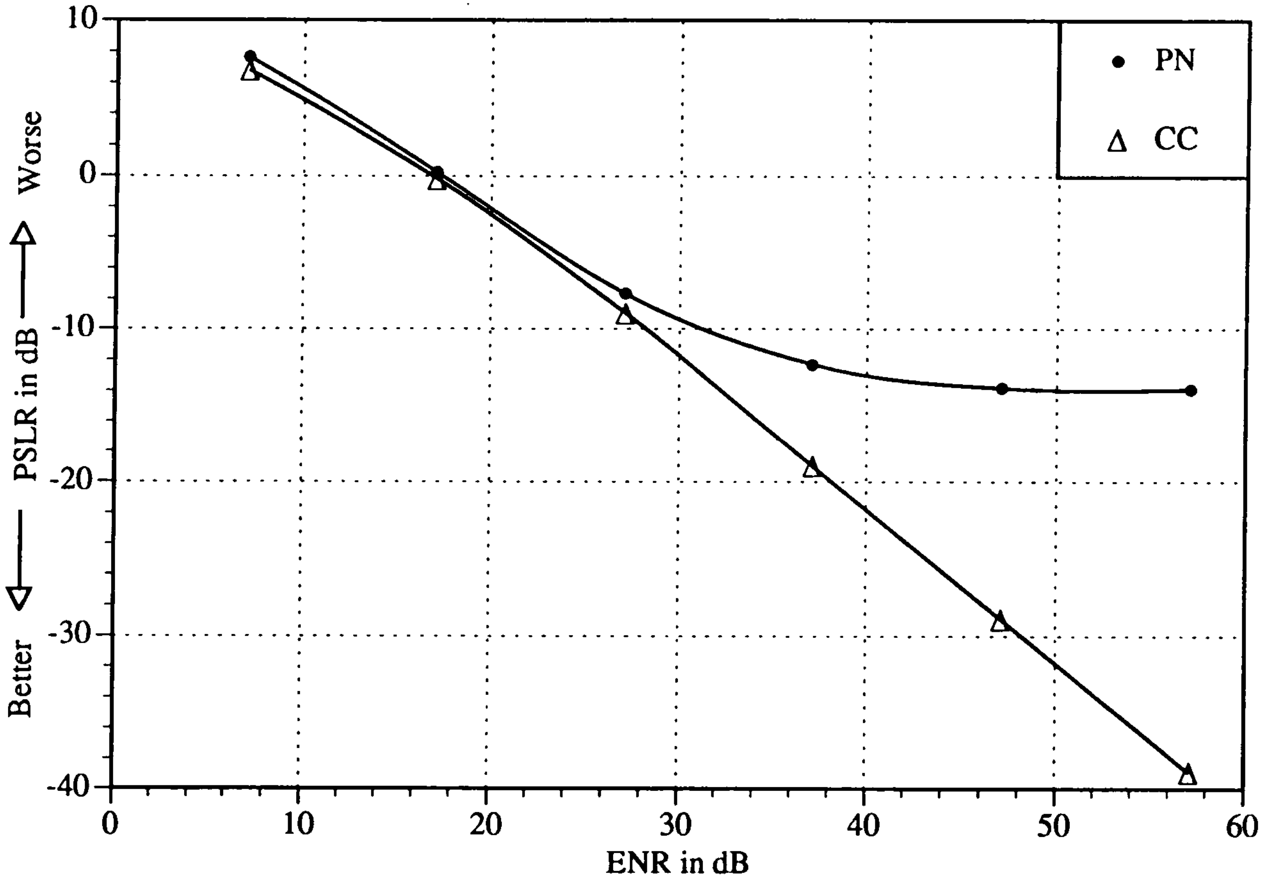

Figure A6.11. Comparison of the PSLR of Hybrid Coded Waveform in AWGN, Swerling I Target Fluctuation, and Slow Fading.

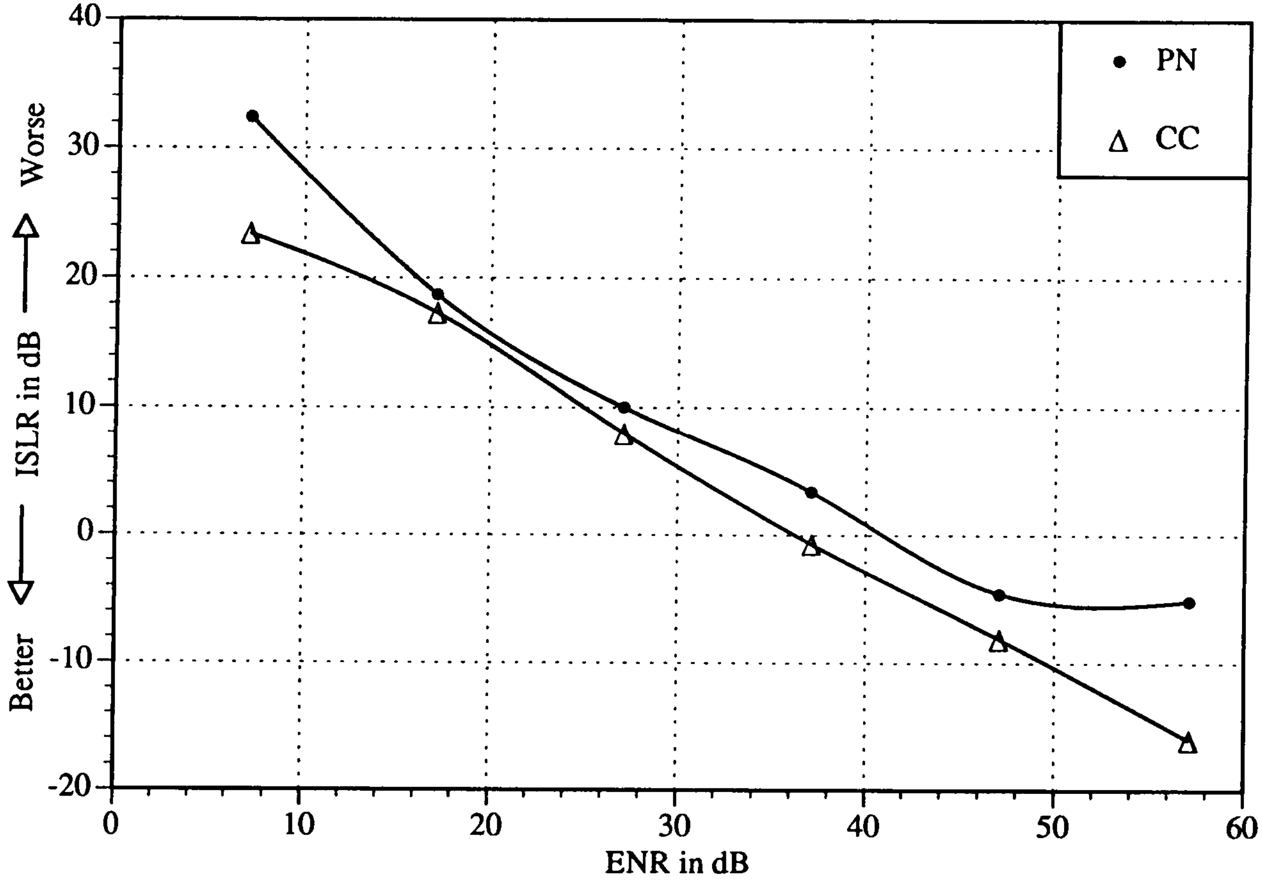

Figure A6.12. Comparison of the ISLR of Hybrid Coded Waveforms in AWGN, Swerling I Target Fluctuation, and Slow Fading.

VITA

Anand Kumar Ojha was born in Jhinkpani, India on May 3, 1951. After graduating from high school in 1967 with a National Merit Scholarship he enrolled at the Bihar Institute of Technology for undergraduate studies, and was awarded a B.S. in Electronics and Communications Engineering in 1973. In 1982, he immigrated to the United States and joined the graduate program in Electrical Engineering of Texas A & M University where he graduated from in 1985 with an M.S. in Electrical Engineering.

While a graduate student at the Texas A & M University, he worked part-time as a Master Control Operator at the KAMU-TV, as an Electronics Technician/Research Assistant in the Physics Department, and taught digital and analog electronics laboratories in the Electrical Engineering Department for five semesters.

His industrial experience includes working for one year (1973-74) in India as an Electrical Testing Engineer in the testing and commissioning of ignitron rectifier systems. He also worked for seven years (1974-81) in a broadcasting organization in India and was responsible for maintaining and testing of broadcasting equipment. During the Summer of 1985, he worked in the VLSI Modeling and Simulation Group of Texas Instruments. Prior to joining the Ph. D. program at the University of Tennessee in 1989, he was a faculty member in the Electronic Engineering Technology Department at the University of Arkansas - Little Rock from 1985 to 1989.

The author's research interests include communications, telecommunications, and networking. His mailing address is: 695 Manor View Dr., Knoxville, TN 37923.